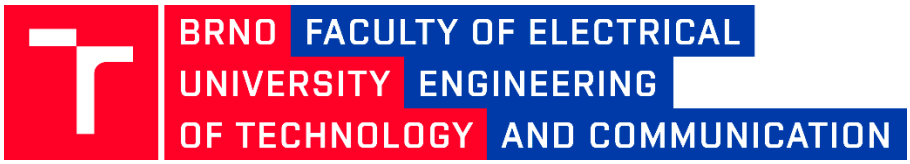

BRNO UNIVERSITY OF TECHNOLOGY
VYSOKÉ UČENÍ TECHNICKÉ V BRNĚ

FACULTY OF ELECTRICAL ENGINEERING AND COMMUNICATION
FAKULTA ELEKTROTECHNIKY A KOMUNIKAČNÍCH TECHNOLOGIÍ

DEPARTMENT OF MICROELECTRONICS
ÚSTAV MIKROELEKTRONIKY

LOW ENERGY SOLID STATE CONVERTERS FOR ENRGY HARVESTING

NÍZKOENERGETICKÉ MĚNIČE V PEVNÉ FÁZI PRO ENERGY HARVESTING

DOCTORAL THESIS
DIZERTAČNÍ PRÁCE

AUTHOR
AUTOR PRÁCE
Ing. Laila Znbill

SUPERVISOR
ŠKOLITEL
Prof. Ing. Jaroslav Boušek, CSc.

BRNO 2021

Abstract

The work aims to extension of existing knowledge towards new suggested and tested concepts of Energy Harvesting converters working on energy level deep below 1 W. Two types of DC/DC converters with lowest input voltage less than 100 mV have been designed and prototyping. The possibility to be connected in parallel to one load is advantageous when processing energy from multiple sources with unstable power and possible outages. Complementary circuits have been tested for the designed and manufactured single J-FET DC to DC converter, which enable a significant increase in efficiency reaching up to 50 percent. Two types of innovative transformers with extremely high conversion ratio have been designed for low-voltage DC to DC converters. The conversion ratio can be larger than 100 and stray inductance on the secondary winding can be simply controlled by design options. In testing process of the photovoltaic cells series resistance and leakage resistance were measured using a new dynamic method. A great advantage of this method is the possibility of measurement of parasitic resistances of the cell in the dark without the use of special instruments. In design of thermoelectric generator, the lowest possible series resistance of functional layers is a major design problem because the voltage of one thermocouple is very small and large number of thermocouples connected in series is required. The new contribution is the optimized arrangement of active layers of organic thermoelectric generator using PEDOT:PSS-Ni thermocouple. The proposed assembly enables the series connection of large number of thermocouples while achieving a low series resistance of the entire thermoelectric generator. The individual thermocouples are placed on the carrier tape and the scaling-up is made by winding the carrier tape into the coil. The number of connected thermocouples is limited only by the total series resistance of the resulting thermoelectric generator. In practice, the number of thermocouples connected in series is 60 to 100 depending on the current being processed.

Key words

Energy Harvesting, photovoltaic cell, photovoltaic single cell, thermoelectric generator, low voltage DC/DC convertor, organic semiconductors.

Abstrakt

Práce si klade za cíl rozšířit stávající znalosti o nové navrhované a vyzkoušené koncepce převodníků pro získávání energie na energetické úrovni hluboko pod 1 W. Byly navrženy a vyzkoušeny dva typy měničů DC / DC s nejnižším vstupním napětím menším než 100 mV. Možnost paralelního připojení k jedné zátěži je výhodná při zpracování energie z více zdrojů s nestabilním výkonem a možnými výpadky. Byly testovány doplňkové obvody pro navržený a vyrobený DC / DC měnič "single J-FET", který umožňuje výrazné zvýšení účinnosti dosahující až 50 %. Pro nízkonapěťové stejnosměrné měniče byly navrženy dva typy inovativních transformátorů s extrémně vysokým převodním poměrem. Převodový poměr může být větší než 100 a rozptylová indukčnost na sekundárním vinutí může být jednoduše ovládána konstrukčními úpravami. V procesu testování fotovoltaických článků byl pomocí nové dynamické metody měřen sériový odpor článku a paralelní odpor článku. Velkou výhodou této metody je možnost měření parazitního odporu buňky za tmy bez použití speciálních přístrojů Pro konstrukce termoelektrického generátoru je hlavním konstrukčním problémem dosažení co nejnižšího sériový odporu funkčních vrstev, protože napětí jednoho termočlánku je velmi malé a je vyžadován velký počet termočlánků zapojených do série. Novým příspěvkem je optimalizované uspořádání aktivních vrstev organického termoelektrického generátoru pracujícího s termoelektrickou dvojicí tvořenou materiály PEDOT:PSS a Ni. Navrhovaná sestava umožňuje sériové spojení velkého počtu termočlánků při dosažení nízkého sériového odporu celého termoelektrického generátoru. Jednotlivé termočlánky jsou umístěny na nosnou pásku navinutou do cívky. Počet takto spojených termočlánků je omezen pouze celkovým sériovým odporem výsledného termoelektrického generátoru. V praxi je počet termočlánků zapojených do série 60 až 100 v závislosti na zpracovávaném proudu.

Klíčová slova

Energy harvesting, fotovoltaický článek, fotovoltaický článek v konfiguraci single cell, termoelektrický generátor, nízkonapěťový DC/DC převodník, organické polovodiče.

Bibliographic citation
Znbill, L.: *Low Energy Solid state Converters for Energy Harvesting*, Brno University of Technology, The Faculty of Electrical Engineering and Communication, 2021, 187 p, Supervisor prof. Ing. Jaroslav Boušek, CSc.

Declaration

I declare that I have written my doctoral thesis on the theme of *"Low Energy Solid state Converters for Energy Harvesting"* independently, under the guidance of the doctoral thesis supervisor and using the technical literature and other sources of information which are all quoted in the thesis and detailed in the list of literature at the end of the thesis.

As the author of the doctoral thesis I furthermore declare that, as regards the creation of this doctoral thesis, I have not infringed any copyright. In particular, I have not unlawfully encroached on anyone's personal and/or ownership rights and I am fully aware of the consequences in case of breaking Regulation § 11 and the following of the Copyright Act No 121/2000 Sb., and of the rights related to intellectual property right and changes in some Acts (Intellectual Property Act) and formulated in later regulations, inclusive of the possible consequences resulting from the provisions of Criminal Act No 40/2009 Sb., Section 2, Head VI, Pt. 4.

Brno, 15 June 2021

_____

Ing. Laila Znbill Author's signature

Acknowledgements

There are lots of people affecting my studies and creating this dissertation who helped me to not only with the thesis but also during the whole PhD studies.

Before anything else, I would like to express the deepest thanks to prof. Ing. Jaroslav Boušek, CSc. for supervising, advising and mentoring my PhD studies. His guidance helped me during the whole time of research and writing of this thesis.

My sincere thanks then go to research teams of Faculty of Electrical Engineering and Communication of Brno University of Technology as well as Faculty of Chemistry of Brno University of Technology for enabling me to do the study and experimental part of the work.

Finally, I would like to thank to my husband and my family for their continuous support during my studies and for continuous believing in me.

This work was supported by projects of Internal Grant Agency: no. FEKT-S-14-2300, "The new types of electronic circuits and sensors for specific applications", and no. FEKT-S-17-3934, "Utilization of novel findings in micro and nanotechnologies for complex electronic circuits and sensor applications".

Content

Introduction

Energy harvesting (EH) is the process by which energy is derived from external sources and stored for feeding of small autonomous devices. In most applications an energy harvesting device puts generated power into a capacitor then the voltage is boosted and stored energy is brought to a second stage with a storage capacitor or battery for the use in the electronic circuits.

In the coming years there is expected an increasing demand for energy harvesting systems in the industrial countries with the perspective of further development to drive the market for more advanced energy harvesting system. Level of manufacturing technology of energy harvesting system is higher than by some traditional equipment. Consequently, many semiconductor companies, as STMicroelectronics, Texas Instruments, Linear Technology or Maxim for example, build their energy harvesting systems.

This work is focused on gaining new knowledge and experience in the field of Energy Harvesting converters working on energy level deep below 1 W. Energy harvesting transducers based on photovoltaic cells and thermoelectric cells, which can work at these energy levels, were investigated. The advantages of these transducers are easy availability of defined power sources, quiet operation, and relatively long lifetime. They also do not need any mechanical and moving parts and, also, there is the possibility of mass production using technologies available in microelectronics. These types of converters were considered for their production with perspective organic semiconductor materials.

Based on the result of experiments and knowledge acquainted by a study of literature for testing EH transducers with photovoltaic cells a single cell option was used. In this case the mutual interference of the individual cells occurring in series connection is suppressed. The design of the entire EH converter is then simpler. In testing process of the photovoltaic cells series resistance and leakage resistance were measured using a new dynamic method which is very simple and uses standard measuring instruments.

Because the voltage of one thermocouple is very small, large number of thermocouples connected in series is required. Therefore, in design of thermoelectric generator, the lowest possible series resistance of functional layers is a major design problem. Consequently, in design of organic thermoelectric generator which is based on PEDOT:PSS-Ni thermocouple new contribution is the optimized arrangement of active thermoelectric layers which enables the series connection of large number of thermocouples while achieving a low series resistance of the entire thermoelectric generator.

However, in case of both thermoelectric generators and single photovoltaic cells EH transducers the output voltage is at the level of a few tenths of a volt. Such voltage level is not enough for common electronic devices and therefore a DC to DC boost up converter capable of handling extremely low input voltages must be used. Two types of DC/DC

converters have been designed for this purpose with lowest input voltage less than 100 mV. The possibility to be connected in parallel to one load is advantageous when processing energy from multiple sources with unstable power and possible outages. Further, to convert very small input voltage to a level of few volts sufficient for standard electronic devices the proposed autonomous DC/DC converters must use transformers with extremely high conversion ratio. New types of this transformers with conversion ratio that can be larger than 100 have been designed for this purpose.

The solved task is very extensive and includes physical and material issues of photovoltaic transducers and thermoelectric transducers and their production processes, as well as issues of design of DC to DC converters, including transformers and control circuits. The text of the thesis therefore summarizes the most important results and details are given in the Appendixes.

1 State of the art

The harvested energy could be generated from motion, solar radiation, thermal gradient, wind, salinity gradients, vibrations, magnetic activity, radiofrequency fields, etc. The energy source for energy harvesters is present as ambient background and is free.

1.1 Principles of EH converters

If the demands on the amount of transformed energy are not too high, many energy sources for Energy Harvesting (EH) can always be found. To ensure reliability, it is sometimes beneficial to draw energy from multiple sources due to the time distribution of their activity. For each type of energy can be found the appropriate type of converter, for example, magnetic sensors for sensing mechanical movement, piezoelectric sensors for vibration and specialized electrode systems for extraction of the energy from chemical activity. Examples of different types of EH transducers can be found elsewhere [67].

Solid state converters for photovoltaic and thermoelectric power generators used for experiments in this work will be mentioned hereunder.

Photovoltaic Energy harvesting

Photovoltaic Energy harvesting is a mature technology for large scale energy generation. Photovoltaic systems are found from the megawatt to the microwatt range producing electricity for wide range of applications. The operation of photovoltaic (PV) cell requires three basic attributes:

1. The absorption of light, generating electron-hole pairs or excitons.
2. The separation of charge carriers of opposite types.
3. The separate extraction of those carriers to an external circuit.

Thermal Energy harvesting

Thermoelectric modules are the main means of harvesting energy from temperature gradients and can generate electric output energies ranging from μW to kW. Temperature gradient leading to heat flow through thermoelectric generators is here converted into electric energy. Thermoelectric material properties are the key parameters in improving both the output power and the power efficiency.

Although the thermoelectric phenomena are used for measurement of temperature and cooling applications quite extensively, thermo-generation of electricity starts to grow only in recent years. Such energy sources are well predictable because they are usually based on stable environmental conditions or stable operation of respective devices.

Thermoelectric Generators (TEGs) are therefore very attractive for possibility of harvesting of waste thermal energy in many applications.

1.2 Processing of the output of EH transducers

The energy harvesting transducer is in most cases not able to supply enough power for continuous operation of relevant devices. Thus the energy needs to be stored until there is enough for operation of the application. Energy harvesting power supply, consisting of energy harvester, converter and storage element needs to fulfill the demand on the output voltage, which is usually in range from 1.5 V DC to 3.5 V DC.

1. Many EH transducers provide a low output voltage, in some cases much less than 1 V. Consequently, there is a great need for converters able to process as low voltages as possible. For DC sources, like single-cell photovoltaic modules and thermal generators, charge pumps can be used to slowly boost the voltage to level usual for regular boost converters. AC sources like vibration harvesters needs to be tuned to their resonance frequency and the voltage needs to be rectified.
2. In low power converters charging the parasitic capacitance of the MOSFET switch could consume a large part of the harvested energy. Therefore, a current-source for gate voltage control rather than a voltage-source is often used.
3. Another technique is to use more than one power converter circuit. The first circuit could be unregulated but capable to boost the output voltage and charge the output capacitor. Once sufficient energy is stored the capacitor it can be used by a more sophisticated power converter circuit.

1.2.1 Types and characteristics of DC/DC converters

For utilization of thermoelectric-generator it is necessary to consider that the output voltage of one thermoelectric element is very small. Even with the integration of many thermoelectric elements in series is not possible to increase the voltage to a level applicable to power conventional electronic circuits. A similar situation can occur with single-cell solar panels applications. The output voltage of multiple-thermo-generators is in order of few tens of mV and the output voltage of single-cell photovoltaic modules or fuel cells is typically less than 0.5 V [12, 23].

This means that there is still a gap between output voltage of some energy transducers and minimum input voltage of low voltage converters which is typically greater than 0.7 V. For optimal use of energy harvesters is therefore necessary to use a DC to DC voltage converter with extremely low input voltage. As a reaction to this problem threshold voltages of semiconductor technologies are scaled down and special low-threshold

voltage transistors are dedicated for ultralow voltage DC/DC converter architectures [30, 34]. We can call this type of converters autonomous.

In majority of cases the energy harvesters have an irregular release of energy and low output voltage. Therefore, they mostly have a build in power regulation that scales up the voltage making it suitable for the relevant applications. Those converters usually cannot start up below a certain input voltage and need a battery for reliable operation. We can call this type of converters non-autonomous. They are often in the form of integrated circuits.

Ultra-low start up voltage oscillator consequently needs to have a very low control voltage. A J-FET transistor is best for this purpose because it is conducting at a zero-gate voltage and can have a low gate threshold voltage when compared to a MOSFET. Example of circuit two possible circuit connections is shown in the Fig.1.

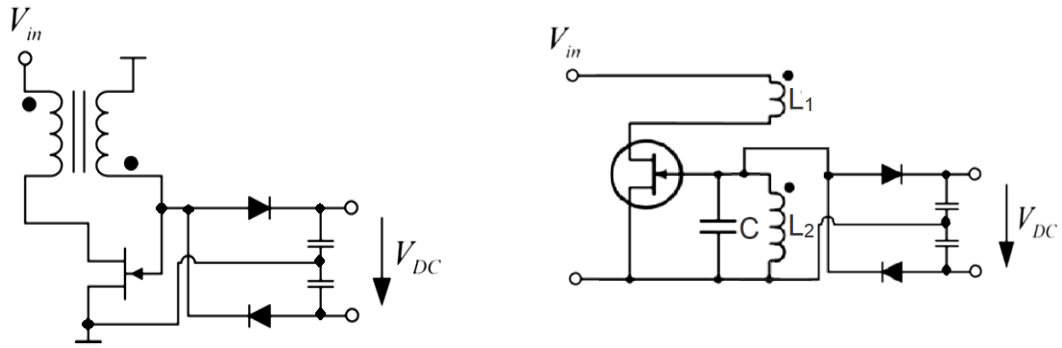

a) **b)**

Fig. 1: Schematic of DC/DC converters containing the voltage-doubler circuit [3]:
a) Relaxation oscillator. **b)** Armstrong oscillator.

When the gate voltage is V_{GS} = 0V the J-FET works with highest possible trans-conductance. Power supply voltage could be very low, typically in the range of some tens of mV. The output voltage is boosted with high transformer ration or (and) by oscillations. A rectifier needed to convert AC output voltage to DC level can be also connected as a voltage multiplier to increase the output voltage.

Power losses in the transformer are summarized in Chapter 1.2.3. The J-FET power losses can be summarized as follows [58, 59]:

1) During the on/off cycle, the parasitic capacitances of the transistor must be charged and discharged. Power loss is:

$$P = \frac{1}{2} C \cdot V^2$$

2) The resistance of the J-FET in ON-state is in order of tens of Ohms. The current flowing here causes a power loss:

$P = R \cdot I^2$

3) The N-channel J-FET used in the connections according to the figure Fig.1 is controlled by a negative voltage. If the polarity of the voltage at the gate of the transistor changes to positive the gate-channel junction of the transistor opens and the forward current of the junction will flow into the gate. Power loss is:
$P = V \cdot I$

1.2.2 Integrated circuits for energy harvesting

Integrated circuits for low voltage converters implement boost converters that require only microwatts of power to begin the operation:

The boost converter implemented in integrated circuit BQ25504 from Texas Instruments can start with input voltage as low as 330 mV. Once started, it can operate down to input voltage 80 mV [169].

Other types for example LTC3107, LTC3108 and LTC3109 from Linear technology, or MAX17710 from Maxim take power supply from output voltage [13, 24]. Therefore, to start up they usually need the external battery. Advantage of this design is that the input voltage could be extremely low. Basic properties of typical integrated circuits are listed in table Tab.1.

Tab. 1: The properties of some low voltage converters on the market

TYPE		Start Voltage	Lowest Voltage	Need power supply	Efficiency / Standby	
BQ25504		330 mV	80 mV	NO	> 50%	0.33 μA
LTC3108		-	20 mV	YES	> 50%	6 μA
MAX17710		-	750 mV	YES	> 50%	1.3 μA

For low voltage converters the required voltage levels are well below the standard voltage of commonly used technologies. Careful circuit modeling must be done to show if the conditions necessary for reliable operation can be fulfilled.

As the integration density increases, the supply voltage naturally decreases. However, special measures are required to use these technologies to process extremely low voltage. Generally, the Low Voltage (LV) or Ultralow Voltage (ULV) design techniques have certain performance limitations such as gain bandwidth (GBW) degradation, increased input noise, increased input impedance or decreased overall transconductance [16, 17].

Operation in sub-threshold region

As to the feasibility of LV design techniques in different technologies, it is advantageous to use techniques employing MOS transistors operating in the sub-threshold region, such as BD MOS transistors and DT MOS transistors, because there is no need for modification of a standard CMOS process technology. Additionally, with those two LV techniques, also low power consumption of designed circuits can be achieved [23,26].

Bulk driven transistors

Drain current I_D of a conventionally connected MOS transistor is usually controlled by the gate-source voltage V_{GS}. In the bulk-driven (BD) design technique, the bulk electrode of the MOS transistor is used as a signal input to modulate drain current. Using bulk-source voltage V_{BS} instead of V_{GS} may introduce unwanted body transconductance g_{mb}, which is approximately 3 times lower than the gate transconductance g_m. The body transconductance g_{mb} is a small-signal parameter of the MOS bulk-driven transistor and it can be expressed as :

$$g_{mb} = \partial i_d / \partial v_{BS} = \gamma \cdot g_m / 2(-2\varphi_F - V_{BS})^{1/2}$$

where φ_F is the Fermi potential and γ is the substrate coefficient [37, 38].

Obviously, g_{mb} is smaller than g_m. This leads to lower gain and worse frequency response.

Further, bulk-driven approach increases the input capacitance and input noise. There is also susceptibility to turning on an unwanted latch-up effect in this approach [35, 36]. Nevertheless, clever physical layout by following the specific layout rules can prevent the circuit against latch-up.

Seen from another side, the BD technique leads to a significantly reduced need to overcome the threshold voltage at the MOS transistor input. The main advantage of this technique is the compatibility with a standard CMOS process, hence there is no need to change the structure of the conventional MOS transistor.

Frequency response in Subthreshold and Bulk-driven modes

When FET operate in the Subthreshold-mode or in Bulk-driven mode the switching processes take an order of magnitude longer times [35, 38]. For the control circuits, a significant extension of the time constants does not matter since the circuits operate at a low frequency. For the intended purpose there could be a problem with the control of the power switch, which must operate with relatively high currents and for optimal use of magnetic elements at frequencies above 20 kHz.

1.2.3 Transformers for DC to DC converters

Conventional transformers have been designed for long time with multiple windings on a single core. The progress in productions of the ferrite cores, which can be molded and machined into almost any shape contributed to the development of new types of transformers.

Flat transformer. Flat transformers use single winding with multiple cores. These cores are packaged in modular block with built-in single-turn secondary windings using simple, stamped and formed parts. The entire network of winding elements behaves like a single transformer. Fundamental concept of flat transformer is depicted in Fig. 2.

The flat transformer is particularly well suited to low profile, low output voltage, high current applications and for high frequency switched- mode power conversion. It has extremely low leakage inductance, high magnetization inductance, excellent coupling, very low temperature rise, and is easily insulated for high dielectric requirements practically with no degradation in performance.

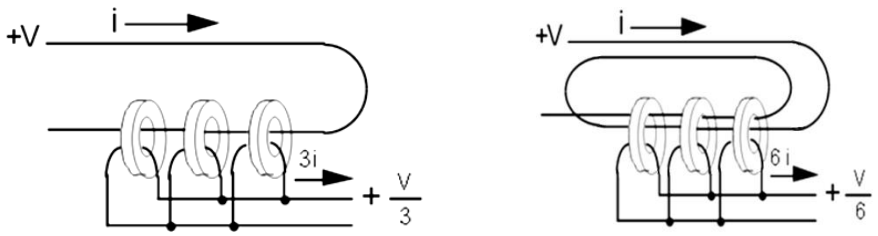

Fig. 2: Flat transformer: Fundamental concept; Transformation ratio 3:1 and 6:1 [5].

The resulting modular transformer has low profile, high power density, and improved thermal properties, a combination not available in conventional transformer designs. In additional, the flat transformer designs can reduce transformer manufacturing costs by as much 50%. It can be used in most convertors for both AC/DC and DC/DC powered supplies comprising push-pull, half-bridge, and full-bridge topologies.

In the flat transformers, the tight couplings between the windings and the absence of multiple turns result in very low leakage inductance. This allows faster switching times with increased efficiency. The flat transformer's nominal operating frequency ranges from 25 kHz to 500 kHz.

Because of improved heat dissipation, the flat transformer achieves high magnetic flux densities and allows tighter packaging for higher power density than its conventional counterpart.

Planar transformer can be constructed as stand-alone component, with stacked layer design or small multilayer PCB, or integrated into the multilayer board of the equipment.

The two basic items that made this technology feasible were the power MOSFETs that facilitated the increase of the switching frequency and enabled the designer to reduce the turns, and the ferrite core, which can be molded and machined into almost any shape.

To summarize, important advantages of planar magnetics are:

- Very low profile.

- Excellent thermal characteristics.

- Low leakage inductance.

- Excellent repeatability of properties.

The assembled planar transformers have very unique characteristics in their finished construction. In the assembled planar transformer, every primary turn is at precise location, governed by the PC board. The primary is always the same distance from the secondary. That means the same value for primary to secondary leakage inductance. Arrangement of planar transformer is given on the figure Fig. 3.

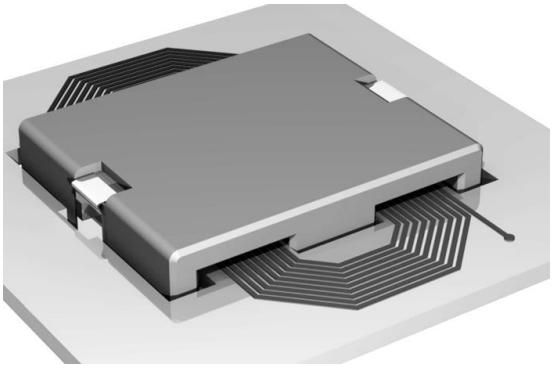

Fig. 3: Arrangement o planar transformer [5].

Using the same insulating material will always provide the same capacitance between primary and secondary. With this type of planar construction, there is always a tight control over leakage inductance, the resonant frequency, and the common-mode rejection.

Transformer design. A DC/DC converter with an extremely low input voltage requires a transformer with a large conversion ratio. The number of turns of the primary and secondary windings will therefore be very different and parasitic properties can be applied if the transformer is not designed properly. Therefore, the basic properties of the transformer and their influence on behavior of DC/DC converter must be considered [52,

54]. This issue is discussed in more details in Appendix A7 (Design of Transformer Windings).

1.2.4 Energy storage in energy harvestings

In general, energy can be stored in a capacitor, super capacitor, or battery. Capacitors and especially supercapacitors are used when the applications provide huge energy spikes.

Batteries

Batteries leak less energy and are therefore used when the device needs to provide a steady flow of energy or store energy for a long time. For each type of battery there is a prescribed charging process that must be followed, otherwise the battery can be destroyed or the battery life may be significantly shortened [67,68]. The requirement to control the charging process complicates the use of the battery in simple EH devices.

Supercapacitors

A supercapacitor (SC), also called an ultra-capacitor, is a high-capacity capacitor with a very high capacitance value. It typically stores 10 to 100 times more energy per unit volume or mass than electricity capacitors. Supercapacitors can accept and deliver charge much faster than batteries and tolerates many more charge and discharge cycles than rechargeable batteries [69, 70].

Unlike ordinary capacitors, supercapacitors do not use the conventional solid dielectric layer. They use electrostatic double-layer capacitance and electrochemical pseudo capacitance, both of which contribute to the total capacitance of the capacitor [71, 72]. Supercapacitors consist of two electrodes separated by an ion-permeable membrane (separator), and an electrolyte ionically connecting both electrodes. Typical construction of the supercapacitor is on figure Fig.4.

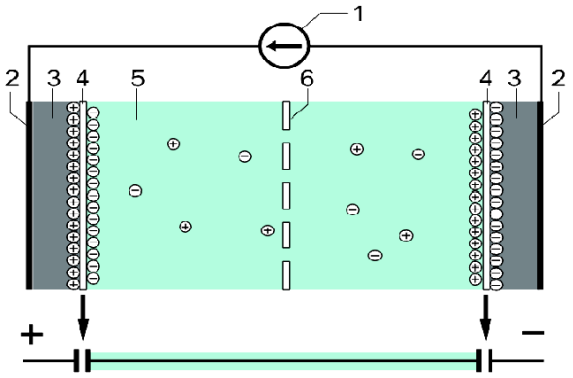

Fig.4 : Typical construction of superkapacitor: 1. Power source, 2. Collector, 3. Polarized electrode, 4. Helmholtz double layer, 5. Electrolyte having positive and negative ions, 6. Separator [73].

When the electrodes are polarized by an applied voltage, ions in the electrolyte form electric double layers of opposite polarity to the polarity of respective electrode. Positively polarized electrodes will have layer of negative ions at the electrode/electrolyte interface along with a charge-balancing layer of positive ions adsorbing onto the negative layer. The opposite is true for the negatively polarized electrode. The extremely large capacity of the whole arrangement is due to very thin layer where the charge accumulates and the large charge of ions which are absorbed here.

Resulting capacitance of supercapacitor

The two electrodes form a series circuit of two individual capacitors C_1 and C_2. The total capacitance C_{total} is then given by the formula

$$C_{total} = \frac{C_1 \cdot C_2}{C_1 + C_2}$$

Supercapacitors may have either symmetric or asymmetric electrodes. Symmetric one implies that both electrodes have the same capacitance value, yielding a total capacitance of half the value of each single electrode (if $C_1 = C_2$, then $C_{total} = 1/2\ C_1$).

For markedly asymmetrical capacitors, the total capacitance can be taken as that of the electrode with the smaller capacitance (if $C_1 >> C_2$, then $C_{total} \approx C_2$).

Summary:

Advantages of supercapacitors:
Higher energy storage compared to conventional capacitor technologies.
Lower Equivalent Series Resistance (ESR) compared to batteries.
Very fast charge/discharge because low ESR allows large currents.
Low temperature performance compared to batteries and electrolytic capacitors.

Disadvantages of supercapacitors:
Low per cell voltage: Typically, it is 2.7V. In series connection requires additional circuits for distribution of charging currents and overvoltage protection.
Cannot be used in AC and high frequency circuits: Their time constant is too large for use in AC or high frequency circuits.

The energy stored in supercapacitor

Supercapacitor charge/discharge curve is on the figure Fig.5. Unlike the battery, the voltage on the supercapacitor depends on the charge being stored.

The energy stored in supercapacitor in case of maximal voltage V_{max} is:

$$Emax = \frac{C(V_{max})^2}{2}$$

The energy stored in supercapacitor in case of minimal voltage V_{min} is:

$$Emin = \frac{C(V_{min})^2}{2}$$

Energy delivered by capacitor in discharging process is the difference of energy stored by V_{max} and the energy stored by V_{min} :

$$E = \frac{C(V_{max})^2}{2} - \frac{C(V_{min})^2}{2}$$

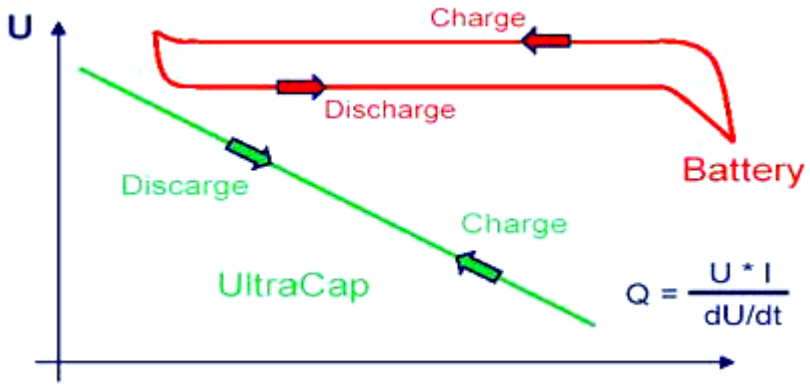

Fig. 5: Voltage on supercapacitor and on battery in charge / discharge process [70].

It depends on the choice of the value of V_{min} how much of the stored energy can be taken from the supercapacitor. Very small value of V_{min} makes little sense, given the quadratic dependence of the accumulated energy on voltage. For $V_{min} = ¼ V_{max}$ the "residual energy" is only 1/16, i.e. 6.25% of the maximal accumulated energy.

Unless there are special requirements, the best choice may be to discharge the capacitor to minimal voltage level $V_{min} = 1/3\ V_{max}$. In this case, 91% of the stored energy can then be taken from the supercapacitor unless the operating voltage is too low.

Super-capacitors are ideal electrochemical energy storage devices that bridge the gap between conventional capacitors and batteries tolerating the applications for various power and energy requirements. In super-capacitors like ordinary capacitor, there are two plates separated by a dielectric and has an electrolyte inside it separating these plates and store more energy than ordinary capacitor by creating double layer of separated charges between two plates. Plates are made from porous, typically carbon-based materials. The energy in super-capacitors is stored by means of ion adsorption at the electrode/electrolyte interface. Consequently, it offers the ability to store or release energy in few seconds with extend cycle life.

1.3 Photovoltaic cells

For energy harvesting applications the photovoltaic cells have many advantages as silent operation, no mechanical part and comparatively high efficiency and long lifetime.

1.3.1 Photovoltaic cells for EH transducers

A comparison of the properties of respective technologies will show that inorganic thin film cells are the most advantageous for EH applications. Between them the cells based on crystalline and multi-crystalline silicon, cadmium telluride (CdTe) and copper indium gallium selenide (CIGS or CGS) are very convenient [7, 74].

Thin film manufacturing technology makes it easier to adapt their operation to special requirements. Approximately 1% of material is required to produce thin-film structures compared to crystalline cells. Compared to crystalline cells there are about of a 30% less technological steps and the entire production process consumes about 50% of the energy [75, 20].

Inorganic photovoltaic cells

Crystalline or polycrystalline silicon photovoltaic cells are to time standard cells with the price less than 0.5 Euro per Watt, depending on the area of the cells and technology. Industrially produced silicon PV modules have efficiencies from 18% to 22%. The current efficiency record (2018) for crystalline Silicon cell is 26.7% [14,77], which is not far from the theoretical limit of approximately 33 % derived considering the spectral characteristic of the light and the Shockley-Queissner limit [1] .

Amorphous silicon photovoltaic cells have the efficiency of energy conversion approximately 10 % but it rapidly drops in operation because of the light degradation process (Staebler–Wronski effect) to about 7 % [80, 81]. Nevertheless, amorphous silicon cells operate very well in low light conditions where the spectral characteristic of the light shifts to shorter wavelengths. Amount of produced energy here could be almost comparable to crystalline silicon cells [14,82].

Silicon thin film cells can be also prepared as a tandem of amorphous cell and microcrystalline cell [84, 85]. Because of different Band Gaps of microcrystalline and amorphous materials such tandem cell is able to absorb larger part of the light spectra and as a result there is higher efficiency of light to energy conversion, which could reach about 13%.

The cell efficiencies for CdTe and CGS measured in lab conditions are beyond 21 % which is comparable to crystalline silicon cells [86, 7]. Cadmium-teluride (CdTe) is very cost-effective but uses toxic cadmium. The usage of rare materials may also become a limiting factor to the large-scale production. The Band Gap of CGS cells varies continuously depending of content of indium and gallium from about 1.0 eV (CuInSe) to

approximately 1.7 eV (CuGaSe) [77]. This can be convenient in case when the spectral characteristic of the cell should be adapted to existing light source.

Perovskite photovoltaic cells

Perovskites are hybrid organic-inorganic materials containing lead or tin halide. In terms of structure and production processes used they are in the area between inorganic and organic cells. Compared to silicone solar cells, their production is much simpler and less time-consuming. Production facilities use significantly cheaper production equipment and need much less material for the same production volume.

After a relatively short research period perovskite-based photovoltaic cells achieve very high efficiencies. The great advantage of perovskites is the possibility of setting the value of the band gap of the respective semiconductor with a suitable composition and structure of the material. Thus, tandem cells with efficiencies greater than the Shockley- Queisser Efficiency Limit for a single junction cell can be made with the same material. However, the simplest form is a tandem cell, which consists of a perovskite layer on crystalline silicon. Here, greater efficiency has already been achieved than for a monocrystalline silicon cell.

Perovskite photovoltaic cell can be ultrathin and enough flexible to be fabricated on flexible substrates. Using a simple printing or solution-based deposition methods allows to make solar cells production extremely cheap. This deposition methods also allows technology of perovskite photovoltaic cells to be highly scalable. However, attempts to enlarger cell area cause higher incidence of defects and pinholes and consequently considerable decrease of efficiency.

Although perovskite cells are environmentally friendly due to the simple manufacturing process and the very thin layer required for a functional cell, there is a problem with lead content. If these panels are to be manufactured on a large scale and used in small installations, the recycling of perovskite cells can present similar environmental problems as the recycling of electronic devices soldered with lead solders.

Further, perovskite films degrade when exposed to heat and moisture. Perovskite photovoltaic modules therefore need to be encapsulated in a weatherproof layer that keeps out moisture for sufficiently long time. Consequently, encapsulation problems and durability still prevent their practical application.

Therefore, to time the perovskite photovoltaic cells are therefore available mostly as laboratory samples. However, they have exceptional power conversion efficiencies which are after only a few years of investigation comparable to crystalline silicone cells. Despite that there are many challenges, the probability that the perovskite solar cells will be commercialized in near future is high [89, 90].

Most important parameters of photovoltaic cells with different technology are given in table Tab.2.

Tab.2 : Most important parameters of photovoltaic cells with different technology: E_G [eV] is Band Gap , λ_0 [nm] is Threshold Wavelength to the respective Band Gap, t_{EL} [years] is Expected Lifetime

TYPE	E_G [eV]	λ_0 [nm]	t_{EL} [years]
C - Si	1.12	1107	≈ 20
Micro - Si	1.4	885	≈ 10-15
Perovskite	1.2- 2.3	1033 - 539	≈ ??
Amorph. Si	1.7	729	≈ 10-15
A-Si+Micro-Si (tandem)	1.7 / 1.4	729 / 885	≈ 10-15
CdTe	1.5	826	≈ 10-15
CGS	1.7 – 1.0	729 - 1240	≈ 10-15

Organic photovoltaic cells

A great advantage of organic photovoltaic cells is in their relatively easy manufacture. The materials used are soluble which could bring high throughput and cheap processes resulting in low production costs in large volume production. Combined with the flexibility of organic molecules, organic solar cells are therefore regarded as potentially cost-effective for photovoltaic applications [92, 93]. The optical absorption coefficient of organic molecules is high, so large amount of light can be absorbed with low materials costs.

The main disadvantages associated with organic photovoltaic cells are low efficiency and low stability compared to inorganic photovoltaic cells [91, 20]. Consequently, after years of investigations, organic photovoltaic cells still remain only a promising technology. Nevertheless, although there are currently many convenient materials for organic cells, the degradation processes still pose a difficult problem. In principle, each photovoltaic cell is a semiconductor diode that converts light into direct current. However, in case of organic photovoltaic cells this process is rather complicated because of electronic properties of organic semiconductors.

Organic semiconductors are based on conjugated system where carbon atoms covalently bond with alternating single and double bonds. These hydrocarbons' electrons p_z orbitals delocalize and form a delocalized bonding π orbital with a π* antibonding orbital [31, 48]. The delocalized π orbital is the highest occupied molecular orbital (HOMO), and the

π* orbital is the lowest unoccupied molecular orbital (LUMO). According to the description used in organic semiconductor physics, the HOMO takes the role of the valance band while the LUMO serves as the conduction band. The energy separation between the HOMO and LUMO energy levels is considered the band gap of organic electronic materials and is typically in the range from 1 eV to 4 eV.

The conversion process starts by absorbing the light and consequent creation of the electron-hole pair called exciton. In next step excitons diffuse to donor/acceptor interface [99]. Different work function of materials on donor/acceptor interface creates the electric field. This electric fields splits the excitons into isolated electrons and holes. In the last step the carriers separated by an electric field move to the electrodes [48, 9].

More details concerning the working principle of organic solar cells and junction types are described in detail in Appendix A2 (Organic Photovoltaic Materials).

1.3.2 Photovoltaic cells in Low-light operation

The light dependence of generated voltage, current and power on the Si solar panel is in figure Fig. 6. It is evident that the current supplied by the photovoltaic generation is approximately linearly proportional to the illumination.

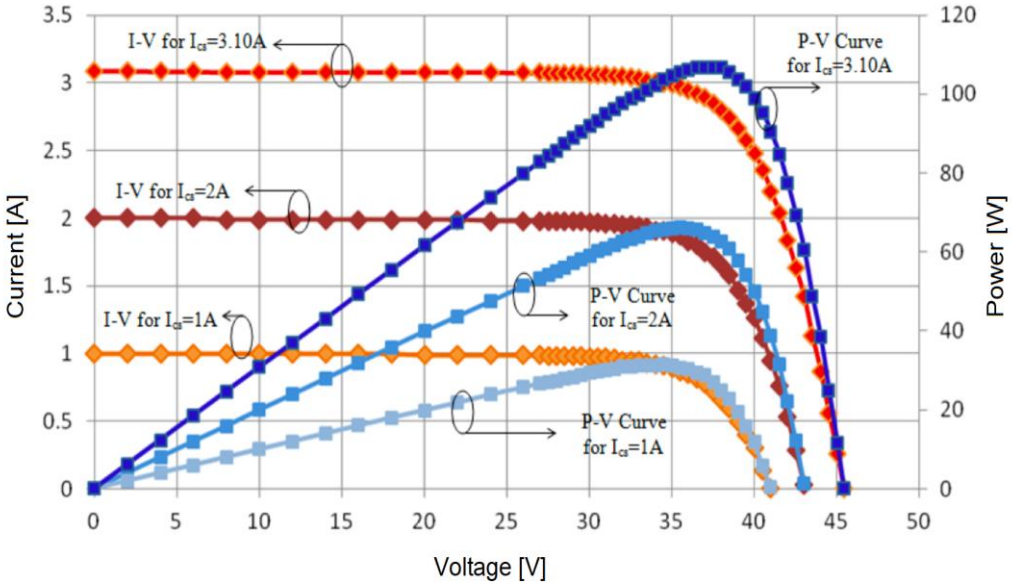

Fig. 6 : A-V characteristics of the silicon photovoltaic panel and the power extracted from the panel in dependence on illumination. [168]

The dependence of the voltage generated by the cell on the illumination is approximately logarithmic [2]. Changing the intensity of light radiation will therefore primarily reflect the change in the current of the cell.

From Fig.6 it is obvious that there is an optimal voltage and current value for the maximum output of the cell. The voltage at which maximum power is reached decreases with light intensity very slowly.

This means that even at an extremely low intensity of incident radiation the voltage on the individual cell will still be a few tenths of a Volt. Thus, the inverter operation will be possible, although the power output will be very small.

Intensity and spectral distribution of the exciting radiation

Excitation of the electron to the conduction band requires energy given by the bandgap of respective semiconductor. The bandgap of crystalline silicon (E_G = 1.1 eV) corresponds to infrared light with a wavelength of about 1.1 microns. This means that only photons from red, yellow and blue light and some near-infrared part of spectra will contribute to photovoltaic power production.

However, in case of absorption of high energy photon the electron has an excess of energy and travels in the crystal lattice until this energy is absorbed and thus the excess of photon energy changes to the heat. Consequently, silicon solar cell can convert only about 33,5 % of the incident sunlight energy, which is called the Shockley-Queissner limit [96, 94].

Spectral composition of the incident radiation is therefore very important. It is well known that the spectral composition of the light may considerably change according to different conditions and this influences the efficiency of photovoltaic conversion [2, 99].

For example, in direct sunlight, great part of radiated energy is in red and infrared part of the spectra. Crystalline silicon cells, which have the maximum absorption just in infrared and red part, are suited for this case.

From the energy of the Band Gap given in table Tab.1 it can be also seen that the optimal Band Gap value for operation on direct sun radiation have the solar cells based on CGS.

At cloudy sky diffused radiation prevails and the spectral distribution is shifted toward shorter wavelengths. Radiation in the field of visible part of spectra will also prevail in case of indoor applications. Here the semiconductors with wider Band Gap are preferred [98].

From Fig. 7 it is obvious that the optimal bandgap for the sunlight application is about 1.5 eV, whereas for indoor application the respective bandgap should be about 2 eV.

The waves we see (visible light) just a small part of a great range of waves that make up the electromagnetic spectrum. Waves somewhat longer than 700nm (the approximate limited of red) are called infrared waves. The infrared region of the spectrum goes from

700 nm at the border of visible light up to about 10^{-4} meters, which is a tenth of millimeter or 100 µm.

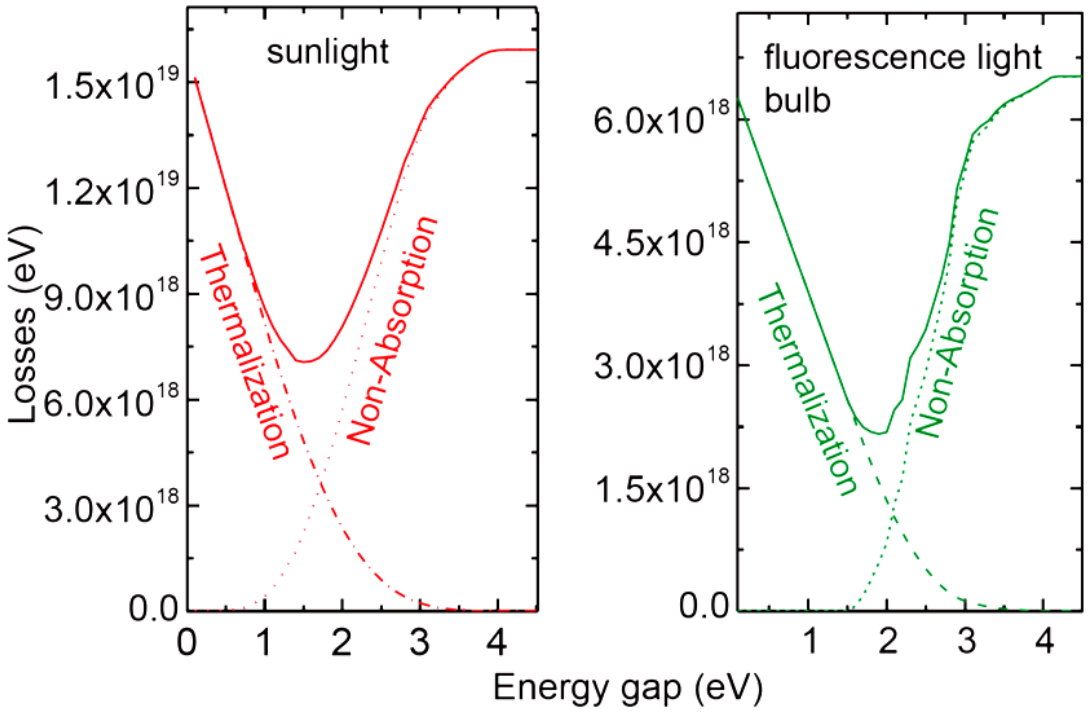

Fig. 7: Thermalization, non-absorption and losses depending on the energy gap [2].

1.3.3 Photovoltaic single cell

Photovoltaic cells are to time reliable and technologically most accessible energy converters. However, when using standard solar cells connected in serial configuration there are some drawbacks. The most significant disadvantages of series-connected photovoltaic cells are as follows [10, 100].

Cells must be sorted according the rated current to achieve maximum efficiency. With larger scattering of cell parameters at production, they must be selected and sorted from large production series of individual cells.

When aging during normal operation, cell parameters may vary unevenly. Faster aging cells will then greatly reduce the overall efficiency of the assembly.

In non-uniform illumination, the achievable power is influenced by the least illuminated cell. In the event of a large difference in illumination, the least illuminated cells can even be polarized in the reverse direction.

To ensure reliable operation of the whole assembly, there must be anti-parallel diodes connected to each cell. When the respective, less illuminated cell, comes to reverse polarization parallel diode will overtake the current generated by the rest of the assembly.

When the efficiency is not the most important parameter the photovoltaic single-cell can be cost-effective in many applications [10, 101]. The structure of the single cell is simple and could be more reliable than the cells connected in serial configuration.

Using a single-cell with a low-voltage inverter will allow take the energy from the photovoltaic cells even in very low illumination.

Comparison of the properties of respective technologies shows that for the intended application are most advantageous inorganic thin film cells [11, 102]. Because of very small area of the cell needed for the low energy EH converters the price of the photovoltaic cell is not an important item in the total cost of an EH converter.

Note: If tandem cells are used in single cell operation, the spectral composition of the lighting should be considered. In standard tandem structures, cells are electrically connected in series. If, due to the uneven distribution of light intensity in individual parts of the spectrum, there is a different level in absorption of radiation in individual cells. Consequently, the properties of the whole pair will be determined by the cell with less energy absorption.

This disadvantage can be circumvented by connecting the two photovoltaic cells in the structure in parallel (as shown in Appendix A3). This can be also realized in the opposite order of the absorption layers in cells, i.e. N_1P_1 x P_2, N_2 or P_1N_1x N_2P_2. However, a very good conductivity of the central electrode must be ensured and at the same time its good transparency for larger wavelengths in the spectrum. See also Appendix A3 Photovoltaic Tandem Cells.

Influence of parasitic resistances

For an ideal photovoltaic cell, the series resistance equals zero while the shunt resistance equals to infinity. However, due to imperfections in production processes, this requirement is often not met.

Low shunt resistance causes power losses in solar cells by providing a path for the light generated current. At very low light levels, the effect of the shunt resistance becomes important because the current flowing through the shunt resistance is taken from the photo-current which is generated by the photovoltaic process. The power loss could be much more than 10%.

High series resistance will influence the operation of the cell at high irradiation. The high current generated by high irradiation causes a voltage drop on serial resistance, which causes a voltage drop on the output of the cell.

Operation of photovoltaic cell can be described by the single-diode model, which is based on the Shockley equation. At a given illumination, the current/voltage relationship is given by following relation [1, 96] :

$$I = I_{\mathrm{ph}} - I_0 \left[\exp\left\{ \frac{q\left(V + R_{\mathrm{s}} I\right)}{n k_{\mathrm{B}} T} \right\} - 1 \right] - \frac{V + R_{\mathrm{s}} I}{R_{\mathrm{sh}}},$$

where I_{ph} , I_0 , R_s and R_{sh} are the photocurrent, the saturation current of the diode, the series resistance and the shunt resistance respectively,

and q, n, k_B and T are the electron charge, the ideality factor, the Boltzmann constant, and the temperature, respectively.

V is the potential on the cell at given conditions.

The effect of individual parasitic parameters significantly depends on the actual potential V on the cell. From the equation, the influence of both parasitic resistances R_s and R_{sh} is evident.

The total magnitude of the parasitic resistances relates to the cell area. Therefore, to compare photovoltaic cells both parasitic resistances R_s and R_{sh} are area normalized. For crystalline silicon cells, for example, the value of series resistance R_s range from 0.5 Ωcm^2 for laboratory samples up to 2.0 Ωcm^2 for commercial solar cells.

The same way is used area normalized shunt resistance R_{sh} which is in range of 10^3 Ω cm^2 for very good samples and may fall to several hundred Ω cm^2 in case of presence of structure defects.

At high currents, the resistances of the collecting electrodes and contact resistance between the collecting electrodes and functional layers are also applied. However, due to the interaction of technological operations, the electrode systems cannot be optimized independently [168].

1.4 Thermoelectric generators

Thermoelectric generators (TEG) have advantages such as silent operation, no moving parts and high reliability. Its use is advantageous in locations where there are poor levels of illumination. There are also some perspective applications as photovoltaic and thermoelectric energy harvesting in one device or use of thermoelectricity produced in household to charge mobile phones and different types of small devices [104, 106].

Harvesting of waste thermal energy in industry and transport applications has very large potential but it needs thermoelectric converters able to work in high temperature range and often in corrosive environments or with increased safety demands. Car companies have been developing thermoelectric waste heat recovery systems with expectations of 3-5% in fuel economy and the power generated reaching up to 1 kW. Nevertheless, the electrification of vehicles and change of conditions for thermoelectric generation in cars give not optimistic view to this application [12, 32].

Wireless sensors are to time probably the largest area for application of TEGs in environments with stable temperature difference [105, 107]. This way battery lifetime and reliability problems are eliminated.

1.4.1 Thermoelectric effects

A simplified representation of the thermoelectric effects is shown in figure Fig. 8:
Seebeck effect: This effect creates potential difference across the connection of two materials module by heating one side of the module and cooling the opposite [12, 108].

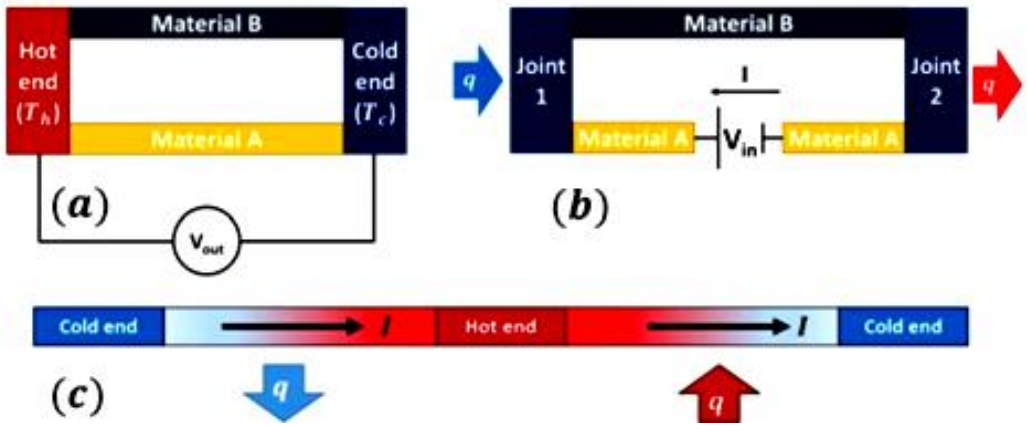

Fig.8: Thermolectric cells; **(a)** Seebeck effect; **(b)** Peltier effect **(c)** Thomson effect [120]

Peltier effect: When current passes through the junction of different materials one side is cooling and the other side is heating. Peltier cells are to time routinely used for cooling but in principle they may be as well used for thermo-electric generators [32,22].
Thomson effect: It describes the heating or cooling of a current-carrying conductor with a temperature gradient. In the same materials the Seebeck coefficient is not constant in temperature, and so a spatial gradient in temperature can result in a gradient in the Seebeck coefficient. If a current is driven through this gradient, then a continuous version of the Peltier effect will occur. Position of the heated and cooled points depends on the direction of the temperature gradient and the direction of the electric current [118,111].

1.4.2 Performance of thermoelectric materials

To evaluate the performance of a thermoelectric material we use a dimensionless ***figure of merit*** (*ZT*), which is defined as

$$ZT = \frac{\alpha^2 \sigma}{K} T$$

where $\boldsymbol{\alpha}$ is Seebeck coefficient, $\boldsymbol{\sigma}$ is electrical conductivity, $\boldsymbol{K}$ is thermal conductivity, and $\boldsymbol{T}$ [K] is temperature [121,110].

Fraction (Z) has the physical dimension K^{-1}. The product of ZT is therefore dimensionless. It takes values from zero to one and describes very well the ability of the material to work in a thermoelectric cell. Normally, it is expected that a TE material should have a large Seebeck coefficient, α, high electrical conductivity, σ, and low thermal conductivity, *K*. However, the three transport parameters: α, σ and *K* are not independent and depend upon a variety of factors such as band structure and carrier concentration [109,111].

Both electrical and thermal conductivities, σ and *K*, increases with an increase in carrier concentration. Seebeck coefficient, α, has an opposite trend compared to σ and *K*. This indicates that figure of merit, *ZT*, cannot be improved by continuously increasing the carrier concentration. Maximizing *ZT* requires optimizing α, σ, and *K*, simultaneously.

The efficiency of a thermoelectric transducer can be estimated using the equation [111, 32]:

$$\eta = \frac{(T_H - T_C)}{T_H} \cdot \frac{\sqrt{1+ZT_m}-1}{\sqrt{1+ZT_m}+\frac{T_C}{T_H}};$$

where the first fraction is the Carnot efficiency.

Further, T_H is the temperature of the hot part and T_C is the temperature of the cold part, *ZTm* is a figure of merit at average temperature *Tm* between T_H and T_C.

If the generator is powered from a source with unlimited heat and cooling and with a guaranteed temperature difference it is possible to apply very useful parameter, Power Factor, defined as [33,118]:

$$PF = \sigma \cdot \alpha^2 [\mathrm{W}m^{-1}K^{-2}]$$

This expression can be obtained by modifying the equation for the electrical power achievable by the thermo-electric generator.

After further modifications we receive:

$$PF = W \cdot (2 \cdot l / A) / (\Delta T)^2,$$

where: ***W*** is obtained power, ***l*** and ***A*** are the length and the cross-section area of the functional layer respectively and ***Δ T*** is the temperature difference.

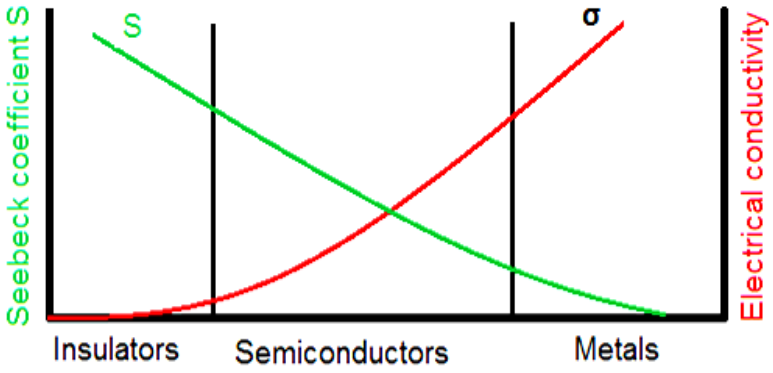

a)

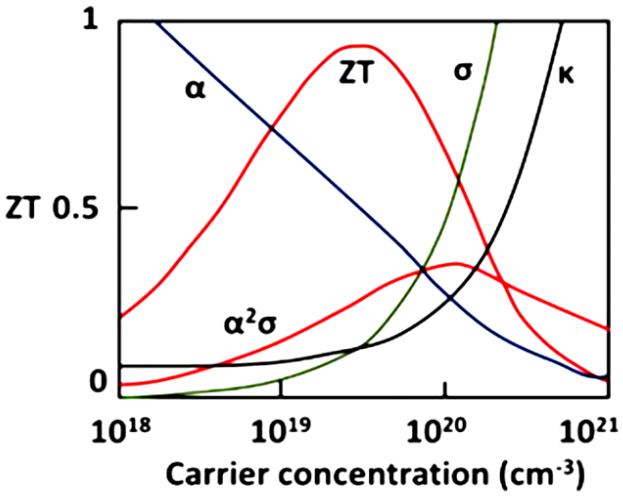

b)

Fig. 9: a) Seebeck coefficient (S) and electrical conductivity (σ) for insulators, semiconductors and metals. **b)** Bismuth telluride Bi_2Te_3; Electrical conductivity (σ), Thermal conductivity (K), Seebeck coeficient (α), Power factor $PF = \alpha^2\sigma$, Figure of merit (ZT) [109,111]

Another often used parameter is electrical power per area of the functional layer at defined temperature difference ΔT:

$$P_A = P_{OUT} / (A_F \cdot \Delta T) \text{ [W m}^{-2} \text{ K}^{-1}\text{]}$$

Typical dependence of Seebeck coefficient and electrical conductivity for different materials is shown in figure Fig. 9 a). The Seebeck coefficient and electrical conductivity both depend on charge carrier density and cannot be simultaneously increased. There is always an optimum that delivers the highest nominator (power factor) of the thermoelectric figure of merit.

Bismuth telluride Bi_2Te_3 is narrow-gap semiconductor with bandgap E_G = 0,21 eV. In the Fig. 9 b) is seen that with different concentrations of electrons, depending on the doping level, its figure of merit considerably changes.

Thus, an important conclusion follows from the definition of figure of merit, *ZT*. The electrical conductivity of thermoelectric materials is the bottle neck that limits the power output of the respective thermo-cell.

1.4.3 Inorganic thermoelectric materials

A combination of Bi_2Te_3 (n-type; negative sign of Seebeck coefficient) and Sb_2Te_3 (p-type; positive sign of Seebeck coefficient) semiconductive materials is to time the best performance option for TEGs, having high Seebeck coefficient, high electric conductivity and low thermal conductivity. The big disadvantage of standard converters with these materials is their high price.

For a production of large number of thermoelectric cells connected in series it is possible to use print screen technology. The screen printable thermoelectric pastes contain thermoelectric materials Bi_2Te_3 and Sb_2Te_3 in form of alloy powders. The paste contains basic compound of the layer (Bi_2Te_3 or Sb_2Te_3), epoxy binder system and solvent.

The adjacent particles are stuck to each other and adhered onto the substrate by the epoxy binder system. The solvent is added into the paste to adjust the viscosity to a screen printable level. The pastes are fully dried after printing and then cured in appropriate temperature depending on the type of paste [22, 33].

However, the price of tellurium, a key component in these materials is high. The other materials used for higher operating temperatures also use tellurium for example PbTe for n-type and GeTe for p-type semiconductors.

Due to increasing tellurium costs, it is necessary to find alternative materials that have comparable figures of merit. Very promising low-price-candidates are bismuth oxides and some metal sulfides [118,121].

1.4.4 Organic thermoelectric materials

Organic materials are not only low cost, light-weight and flexible but also potentially abundant and in most cases also soluble. Moreover, the development of organic electronics has provided a lot of organic semiconductors with high field-effect-mobility. In practical, there are two features of organic solids that justify considerations to exploit organic thermoelectric materials [112,121]:
a) Thermal conductivity of organic material is typically well below $1 Wm^{-1}K^{-1}$, which is lees than the lower limit of thermal conductivity of inorganic thermoelectric materials.
b) Electronic structures of organic semiconductors are fairly tunable through molecular chemistry and doping treatments and they can have a large Seebeck coefficient.

Despite the advantages mentioned above, to time the organic-based TE generators show very low output power density due to several limitations of the polymer as a low power factor (figure of merit), high contact resistance with a metal electrode and low electrical conductivity [118,114]. Consequently, future development in organic thermoelectric materials will be probably impeded by these problems as consequence of low carrier mobility in organic materials.

More details concerning the properties of materials for organic thermoelectric cells are in Appendix A4 (Organic Thermoelectric Materials).

1.4.5 Structures for thermoelectric generators

Although the thermoelectric effect is used for a long time to measure temperature, thermoelectric generators are still mostly available in the form similar to Peltier cells used for cooling. In reverse operation, these cells can supply electrical energy. However, they differ from Peltier cells by a modified construction and are much more expensive [12, 118]. Their practical use is also limited by the rigidity of the structure. Therefore, new possibilities of preparation of thermoelectric cells are searched with orientation on available materials and cheap production processes.

Critical factors for efficient thermoelectric power conversion can be summarized as follows [115, 117]:

a) Basic parameter is the difference in work functions of used materials and corresponding Seebeck coefficients.

b) The electrical conductivity of the respective thermoelectric material is the bottle neck that limits the power output of the thermo-cells.

c) The heat flux must be successfully moved to the module.

d) The thermal conductivity of module material between hot and cold side must be as low as possible.

High thermal conductivity is a problem by almost all inorganic semi-conductive materials. Mostly used long lateral structures with low thermal conductivity provide a good spatial separation of the heat source and heat sink and require an easy deposition process.

However, in this case the electrical resistance of materials used for the thermocouple legs causes a high total electrical resistance of the TEG. This leads to a low power delivered by the generator [23, 116].

Moreover, in this case, the heat flow is transmitted along the length of the thermoelectric converter, and the heat flow capture area is therefore very small. This can be overcome by parallel arrangement of foils containing thermoelectric transducers or, in case of elastic films, by rolling them into spiral shapes [117, 120]. However, such a mechanical arrangement is complicated.

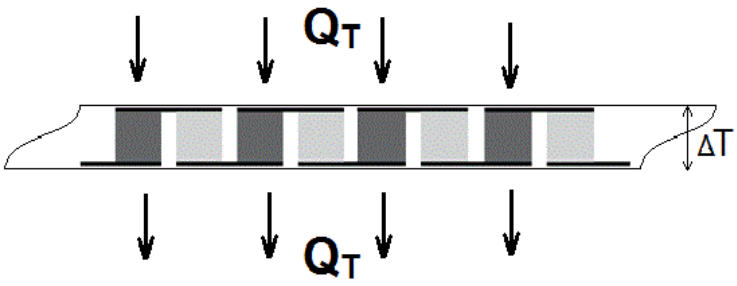

Fig. 10: Vertical design of thermo-electric generator [104]. Heat flux passes through the entire surface of TEG transducer.

If the length of the legs is reduced such as with the vertical design the electric resistance is smaller [117,121]. However, the thermal efficiency is in such case limited by thermal conductivity of used materials.

Contrary to the lateral arrangement, there is an advantage in a substantially larger area of the thermoelectric converter since the heat flow being processed passes through the entire surface of the transducer as shown in Fig. 10.

An increase in heat transfer area is possible in the lateral arrangement of thermocouples in the structure shown in Fig. 11. Individual thermocouples are printed on a material with low thermal conductivity. The same material also thermally insulates thermocouples from the top.

Electrically insulated copper extensions with high thermal conductivity ensure that there is approximately the same temperature difference between the ends of individual

thermocouples as is the temperature difference across the hot and cold side of thermoelectric transducer.

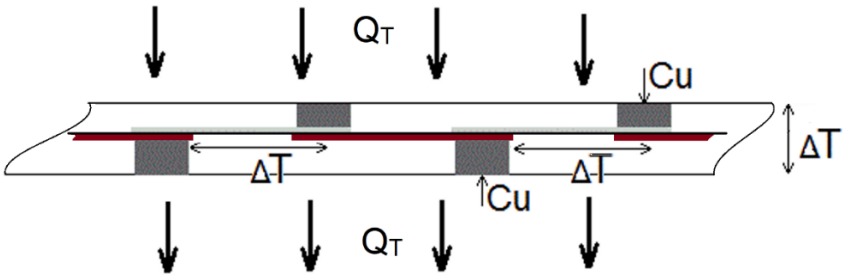

Fig. 11: Combined design. Copper electrodes ensure large temperature difference between thermocouple ends [25].

Both lateral and vertical printed structures need to balance between thermal conductivity and electrical conductivity of the respective structures and the area of heat flow surface. A combined structure with lateral arrangement of short thermo-coupler legs placed in double-layer of thermal insulator could ensure good balance between electrical and thermal conductivity and enhance a large heat flow perpendicular to the matrix of thermo-couplers, which contributes to higher power output and higher conversion efficiency

1.5 Preparation of functional layers of EH converters

Energy Harvesting (EH) transducers can take different forms and can use different operating principles. Other technologies can be used in addition to the standard processes used in semiconductor technology. They are above all the screen-printing technology, inkjet printing technology and thin film deposition using vacuum processes. Use of printing technologies also facilitates implementation of equipment with otherwise costly production or difficult manufacture by standard processes.

Motivations for using printed electronics include the potential economy with high-throughput printing methods and the possible compatibility to the roll-to-roll processing on large-area plastic or paper substrate [122,123]. Suggestions to use the roll-to-roll technology emerged in the early era of the evolving technology of photovoltaic cells in the 1980s. However, most projects remained in the stage of reflection and unrealized proposals [7,47]. Today's technologies are more sophisticated, but there are still no common roll-to-roll applications.

1.5.1 Screen printing

A schematic representation of the screen-printing process is shown on figure Fig.12. During deposition, a screen with the pattern is placed above the surface of the substrate. The polymer ink is loaded onto the screen, which is then swept by a rubber “squeegee” with a certain velocity across the surface of the screen. At the point of contact, the solution flows through the screen patterns to the surface of the substrate. The material is thus transferred to the substrate, forming the desired pattern [39, 126].

The screen is typically made of a porous mesh, from materials such as a porous fabric or stainless steel. The process is very simple and cheap compared to other methods. The thickness of the deposited layer is dependent on the solution viscosity and velocity of the squeegee movement.

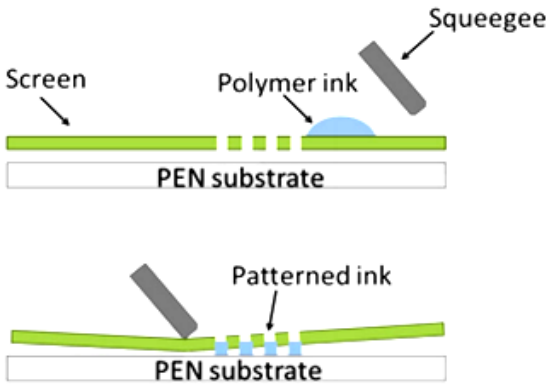

Fig. 12: schematic representation of the screen-printing process using polymer ink [124].

Screen printing is the most important technology in the field of functional printing. The resolution is limited to 20-100 μm, similar to inkjet printing, and the maximal printing speed could be up to several m^2/s [124].

The main disadvantages of this technique are difficulties of producing thin and homogeneous layers, wasting of big quantity of material which stay on the screen during deposition, and high consumption of solvents for screen cleaning [125,127].

1.5.2 Inkjet printing

The inkjet printing process is noncontact digital printing method. In this technique a nozzle is used to deposit small volumes (droplets) of the solution on different locations of the substrate, similar to a desktop printer, as shown on figure Fig.13.

The absence of mask or screen, which are used for other techniques, allows fast and easy changes to desired design and avoid material waste. Inkjet printing is relatively compact set-up, which makes it commonly used for the laboratory scale. The achievable resolution with conventional inkjet printing is 20-50 μm [128,129].

Solvent type, ink concentration and viscosity fine-tuning are required to control the shape, thickness and morphology of the droplet.

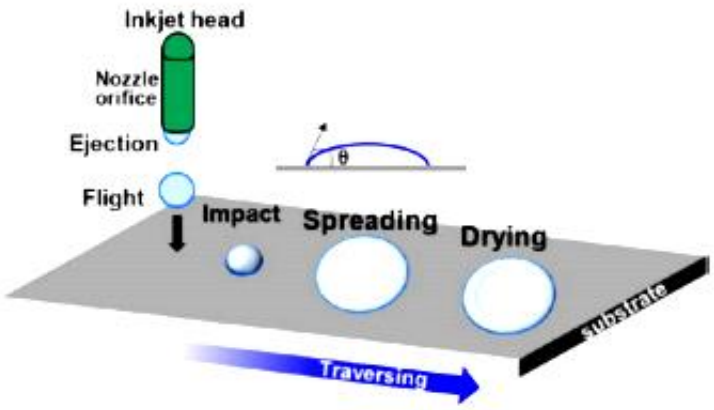

Fig. 13: Schematic representation of the inkjet printing process [129].

The inkjet printing has some disadvantages compared to mass-printing technologies. Using nozzle causes yield-limiting factor in terms of throughput (0.01-0.05 m^2/s). Moreover, film uniformity and homogeneity are also limited because of the drop-wise deposition of layers [130, 132].

1.5.3 Electroless plating

Electroless plating is a well-established surface coating process involving deposition of a metal-alloy-coatings on various substrates. Among many metals that can be coated using this technology the most widely used nickel which forms a Ni-P compound [133,134].

Ni-P compound has very good mechanical properties, good adhesion and is relatively resistant to corrosion. From the point of view of use in thermoelectric generators, nickel is very advantageous because it has negative sign of the Seebeck coefficient. Moreover, the Ni-P composite also has a lower thermal conductivity than Ni which is another advantage for use in thermocouples [134,136].

Electroless deposition of Ni-P alloy is made by the reduction of Ni ions in a bath of aqueous solution of Ni metal ions. A chemical reducing agent in solution supplies the electrons required for converting metal ions to metal deposit. When the sodium hypophosphite is used as a reducing agent then the deposits are binary alloys of nickel and phosporus. The Phosphorus concentration can be as high as 9% depending on the deposition conditions [136].

The parameters which determine the P content in electroless Ni-P deposits are[136,133]:

Nickel and reducing agent concentrations,
Type and concentration of the inhibitor and accelerator in the plating solution,
Temperature and pH of the solution.

It is also reported that the high phosphorous deposits are supersaturated solid solution of P dissolved in crystalline nickel [134] and deposits from acidic baths can have a higher level of P content [135,136].

1.5.4 Vacuum thin film deposition technologies

Thin layers are layers with a thickness ranging from a few nanometers to several micrometers. Thin-film deposition technologies are either purely physical, such as evaporation technology, or purely chemical methods, such as gas-and liquid-phase chemical processes [137,138]. A considerable number of processes that are based on glow discharges and reactive sputtering combine both physical and chemical reactions; these overlapping processes can be categorized as physical-chemical methods [137,139]. There will be briefly described only two most common technologies applicable for thin film deposition in this work – evaporation technology and sputtering technology. For more details see Appendix A5 (Vacuum Thin Film deposition).

Thermal evaporation

Thermal evaporation or vacuum evaporation is still used in the laboratory and some industry processes despite that it is one of the oldest techniques used for depositing thin films. The biggest advantage is a very simple deposition equipment and very simple deposition process. A vapor is generated by boiling or subliming a source material. The vapor is transported from the source and it impinges on all surfaces that are in direct line of sight from the vapor source. At this point, the vaporized particles lose energy and condense.

There are many ways to ensure the evaporation of materials, so there are also many evaporation sources including resistance-heated filaments, electron beams, crucibles heated by conduction, radiation, or RF induction, arcs and exploding wires.

For more details see Appendix A5.

Sputtering

Sputtering is based on the particle collisions which involve an elastic transfer of momentum that causes the releasing of the surface atoms of the target. The atoms releasing from the target can be utilized for deposition process of a thin film of target material on the substrate [140,141].

In this technique, ions are accelerated toward a target by utilizing electric field. These ions are usually originated by exciting a neutral gas by electrical discharge. In special cases the ions are produced in ion gun and are accelerated to the target at precisely given energy. As the ions bombard the target surface, they dislodge the target atoms. The forceful collision of ions onto target thus ejects target atoms into the space. Ejected atoms then travel some distance until they reach the substrate and start to condense into a film.

To prevent the collision of the sputtered particles with the gas the sputtering process is possible only in low pressure gas. A negative voltage is applied to the target (cathode) and the substrate is attached to the ground or to the insulated electrode which may be biased with DC or Radio-Frequency (RF) voltage [14,142].

By sufficiently high voltage between the electrodes there is an electrical discharge which produces the plasma containing the ions of sputtering gas and electrons. This type of plasma is called as a glow discharge due to the light emitted.

Advantages and limitations of sputtering. The greatest advantage of sputtering technology is the high energy of the particles that strike the substrate and consequently very good adhesion and quality of the sputtered layers [143, 14]. The disadvantage is relatively low sputtering rate, which for most materials is in the order of tens of nanometers per minute, depending on the pressure and discharge-power used [140,143].

For more details see Appendix A5.

1.5.5 Cleaning of processed surface

A number of proven methods can be used to clean substrates.

Mechanical cleaning. The standard procedure is the use of ultrasound. Contact cleaning is problematic. There is always a risk of contamination and in case of non-conductive substrates there is a high probability of static charge formation. However, it is possible to use cleaning with elastomeric rollers rolled over the cleaned substrate. This technology is used by the Scottish company TENKEK. There is a perfect removal of dry loose particles from the cleaned surface up to the size of one micron. The removed contamination is then transferred to an adhesive roll with pre-cut sheets with an adhesive layer [144, 145].

Use of cleaning fluids. These are surface tension reducing agents (detergents) or solvents - for example Iso-Propyl-Alcohol (IPA) and gasoline [145,146].

Plasma activation. If the substrate surface is chemically inert and non-porous and has a low surface tension, it is likely that the adhesion of the functional layers to the substrate will not be sufficient. The surface of the substrate must therefore be activated before deposition of the functional layers. Very effective surface activation can be achieved through plasma processes [147, 144].

Plasma activation disrupts the bonds in the molecules that are on the surface of the film. These molecules are then chemically active and tend to bind to the printed material. This process results in a very substantial increase in adhesion. The advantage of using plasma is that the whole process takes place at ambient temperature. The energy required to break the surface bonds is supplied primarily by electrons and excited particles from the plasma.

Corona discharge cleaning. The high-frequency voltage is applied to the surface of the substrate via a high-voltage transformer by means of ceramic or metal electrodes. The electrical arrangement must ensure an even distribution of the corona discharge on the substrate [147, 149].

Atmospheric plasma cleaning. High voltage electrodes ionize the air around the substrate being cleaned. The total plasma density is higher than in case of corona discharge and the cleaning efficiency is higher [149,148]. It is also possible to clean shaped surfaces.

Surface plasma activation. The surface activation device uses the Dielectric Barrier Discharge (DBD). It is a discharge that occurs at atmospheric pressure. The dielectric barrier discharge plasma is non-isothermal. The electrons here have the energy in the order of electron-volts, but the gas atoms and ions that are produced during the gas ionization have a temperature corresponding to the ambient temperature. Electron energy is sufficient to initiate chemical reactions, but the activated surface is not thermally loaded [150,151].

Depending on the gas composition the Dielectric Barrier Discharge there may be excited particles in the plasma that can transfer the energy upon return to the ground state. This

process also takes place at a temperature close to ambient temperature. For more details see Appendix A6.

The DBD plasma equipment that was used to activate the surface works with coplanar arrangement of electrodes. This is a variant of the DBD process operating with surface discharge (see Appendix A5 for details). This process is called as the Diffuse Coplanar Surface Barrier (DCSBD) discharge [155, 154].

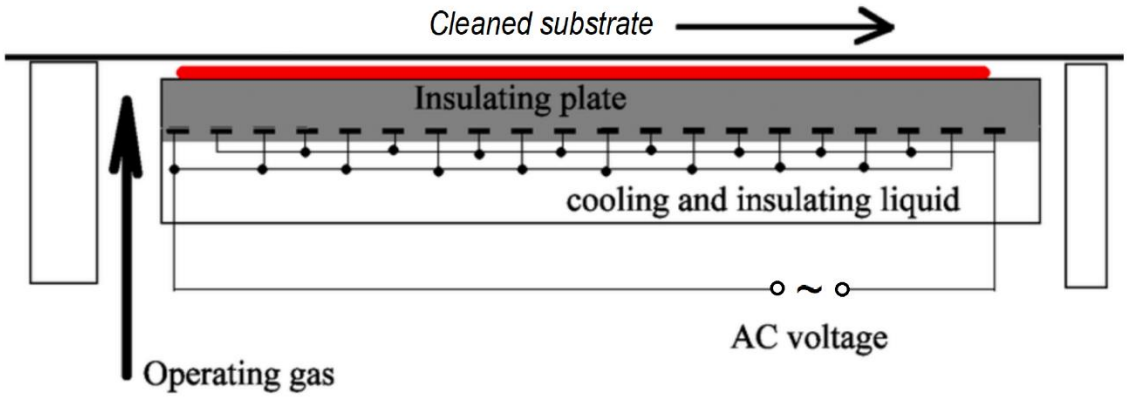

Fig. 14: Arrangement of a DCSBD electrode system [156,157].

The arrangement of DCSBD devices is shown in figure Fig. 14. Thanks to the concentration of the surface discharge in the area between the electrodes DCSBD technology is capable to create a thin layer of macroscopically uniform high-density plasma. This is unique property of DCSBD plasma technology that clearly differentiate it from other plasma technologies [157,156].

2 The aim and objectives of dissertation

Based on the analysis in the previous chapter in the framework of this thesis the photovoltaic and thermoelectric EH transducers were selected as low energy EH converters.

Photovoltaic transducers are well accessible but suffer from unpredictable drop-outs. Further, out of direct solar radiation there is in many cases not sufficient light intensity and the efficiency of photovoltaic converters depends on the spectrum of available lighting. Serial connection of photovoltaic cells may be affected by uneven lighting or failure of one of the cells. Single-cell photovoltaic transducer is less prone to various failures and if energy efficiency is not a monitored parameter single cell transducer can be an advantageous solution in many cases.

In almost all devices there is a release of large amount of waste energy. Such energy sources are well predictable because they are based on stable operation of respective devices. Thermoelectric Generators (TEGs) are therefore very attractive for possibility of harvesting of waste thermal energy in many applications. Further, the TEG devices have advantages such as silent operation, no moving parts and high reliability. Its use is advisable in locations where there are poor levels of illumination but where there is sufficient waste heat.

However, the voltage generated by one thermoelectric junction is quite low even in case of large temperature difference. Therefore, large number of thermoelectric cells must be connected in series. Serial electric resistance may be a bottleneck of this solution and must be taken in consideration.

In all applications single-cell solar panels and multiple-cell thermo-generators produce low output voltage not sufficient for normal operation of electronic devices. Using special electronic circuits, we may boost the output voltage to a level sufficient for operation of standard inverters or low voltage circuits. DC-to-DC converter also may ensure energy availability, especially by small and irregular energy supply when there is a need to store the harvested energy in supercapacitors or in the battery.

Considering above stated properties of low energy single-cell photovoltaic and thermoelectric EH transducers and the demands for their use - the objectives of the dissertation could be divided into individual tasks which can be summarized as follows:

1) Compile overview concerning preparation of EH photovoltaic structures and suggest solutions for their operation on low energy level.

Details: Prefer cheap production processes and cheap large scale production. For both single cell and series arrangements consider the possibilities of using materials based on organic semiconductors. Photovoltaic cells of the third generation which use a tandem

configuration should be also considered. The main selection criteria are easy availability, reliability and the ability to work in very low light intensity.

2) Compile overview concerning preparation of EH thermoelectric cells and suggest solutions for their operation on low energy level.

Details: Compare the possibilities of inorganic and organic thermoelectric materials. Focus on organic materials and methods of their preparation and adaptation to the requirements for use in thermoelectric generators. Mind that the electrical conductivity could be the bottleneck for all organic materials. Suggest possible solutions of thermoelectric generators. The requirement is a simple mechanical construction and the use of available materials.

Mastering the auxiliary goals in objectives ad1) and ad2) is necessary for successful work on the assigned topic.

3) Research and design of a low voltage low energy DC/DC converter to process the output from EH transducers.

Details: It is necessary to solve startup and continuous operation of the inverter at the lowest considered power capacity of the EH power source. The power which is needed to drive the switching transistor of the converter must be much lower than the energy which can be obtained from the EH transducer. Further, the energy consumption of control and driving circuits also must be considered. A capacitor, a supercapacitor, or a battery can be used to energy accumulation. For these converters, it is necessary to design and manufacture special transformers with a small rated power and a large transformation ratio. It is also necessary to consider possible solutions in low-voltage integrated circuit technologies.

4) Research and design of a thermoelectric converter using simple technologies and available materials

Details: Prefer available production processes and consider the possibilities of using of materials based on organic semiconductors.

The objectives of the dissertation are based on the analysis of state-of-the-art presented in the first chapter and build on existing research and published solutions. EH converters prepared in frame of this work should be used in various applications such as power supply for wireless devices and low energy chargers for different types of portable electronics. However, it is necessary to analyze the model situations of their use in the external and internal environment and to define possible problems associated with their operation.

3 Methods and Results

In this part of the work the attention is paid to the possibilities of using photovoltaic cells and to design of thermoelectric converters. The simple thermoelectric converter is designed so that cheap and available materials can be exploited and expensive manufacturing processes are avoided. Special attention is paid to design of suitable DC / DC converters and verification of their operation, too. Described experiments were mostly carried out in the premises of the Department of Microelectronics.

The scientific benefit is the extension of existing knowledge towards new structures of photovoltaic cells and heat generators using organic semiconductors according to current possibilities, as well as towards new concepts of DC / DC converters for voltages less than 100 mV.

3.1 DC to DC converters with low input voltage

All thermoelectric energy harvesting transducers typically provide a low output voltage not sufficient for electronic devices. A similar situation can occur with single-cell solar panels applications.

For optimal use of energy harvesters is therefore necessary to use a voltage converter with extremely low power supply voltage that requires only microwatts of power to begin the operation. A DC to DC converter is needed to boost the voltage from the level of several tenths of volt to the level of approximately 3 V, which may be applicable to most devices.

To design the converters of this type, transformers with a large ratio and switching components capable of operating with extremely low voltage are needed.

3.1.1 Design of high ratio transformers

Possibilities of manufacturing transformers with high conversion ratio are given in Chapter 1.2.3. The construction of the flat transformer and the planar transformer designed and used in the work will be briefly described here.

Flat transformer

To verify the effect of stray inductance on the resulting transformer properties, a larger gap was intentionally set between the toroidal cores.

The basis of the construction of this type of Flat Transformer is a printed circuit board. The primary thread loops are soldered directly into the printed circuit board (PCB) and this way they attach the individual toroidal cores to the printed circuit board with a fixed spacing. The distance between the cores is 2.5 mm. The printed circuit board thus serves as the supporting structure of the transformer.

The arrangement is clear from the figure Fig. 15. The core of the flat transformer consists of five toroidal cores with an outer diameter of 10 mm. The primary windings are arranged in parallel. Each primary winding has one conductor loop. The secondary winding has 25 turns. Consequently, the conversion ratio is 125.

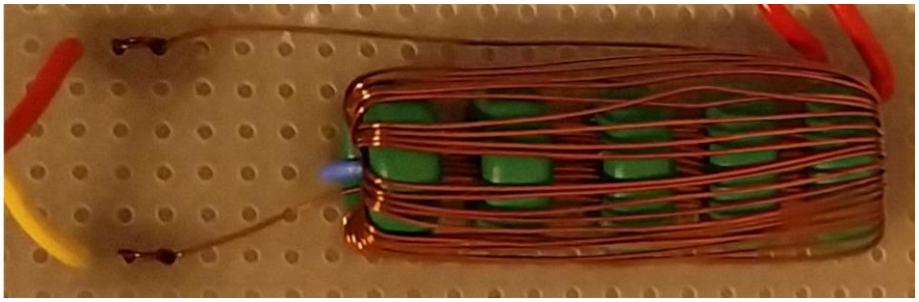

Fig. 15: Flat transformer type A with a looser arrangement of toroidal cores: 1 One loop of primary winding connected in PCB; 2 Primary input/output; 3 Secondary winding (25 turns); 4 Secondary input/output; 5 Toroidal core.

The transformer parameters were measured at a frequency of 10 kHz. Primary winding inductance L_1 = 0.42 μH, Secondary winding inductance L_2 = 6,52 mH, Secondary leakage inductance $L_{2\sigma}$ = 4,21 mH; Series resistance of the primary winding R_{S1} [Ω] Serial resistance of the secondary winding. R_{S2} [Ω]

The measured values correspond to the technological parameter of the core. (Al = 2.15 μH/ N^2). For clarity, they are arranged in the table Tab.3.

It is clear that the stray inductance is relatively large. This property is manifested mainly by a change in the conversion ratio of the transformer under load and the tendency of the secondary winding to its own oscillations. The actual oscillations of the secondary winding are very pronounced, for example, when excited by a rectangular signal. In this case, there are sinusoidal oscillations on the secondary winding instead of a rectangular signal. Their frequency is given by the stray inductance and the sum of all capacitances (including parasitic ones) in the secondary circuit.

Tab.3: Measured parameters of flat transformer, type A, frequency 10 kHz; Department of Microelectronics:

L_1 [μH] is Primary winding inductance; L_2 [mH] is Secondary winding inductance; $L_{2\sigma}$ [mH] is Secondary leakage inductance; R_{S1} [Ω] is Series resistance of the primary winding; R_{S2} [Ω] is Serial resistance of the secondary winding.

L_1 [μH]	L_2 [mH]	$L_{2\sigma}$ [mH]	R_{S1} [Ω]	R_{S2} [Ω]
0.42	6.52	4.21	< 0.1	~ 0.9

To reduce the stray inductance, it is necessary to ensure a tight connection of the cores. Details of low stray inductance assembly are clearly shown in the figure Fig. 16. The

arrangement is similar to the previous case, except that there is a minimum distance between the cores, thus ensuring good magnetic coupling and minimal stray inductance.

Again, the core of the flat transformer consists of five toroidal cores with an outer diameter of 10 mm. Each primary winding has one loop and primary windings are arranged in parallel. The secondary winding has 25 turns and this way the conversion ratio is 125.

The toroidal cores are mounted on a spacer tube having an outer diameter equal to the inner diameter of the toroid. The gap between the toroidal cores is variable. On the connection side of the primary winding, the pitch it is given only by the diameter of the primary winding and the necessary insulation. On the opposite side, the toroidal cores are pressed tightly. The terminals of the primary winding are soldered to the distribution bar of the primary winding, which is realized on the printed circuit board.

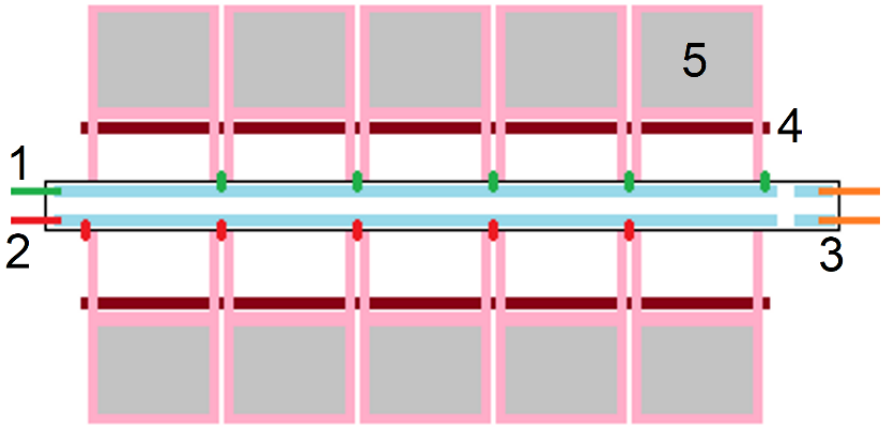

Fig. 16: Flat transformer type B with tight arrangement: 1 Primary input; 2 Primary output; 3 Distribution bar; 4 Spacer tube; 5 Toroidal core; Secondary winding (30 turns) is not shown.

The secondary winding passes freely through the spacer tube. The terminals of the secondary winding are also on the distribution bar of the primary winding. The small spacing of the terminals of the primary and secondary windings allows easy connection with a twisted pair cable. It is obvious that the number of turns of the secondary winding may have without difficulties more turns than the current 25.

The resulting transformer assembly B has approximately the same conversion ratio as assembly A. However, it changes significantly less with load. Compared to a planar transformer for both assemblies of flat transformer A and B have lower series resistance of both secondary and primary windings.

Measured parameters of flat transformer, type B are in table Tab.4. The main change compared to assembly A is in the scattering inductance on the secondary winding.

Tab.4: Measured parameters of flat transformer, type B, frequency 10 kHz; Department of Microelectronics:
L_1 [μH] is Primary winding inductance; L_2 [mH] is Secondary winding inductance; $L_{2\sigma}$ [mH] is Secondary leakage inductance; R_{S1} [Ω] is Series resistance of the primary winding; R_{S2} [Ω] is Serial resistance of the secondary winding.

L_1 [μH]	L_2 [mH]	$L_{2\sigma}$ [mH]	R_{S1} [Ω]	R_{S2} [Ω]
0.42	6.73	1.35	< 0.1	~ 0.9

Again, to compare the two assemblies A and B the response of the transformer to the excitation by the sinusoidal and rectangular signal was measured. Clearly, the response to the excitation by the rectangular signal is close to the voltage shape on the primary winding. The significant difference compared to the type A transformer is due to the much smaller leakage inductance of the secondary winding.

Flat transformer with toroidal cores is very advantageous for low power applications because toroidal cores are manufactured up to very small dimensions. However, when using toroidal cores with small dimensions, magnetic leakage problems can occur with this design.

Flat transformer rather works better with larger toroidal cores. The induction flux is here closed over a large area and the technological gaps between the toroidal cores have less effect. Technological gap can be further reduced by using thin conductors connected in parallel or by using strip conductors.

In case of small dimensions, the ratio of the core area to the area of the technological gap between the cores is smaller and a larger leakage inductance must be considered. However, when using this transformer for an Armstrong oscillator, a certain amount of leakage inductance is not a problem. On the contrary, it allows more reliable operation of the oscillator.

With both arrangement (A and B), it is very easy to use taps on the winding to change the transformer ratio. Clearly, depending on the tap used, not only the transformer ratio but also the inductance on secondary and the secondary leakage inductances are changed. This must be considered in practical applications especially when used in frequency related circuits, as an Armstrong oscillator used in this work.

Planar transformer

The design of the planar transformer was created within this work. PCB windings were manufactured by GATEMA Boskovice. The transformer winding is on double-sided printed circuit boards. The number of turns of the secondary winding is limited by the resolution of the technology, which determines the thickness of the lines and their pitch.

To suppress the leakage inductance, the winding is made as coplanar. Both sides of the board contain the same motif - one thread of the primary winding and 10 turns of the secondary winding. All primary windings are connected in parallel. All secondary windings are connected in series.

The parallel connection of the primary windings creates one loop regardless of the number of printed circuit boards (PCB) used for the construction of the transformer winding. The transformer conversion is then determined by the number of boards used. There are 10 turns of the secondary winding on each side of PCB. Thus, when the secondary windings are connected in series, each additional PCB means that the number of turns in the secondary winding increases by 20.

Primary winding. The jumpers on the primary windings are made by interconnecting their terminals on one side of the board.
Secondary winding. The secondary winding has the same direction in both layers of the printed circuit board. From the terminal on the side of the soldered jumpers, it continues to the center, where it passes into the opposite layer and in the same sense continues back to the terminal on the side of the soldered jumpers.

(1) **(2)** **(3)** **(4)**

Fig. 17: Planar transformer: Four types of secondary coils.

To interconnect multiple boards by simply soldering, the board outlets are offset from each other. To connect any number of boards, four motifs of the winding arrangement are sufficient. These motifs are shown in Fig. 17 in the cut-out from the printed circuit board.

The procedure for connecting the secondary windings of the individual boards is shown in Fig. 18.

(1) The winding passes along the underside of the board from point (a) to the center of the board, where it passes to the top. At the top, the winding continues to point (b). Point (b) is common to both plates (1) and (2).

(2) The winding passes along the underside of the board from point (b) to the center of the board, where it passes to the top. At the top of the winding plate, it continues to point (c). Point (c) is common to both plates (2) and (3).

(3) The winding passes along the underside of the board from point (c) to the center of the board, where it passes to the top. At the top of the winding plate, it continues to point (d). Point (d) is common to both plates (3) and (4).

(4) The winding passes along the underside of the board from point (d) to the center of the board, where it passes to the top. At the top of the winding plate, it continues to point (e). Point (e) for plate (4) is common to point (a) on the next plate (1). From point (a) to the plate (1), the winding continues in the same way as already described.

In addition to the trouble-free connection of the secondary windings, the crossing of the secondary winding conductors during interconnection is also solved with this arrangement.

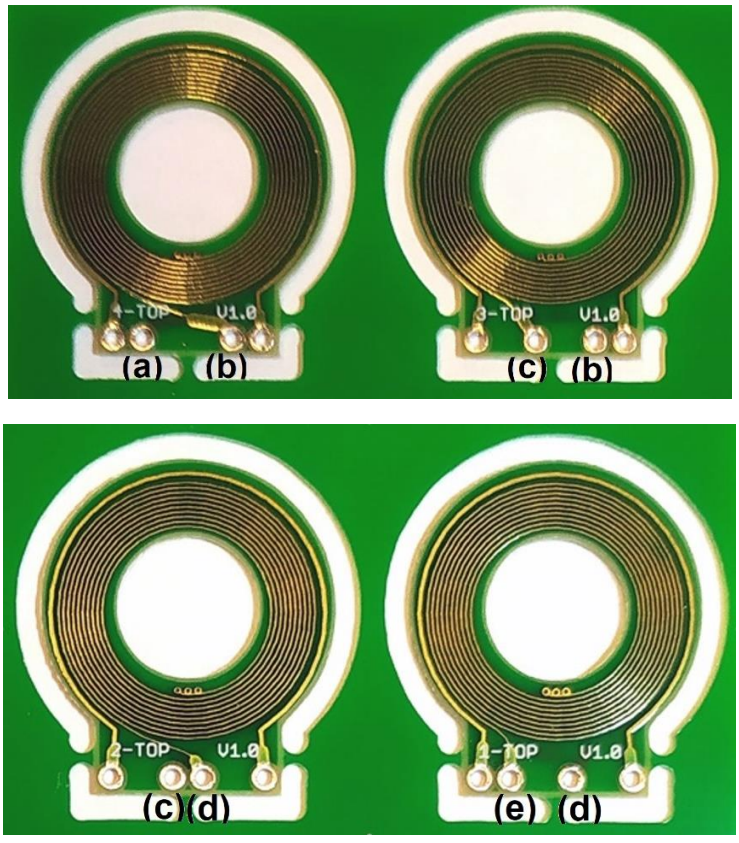

Fig. 18: Planar transformer: Interconnection of secondary coils.

The assembled parts of the planar transformer winding are shown in Fig. 19. The arrangement of the soldered jumpers is clearly visible. Seven of the eight printed circuit boards with planar windings are currently located on the core. On the transformer core there are 4 boards on the right and 3 boards on the left.

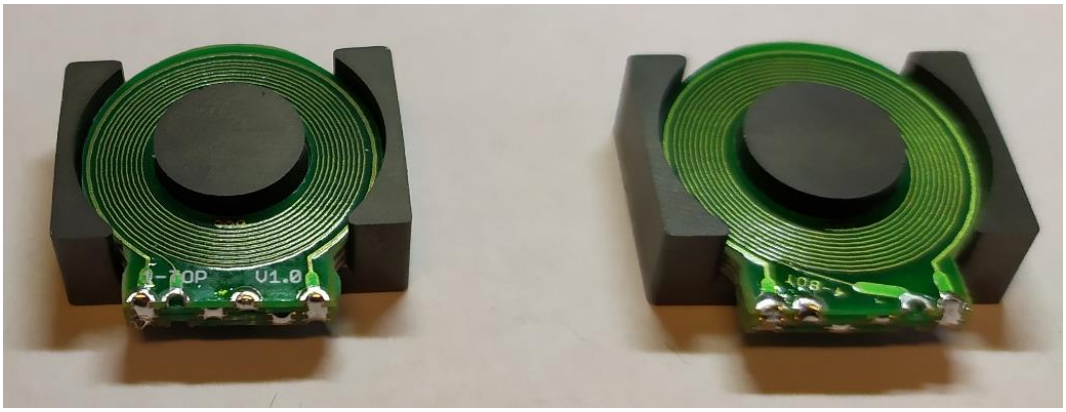

Fig.19: Planar transformer: Individual PCBs on the core.

The overall arrangement and connection of the terminal of this transformer is shown in Fig. 20

The advantage of this arrangement are stable transformer parameters and the possibility of reproducible variation of the leakage inductance.

A partial disadvantage of the design of the planar transformer is the limited number of core types and virtually zero core offerings for low power applications. Measured parameters are in table Tab.5.

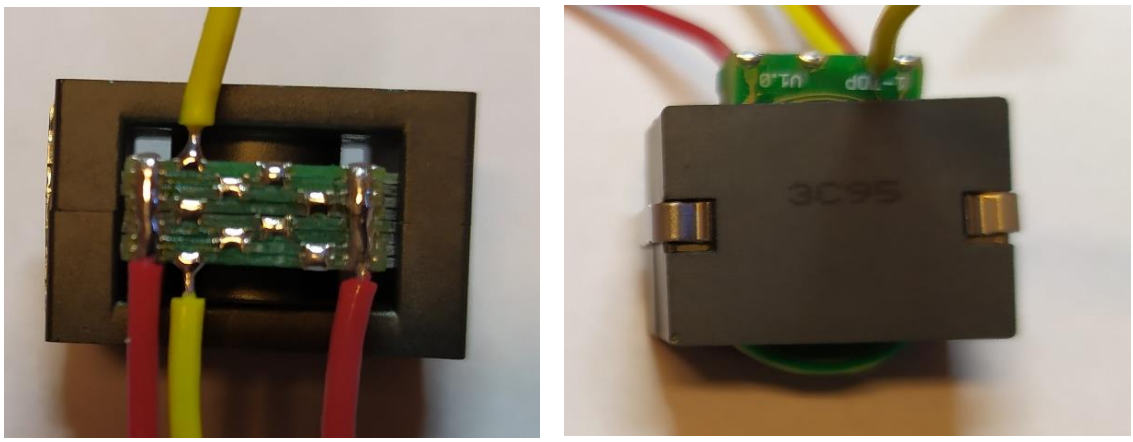

Fig.20: Planar transformer: Interconnection of secondary coils and arrangement of terminals.

Tab.5: Measured parameters of planar transformer, frequency 10 kHz; Department of Microelectronics:
L_1 [μH] is Primary winding inductance; L_2 [mH] is Secondary winding inductance; $L_{2\sigma}$ [mH] is Secondary leakage inductance; R_{S1} [Ω] is Series resistance of the primary winding; R_{S2} [Ω] is Serial resistance of the secondary winding.

L_1 [μH]	L_2 [mH]	$L_{2\sigma}$ [mH]	R_{S1} [Ω]	R_{S2} [Ω]
1.12	13.52	2..21	< 0.2	~ 2.3

Similarly to assembly B of the flat transformer B the response of the planar transformer to the excitation by the sinusoidal and rectangular signal was measured. The response to the excitation by the rectangular signal is close to the voltage shape on the primary winding. The significant difference compared to the type A transformer is due to the much smaller leakage inductance of the secondary winding.

3.1.2 DC to DC converter based on Armstrong oscillator

Armstrong oscillator was already mentioned in chapter 1.2.1. Principal scheme of Armstrong oscillator is shown in Fig. 21. For the oscillator to operate at a supply voltage of tens of millivolts it is necessary to ensure sufficient transformer conversion. A voltage of the order of volts is required to control the gate. This means that the transformer ratio should be at least in the range 1:30 to 1:100. Such large transformer ratio is difficult to implement and, consequently, the transformer will have a certain value of stray inductance. In case of an oscillator, however, the stray inductance does not prevent the circuit from functioning. Conversely, a looser coupling between the primary and secondary windings is a certain advantage.

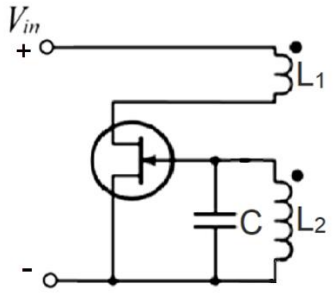

Fig. 21: Scheme of Armstrong oscillator.

The secondary winding connected to the gate provides a quiescent DC voltage at the gate U_{GS} = 0V. In this case, the J-FET transistor operates with maximum transconductance.

The transformer provides the positive feedback needed to maintain the oscillations. Changing the voltage on the resonant circuit, which is connected to the gate, the transistor opens and closes periodically. With a sufficiently large input voltage, the amplitude of the voltage at the gate is so large that the transistor is completely closed and opened. This way, from the side of the connected input circuit, the transistor works as a switch.

Operating at resonance the voltage on the resonant circuit CL_2 increases significantly. The magnitude of the voltage generated at the resonant circuit is determined by the quality of the resonant circuit. Therefore, the low serial resistance of the secondary winding of the transformer is important to achieve high quality resonant circuit. The size of the leakage inductance, which determines the degree of reverse transformation of the primary winding into the secondary circuit, is also not negligible.

Estimation of quiescent current of the converter

The DC current drawn by the DC converter at quiescent state (i.e. when the channel of J-FET is fully opened due to the V_{GS} zero value) can be estimated from the channel resistance at V_{GS} = 0. The current that is drawn from the EH converter can be then computed using the channel resistance of the J-FET in series with the transformer primary winding.

The resistance of the fully open JFET channel is difficult to determine from catalog values and it is preferable to measure it in some simple circuit. The connection for measuring of the channel resistance is shown in Fig 22.

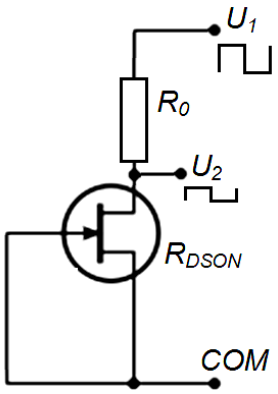

Fig. 22: The connection for measuring of the channel resistance of JFET; R_0 = 100 Ω, V_1 = 100 mV, V_2 = 40 mV

The resistance R_0 forms a voltage divider with the channel resistance R_{DSON}. This divider is powered by rectangular pulses from the generator. The dividing ratio is determined by the value of both resistors. For voltage values given in the Fig.22 and the resistance value R_0 = 100 Ω, the channel resistance R_{DSON} is:

$$R_{DSON} = R_0 \cdot V_2 / (V_1 - V_2) = R_0 \cdot 40/ (100 - 40) \approx 66.6\ \Omega$$

The value of parasitic resistance of primary winding is R_P = 1 Ω. (This value was measured as DC resistance by means of a multimeter M3800.)

The load resistance of the EH generator is then

$R_{CONV} = R_{DSON} + R_P \approx$ 66.6 Ω + 1Ω = 67.6 Ω

Assume the voltage at the output of the EH converter is 50 mV. The quiescent current drawn by the DC converter at quiescent state will then be:

$I = V_{EH} / R_{CONV}$ = 50·10^{-3} V / 67.6 Ω ≈ 0.73 mA.

In case that the starting voltage of the converter is 50 mV, the EH generator must be able to supply at that voltage the current at means 0.73 mA. After the converter starts, the current consumption drops. For different levels of starting voltage, the bias current will vary approximately linearly with the voltage. Obviously, an extremely low starting voltage is very advantageous in this case.

The DC / DC converter using Armstrong oscillator is shown in the figure Fig.23 . The transformer conversion ratio is 1: 100. The circuit starts at 50 mV. The output voltage is taken from the resonant circuit on the gate of the transistor. Voltage multiplier with capacitor C_2 and diodes D_1 and D_2 is used to rectify the voltage on the resonant circuit. At the same time, the multiplier acts as a current limitation of the battery power supply. The capacitance C_2 is a part of the resonant circuit and there is no significant damping of the resonant circuit during rectification.

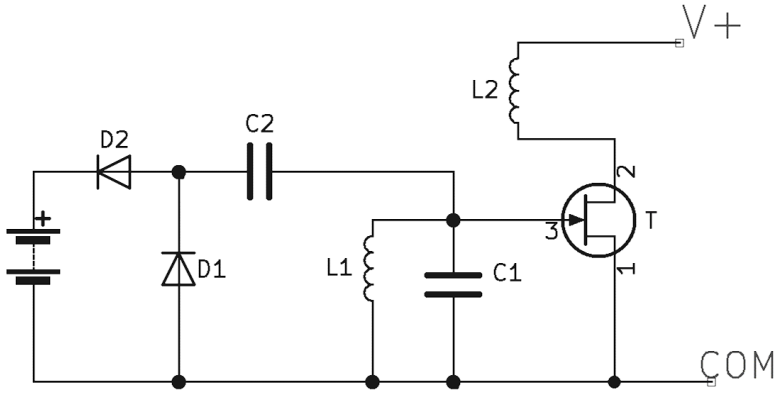

Fig. 23: DC converter based on Armstrong oscillator.

If the voltage at the resonant circuit drops at a low input voltage, the battery stops charging and the resonant circuit load is reduced. The oscillator is then maintained in operation even at very low input voltage. A similar situation also occurs when starting at low

voltage. The oscillator starts “no load” and the rechargeable battery is connected at a certain amplitude of the voltage on the resonant circuit.

3.1.3 Single JFET DC to DC converter

A generator with JFET in this circuit has the advantage of generating a negative bias on the capacitor in the gate circuit. This closes the transistor and draws current only when the transistor is activated by the voltage on the secondary winding. The circuit is therefore highly efficient. The transformer conversion ratio is not as demanding as in case of the Armstrong oscillator. However, a large transformer ratio is convenient also in this case.

Block diagram and the scheme of converter are on figures Fig. 24 and Fig. 25 respectively.

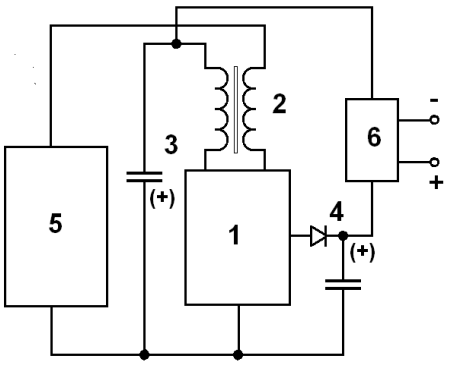

Fig. 24: Block diagram of converter

The transformer (2) is used to increase the voltage at the inverter output. This transformer is also used to control the switching element (1). The output voltage is taken between the capacitors (3) and (4). The energy harvester (5) supplies a voltage less than 1 V. The voltage level to operate the device (6) at the inverter output is several volts.

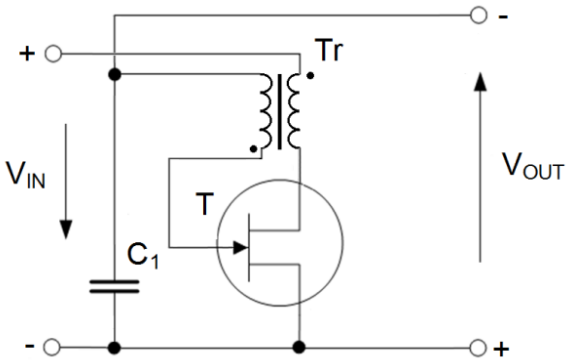

Fig. 25: Basic scheme of the converter: Transformer and switching J-FET.

The modified circuit shown in figure Fig.26 utilizes the energy stored in the transformer during the switch-on state. As soon as the switch-off starts a voltage pulse appears on the

primary winding, which charges the capacitor C_2. This is due to the drop of magnetizing current and subsequent collapse of the magnetic field in the transformer core.

It was verified that the circuit can operate in a large range of frequencies:

- The working frequency of the circuit is determined by the transformer.

- To ensure high efficiency, it is necessary that the transformer should minimize leakage inductance.

- At low frequencies, the switching losses are small but the transformer is bulky and it is a problem to achieve a small leakage inductance.

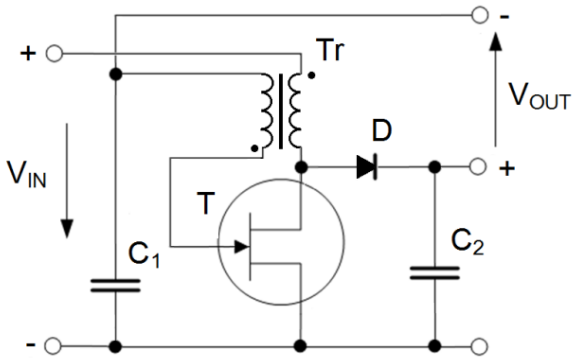

Fig. 26: Converter with increased output voltage

When using a toroidal transformer with a diameter of 8 mm the operating frequency of the circuit was 700 kHz. In this case, the efficiency has been limited by dynamic losses on the switch (J-FET) and on the diode D.

In table Tab.6 there are results of testing of inverter operated at frequency 700 kHz for both modifications of the inverter according to Fig.25 and Fig.26. The threshold voltage V_T of JFET was V_T = 2 V. The transformer secondary to primary ratio was N_S:N_P = 10:1.

For the converter, which utilizes energy stored in the transformer core, the efficiency is slightly higher. The output voltage is here greater however the current capacity is smaller.

Tab.6: Modifications of the circuit according to Fig.31and Fig.32; measured.

MOD	Start Voltage	Stop Voltage	Output Current / Voltage	Power / Efficiency	
A	0,5 V	0,3 V	3V / 100 µA	300 µW	45 %
B	0,6 V	0,3 V	4 V/ 80 µA	320 µW	50 %

Efficiency of the converter reach up to 50% but it could be possible to increase it in further optimization, particularly in the design of the transformer.

To ensure high efficiency the transformer must have minimal leakage inductance. To limit the impact of dynamic losses the operating frequency of 800 kHz should not be exceeded. Here it is necessary to find a compromise between the size of the inverter and its effectiveness [11].

The start-up voltage could be much lower by higher transformer ratio and/or when using the transistor with lower threshold voltage. In both cases however the energetic efficiency of the circuit drops.

After interruption of the oscillation, the inverter is temporarily blocked by a negative voltage on the capacitor C_1.

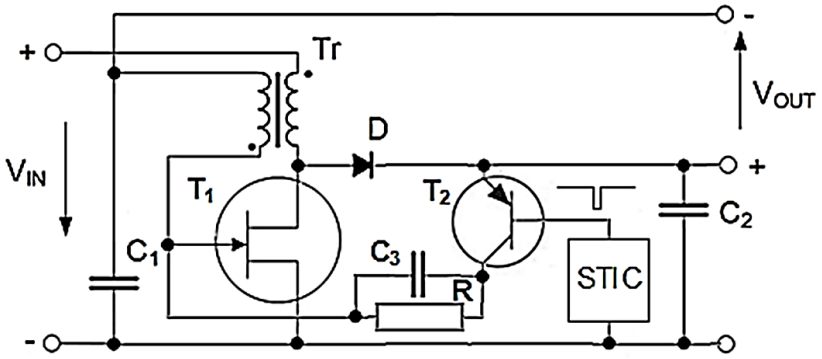

Fig. 27: Low voltage converter with improved low-current performance

Then the voltage on the capacitor gradually decreases, thus enabling the inverter to start again. However, if the voltage at the collection capacitor does not rise above the start voltage, the current taken in the quiescent state may prevent further voltage increase on the collector capacitor and the inverter will not start.

This situation can be avoided by modifying the second version of the inverter according to figure Fig. 27. Here, the supercapacitor or the battery is used instead of the collector capacitor C_1, so its voltage does not change much after the oscillations end and depends mainly on the load current. The inverter is therefore permanently in a locked state.

The starting impulse with a repeating interval adjustable within a few seconds is used to start the converter. The energy to generate start-pulses is taken from an auxiliary source using the diode and the capacitor C_2 that is powered by the energy stored in the transformer core when the transistor T_1 is switching off.

The starting impulse is produced by charging the capacitor C_3 when the transistor T_2 is switched on. The control pulses for this transistor are derived from the start-timing-circuit STIC. Resistor R connected in parallel with C_3 ensures that the “starting capacitor” C_3 is before each starting cycle discharged to zero voltage.

The charge transmitted in each trigger pulse is therefore determined by the value of the capacitance of the "starting capacitor" C_3 and the voltage difference between capacitors $C_1$and C_2.

Starter Circuit Requirements

1) To activate the DC / DC converter, pulses with a duration in order of microseconds are required. The pause between pulses should be in seconds.

2) The power consumption of the starter pulse generator must be substantially less than the mean power supplied by the EH converter. The means that starting power of the pulse generator should be in the order of microwatts. The starter circuit is fed from a capacitor C_2 and the EH converter is loaded only by a JFET quiescent current that is of in the order of 0.01 μA.

Comment: Most converters for EH applications are designed to draw minimum current in standby mode. Of the available integrated inverters, BQ25504 from Texas Instruments has the lowest bias current. The idle current is 0.33 μA and the startup voltage is as low as 330 mV [169]. Thus, the maximum power dissipation in standby mode is approximately 0.1 microwat for this circuit. However, the quiescent current continually loads the output of the EH inverter and the inverter may not start at very low current.

3) The optimum starter power supply voltage should be less than 1 V. The circuit should be able to operate even if the supply voltage drops significantly.

Simultaneous compliance with the above requirements is very difficult to meet.

For FETs, these parameters can only be achieved with low voltage integrated circuits that use special technologies. Circuit design is time consuming and must be verified by simulation. This simulation was already done and is described in Chapter 3.5.

In case of bipolar transistors, that works in low current mode the low voltage operation is fairly possible. At this mode the voltage at the BE junction is substantially less than 0.5 V and the collector-emitter saturation voltage is very small, typically in the order of 10 mV. The minimum applicable power supply voltage in this mode depends on the temperature and the type of bipolar transistor and can be about 0.5 V.

Bipolar transistor in low current mode

The minimum operating voltage of the bipolar transistor is determined by the voltage needed to open the base-emitter junction. For common use of a bipolar transistor, the collector current is usually selected in the order of milliamperes. Consequently, at current gain factor $\beta \approx 100$ the base current is in the order of tens of microamperes. This corresponds to a base-emitter voltage of about 650 mV. This value varies depending on the type of transistor and is highly temperature dependent. The temperature coefficient is around 2,3 mVK^{-1} depending on the type of transistor and current temperature.

Therefore, regardless of the type of transistor and operating conditions, in low-signal circuits the voltage of the base-emitter junction will be in the range of 0.6 to 0.7 V.

The base-emitter junction voltage derived from the Shockley equation can be used to estimate the base-emitter junction voltage when the collector current decreases.

$V_{BE} = m \cdot V_{T.} \ln (I_B / I_S)$,

where V_T is thermal voltage, I_S is the saturation current of the base-emitter junction and m is the ideality coefficient, for low-frequency small-signal transistors $m \approx 1{,}4$.

Thus, if the base current drops by one order, the voltage on the base will drop by about 100 mV. Consequently, when the collector current drops from 1 mA to 1 μA, the base current will also drop about 3 orders and the voltage on the base should drop by approximately 300 mV. Exactly, this voltage drop will be slightly smaller, because at very low collector currents, the current gain factor decreases significantly and the base current must then accordingly increase, so the base current will drop by less than three orders.

This behavior has been verified by measurement. Since a very low current measurement would require a voltmeter with extremely high input resistance to measure the base-emitter voltage and the measurement would be complicated by interference, the base voltage was calculated from the voltage drop across the elements in the base and collector supply circuits. For very low currents, it is also necessary to consider the voltage drop on the internal resistance of the micro-ammeter. Therefore, the calculation was performed by considering series resistances of current-meters as shown on the figure Fig 28.

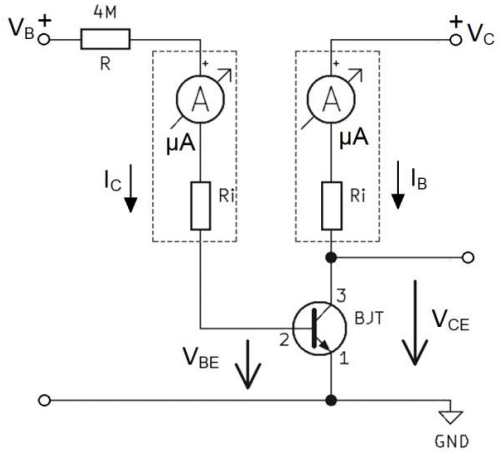

Fig. 28: Measurement of BJT parameters in low current operation. Voltages V_{BE} and V_{CE} are calculated using the voltage drop across the internal resistance of the micro-ampermeter.

For collector current in the range of 0.3 μA - 1 μA, the measured values of base current, current gain factor and base-emitter voltage are given in table Tab.7. The collector voltage is selected so that the transistor is at the boundary between the active and saturation modes.

Tab.7: The measured values of base current, current gain factor and base-emitter voltage. T= 300 K (Department of Microelectronics)

I_C [μA]	0.3	0.5	0.7	1.0
I_B [μA]	0.031	0.042	0.045	0.050
β [-]	10	13	17	20
V_{BE} [V]	0.298	0.301	0.308	0.310
V_{CE} [V]	0.1	0.1	0.1	0.1

Tab.8: The transistor output characteristics (Department of Microelectronics)

V_{CE} [V]	0.03	0.05	0.1	0.3
I_C [μA]	**0.59**	**0.79**	**1.00**	**1.02**
I_B [μA]	0.050	0.050	0.051	0.050
V_{CE} [V]	0.03	0.05	0.1	0.3
I_C [μA]	**0.33**	**0.41**	**0.50**	**0.50**
I_B [μA]	0.040	0.041	0.040	0.041

The transistor output characteristics for collector currents 0.5 μA and 1 μA are shown in table Tab.8. From the measured values it follows that the considerations above are relatively accurate. Further, when the temperature rises, the V_{BE} voltage drops by about two millivolts per Kelvin. When the temperature drops the V_{BE} voltage correspondingly increases.

Timing circuit with the astable flip-flop in low current mode

The circuit connection of the astable flip-flop used to generate the starting pulses is shown in figure Fig. 29. Here, the active elements alternately switch ON and OFF and their states are repeated periodically. The switching time is set by the value of timing capacitors and their discharge currents. This type of the astable flip-flop is also called as multivibrator. It is one of the oldest timing circuits but is still used for its simplicity and reliability.

For optimal operation it is advantageous if the switching period of both transistors is approximately the same. In case of significantly different periods, it is necessary to ensure

a sufficiently fast charge of the capacitor with a higher capacity via respective collector resistance and the open base-emitter junction of respective transistor.

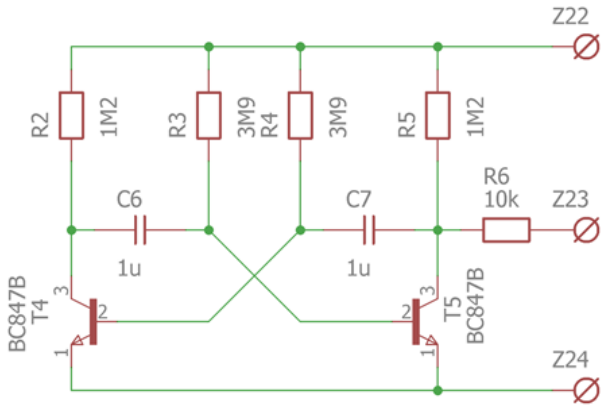

Fig. 29: Generator of starting pulses.

The pulses for starting the JFET generator must be shorter than the period corresponding to the operating frequency. For example, for 250 kHz, the period is 4 μs and the start pulse length should not be longer than 2 μs.

The length of the start pulse is set by charging the capacitor C_3 with the current of the transistor T_2 in switch ON state. The charge transmitted in the control pulse is determined by the magnitude of the voltage change and the value of the capacitance:

$$Q \approx C \cdot \Delta V$$

The parameters of the starting pulse generator depending on the power supply voltage are given in the table Tab.9.

Comment: It is necessary to respect the high impedances in the circuit. If we will use the oscilloscope probes with the division ratio 1:1 the measurement is influenced by 1MΩ oscilloscope input resistance comparable to the resistance values in the circuit. Partial distortion of the measured values occurs even when using a probe 1:10, which guarantees an input resistance of 10 MΩ. This should be considered when evaluating measurements.

Tab. 9: The parameters of the starting pulse generator depending on the voltage.

Operating voltage [V]	***0.5***	***0.8***	***1,0***
Current drawn [μA]	0.5	0.8	1.1
Power dissipation [μW]	0.25	0.64	1.1
Control pulses [V]	0.4	0.75	0.9
Control pulses [nC]	0.06	0.11	0.14

The function of the starter circuit

The function of the starter circuit was verified in the model wiring. The simulation of the voltage at the converter input was first set using a triangular voltage from the laboratory generator. The triangular voltage period was several tens of seconds to verify the dynamic start-up processes. In this model the starter circuit worked as expected. Accidental voltage changes, however, resulted in instabilities and in some cases, the generator was blocked. Since such states cannot be excluded during operation of EH inverters, the concept of reducing the load on the EH transducer by switching off the inverter and using the starter circuit has been evaluated as problematic.

Reducing the load on the EH transducer at low power

To reduce the load on the EH converter at low output power, the concept of load disconnection was tested. The disconnection takes place when the output voltage dropped below a preselected level. The load disconnection is reliable and is not connected with any transients. However, it is difficult to select the optimum cut-off voltage for variable loads.

Reducing the load on the EH transducer by disconnecting the charging current

Finally, a simple and reliable solution was found in connection of the DC / DC output to the circuit with a rechargeable battery or supercapacitor by means of a diode. The principle of operation is similar as is used with the Armstrong oscillator.

Final version of the DC / DC converter is given on the figure Fig.30. Charging of the storage element is only possible if the amplitude of the voltage at the DC / DC converter output is greater than the voltage at the battery or supercapacitor.

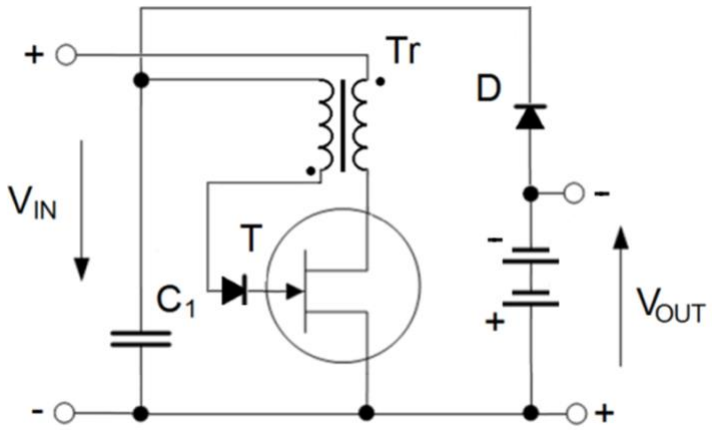

Fig. 30: Final version of the DC to DC converter

At growing input voltage the output voltage of inverter increases rapidly because the inverter is running without load. The output voltage of inverter grows until the diode separating the inverter output from the battery or supercapacitor opens.

When the diode opens, the output voltage of the inverter stabilizes to the voltage that is currently on the storage element. Depending on the processing power, only the inverter output current changes. A Schottky diode is used to separate the generator and the storage element from each other. At very low currents with that the inverter operates, the voltage drop across the diode is negligible.

The charging current of the battery decreases as the power drops. If the voltage on secondary winding drops to a value close to the threshold voltage of the JFET used, the voltage on the capacitor C_1 drops and the battery will be completely disconnected. The DC to DC converter then operates without load and the current drawn from the EH transducer is significantly reduced.

Another advantage of this solution is the possibility of connecting several DC to DC converters in parallel to a common storage element, supercapacitor or rechargeable battery.

The Schottky diode between the gate and the secondary winding protects the gate-channel junction of the JFET from electrical breakdown because at high power the negative pulses on the secondary winding have amplitude of several tens of volts. The Schottky diode used has a large rated current, so it has a small drop in the forward direction and the reverse current of the diode is enough to keep the J-FET closed.

3.1.4 Single JFET DC to DC converter in low voltage operation

When processing low voltage EH transducers, the efficiency of the designed DC to DC converters deteriorates because of the voltage drop across the resistance R_{DSON} of the transistor switch.

This is especially evident in DC to DC converters for thermoelectric transducers, where the voltage is in principle very low and relatively large currents are required to transfer the required power.

From the point of view of low resistance R_{DSON}, the most advantageous of the available J-FETs is type J111 (MMBFJ111) which has $R_{DSON} = 30\ \Omega$ (See the table in Appendix1).

For an approximate estimate of power losses, we assume that the transistor is ON for only one half of the period.

Furthermore, for simplicity, we assume that when switched ON, the current flowing through the transistor is twice the current supplied by the EH transducer. Suppose the mean value of the current I_{MEAN} = 1mA.

The power loss on the J-FET will then be very approximately:

$D \cdot R_{DSON} \cdot (2. I_{MEAN})^2 = 0.5 \cdot 30 \cdot (2 .10^{-3})^2 = 0.5 \cdot 30 \cdot 4.10^{-6} = 60\ \mu W.$

Here D = 0.5 is duty cycle corresponding the switching ON in one half of the period.

In fact, power loss will be even higher due to the shape of the current flowing through the transistor. Moreover, if we increase the current twice, these losses will increase approximately fourfold.

These values correspond to the efficiency values that were measured for both DC to DC converters under different operating conditions. For details, see Appendix 6 (Efficiency of Low Light Photovoltaic Converters).

It should be also considered that at the peak of the current consumption, the current peek is much higher than its mean value and the voltage drop across the transistor may be so large that it limits the further increase in current through the primary winding of the transformer. Of course, the efficiency of the entire inverter will drop very significantly in this case.

Although the inverters work at such conditions, they have large power losses with a large R_{DSON} due to the large processing current. The use of another J-FET type with a smaller R_{DSON} solves this problem only in part, because with a smaller R_{DSON} there must be a larger channel area and consequently there will be a larger input capacitance and commutation losses will be larger.

For use in connection with thermoelectric transducers, where it is necessary to work with extremely low voltage, a modification of a single J-FET converter was therefore proposed. Reduction of R_{DSON} is achieved by connecting a N-type MOS FET transistor with a small gate capacitance parallel to the J-FET switch. This additional transistor is controlled by pulses taken from the secondary winding of the transformer via a coupling capacitor.

The activation of a parallel switch with an N-FET transistor occurs only at a higher processing power. In high processing power the voltage amplitude on the secondary of transformer grows and the N-FET gate control pulses are significantly higher than the threshold voltage V_T.

As the processing power is further increased, the amplitude of the pulses on the secondary winding of the transformer further increases and the additional N-FET is controlled in the gate by a higher voltage and its channel resistance $R_{DSONFET}$ decreases.

The method of connecting the additional N-FET is shown in Fig. 31. With a negative pulse at the transformer secondary the coupling capacitor, C_{COUP}, is charged via diode D to a negative voltage V_{COUP}. In next part of the cycle with a positive pulse at the transformer secondary, there is a positive voltage at the J-FET gate, the magnitude of which is determined by the voltage drop at the open gate-source PN junction. Obviously, $V_{GSJ\text{-}FET} = 0.7$ V.

The voltage on the gate of the additional N-FET will therefore be the sum of the voltage on the open gate-source PN junction of J-FET and of the voltage V_{COUP} on the coupling capacitor : $V_{GSFET} = V_{GSJ\text{-}FET} + V_{COUP}$.

The commutation charge of the switch connected in this way is determined by the input capacitance of the additional N-FET. The change in voltage on the coupling capacitor C_{COUP} is very small. However, it must be considered that the commutation charge passes through this capacitor and the total charge in the output capacitor C_1 is reduced by the value of commutation charge of the additional N-FET.

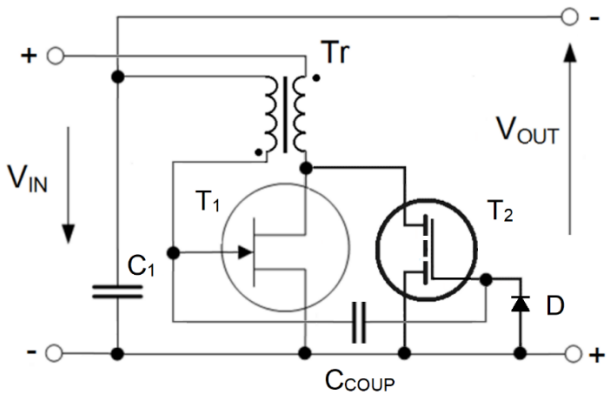

Fig. 31: Parallel connection of J-FET and N_FET to reduce influence of R_{DSON}

The advantage of this connection is that the gate control circuit does not contain resistive elements. Active losses occur only at diode D and at the open gate-source PN junction of the J-FET.

The N-FET BS 170 VT (ON-Semi) transistor is suitable for this connection. The parameters are as follows: $R_{DSON} = 5\Omega$, $V_T \leq 3$ V , $C_{ISS} \sim 40$ pF. When controlled by voltage $V_{GS} = 6$ V, the commutation charge can be estimated at 240 pC.

Conclusions follows from the performed experiments:

a) Converters with low secondary to primary transformer ratio (~ 10) start at a voltage of around 500 mV. When the input voltage drops, they work to a voltage around 300 mV. The efficiency is relatively high and it is possible to achieve up to 50%.

b) Converters with medium secondary to primary transformer ratio (~ 30) start at a voltage of around 200 mV. When the input voltage drops, they work to a voltage around 100 mV. The efficiency is between 30% and 40%. The effect of R_{DSON} size is already evident here. These inverters are suitable for photovoltaic cells in a single cell modification.

c) Converters with an extremely large secondary to primary transformer ratio (>100) start at a voltage of around 50 mV. When the input voltage drops, they work with a lower voltage, but not significantly lower. The efficiency is around 20%. The effect of R_{DSON} size is fully manifested here. These converters are suitable for thermoelectric generators with low output voltage but to achieve acceptable efficiency, it is necessary to ensure that the voltage drop across the switch is as small as possible.

3.1.5 Modifications of designed DC to DC converters in IC technology

To achieve low operation voltage we used the FET-IC technology implemented at the Department of Microelectronics which has a resolution of 130 nm. In modeling/simulation experiments different variants of the starting pulse generator were investigated and also the possibilities (within implemented FET-IC technology) to make a switch with high current capability.

Generator of starting pulses

The commonly used method of deriving time intervals from a high frequency reference obtained by a crystal oscillator or a ring oscillator composed of several gates is not very advantageous in this case.

Because the time in seconds is required, the number of divider circuits must be large. For example, if the generator frequency is 4 MHz and the required time is around 4 s, it will be necessary to include 24 flip-flops connected as a frequency divider.

The resulting output frequency will then be:

$F_0 / 2^{24} = 4$ MHz $/ 2^{24} = 4\,000\,000 / 16\,777\,216 = 0{,}2384185791015625$ Hz

And corresponding time is $t = 1/f = 1/ 0{,}2384185791015625$ Hz $= 4{,}194304$ s

However, flip-flops operating at a frequency in the order of MHz will have a large consumption due to transients, and the total consumption of the divider, including the reference frequency generator, will then be in the order of tens of microwatts.

Dynamic losses can be reduced if the reference frequency is significantly lower. In this case, it is necessary to use a capacitor as a timing element and to control its charging with a very small current. Even here, however, there are power losses on charging current sources and switches.

The simple timing circuit connected according to the figure Fig.32 proved to be an acceptable compromise from the modeling/simulating results.

The connection uses standard function blocks. Both capacitors C_1 and C_2 are charged with a current which is set by means of a current source CS and current mirrors with transistors T_1 to T_3. INV_1 and INV_2 inverters serve as voltage comparators. The flip-flop circuit RS decides on the current state of the entire circuit and controls the charging of capacitors C_1 and C_2.

Switches with transistors T_4 and T_5 are controlled from the output of the flip-flop circuit RS. It is obvious that depending on the current state of the flip-flop, only one of these transistors can be switched on.

The capacitor connected to the transistor that is currently open is charged with current from a current source formed by either transistor T_2 or transistor T_3 and the voltage on this capacitor gradually increases.

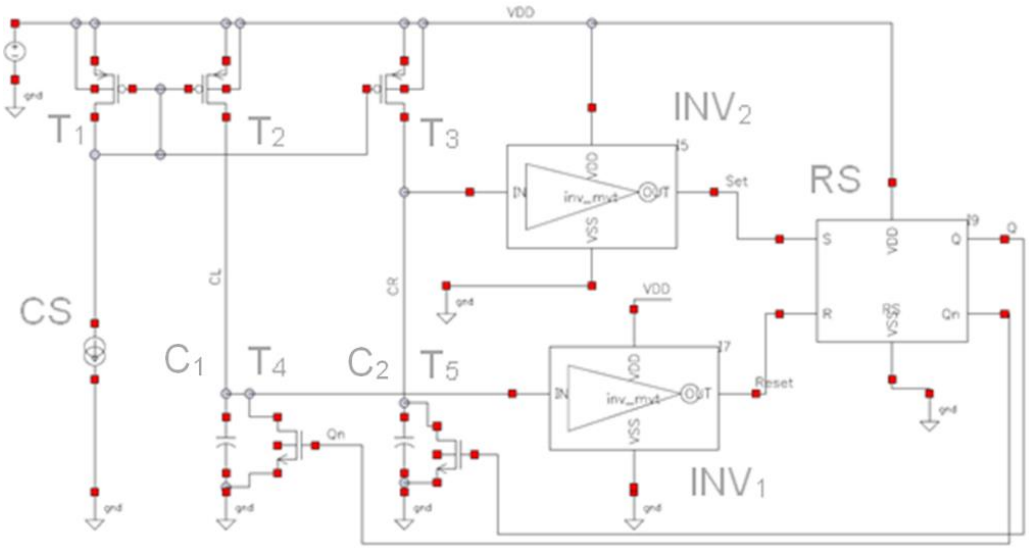

Fig. 32: Timing circuit for generator of starting pulses.

Assume that switch T_4 is open and capacitor C_1 is charging. As soon as the voltage on the capacitor C_1 reaches the decision level of the inverter INV_1, the inverter changes the state at the output and causes the flip-flop circuit RS to flip. This closes the switch T_4 on the capacitor C_1 actually being charged and the switch T_5 on the capacitor C_2 opens. It is now possible to charge the capacitor C_2 with current from a current source formed by a transistor T_3. As soon as the voltage on the capacitor C_2 reaches the decision level of the inverter INV_2, the inverter changes the state at the output and causes the flip-flop circuit RS to return into its default state. The described action is constantly repeated.

Due to the required frequency, the capacity of the timing capacitors must be in the order of microfarads. This can only be ensured in integrated circuit technology by using an external capacitor. Furthermore, to ensure low energy consumption, the operating currents must be very small. This places great demands on the timing capacitors C_2 and C_2 in terms of their leakage resistance. However, a capacitor with a high-quality dielectric can be used as an external capacitor and operation with small charging currents is possible. It is also necessary to consider influencing the capacitor charging by the leakage current of open switches T_4 and T_5.

In the modeled case, 1 microfarad capacitors were used. For the start signal period of 4 s, the charging time of capacitors C_1 or C_2 must be 2 seconds.

At the decision level, V_{INV} = 0.5 V, of the inverter the charging must be:

$I = (C \cdot V_{INV}) / t = (10^{-6} \cdot 0{,}5) / 2 = 0.25\ \mu A.$

Because of use of current mirrors there are the charging currents of both capacitors and the current of the reference current source passing through the circuit. The total current will therefore be:

$2 \cdot I_C + I_{SC} = 2 \cdot 0.25 + 0.25 = 0.75\ \mu A.$

Consumption of other parts of the circuit is negligible due to the very low operating frequency.

Thus, at a supply voltage of 1 V, the power input (power loss) of the circuit can be calculate as:

$P_{IC} = 0.75 \cdot 1V = 0.75\ \mu W$

According to table Tab 9. in Chapter 3.13, this power is comparable to the power input (power loss) of a starting pulse generator with a bipolar transistor.

High current switch.

The IC technology implemented at the Institute of Microelectronics capable operate with low power supply voltage has a resolution of 130 nm. Due to the very small structures, a relatively low channel conductivity is set here as standard. Because increasing the conductivity of a channel by increasing its area requires a change in the geometry of the structures this is only possible within certain limits. The requirement for a large operating current can only be solved by connecting transistors in parallel. Given the current capacity of the transistors, a large number of transistors is required to be connected in parallel to set the required resistance in the R_{DSON} on state less than 10 Ω. Depending on the change in the structure, this number can be greater than ten.

Shifting the operating point of the structure and changing the geometry affects the change in C_{GS} capacity and circuit time constants. Compared to discrete JFETs, the structure of parallel connected transistors is slower.

The requirement for parallel connection of switching transistors complicates the possibilities of using transistors in BULK DRIVEN mode. Here is the compromise solution to use transistors with a very low threshold voltage. However, these transistors will not be completely closed at $V_{GS} = 0$ and a negative voltage will be required to completely close the transistor. Negative voltage is not available during normal operation of integrated circuits but in case of designed DC / DC converters, this voltage is generated by a transformer. The FET in the integrated circuit structure then behaves like a depletion mode FET (or like J-FET) with a very low threshold voltage. The advantage is that a transformer with a small transformation ratio (e.g. 1:10) is sufficient for the operation of the generator in this case.

3.1.6 Summary of chapter 3.1 DC to DC converters with low input voltage

In this part of work the scientific and engineering contribution is the extension of existing knowledge towards new suggested and tested concepts of DC / DC converters for voltages less than 100 mV. To achieve high reliability, robust production processes have been preferred. Standard components are used, so the production is not tied to one supplier, or the lack of some type of components.

a) It has been verified that it is possible to work with a BJT with a very low supply voltage and extremely low power consumption, but the use of a BJT in this mode is very unusual. However, it must be considered that for integrated circuits where FET-type transistors are used, it is also necessary to use FET-type transistors under unusual operating conditions to achieve an extremely low operating voltage.

b) The circuit arrangement of DC to DC converter in integrated circuit technology, which is available at the institute, was designed. However, using available IC technology, to achieve low operating voltage, FET-type transistors must operate in the subthreshold mode or BULK-DRIVEN mode.

c) Two types of inverters have been designed and prototyping.

The Armstrong oscillator allows multiple transducers to be connected in parallel to one load. This is very advantageous when processing energy from multiple sources with unstable power and possible outages. This type of inverter is not sensitive to the stray inductance of the transformer.

A single FET DC to DC converter is more efficient than an Armstrong oscillator. However, it requires a transformer with low stray inductance. Complementary circuits have been tested for the designed and manufactured single FET DC to DC converter, which enable a significant increase in efficiency reaching up to 50 percent.

d) In order to maintain the functionality of the EH transducer at a very low power input, the START-STOP operation of the generator with the start of the generator by means of start pulses was proposed and tested for the single J-FET converter. In this case, the EH

transducer is not loaded by the connected DC to DC converter and is able to supply current to charge the capture capacitor at the input of the converter. Under laboratory conditions, this method has proven to be operational. However, it is not recommended for practical use due to the possible uncertainties in starting and stopping the generator and the associated reduction in reliability. Therefore, in the final design stable no-load operation was preferred over switching off the EH converter and resetting with start pulses.

f) Two types of innovative transformers with extremely high conversion ratios have been designed for low-voltage DC to DC converters:

Flat transformer allows very simple production. With this type of transformer, it is also possible to make miniature transformers, where the nominal power input can be much less than 1W. Scaling of transmitted power can be achieved by using a larger number of toroidal cores or by increasing the dimensions of toroidal cores. It is very easy to achieve a conversion ratio greater than 100. The stray inductance depends on the way the core of flat transformer is composed.

A planar transformer is more complex because it requires high-resolution multilayer PCB technology. The small stray inductance on the secondary winding of the transformer is ensured by a suitable distribution of the primary and secondary windings on the printed circuit boards of the individual layers. The conversion ratio can be much larger than 100 and can be set by the number of individual printed circuit boards in the assembly. The addition of one more plate always increases the conversion ratio by 20. The disadvantage of this type of transformer is the dependence on the range of ferrite cores. It is therefore not possible to achieve arbitrarily small dimensions and extremely small rated power.

g) Further, from the performed experiments it follows:

i) Converters with low secondary to primary transformer ratio (~ 10) start at a voltage of around 500 mV. When the input voltage drops, they work to a voltage around 300 mV. The efficiency is relatively high and it is possible to achieve up to 50%.

ii) Converters with medium secondary to primary transformer ratio (~ 30) start at a voltage of around 200 mV. When the input voltage drops, they work to a voltage around 100 mV. The efficiency is between 30% and 40%. The effect of R_{DSON} size is already evident here. These inverters are suitable for photovoltaic cells in a single cell modification.

iii) Converters with an extremely large secondary to primary transformer ratio (>100) start at a voltage of around 50 mV. When the input voltage drops, they work with a lower voltage, but not significantly lower. The efficiency is around 20%. The effect of R_{DSON} size is fully manifested here. These converters are suitable for thermoelectric generators with low output voltage but to achieve acceptable efficiency, it is necessary to ensure that the voltage drop across the switch is as small as possible.

3.2 Photovoltaic structures

The use of photovoltaic cells is facilitated by the fact that it is a mature technology and there are many types of photovoltaic cells on the market. Attention is therefore paid to comparison of individual cell types according to technology and selection of suitable cell type. For the intended use in low energy harvesting was considered above all the use of the cell in a single cell configuration. Attention was also paid to the possibility of using organic photovoltaic cells. A model calculation of the profitability of an organic cell photovoltaic power plant is presented in the last chapter of this section.

3.2.1 Materials and production technologies of photovoltaic cells

The aim of the research and experiments with photovoltaic cells of different technology was to verify the possibilities of their use in low-energy applications. The benefit of this work was not only to gain practical experience with different types of photovoltaic cells but also to verify the theoretical assumptions obtained by studying the literature. The results are summarized in following table Tab.10.

In first part of the experiment the most impotent properties of the cells were compared. The maximal cell voltage that is represented by the open-circuit voltage V_{OC} is given by the built-in voltage of the respective junction. The built-in voltage is mainly given by the energy of the forbidden band-gap of respective semiconductor. For moderately doped junctions without crystal defects and impurities, the built-in voltage is approximately 0.4 V smaller than the band gap of the respective semiconductor expressed in volts. Further, built in voltage it is affected by the level of doping of the respective junction.

However, the open circuit voltage of photovoltaic cells in experiments differs from values expected when considering the band-gap-energy of the individual semiconductors. The reason is possibly immature technology of experimental cells and huge recombination in the cell as a consequence of defects.

For example, the voltage difference between crystalline silicon cells and amorphous silicon cells is less than 0.3 V, despite that amorphous (hydrogenated) silicon has the largest band-gap (reaching up to 1,8 V depending on the concentration of hydrogen) of all used semiconductors

The table also shows that the cells differ significantly in the size of the short-circuit current, I_{SCA}. This parameter depends not only on the efficiency of the cell corresponding to given technology, but also on parasitic resistance of the cell in experiment. At high current, the power losses are affected by the series resistance, R_S, and at very low currents the cell efficiency is greatly influenced by the leakage resistance, R_{SH}, of the cell.

For use in the proposed low-energy converters, it must be ensured that the cell will be able to supply sufficient current to maintain the cell voltage at the value required to start the DC/DC converter under all operating conditions. The cell area must therefore be selected according to this current. With very low illumination intensity it is necessary to consider that the cell current will decrease much faster than the intensity of illumination due to parasitic resistance R_{SH} in the structure.

Table 10: Measured parameters of photovoltaic cells:
V_{OC} [V] is Open Circuit Voltage, I_{SCA} [mA] is Short Circuit Current, A [cm^2] is area of the cell, I_{SCA} [mA/cm^2] is Short Circuit Current per area of 1 cm^2

TYPE	**V_{OC}** [V]	**I_{SC}** [mA]	**A** [cm^2]	**I_{SCA}** [mA/cm^2]	**P_A** [mW/cm^2]	**P_{AX}/P_{ASi}** [-]
Crystalline Si *)	0.61	350.0	12.5	28.0	17.8	1.0
Micro Si	0.55	72.0	4.5	16.0	8.8	0.49
Perovskite	0.85	102.6	6.0	15.1	12.8	0.72
a-Si:H	0.82	45.4	4.5	10.1	8.3	0.46
a-Si:H + Micro Si / tandem	1.25	43.2	4.5	9.6	12	0.54
CGS	0.65	221.4	9.0	24.6	15.99	0.90

Samples:

Crystalline Si: Provided by company Fill Factory s.r.o. Roznov pod Radhostem, Czech Republic; Dimension 100 mm x 100 mm (full size); As needed cut to smaller parts; Screen printed BUS-bars. *) dimensions 25 mm x 50 mm.

Micro Si: Provided by the Institute of Physics of the Czech Academy of science (FZU), Prague Czech Republic; dimension 15 mm x 30 mm; Evaporated contacts

Perovskite: Provided by Chemical Faculty BUT BRNO; Dimensions 30 mm x 20 mm. Lab sample; Thin film contacts.

a-Si:H: Provided by FZU; Lab sample; Dimensions 15 mm x 30 mm; Evaporated contacts.

a-Si:H + Micro Si (tandem): Provided by FZU; Dimensions 15 mm x 30 mm; Lab sample; Evoparated contacts.

CGS: Provided for measurement by the Department of Microelectronics FEEC BUT BRNO; Lab sample; Dimensions 30 mm x 30 mm. Thin film contact.

When using semiconductors with a larger band gap, the corresponding PN junction has a larger built-in voltage. Consequently, the open circuit voltage, V_{OC}, of the cell will be higher and the short circuit current, I_{SC} , at the same light intensity will be less.

The maximum value of the open circuit voltage, V_{OC}, corresponds to the built-in voltage for the respective PN junction. This voltage is usually approximately 0.4 V less than the width of the band gap. However, for materials with increased recombination, the voltage drop is larger and the open circuit voltage, V_{OC}, is much less than the built-in voltage.

Different current magnitudes for cells with different band gap widths under the same illumination are reflected in tandem cells in series arrangement. There is a higher voltage, but in principle a smaller current, because it is determined by a cell with a lower current. In a very simplified view, it can be stated that under optimal conditions, the operation mode of the cell with a semiconductor with a larger band gap width is shifted towards the operation in a short circuit. Consequently, the operation mode of the cell with a smaller band gap width is shifted towards an open circuit operation. A partial solution to this problem is a structure where tandem cells are connected in parallel. A detailed explanation is in the Appendix A3 Photovoltaic Tandem Cells

A 50W halogen bulb was used as the lighting source. For the halogen bulb, the luminosity can be estimated as 20 lm per Watt of input power. Correspondingly, a 50 W halogen bulb will give the luminosity 1000 lm. The distance of the illuminated area from the bulb was 110 mm. At this distance and at a luminosity of 1000 lm of the halogen bulb, the light intensity can be estimated at approximately 82 thousand lx. This corresponds roughly to 80% of AM1.5. However, it must be considered that the spectrum of a halogen bulb does not exactly match the spectrum of daylight. See for details in chapter Chapter 3.3.2.

Series resistance

The series resistance of the cell can be determined by using this transient action when the current forced into the cell is switched off.

The wiring diagram for the measurement is shown in Fig. 33. At the time of disconnection, the voltage on the cell is maintained by a charge in the barrier capacity of the cell, so that the voltage drop that is detected at the time of disconnection is given by the voltage drop across the series resistor. Knowing the current of the cell, we can determine the series resistance R_S from the voltage drop:

$$R_S = \Delta V_{SC} / I_{SC} ,$$

where I_{SC} is the current forced in dark conditions to the photovoltaic cell;

ΔV_{SC} is voltage drop on the photovoltaic cell after switching off the current I_{SC}.

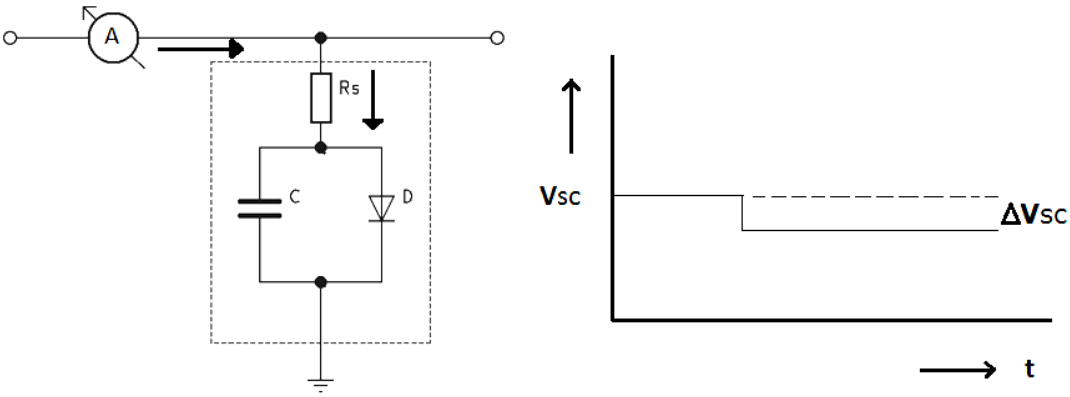

Fig. 33: Measurement of the series resistance R_S.

The series resistance is given by the sum of the resistance of the conductive paths, the contact resistance at the electrodes and the resistivity of the substrate material. The resistivity of the material decreases under illumination. How the reduction in material resistance under illumination affects the overall series resistance depends on the design of the cell.

Shunt resistance

In particular, crystalline silicon cells are very susceptible to leakage currents. Contact electrode systems are formed here using conductive pastes that are fired at a temperature of about 800 °C. The firing process must not only evaporate the solvents and connect the conductive microparticles together when the paste is hardened, but also burn the collecting electrodes through the passivation layer to ensure good contact of the conductive paths to the surface of the photovoltaic cell itself.

The contacting process greatly influences the series resistance of the cells and thus their efficiency at high currents. However, when the paste is burnt through the passivation layer various defects often spread to the substrate volume. These defects then create leakage currents of the cell.

While leakage current defects are typical of crystalline silicon cells, leakage currents can be very low in thin-film cells with optimally set technology. In this case, the electrodes are usually applied by vacuum processes and the probability of defects occurring inside the cell is very low. Photovoltaic cells made from amorphous silicon can thus exhibit a very high value of shunt resistance and can have excellent performance for low light intensities making them particularly suitable for indoor applications.

Measurement of the shunt resistance

The processes applied to the leakage current can be voltage-dependent. In addition to the ohmic conductivity, many other mechanisms can take place here that concentrate the leakage current in material defects and cause tunnel-jump conduction at the inhomogenities. The leakage resistance measurement is therefore subject to errors, depending on the cell type and measurement method used.

Of course, following considerations apply only to the currents of the photovoltaic cell in the dark.

The measurement of the leakage resistance further complicates the fact that the current through the cell is the sum of the current flowing through the leakage resistances and the normal current of the junction. At forward bias on the junction, there is a diffusion current that complicates the measurement of leakage resistance. The actual junction current can be then calculated using the Shockley equation. At a voltage of less than 300 mV, the junction current will be small enough and the cell current will be predominantly determined by the leakage currents.

In case of reverse bias of the cell-junction, the reverse current of the junction does not have any influence on the measurement of leakage current. However, in reverse bias the mechanism which cause the leakage current may be different from that which apply in forward polarization of the junction. Therefore, the measurement in forward bias allows a better evaluation of the real situation. Because leakage currents can be voltage dependent, it is advisable to measure the leakage resistance depending on the applied voltage.

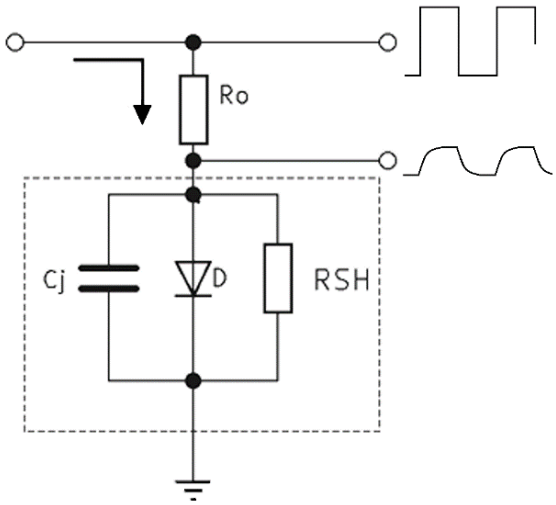

Fig. 34: Measurement of the leakage resistance using the square-wave voltage.

The method of measuring the leakage resistance used in this work is shown in Fig. 34. To determine the voltage dependence of leakage currents, the photovoltaic cell is powered from a current source. The current forced from the current source sets the voltage bias on the cell. The current source does not affect the voltage excitation, which is performed by a square-wave signal with a small amplitude. The amplitude is chosen so that the cell junction remains in the linearity range and is set to 30 mV peak-to-peak. The actual magnitude of the leakage resistance is determined by means of a voltage divider consisting of a resistor R_0 and the impedance of the photovoltaic cell.

It is obvious that the current-response to voltage excitation is influenced by the geometric capacitance C_J of the junction. Moreover, there may also be an effect of the dynamic resistance of the junction, which in this case connects in parallel with the shunt resistance R_{SH}.

If the period of the square signal is long enough, the time constant associated with the cell capacity does not apply. The dynamic resistance of the cell junction does not apply to a DC voltage bias in forward direction of approximately 200 mV. For DC voltage bias higher than 200 mV, the cell response is already affected by the cell junction dynamic resistance and it is given by a parallel combination of leakage resistance and cell junction dynamic resistance. In such case it is necessary to determine the dynamic resistance of the cell-junction for each measurement separately.

The calculation of the value of the leakage resistance is performed considering that the cell response is given by parallel combination of both resistances R_{SH} and r_D. Details of this procedure are in Appendix A10 Leakage Resistance of Photovoltaic cells

In the simplest case, the shunt resistance forms a voltage divider with the resistance R_0. From the ratio of the input voltage of the divider to the voltage on the cell, the value of the resistor R_{SH} can be simply calculated as follows:

$$R_{SH} = R_0 \cdot V_2 / (V_1 - V_2)$$

where V_1 is the amplitude of square-wave on input of resistive divider,

V_2 is the amplitude of square-wave voltage on the cell.

Resistor R_0 is selected according to the expected value of respective R_{SH}. It is preferred that the resistances of both resistors are approximately comparable. For cells with large R_{SH} or cells with small area, the measurement could be influenced by the input resistance of the oscilloscope. In this case a 1:10 probe should be used.

Voltage-dependent faults can also be detected using a triangular signal according to the circuit on figure Fig 35. If the triangular signal on the R_{SH} resistor is distorted, the current dependence of the voltage drop on resistor R_{SH} is not linear.

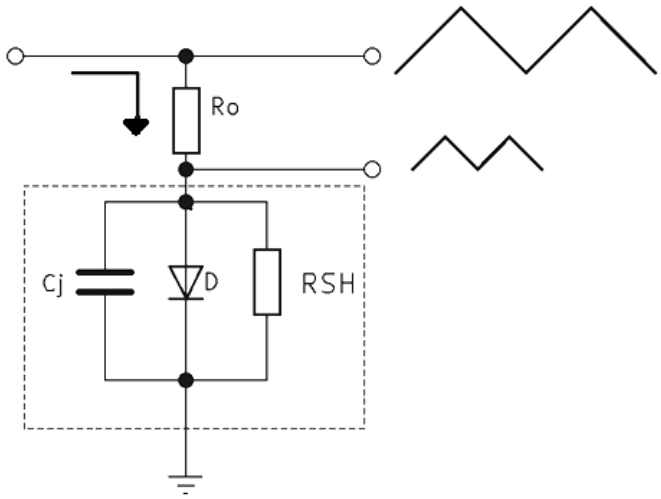

Fig. 35: Measurement of the leakage resistance using the square wave voltage.

From the distortion of triangular signal there is possible to determine at what voltage the respective anomalies occur. However, the signal distortion must be distinguished from the distortion of the triangular signal that occurs due to the nonlinear ampere-volt characteristic of the diode.

Series resistance and shunt resistance of the photovoltaic cells in experiments are arranged in table Tab.11. The samples were the same as in the experiment with the measurement of basic parameters for which the results are in Table 8.

Table 11 : Series resistance and shunt resistances of photovoltaic cells:
A [cm^2] is area of the cell, R_S [Ω/] is Series resistance, R_{SA} [Ω/cm^2] is Series resistance per area, R_{SH} [Ω/] is Shunt resistance, R_{SHA} [Ω/cm^2] is Shunt resistance per area,

TYPE	**A** [cm^2]	**R_S** [Ω]	**R_{SA}** [Ω.cm^2]	**R_{SH}** [Ω]	**R_{SHA}** [Ω.cm^2]
C - Si	12,5	0,152	1,9	85	10 62
Micro - Si	4,5	0,557	2,5	60	270
Perovskite	6,0	1,56	9,38	22	132
Amorphous Si	4,5	0,711	3,2	78	351
A-Si + Micro-Si (tandem)	4,5	0,762	3,43	95	430
CGS	10	0,210	2,1	67	670

A great advantage of the described measurement of parasitic resistances of the cell is the possibility of measuring in the dark without the use of special instruments. The measured values do not depend on the lighting and describe the physical properties of photovoltaic cells very well. The parameters measured at full illumination may differ from the parameters measured at dark due to the increase in the conductivity of the substrate during illumination.

Crystalline silicon cells versus thin film cells

Due to the fall in prices for crystalline silicon cells, thin-film cells cannot be serious competition for the production of solar panels. However, they can be very well applied in interior spaces where they may have comparable or even better properties compared to crystalline cells.

Unlike crystalline silicon cells, where the surface treatment prevents reflection of the radiation over a wide range of incident angle, in case of thin film cells the relative angle between the incident radiation and the cell surface can have a significant effect on absorption of the incident radiation. Thin-film cells are therefore more suitable for diffuse radiation, which occurs under cloudy conditions or, eventually, when used indoors,

The thin-film photovoltaic cells in this experiment are laboratory samples. They therefore have a relatively large series resistance and a low value of shunt resistance. This is especially evident in the Perovskite sample. However, it is clear from the magnitude leakage resistances and series resistances of the cells that silicon crystalline cells are most suitable for operation in low light intensity.

Scaling of crystalline silicon cells

When testing solar cells, the lighting intensity AM1.5 is considered as the lighting reference value. Under AM1.5 illumination crystal silicon commercial cells have short-circuit current between about 28 mA/cm^2 and 35 mA/cm^2.

The definition of lighting according to parameter AM1.5 is explained in detail in Appendix A12 Solar radiation in characterization of PV cells. The illuminance under AM1,5 is given as 109 870 lux and corresponds to radiant power 1000.4 W/ m^2. However, during the day the light intensity fluctuates. When the sky is cloudy, the light intensity is around 1000 lx. Interior lighting intensity in households is usually in range 100 lx to 500 lx.

For example: A 10 W LED lamp with a luminosity of 1000 lm produces a light intensity of 1000 lx on a spherical surface with a radius of 1 m, a light intensity of 250 lx on a spherical surface with a radius of 2 m and a light intensity of 111 lx on a spherical surface with a radius of 3 m.

Therefore, if the photovoltaic EH converter have to operate indoors, it should be able to process the radiation intensity at a level three orders of magnitude smaller than the AM1,5 standard.

For the lower limit of the above short-circuit current density, this will be:

(28 mA /cm^2) / 10^3 = 28 μA /cm^2.

An area that will be required to supply 1 mA current:

1mA/ (0,28 μA/cm^2)= 35.7 cm^2.

However, it is not economical to produce cells with such small dimensions. A similarly large area of the cell can be obtained by dividing the crystalline silicon cell with standard dimensions into several parts.

With the standard cell dimensions of 156x156 mm, the cell area is 243, 36 cm^2.

By dividing it into 8 parts we get the area:

243,36 / 8 = 30.42 cm^2

Dividing into 6 parts we get the area:

243,36 / 6 = 40.56 cm^2

The difference from a standard photovoltaic cell is in the arrangement of the collecting electrodes, which must be optimized to collect the current generated in the individual cells.

NOTE 1: When assembling photovoltaic cell modules, the cells must be sorted according to the rated current. If due to faults and crystal defects the rated current of a cell is less than the minimum value, the inclusion of this cell in the solar module is disadvantageous, as it can adversely affect the function of the entire module. However, this discarded cell can be still used when divided into several smaller area cells for use in EH low energy devices. To ensure reliable collection of the generated charge in all single cells thus formed, the cell must be divided according to the actual arrangement of the collecting electrodes. Therefore, the dimensions of individual single cells will not be the same and more types of single cells with different dimensions and different working areas will result.

NOTE 2: In connection with the possibility of cutting photovoltaic cells into several parts with a smaller active area for use in special cases, the idea also arises that the cells obtained from recycled photovoltaic panels could be used for this purpose. However, such procedure is complicated by the fact that the cells are laminated in the photovoltaic panel with very resistant layers. An intact cell can only be released from laminated layers by thermal processes. Upon annealing at a temperature of 500 Celsius, the plastics in the laminating layers are released and evaporated. Subsequently the evaporated plastics are

burned in a combustion chamber. In the standard process, current collectors as well as anti-reflective layers and doped layers are chemically removed from the photovoltaic cells that are released from the panel after this operation. This gives a material which is substantially identical to the starting material [170]. The etched layers comprise less than 1% of the total thickness of the material. This process is fully automated. The probability that such separated cells will be fully functional is small and diagnostics and sorting of functional cells would complicate and increase the cost of the recycling process.

3.2.2 Photovoltaic energy harvesting in low light condition

The behavior of selected single cells under real operating conditions was tested for an EH converter operating at total energy level deep below 1 W. The low voltage at the cell output was boosted-up using the low voltage DC to DC converter.

The wavelength from which a photovoltaic cell can absorb incident photons depends on the width of Band Gap of semiconductors in the structure of the respective photovoltaic cell. Because of different light levels and spectral composition of the incident light, it is very important to consider the operating conditions and adapt the selection of the photovoltaic cell to these conditions.

Figure Fig. 36 shows the spectral distribution of solar energy impacting on Earth surface after filtration in the atmosphere. It is obvious that the bulk of performance is approximately between the wavelengths 400 nm and 1100 nm in the range of the visible spectrum and in the near infrared region.

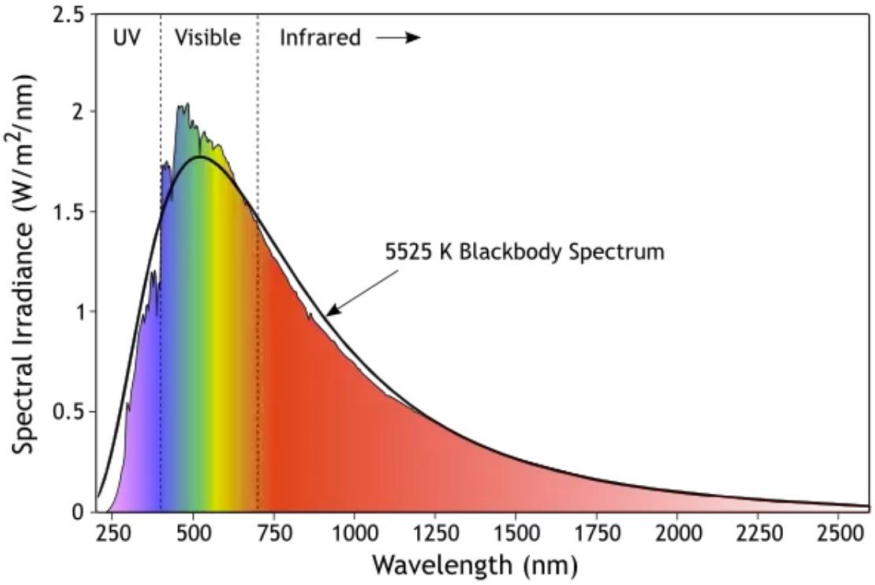

Fig. 36: Spectral distribution of solar energy impacting on Earth surface [97]

As the wavelength decreases, the intensity of the radiation at the respective wavelength decreases and thus the share of usable energy also decreases. Further, radiation with a longer wavelength is more suitable for the absorption of solar radiation. With a small wavelength and thus a higher radiation energy, the absorption coefficient increases and the depth of penetration of the radiation decreases. Consequently, for short wavelengths, therefore, extremely narrow junctions prepared by thin-film technology are required.

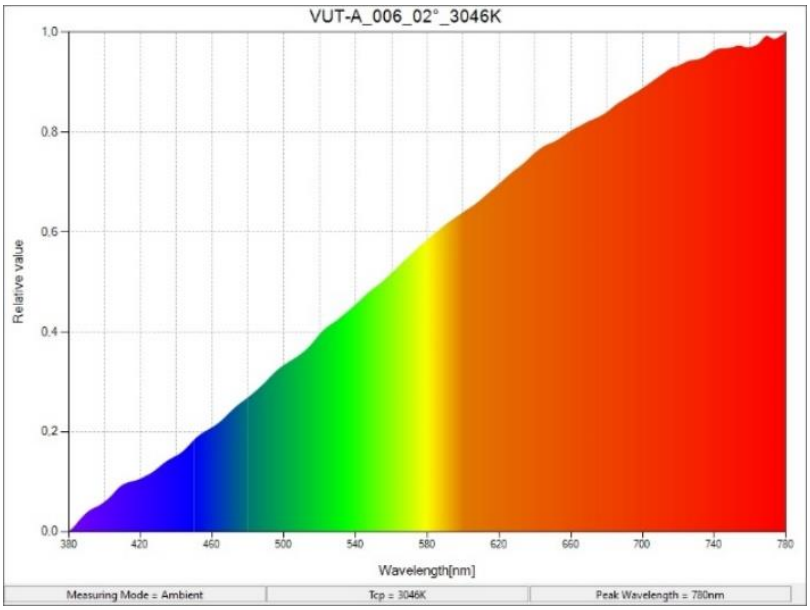

Fig. 37: Spectral distribution of halogen-lamp radiation.

Semiconductor materials used in photovoltaic cells have a band gap width ranging from 1.12 eV/1100 nm (Si) to approximately 1.8 eV/700 nm (amorphous silicon.)

Therefore, sources with xenon lamps are used as standard when testing photovoltaic cells. The spectral characteristic is similar to daylight with pronounced peaks in the red and infrared regions.

In case of silicon photovoltaic cells, it is also possible to use a halogen bulb. The spectral distribution measured for a halogen lamp is shown in figure Fig. 37.

In the region of the visible spectrum, the intensity of radiation from a wavelength of about 650 nm decreases almost linearly with decreasing wavelength, and in the light intensity the region of blue it is already very low. However, this course does not have a significant effect on the simplified testing of silicon photovoltaic cells for the following reason. In case of crystalline silicon at wavelengths below 600 nm the photovoltaic conversion efficiency quickly decreases and a large part of the incident radiation is converted into heat. Therefore, in case of crystalline silicon cells the anti-reflection layer is designed in

such a way that the reflectivity increases significantly for radiation below 600 nm. The standard shape of the spectral characteristic of the anti-reflective layer used for crystalline silicon photovoltaic cells is shown in Fig 38.

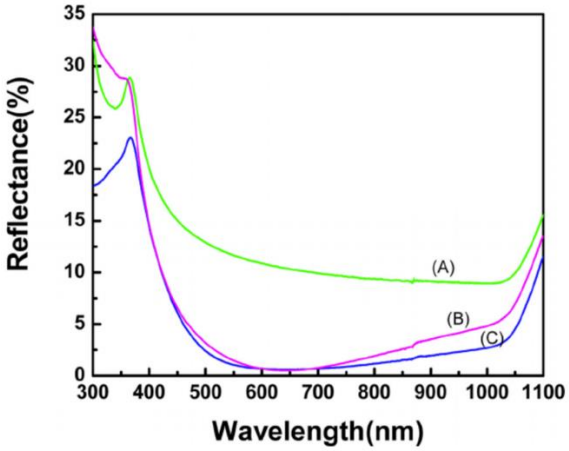

Fig. 38: Crystalline silicon PV cell. Typical shape of spectral distribution of reflectance of antireflexive layer for different technology and thickness of antireflexive layer [168].

For simplicity, when testing with a halogen lamp, it is possible to estimate the degree of irradiation of the samples as follows.

Depending on the type of halogen bulb the radiation intensity is close to 20 lumens per Watt. For 100 W halogen it will be approximately 20 x 100 = 2000 lumens.

It is not possible to change the light intensity in a wider range by the power input, because the spectral characteristics and dependence of radiated energy on power input would change significantly. For the low energy harvesting experiments, it is possible to change the illumination intensity by changing the distance between light source and illuminated area. Estimated light intensity for halogen lamps with input power 80 W and 230 W as a function for source to illuminated-area distance is in table Tab.12. The derivation of lighting intensity is analogous to that in the previous chapter.

Table 12 : Estimated light intensity for halogen lamp : d [m] is Distance between light source and illuminated area ; E_{80} , E_{230} [lx] is Estimated light intensity for 80W and 230W halogen lamps respectively.

d [m]	0.5 *	0,7	1,0	1,4	2,0	3,0
E_{80} [lx]	8000 *	3200	1600	800	400	178
E_{230} [lx]	18400 *	9200	5600	2300	1150	222

The intensity range for lighting experiments was chosen with respect to the European standard for lighting, according to which in areas with permanent residence of persons, the illuminance should not be less than 200 lx. The upper limit of illumination is given

by the heating of the photovoltaic cell at a distance of the halogen lamp and the illuminated sample of less than 1 m.

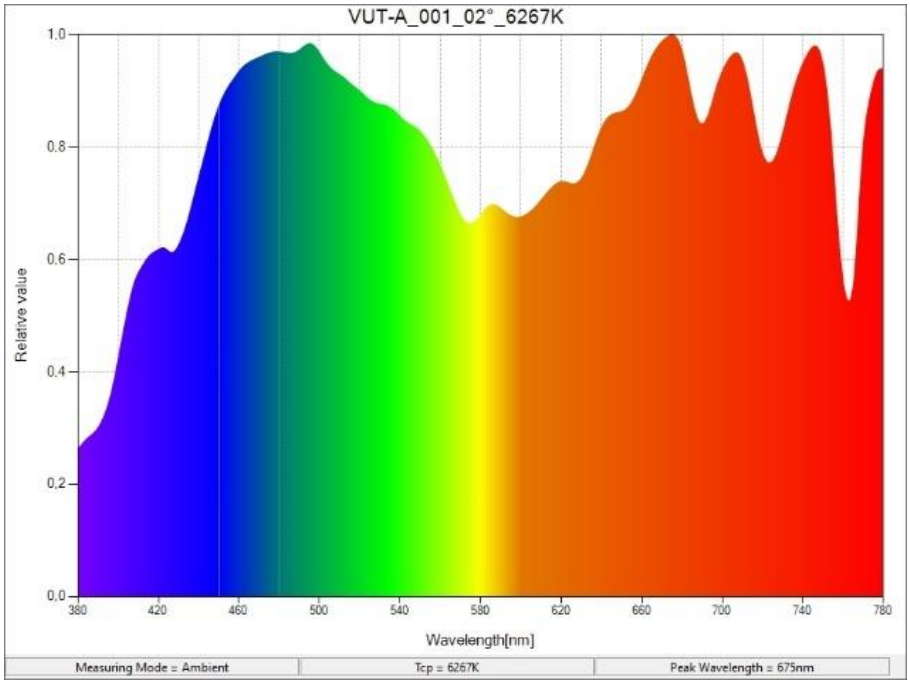

a)

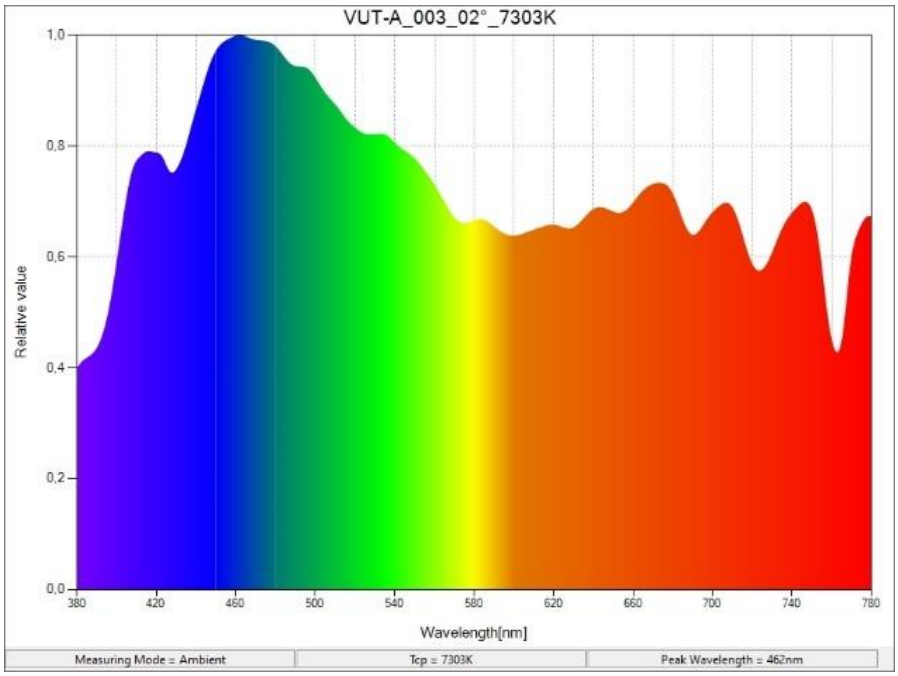

b)

Fig. 39: Spectral distribution of daylight.
a) partly cloudy sky late afternoon **b)** completely cloudy sky in the morning

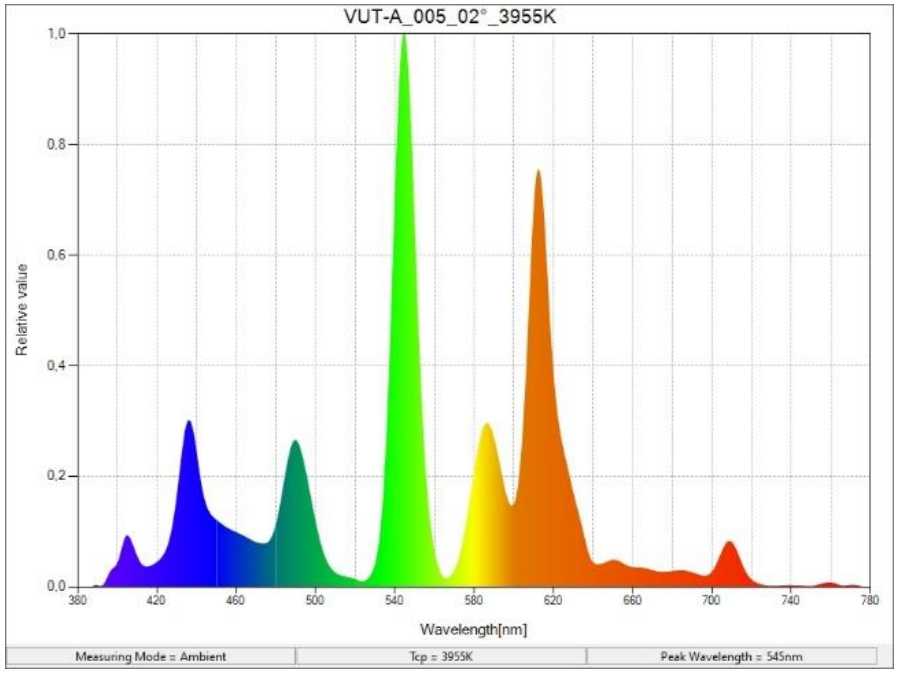

a)

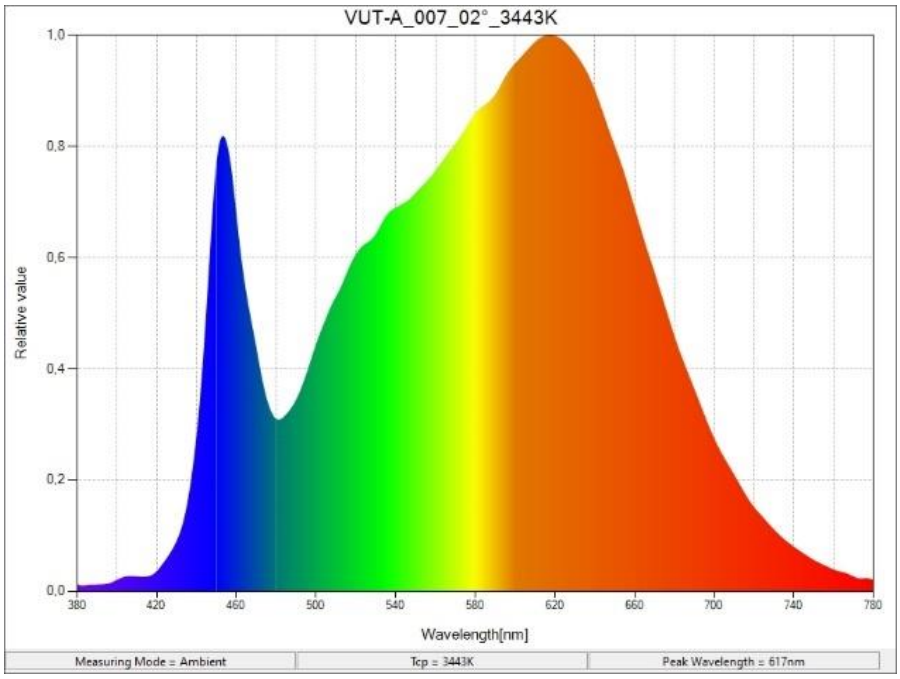

b)

Fig. 40: Spectral distribution of lighting in the room.

a) Fluorescent lamp for standard lighting. **b)** LED luminaire; warm white with a specified temperature of 3500 K

As stated above, the fluctuation of the light intensity during the day could be more than one order of magnitudes. Depending on the time of day and the current weather there is also a noticeable change in the spectrum of radiation entering the earth's surface.

The radiation spectrum for the experiment was measured at Department of Power Electrical and Electronic Engineering using Spectroradiometer KONICA-MINOLTA CS-1000A. The measured spectrum overlaps only with the visible region of the spectrum, but the measurement results still provide enough information to assess the lighting conditions when using photovoltaic cells under different conditions.

The spectral composition of the light under very different conditions including partly cloudy sky late afternoon (a) and completely cloudy sky in the morning (b) is shown in Fig. 39.

Partly cloudy sky late afternoon. In the spectrum in Figure 39 a) a significantly higher intensity of radiation in the red part of the spectrum is evident. The illumination intensity corresponded to 10,000 lx and the derived color temperature to 6267 K.

Completely cloudy sky in the morning. In spectrum presented in Figure 39 (b) there is a significant decrease in the red area and emphasis on the blue part of the spectrum. The illumination intensity was 1500 lx. The shift of the spectrum towards shorter wavelengths also corresponds to the change of color temperature from 6267 K up to 7303 K.

It is clear from the pictures that the spectra differ mainly in the content of the red component of radiation, which decreases when the sky is cloudy and the angle of incidence of the sun's rays is greater. However, the spectrum is still evenly distributed and the derived color temperature is relatively high.

Figure 40 shows the spectral composition of the lighting for standard fluorescent lamps (a) and LED luminaire (b).

Fluorescent lamp for standard lighting. In the spectrum Figure 40 (a) the radiation peaks corresponding to the excitation of the phosphor used here to generate the visible radiation are clearly visible. The peaks at 404 nm, 435 nm and 546 nm correspond to the spectral composition of the mercury lamp radiation. The presence of sharp peaks causes the nature of the emitted radiation to approach a discontinuous spectrum. The maxima are distributed throughout the visible spectrum, but a significant part of the energy is in the region of shorter wavelengths.

LED luminaire; warm white 3500 K. The spectrum Figure 40 (b) shows a distinct peak at 455 nm, which corresponds to the radiation of a blue light-emitting diode, which serves to excite the phosphor used to generate radiation at longer wavelengths to create the perception of white light. The phosphor emits a continuous spectrum with a maximum at a wavelength of 620 nm corresponding to the region of red light. The spectrum is continuous and a significant part of the energy is in the region of longer wavelengths.

Operation of photovoltaic cells at low intensity of incident light

The characteristic behavior of the photovoltaic cell at change of the incident light intensity is clearly visible from the graphs in Figure 41. The current supplied by the photovoltaic cell is approximately linearly proportional to the illumination. The dependence of the voltage generated by the cell on the illumination is approximately logarithmic. Changing the intensity of light radiation will therefore primarily reflect the change in the current of the cell.

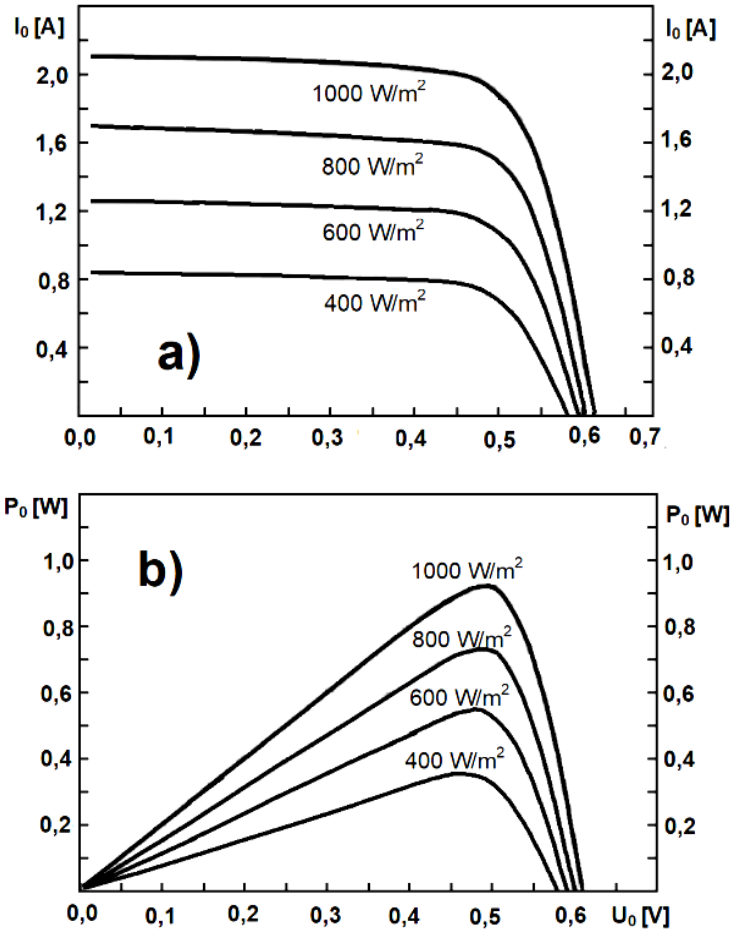

Fig. 41: **a)** A-V characteristics of the silicon photovoltaic cell
b) The power extracted from the cell

For each intensity of the light used there are optimal voltage value and optimal current value for the maximum energy output of the cell. Because of logarithmic dependence the voltage at which maximum power is reached decreases with light intensity very slowly. This means that even at an extremely low intensity of incident radiation the voltage on

the cell will still be a few tenths of a Volt. Thus, the inverter operation will be possible, although the power output will be very small.

The graphs in Figure 41 show that when changing the illumination of the cell 2.5 times the position if maximum cell power changes by approximately 0.3 V from about 0.47 V to 0.5 V. Obviously the maximum of power efficiency will shift logarithmically and the character of dependencies will be preserved. The offset of the peek-power efficiency can be estimated from the Schockley equation and will be approximately 100 mV for each change in radiation intensity by one order.

Operation with multiple EH converters

The circuit design of the DC / DC converters designed in this work allows connection of multiple EH converters to one load. Therefore, there may be a combination of several cells from different positions against a changing lighting source. The inverters are connected in parallel so that even the very little energy that is available can be processed.

Testing of selected photovoltaic cells

The behavior of selected single cells under real operating conditions was tested for an EH converter operating at input energy level deep below 1 W [132]. The low voltage at the cell output was boosted-up using the low voltage DC to DC converter. The result obtained should be assessed not only with respect to the level of illumination but also with respect to the spectral characteristics of the light radiation and the wavelength from which a photovoltaic cell can absorb incident photons.

For each measured sample, the current and voltage under load of the DC / DC converter and the output voltage of the converter were recorded under the given illumination. The inverter output was loaded with a 100 kΩ resistor.

The illumination level was changed by the distance when moving the entire set of measured cells in the room or switching on the light sources. The spectral characteristics of the light were estimated using the measured spectral characteristics given in the figures Fig. 40 to Fig. 44. Despite the fact that it is only indicative the measurement fits well with the possibility of using photovoltaic cells for the processing of light radiation from low-energy sources. At the same time the trouble-free operation of the designed inverters was verified.

For practical reasons, this experiment was performed only with crystalline silicon cells. Other cells proved to be unsuitable due to insufficient mechanical stability of the contacts. Commercial CGIS cells were also not included. The results are presented in table Tab. 13 for the converter based on Armstrong oscillator and in table Tab. 14. for the converter based on single J-FET DC/DC converter.

Samples:

Crystalline silicon cells. Screen printed BUS-bars. Area and dimension as follow.

PH_1, PH_3: A = 15 cm^2 (50 mm x 30 mm)

PH_2: A = 25 cm^2 (50 mm x 50 mm)

PH_4a, PH_4b: A = 25 cm^2 (50 mm x 50 mm)

PH_5a, PH_5b: A = 15 cm^2 (50 mm x 30 mm)

Tab 13: Photovoltaic EH transducers. Measured values of input and output parameters using Armstrong generator: V_{EP} *[V]* Voltage supplied by a photovoltaic cell; I_{EP} *[μA]* Current supplied by a photovoltaic cell; V_{GT2} *[V]* Negative voltage amplitude at the transistor gate; V_{OUT} *[V]* Mean value of output voltage at 100 kΩ resistance load. T= 300 K; Estimated light intensity E_{PH} ~ 0.01 AM.

Sample	PH_1	PH 2	PH_3	PH _4_a	PH _4_b	PH _5_a	PH _5_b
V_{EP} *[V]*	0.31	0.33	0.30	0.31	0.32		0.33
I_{EP} *[mA]*	1.24	2.01	1,15	2.00	1.90		1.17
V_{OUT} *[V]*	3.5	4.6	3.3	4.4	4.5		3.4

Tab 14: Photovoltaic EH transducers. Measured values of input and output parameters using single J-FET DC/DC converter; V_{EP} *[V]* Voltage supplied by a photovoltaic cell; I_{EP} *[μA]* Current supplied by a photovoltaic cell; V_{GT2} *[V]* Negative voltage amplitude at the transistor gate; V_{OUT} *[V]* Mean value of output voltage at 100 kΩ resistance load. T=300 K; Estimated light intensity E_{PH} ~ 0,01 AM.

Sample	PH_1	PH 2	PH_3	PH _4_a	PH _4_b	PH _5_a	PH _5_b
V_{EP} *[V]*		0.32	0.29		0.31	0.29	
I_{EP} *[mA]*		2.1	1,24		2.1	1.3	
V_{OUT} *[V]*		4.9	3.6		4.8	3.6	

Starting voltage of Armstrong oscillator and J-FET DC/DC converter were 50 mV and 80 mV respectively. The efficiency of the inverter with Armstrong oscillator is in this connection less than 33%. For the J-FET DC/DC converter the efficiency is around 36 %. This inverter also puts more strain on the photovoltaic cells, so there is slightly lower voltage and slightly more current under the same lighting. (See Appendix A9.)

3.2.3 Photovoltaics based on organic solar cells

Comparison of the properties of respective technologies shows that for low-light operation there are most advantageous inorganic thin film cells. However, organic photovoltaic cells have been attracting researchers because they offer the prospect of very cheap mass production.

The materials used are available, mostly non-toxic and environmentally friendly. The properties of organic semiconductors can be modified so that they can be optimized for their intended use.

As stated in Chapter 1 organic cells also have a disadvantage as follows:

a) Solar radiation can activate degradation processes.

b) Layers of organic materials may be sensitive to moisture and may degrade by the action of some gases or even air oxygen. It is therefore necessary to solve the perfect encapsulation. However, this makes production more expensive and one of the advantages of organic cells is lost.

c) The temperature resistance in both high and low temperatures can be a major problem. Temperature cycles can also have a great influence on the service life.

However, when the OSC are used indoors the disadvantages mentioned above apply only marginally or not at all. By suitably selected materials, the spectral characteristics of the cells can be shifted to a shorter wavelength range, i.e. adapted to the nature of the indoor lighting.

The moisture, thermal gradients, extremely high or extremely low temperature or high level of radiation does not happen indoors. Nevertheless, the problems associated with low efficiency, low shunt resistance and high serial resistance remain.

Testing of selected organic photovoltaic cells

Since organic cells are not mass produced, they are not readily available on the market. Therefore, organic photovoltaic cells were not included in the experiment described at the beginning of this chapter. Consequently, two organic cells based on Diketopyrrolopyrrole (DPP) were measured in cooperation with the BUT Faculty of Chemistry in frame of the testing of DC to Dc converters.

Sufficient level of efficiency was achieved only with samples activated by thermal annealing. In this case, the efficiency was greater than 3.5%. The measurement results were similar to the results obtained for inorganic cells from the original set. However, due to the significantly lower efficiency the cells provide less current.

Economy of organic photovoltaics in large equipment

From the above results, it is evident that organic photovoltaic cells may be suitable for small systems designed to meet special requirements. In this case, however, organic photovoltaic cells have a lot of competition in other types of cells, because in such devices the price of the photovoltaic-cell-system itself is usually not essential.

Also, in case of large installations, where the price is also determined by the interconnection costs and the costs of operation and maintenance, the low price of organic photovoltaic cells is reflected only indirectly. In any case, the plastics supports used in organic solar cells fabrications facilitate low production costs in high volumes.

Combined with the flexibility of organic molecules, organic photovoltaic cells they can be considered potentially cost-effective for photovoltaic applications [91]. However, while module costs are proportional to the installed power, the installation costs grow with the installed area. Consequently, PV modules with low efficiency will need large area with higher installation costs and may not be able to compete with equipment based on standard cells.

In an optimal case installation costs are about 30 - 40% of the overall costs but in case of low conversion efficiency they could be much higher. Consequently, it can be estimated that for organic photovoltaic cells a minimum efficiency of 8% is considered as necessary to compete with 15% efficient inorganic PV modules.

Considering the maintenance of organic power plant the problem turns to be more complex. If the reduction in efficiency of installed organic photovoltaic cells continues there can happen that the funds received for produced electricity does not even cover maintenance costs.

To avoid such a negative case there is a possibility to replace original photovoltaic cells at an appropriate time. It is assumed that over several years the price of organic solar cells (OSC) falls, the conversion efficiency will be larger and degradation slower. Investment in this power plant which is largely shaped by the cost of installation would be this way preserved.

The return on investment in organic photovoltaics can be shown by the example of a photovoltaic power plant based on organic cells as follows. For basic assessment we consider the average price of organic solar cells (OSC), the average price of electricity for the end customer, the average increase of price of electricity per year, the average efficiency of OSC expressed in percentage use of impacting radiation power.

To model a real situation, we must also consider step by step decrease of the efficiency of original OSC and regular maintenance costs (per year in percentage of the total investment). We also need to reckon with the repair of serious failures which may happen approximately in period of three years.

Replacing the old solar cells with new ones after few years we may probably profit from the probable increase in efficiency and reliability and at the same time there will be probably noticeable drop in purchase price.

Basic considerations of income and payments are as follows:

The income that could be taken from the 1 m^2 is computed using the solar radiation per year per one m^2 (***RAY = 1MWh / year. m^2***).

When considering the efficiency of respective organic photovoltaic cells F = 8%, the energy which could be taken in period of one year for each squared meter of solar power plant is ***RE = 80KWh***.

The annual income (AI) for this case is consequently expressed using the price of electricity (E) as:

AI = RE · E = 80 KWh/year . m^2 . 4,75 CZK/KWh = 380,- CZK/year . m^2

Price of the maintenance per year / 2% of total cost; for actual value/ :

MTN = TI · 2% = TI · 2/100 = 4400 · 2/100 = 88,- CZK

Price of the maintenance for serious failure each third year / 2% of total cost / :

FLR = TI · 2% = TI · 2/100 = 4400 · 2/100 = 88,- CZK

The annual income is computed considering the year income and maintenance cost for respective year (each third year with serious failure).

Total income is computed as a sum of individual incomes in each year of the solar power production. Note that the total income is influenced by gradual drop of the efficiency, by maintenance costs and by purchase of new solar cells after few years of production.

As a result of modeling there is possible to define two important limits:

1) If the efficiency of installed cells is less than 8 % and the drop in efficiency is 5 % per year the investment will never pay back.

2) The efficiency of initially installed cells must be at least 10% to and the drop in efficiency should not exceed 5 % per year to return of the investments in 20 years.

Example of model assessment for this case is depicted in Fig.42 and in Fig.43. The concept of replacement of "worn-out" organic solar cells seems to be convenient. Here the cell efficiency is 10% and annual drop in efficiency is 5%.

Cost of investment per 1 m^2 is 4000 CZK. After 11 years the original cells were replaced by cells with the same efficiency.

The detailed analysis shows that considering the current costs of installation and current price of electricity the efficiency of initially installed cell must be at least 10% to ensure that these investments will return in less than 20 years.

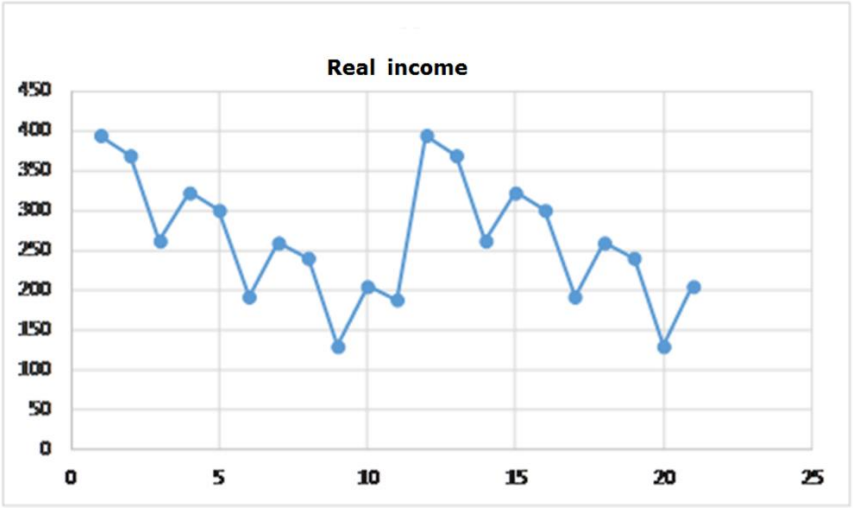

Fig. 42: Model solar-power-plant with organic cells. Annual income for the electricity produced by the solar-power-plant in CZK/m^2 for individual years of operation. Maintenance costs and emergency repairs considered.

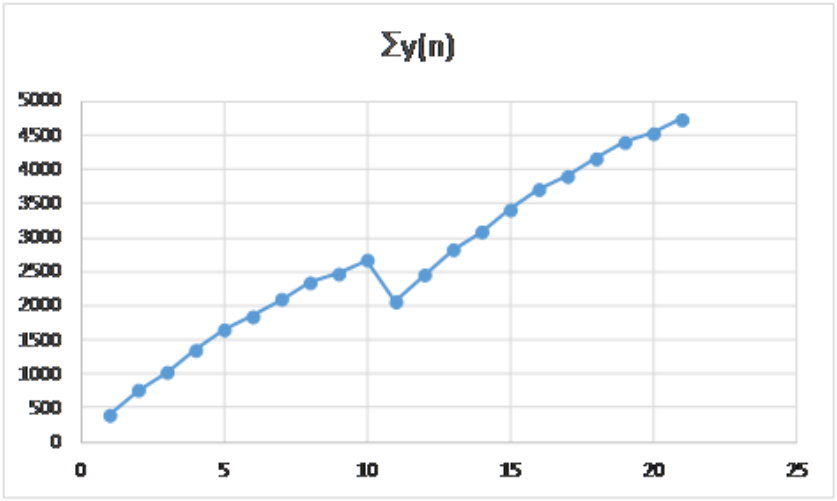

Fig. 43: Model solar-power-plant with organic cells. Total income for the electricity produced by the solar-power-plant in CZK/m^2 for individual years of operation.
Note that return on investment is about 18 years. Note the decrease just after 10th year due to the purchase of new cells

Clearly, long-term stability and reliability is a fundamental problem for organic photovoltaic cells. Although much progress has been made recently in understanding the technological processes of organic solar cells and the efficiency of photovoltaic conversion in laboratory conditions is approaching 18% [6, 11], mass use of organic photovoltaic cells is still unlikely in the foreseeable future.

A detailed description of the whole model is in [19].

3.2.4 Summary of chapter 3.2 Photovoltaic structures

Photovoltaic cells with different technologies donated or borrowed from various institutions were used in the experiments. In addition to standard measurements, the series resistance and leakage resistance were also measured using a new dynamic method which was proposed in frame of this work. A great advantage of this method is the possibility of measurement of parasitic resistances of the cell in the dark without the use of special instruments. The measured values do not depend on the lighting conditions and well describe the physical properties of photovoltaic cells. The following conclusions were drawn from mutual comparison of the cells in the experiments presented in this chapter. They are in accordance with the knowledge gained in the study of literature according the objective No 1 defined in Chapter 2.

a) Despite the abundant literature, the application potential of organic photovoltaic cells was overestimated at the time of the assignment. However, the technology of organic photovoltaic cells developed during the elaboration of the presented work. The most significant change is the abandonment of fullerene-based absorbers in favor of new materials. When using these materials, the photovoltaic conversion efficiencies achieved in laboratories usually already exceed 10%, but the problems with stability and sensitivity to external influences remain. However, the organic cells available in this work were only around 5% effective. Tests of application possibilities of organic cells were therefore only indicative, although from the point of view of spectral sensitivity these cells very well meet the requirements for use in indoor spaces, where many of their problems associated with short life would not manifest themselves.

b) In addition to technological improvements, the price per Wp of crystalline silicon cells decreased significantly. In experiments, it has been designed and verified that due to current prices and technological possibilities, the single cell variant is very advantageous for low-energy photovoltaic EH converters, where cells with an area from 30 cm^2 to 40 cm^2 are mass-produced on standard-sized silicon wafers and divided into individual functional cells at the end of the production cycle. The cells are highly efficient and very robust. Given their current price of 0.2 Euro per Wp, it is also an economic option.

c) It has also been verified that DC to DC converters designed in this work are able to operate with very low input power delivered from photovoltaic cells in low light operation and that they are able to operate in parallel in one load. This significantly expands the possibilities of capturing energy from various unstable sources with possible outages. Based on the testing of individual types of photovoltaic cells, for these experiments silicon crystal cells were selected.

3.3 Organic thermoelectric generator

Organic thermoelectric materials are based on conductive polymers, including conjugated polymers and certain coordination polymers. In case of highly conducting polymers the thermoelectric properties are strongly affected by their synthesis and deposition and also by post-processing conditions. Materials prepared by solution-process are optimized through doping and blending.

Organic materials are mostly good insulators but there are several types of organic compounds whose electrical conductivity is large enough for use in electronic devices. Their conductivity could be changed in wide range when changing the structure of polymer chains. The main requirements for the properties of materials for use in thermocouples for thermoelectric generators are summarized in Chapter 1.4. The organic material that best meets the requirements for use in thermoelectric generators is poly (3, 4-ethylenedioxythiophene) standardly referred to as PEDOT. Based on the comparison in the introductory part of the work, we use this material in our research.

3.3.1 PEDOT:PSS

PEDOT /poly (3, 4-ethylenedioxythiophene)/ was developed in 1980s at Bayer AG research laboratories in Germany. Its backbone is shown on the figure Fig. 44.

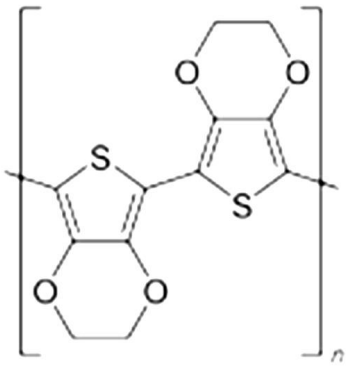

Fig. 44: PEDOT a) basic molecular structure [164].

PEDOT has high electric conductivity, good stability on oxidized state and transparency. However, it has a large disadvantage which is poor solubility. PEDOT low solubility problem was solved with further research by mixing it with water-soluble polystyrene sulfonate (PPS). The resulting combination referred to as PEDOT:PSS is water-soluble system with good film forming properties including high electric conductivity, high visible light transmissivity, and excellent stability.

The disadvantage of this process is the high acidity of the resulting compound. This is caused by hydrogen ions that are easily released from the PSS. The structure of the PSS is shown in Fig. 45 for clarity

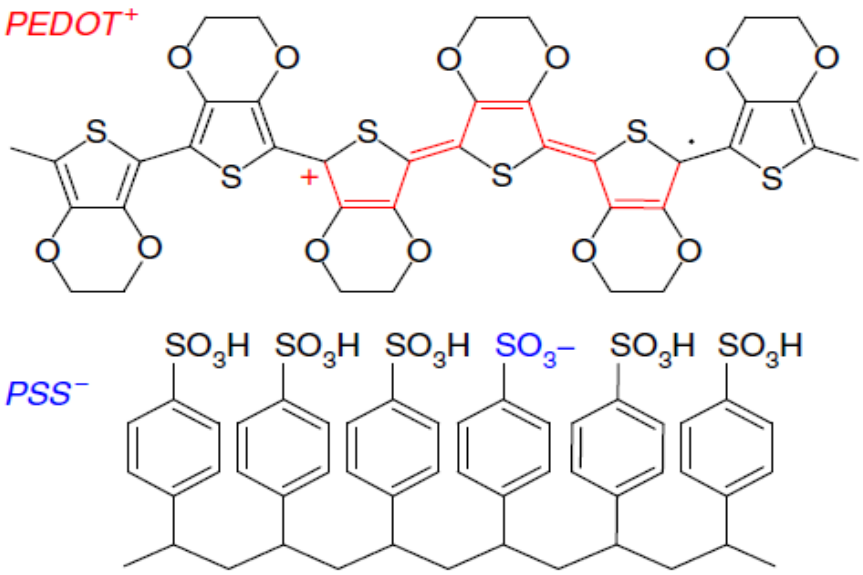

Fig. 45: PSS causes the acidity of the PEDOT:PSS compound [164].

Thanks to combination of good conductive properties and transparency, the PEDOT:PSS compound is widely used in different type of organic electronic devices. Due to its high electrical conductivity and low thermal conductivity, PEDOT: PSS has suitable properties for use in organic thermocouples. Moreover, films of PEDOT:PSS can be heated in air at 100^0C for over 1000 hours with only a minimal change in conductivity. For application in TEGS, PEDOT:PSS has very advantageous properties and its use for this purpose has already been described in the literature [164].

3.3.2 Lateral structure of organic thermo-generator

The arrangement of our organic thermocouple cell uses similar structures as the inorganic thermocouple cell described in the Chapter 1.4.5.

The philosophy of the proposed organic cell is based on a standard Ni-NiCr cell. Here, Ni has a negative Seebeck coefficient and NiCr has a positive Seebeck coefficient. Therefore, the organic compound PEDOT:PSS was chosen, which also has a positive Seebeck coefficient and can be used instead of NiCr. Because there is a relatively small

selection in materials having a negative Seebeck coefficient, the original Ni material with a negative Seebeck coefficient was left in the structures of the proposed thermocouples.

Depending on the composition and deposition process, PEDOT:PSS has a Seebeck coefficient from +15 μV/K to more than +35 μV/K. [164]

At ambient temperature pure nickel has a Seebeck coefficient of -19 μV/K. As the temperature increases, it grows to -25 μV/K at a temperature of around 200 ^{o}C [167]. When nickel and PEDOT are combined, the temperature sensitivity of resulting thermocouple will reach 30 μV/K to 35 μV/K at ambient temperature.

In this structure, a significant disadvantage of PEDOT:PSS is its very strong acidity, which can reach up to pH < 2. In most applications, it is also necessary to consider its hygroscopicity. Therefore, when it is combined with nickel, corrosion processes can occur. Consequently, the cells lose their functionality in a relatively short time.

Possible solution is chemical neutralization of PEDOT:PSS compound by NaOH:

$$PSS^{-}H^{+} + Na^{+}OH^{-} = H_2O + Na^{+}PSS^{-}$$

This can yield the change of pH in large range. However, in this process the electric conductivity sharply drops and Seebeck coefficient (moderately) grows. If a compromise is found, the pH values can rise up to the level of pH = 4 up to pH = 6.

Under normal circumstances, pure nickel is stable against corrosion in alkaline environment, typically by pH > 7. In acid environment the corrosion depends on chemistry of possible surface reaction. Corrosion usually accelerates in the presence of oxygen.

In case of serial connection, it is necessary that the total resistance of all thermocouples connected in series, including the contacts between individual cells, does not significantly exceed 10 Ω. This can be a problem for thin PEDOT:PSS layers. Although PEDOT:PSS is used as an extremely conductive organic material, its conductivity is still low compared to metals.

The smallest number of technological steps requires the combined structure with lateral arrangement of short thermo-coupler legs described at the beginning of chapter 3.6. and shown in Fig. 46.

The functional layers of the individual thermocouples are applied on both sides of the carrier tape in the form of strips. The materials of the two layers overlap at the interface of the strips.

The temperature gradient is ensured by means of thermally conductive extensions, which alternately heat and cool the areas where the functional layers come into contact.

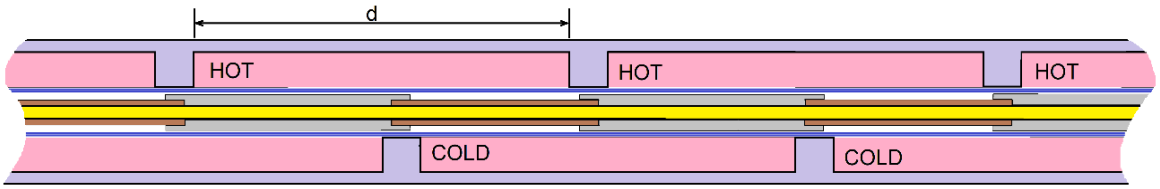

a)

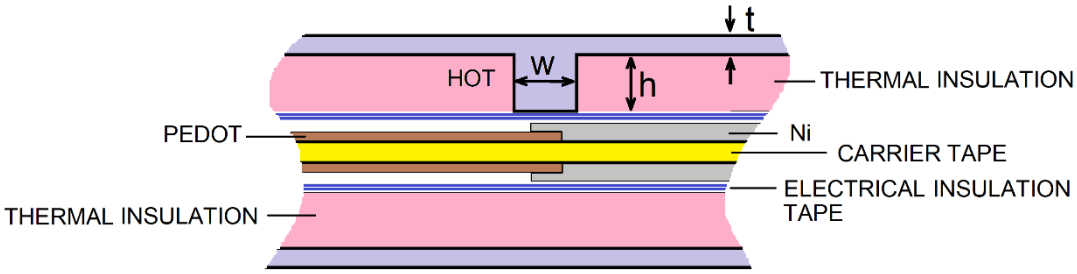

b)

Fig. 46: a) Designed structure with lateral arrangement of short thermo-coupler legs.
b) Functional layers near the thermal extension.
DIMENSIONS: Width of thermal extensions **w** = 2 mm; Height of thermal extensions **h** = 2 mm; Thickness of thermally conductive profile **t** = 1.4 mm; Distance of thermal extensions **d** = 14 mm

The structure of the thermocouples is electrically insulated from the thermal extensions on both sides by a dielectric tape. Both the support tape and the insulation tape are thin, so they do not significantly impair heat transfer.

The space between the temperature extensions is filled with thermal insulation material. In addition to the thermal insulation function, this filling ensures a defined position of the thermocouple support tape against the thermal extensions.

The distance of the thermally conductive adapters should be optimized in terms of the thermal conductivity of the whole arrangement between the cold and hot ends and also of the accuracy of placement of the thermocouples and their alignment with respect to the thermal adapters.

Having the pitch of extensions 14 mm, the distance between hot and cold ends is 7 mm. With a length of the entire profile of 140 mm, it is thus possible to place 20 thermoelectric junctions on one thermoelectric-tape.

Because the hot and cold ends of thermocouples alternate, there are two junctions for one thermocouple. Consequently, we can calculate the generated voltage using following formula:

$10 \cdot (T_1 \cdot S_{12} - T_2 \cdot S_{12}) = 10 \cdot (T_1 - T_2) \cdot S_{12}$,

where S_{12} [µV/K] is temperature sensitivity of individual thermocouple.

Suppose temperature sensitivity S_{12} = 30 µV/K and temperature difference T_1-T_2 = 40K. Then the voltage between the ends of the thermoelectric-tape with 20 thermoelectric junctions will be as follows:

$V_{TP} = 10 \cdot (T_1\text{-}T_2) \cdot S_{12} = 10 \cdot 40\ K \cdot 30\ \mu V/K = 10 \cdot 1200\ \mu V = 12\ mV$

With the voltage of one thermoelectric-tape according to previous equation it is possible to achieve a voltage of $V_{TP6} = 6 \cdot 12$ mV = 72 mV with a series connection of six thermoelectric tapes. This is the voltage that is already sufficient for the operation of DC to DC converters described in chapter 3.1.

Series resistance of lateral arrangement

The arrangement of the individual thermoelectric tapes is shown on the figure Fig. 47. When connected in series, the total series resistance of the entire generator increases. To achieve required conductivity the width of the carrier tape must be chosen in respect to a sufficient cross-section of the individual functional layers. Considering the thermoelectric-tape preparation process and mechanical handling, the width of the thermoelectric-tape of 20 mm seems to be optimal.

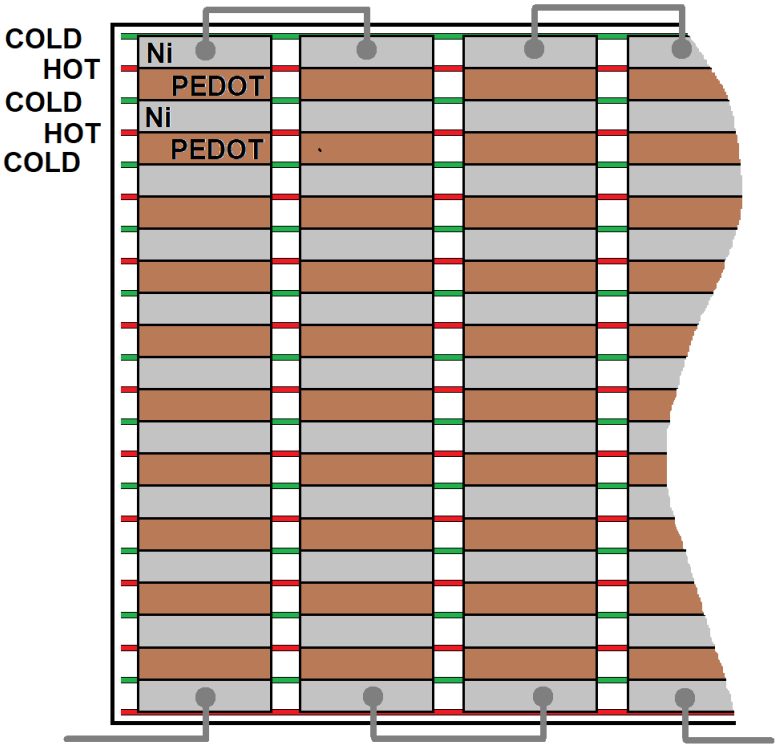

Fig. 47: Design of series connection of individual thermoelectric strips in structure with lateral arrangement. ***DIMENSIONS:*** HOT to COLD distance d = 7 mm; Thermoelectric tape width w_{TET} = 20 mm; Other dimensions see Fig. 46.

The total series resistance of thermoelectric tapes can be estimated in a very simple way as follows.

a) The series resistance of the cell will be determined by the conductivity of the PEDOT:PSS layer. The conductivity of the metallic functional layer is more than an order of magnitude larger and does not affect the total series resistance of the thermoelectric structure.

b) During curing, the PEDOT:PSS functional layer dries to a fraction of the thickness just after application. The optimal layer thickness is approximately 100 nm. Trying to achieve greater thickness, the properties of the layer deteriorate, however the resulting thickness of the layer around 1000 nm is still possible.

c) PEDOT:PSS layers with extremely high specific conductivity, which can be in the order of 1000 S/cm have pH around 2 and can cause accelerated corrosion of metallic functional layers. It is therefore necessary to reduce the acidity with other additives. This always reduces the electrical conductivity. When a compromise is reached, the resulting values are for conductivity ϱ_{PD} = 800 S/cm and for the thickness of functional PEDOT:PSS layer d = 800 nm.

d) For simplicity, we consider that the sum of the lengths of the individual PEDOT:PSS layers will be 50% of the length of the thermoelectric tape. With a thermoelectric tape length of 140 mm, the length of the PEDOT:PSS functional layer will be 70 mm. With a thermoelectric structure on both sides of the tape, the series resistance of the entire thermoelectric-tape can be estimated as follows:

$R_S = R_{SPD} / 2 = [(\varrho_{PD} \cdot l) / (d \cdot w)] / 2$, where

R_S [Ω] is series resistance of thermoelectric-tape

R_{SPD} [Ω] is series resistance of single PEDOT:PSS layer

ϱ_{PD} (= $1.25 \cdot 10^{-3}$ Ω.cm) is resistivity of PEDOT:PSS layer ; $\varrho_{PD} = 1/ \sigma_{PD}$ [$S.cm^{-1}$];

l (= 7 cm) is the length of the PEDOT:PSS functional layer,

d (= 800 nm) is the thickness of the PEDOT:PSS functional layer,

w (= 2 cm) is the width of the PEDOT:PSS functional layer.

For the values of the variables defined above :

$R_S = R_{SPD} / 2 = [(\varrho_{PD} \cdot l) / (d \cdot w)]/2 = (1.25 \cdot 10^{-3}\ \Omega\ cm \cdot 7\ cm) / (800 \cdot 10^{-7} cm \cdot 2\ cm)/2 = (8.75 \cdot 10^{-3} / 1.6 \cdot 10^{-4}) / 2 = (5.47 \cdot 10^{1})/2 = 27.3\ \Omega$

With six thermal tapes in series, the total series resistance is: $R_{ST} = 6 \cdot 27{,}3 = 163{,}8\ \Omega$.

Short-circuit current of the entire TEG (at open circuit voltage V_{TP} = 72 mV and a series resistance R_{ST} = 163.8) is:

$I_{SH} = 72 \cdot 10^{-3} / 163.8 = 0.440$ mA

With a minimum operating voltage of the DC/DC converter of V_{LL}=50 mV, there would be a ***voltage drop on series resistance R_{ST}:***

V_{TP} - V_{LL} = 72 mV - 50 mV = 22 mV.

Then we can calculate:

The current supplied into the DC/DC converter:

I_{LL} = (V_{TPV} - V_{LL}) / R_{SVT} = 22 mV / 163.8 Ω = 0.134 mA

The power delivered to the DC/DC converter input:

$P_{OUT} = V_{LL} \cdot I_{LL} = 0.134 \cdot 10^{-3}$ A $\cdot$ $50 \cdot 10^{-3}$ V = 6.7 μW

At voltage 50 mV the DC / DC converter will be close the lower limit (V_{LL}=50 mV) its operating range and the supplied power (current) will be consumed almost entirely for the operation of the generator, because it is necessary to cover the conductivity losses in generator and commutation losses caused by charging and discharging the parasitic capacitances of the transistor switch. Consequently, the power delivered on the output of the DC/DC converter will be very low.

Reducing the series resistance is possible by increasing the width of the thermoelectric tape. However, to reduce the total series resistance of the generator to acceptable value, it would be necessary to increase the width of the thermal tapes considerably and the total area of the resulting thermo-electric-generator needs to be disproportionately large. This thermo-generator with lateral structure [25] was therefore abandoned in favor of a structure with a vertical arrangement of functional layers. The structure with vertical design is described in the following chapter.

3.3.3 Vertical design of thermo-generator

A structure that meets the requirement of low series resistance better than the lateral structure described in previous chapter is shown in figure Fig. 48. The individual thermo-cells are connected in series. The large width of the PEDOT:PSS layer ensures its large cross-section and thus low resistance. At the same time the large width of the PEDOT:PSS layer also allows the capture of a large heat flux across the body of the thermoelectric transducer.

The nickel layer is formed by galvanic electroless deposition. Nickel deposited by electrodeless deposition has tendency to form Ni:P clusters. This facilitates the formation of an amorphous structure that is more resistant to corrosion. This property depends on the total Phosphor content and the deposition conditions and on thermal post-treatment. For the proposed TEGS technology of the electroless deposition and the possibility of increasing the corrosion resistance by Ni:P this option is very convenient.

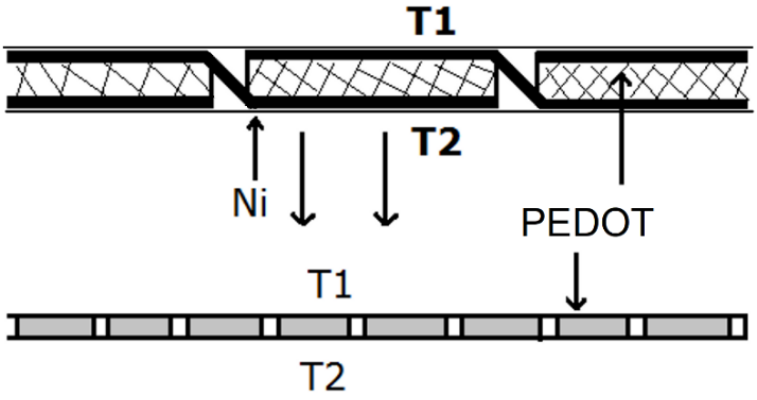

Fig. 48: Proposed vertical structure of PEDOT:PSS - Ni based organic thermo-generator.

To reliably deposit nickel on the plastic surface by electroless deposition the plastic surface must be activated. The best method for this purpose is plasma activation at atmospheric pressure using a dielectric barrier discharge (DBD). DBD plasma surface activation has very long durability and, further, greatly improves the surface adhesion. This technology is available at the Faculty of Chemistry, Brno University of Technology.

The electrical conductivity of electroless deposited nickel is lower than that of metal nickel. The reason is that there are phosphorus atoms in the structure left from electrolyte.

Thermal conductivity of electrode-less deposited nickel also drops considerably. For thermo-generator the drop of thermal conductivity is convenient because low value of thermal conductivity prevents the heat flow through the generator.

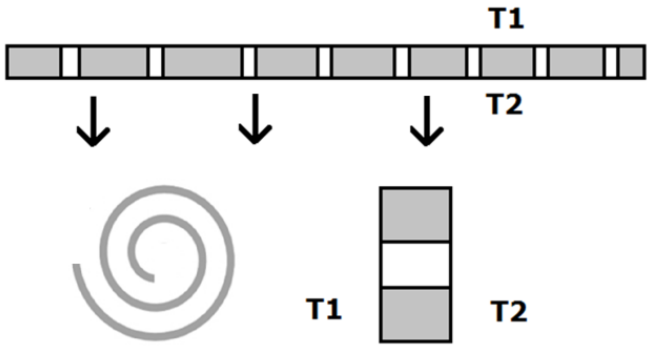

Fig. 49: The spatial arrangement of the thermocouple support strip.

With sufficient tape length, any number of thermocouples can be connected in series. In practice, the number of series-connected thermocouples is limited by the series resistance of the entire combination since at the series resistance a voltage drop occurs with the current being drawn by the DC/DC converter.

The spatial arrangement of the thermocouple support strip is shown in figure Fig. 49. The tape is wound into a spiral that also forms the mechanical support of the thermocouples. The temperature gradient has the same direction as the coil axis.

The electrical conductivity of the whole combination is influenced by the resistance of all contacts connected in series, because this resistance is added to the series resistance of the cell. If the contact resistance is high, the cell does not work optimally. Contact resistance is influenced by many parameters of the technological process - the surface tension and wettability of both bonded surfaces, the chemical nature of both surfaces, the structure of both surfaces, the total contact surface and the tightness of the bonding of the two layers mutually. The processes of contact formation are further influenced by the temperature and temperature profiles as a function of time, both during contact formation and in the event of subsequent annealing.

In the original concept of the cell, there is first the deposition of the nickel on a plasma activated substrate surface. The PEDOT:PSS layer was deposited on the nickel electrodes on the substrate.

The reverse method, i.e. deposition of the PEDOT:PSS layer in the first step and deposition of the nickel layers on the already deposited PEDOT:PSS layer, seems more advantageous in terms of minimizing the resistance of PEDOT:PSS layer. One more PEDOT:PSS layer may be applied to the structure thus prepared. In terms of the series connection of the cells, two PEDOT:PSS layers are connected in parallel and the whole arrangement has greater conductivity. In the second PEDOT:PSS layer, the contact resistance is not critical since it is conductively connected to the PEDOT:PSS layer applied in the first technological step.

However, the nickel electroless deposition works better on a plasma-activated surface. Further, PEDOT:PSS layer must be stabilized so that it does not decompose during electrode-free nickel deposition.

Representation of individual steps in preparation technology of thermoelectric tape is shown in figure Fig. 50.

a) The nickel functional layer is applied to the carrier tape by electrodeless deposition technology and has a continuous surface.

b) The division into sub-systems of individual thermocouples requires the interruption of the nickel layer. This is done by punching holes on both sides of the tape.

c) The joints between the hot-nickel and cold-nickel parts of the structure are applied after electrodeless deposition of the nickel layer. Couplings can be deposited with standard nickel paste, as this part of the nickel layer is not in contact with the PEDOT:PSS layer.

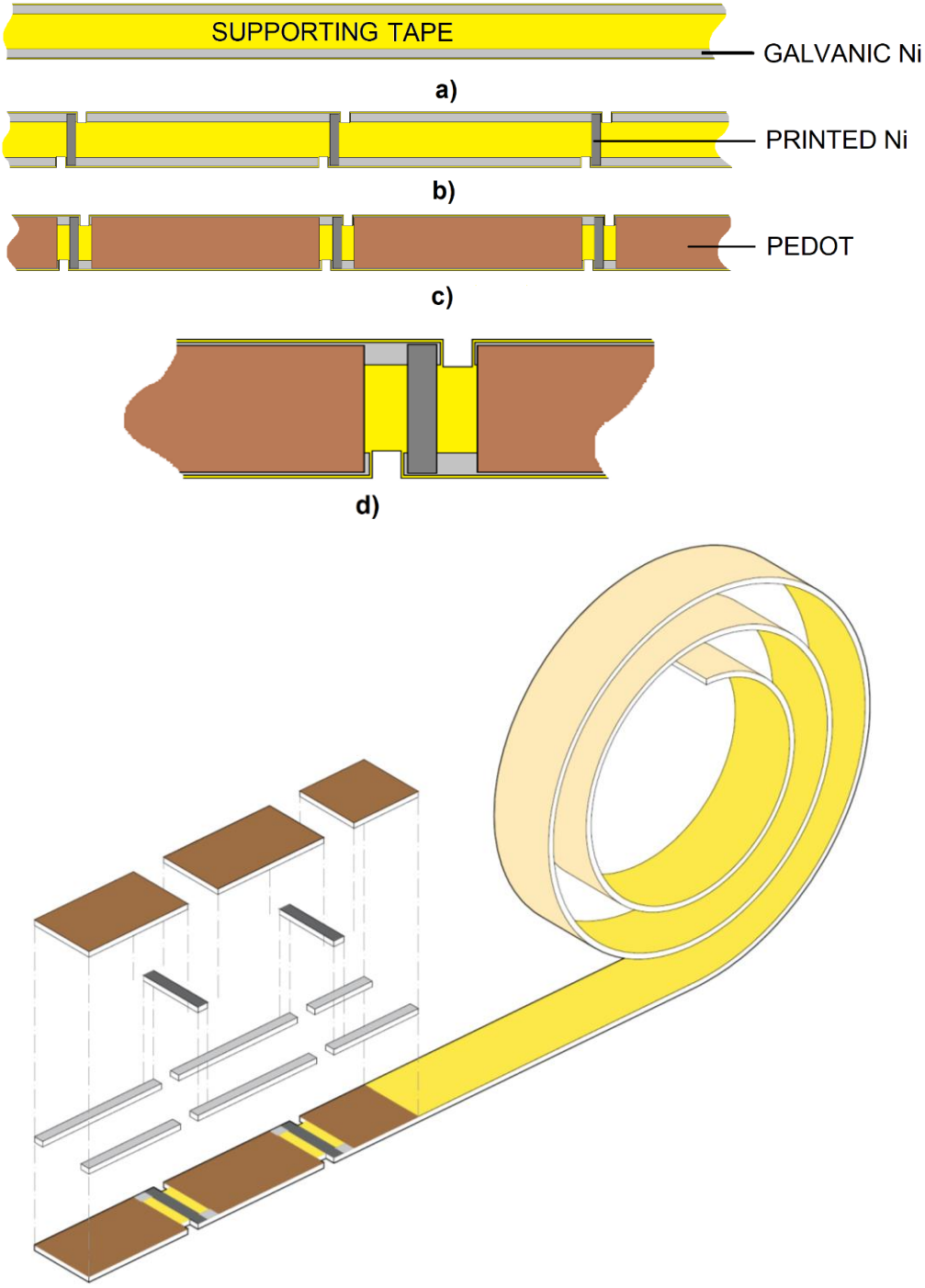

Fig. 50: Vertical structure of PEDOT:PSS -Ni thermo-generator: **a)** Functional Ni layer. **b)** Splitting of Ni layer to individual into sub-systems and their serial connection with printed Ni Layer. **c)** Functional layer of PEDOT:PSS d) Detail of the layout on the joint. ***DIMENSIONS:*** Width of the tape w = 5 mm; Length in which the PEDOT: PSS layer is applied l = 200 mm; Width of Ni-strips w_{Ni} = 1 mm (For the sake of clarity, the sketch is not proportional.)

We designed and tested the following procedure:
The PEDOT layer is applied to the nickel functional layer in the entire required width by screen printing using a very simple rectangular mask.
The top layer is applied first.
The bottom layer can be applied only after the top layer of PEDOT:PSS is completely cured.
The bottom layer is applied in the same way with the tape inverted.
When using a parallel layer arrangement, in addition to reducing the series resistance, the reliability of the resulting structure is also significantly increased

In order to prevent the conductive layers on both sides from short-circuiting in a coiled state the thermoelectric tape must insulated with the dielectric tape which provides electrical insulation between the individual turns of the coiled thermo-tape. Dielectric tape is thin so that its contribution to the thermal conductivity of the whole structure is minimal. Arrangement of insulation-tapes between the individual turns of the coiled thermo-tape is visualized in figure Fig. 51.

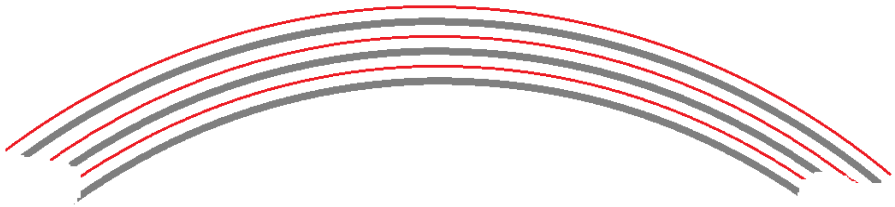

Fig. 51: Insulation between the individual turns of the coiled thermo-tape made by the dielectric tape.

The series resistance of the whole thermo-generator can be estimated in a similar way as in case of the lateral structure. First, we calculate the resistance of one thermocouple. Again, we consider only the resistance in the PEDOT:PSS functional layers which are on both sides of the carrier tape. In terms of total resistance, PEDOT:PSS layers are connected in parallel:
$R_{SV} = R_{SPDV}/2 = [(\varrho_{PD} \cdot l) / (d \cdot w)]/2 = (1.25 \cdot 10^{-3}\ \Omega\ \text{cm} \cdot 0.5\ \text{cm})/(800 \cdot 10^{-7}\text{cm} \cdot 20\ \text{cm})$
$= (6.25 \cdot 10^{-4} / 1.6 \cdot 10^{-3}) / 2 = (3.9 \cdot 10^{-1})/2 = 0{,}195\ \Omega$

Here: R_{SPDV} [Ω] is the resistance of one PEDOT:PSS strip,

R_{SV} [Ω] is the resistance of two PEDOT:PSS strips in parallel,

ϱ_{PD} (= $1.25 \cdot 10^{-3}$ Ω.cm) is resistivity of PEDOT:PSS layer $\varrho_{PD} = 1/\sigma_{PD}$ [$S.cm^{-1}$],

l (= 0.5 cm) is the length of the PEDOT:PSS functional layer,

d (= 800 nm) is the thickness of the PEDOT:PSS functional layer,

w (= 20 cm) is the width of the PEDOT:PSS functional layer.

To achieve the same voltage as in case of the lateral structure, it is necessary to connect 60 thermocouples in series.

The total series resistance, R_{SVT}, will then be: $R_{SVT} = 60 \cdot 0{,}195\ \Omega = 11{,}7\ \Omega$

At open circuit voltage of the generator V_{TPV} = 72 mV, with a series resistance of given value R_{SVT} = 11.7 Ω, ***short-circuit current of*** the entire thermo-generator will be:

$I_{SH} = 72 \cdot 10^{-3} / 11.7 = 6.15$ mA

Similarly as for lateral structure, with a minimum operating voltage of the DC/DC converter of V_{LL}=50 mV, there would be a ***voltage drop on series resistance R_{SVT}:***

$V_{TPV} - V_{LL} = 72$ mV - 50 mV = 22 mV.

The current supplied into the DC/DC converter then will be:

$I_{LL} = (V_{TPV} - V_{LL}) / R_{SVT} = 22$ mV / 11.7 Ω = 1,88 mA

The power delivered to the DC/DC converter input is:

$P_{OUT} = V_{LL} \cdot I_{LL} = 1{,}88 \cdot 10^{-3}$ A $\cdot$ 50.10^{-3} V = 94 μW

The delivered power is more than ten times larger than in case of a vertical structure.

The required length of the thermo-tape can be calculated as follows.

$L_{TT} = (W_{PD} + W_{IH}) \cdot N$, where

W_{PD} (= 20 cm) is the width of the PEDOT:PSS functional layer,

W_{IH} (= 2 mm) is the width of the insulation gap in the carrier tape,

N (= 60) is the number of individual thermocouples in series.

After setting the values:

$L_{TT} = (W_{PD} + W_{IH}) \cdot N = 0.202$ m $\cdot$ 60 = 12.12 m ;

Coiled thermo-generator-tape

For a medium coil diameter of d_{CTG} = 8 cm:

Average coil circumference:

$C_{CTG} = \pi \cdot d_{CTG} = \pi \cdot 8 =$ 25,15 cm = 0.2515 m

Number of turns:

$N_{TH} = L_{TT} / \underline{C_{CTG}} = 12.12$ m / 0.2515 m = 48.19085… 48

Width for winding thermo-tape:

W_{CTG} = Thermo-tape + Dielectric-tape ~ 0.3 mm max.

Cc = 0,3 $\cdot$ 48 = 14.4 mm

Coil dimensions:

R_1 = 8 – 1.44 = 6.56 cm; R_2 = 8 + 1.44 = 9.44 cm

The area of energy flow:

A_E = 25.15 · 1.44 = 36.216 cm^2

Compared to whole TEG area the total area of functional layers is negligible:

$A_F = (0.8 + 0.8)\cdot 10^{-6} m \cdot 12.12\ m = 19.392\cdot 10^{-6}\ m^2$

Consequently, most of the heat flow goes outside the functional layers of the TEG.

Electrical power per area of the functional layers at the considered Δ T = 40 K :

$P_A = P_{OUT} / A_F$ = 94 µW / $19.392\cdot 10^{-6}\ m^2$ = 4.847 W m^{-2}

Calculated for temperature difference:

P_{AT} = 4.847 W m^{-2}/ 40 K = 0.121175 W m^{-2} K^{-1}

Maximal power delivered to the load depends on the size of the load. For optimal matching, the load resistance should be approximately equal to the series resistance of the entire TEG, which is 11.7 Ω. It is clear from Figure 52 a) that for optimal power matching, the load resistance should be in the range of 8 Ω - 20 Ω.

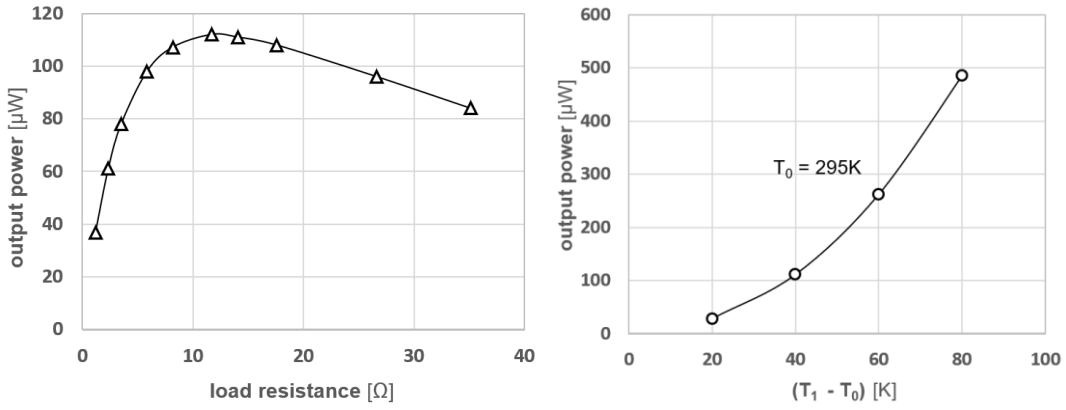

a) **b)**

Fig. 52: a) Output power in dependence on load resistance. **b)** Maximal output power of TEG in dependence on temperature difference between hot and cold ends. Calculated and verified by measurement.

At a voltage of 50 mV and a current of 1.88 mA, which can be drawn at this voltage by a DC / DC converter, there is a substitution resistor that simulates the current consumption of the converter:

R_{DC} = 50 mV / 1.88 mA = 26.6 Ω.

The power supplied to the inverter is:

P_{DC} = 50 mV · 1.88 mA = 94 μW.

It is obvious that in this case the TEG works with good efficiency and a possible increase in the current consumption of the inverter will not have a negative effect on the efficiency of the whole device.

The minimum temperature difference between the hot and cold ends of the thermoelectric generator, at which the whole device including DC/DC converter will still work, is therefore 40K. As the temperature difference increases, the maximum delivered power will increase very quickly.

The dependence of the maximum achievable power on temperature shown in Fig. 52 b) is approximately quadratic, because of the quadratic dependence of power on voltage, $P=(V^2)/R$. In addition, the Seebeck coefficients of both materials increase slightly with temperature.

The efficiency of vertical TEG structure

The efficiency of a thermoelectric transducer can be estimated using the equation:

$$\eta = \frac{(T_H - T_C)}{T_H} \cdot \frac{\sqrt{1+ZT_m}-1}{\sqrt{1+ZT_m}+\frac{T_C}{T_H}};$$

Where the first fraction is the Carnot efficiency; here T_H is the temperature of the hot part and T_C is the temperature of the cold part,

ZTm is figure of merit defined in chapter 1.4.2 as: $ZT = \frac{\alpha^2\sigma}{K}Tm$; here α is Seebeck coefficient, σ is electrical conductivity, *K* is thermal conductivity, and *Tm* is average temperature between T_H and T_C.

The Seebeck coefficient is for Ni α_{Ni} = - 19 μV/K and for the second material in the cell PEDOT:PSS it is α_{PD} = 20 μV/K.

The electrical conductivity is for Ni $\sigma_{Ni} = 1.4 \cdot 10^7$ Sm^{-1} and the electrical conductivity for PEDOT:PSS is $\sigma_{PD} = 8 \cdot 10^4$ Sm^{-1}

The thermal conductivity of Ni is tabulated and at 20 Celsius K_{Ni} = 91 W $m^{-1}K^{-1}$. The thermal conductivity of nickel compounds and electrolytic nickel alloys is lower, depending on the actual composition of the layer. For electrolytic nickel, the thermal conductivity it depends on the structure and content of the amorphous Ni:P phase. Mostly, the value around K_{NiP} ~ 50 W $m^{-1}K^{-1}$is usually considered.

The thermal conductivity of PEDOT:PSS depends on many of its parameters and should be determined individually for a given material composition. However, the determination

of thermal conductivity is difficult for such thin layers. In the literature, the thermal conductivity of PEDOT:PSS is mostly reported in the range from K_{PD} ~ 0,3 W $m^{-1}K^{-1}$ to more than K_{PD} ~ 1,0 W $m^{-1}K^{-1}$.

For the values of Z then follows:

$$Z_{Ni} = \frac{(19 \cdot 10^{-6})^2 \cdot 1.4 \cdot 10^7}{50} = \frac{361 \cdot 10^{-12} \cdot 1.4 \cdot 10^7}{50} = \frac{361 \cdot 1.4 \cdot 10^{-5}}{50} = \mathbf{1.001.10^{-4} K^{-1}}$$

$$Z_{PD} = \frac{(30 \cdot 10^{-6})^2 \cdot 8 \cdot 10^4}{0{,}3} = \frac{900 \cdot 10^{-12} \cdot 8 \cdot 10^4}{3.10^{-1}} = \frac{9.8 \cdot 10^{-5}}{3} = \mathbf{2.4 . 10^{-4} K^{-1}}$$

The ZT value increases with temperature. Suppose operation contitions T_H = 300 K and T_C = 400 K. Then T_m = 350 K and ZT_m for Ni equals:

$ZT_m = 1.001 \cdot 10^{-4} \cdot 350 = 3.5 \cdot 10^{-2} = 0.035$.

And for PEDOT:

$ZT_m = 2.4 \cdot 10^{-4} \cdot 350 = 8.4 \cdot 10^{-2} = 0{,}084$.

The maximum achievable efficiency for Ni:

$$\eta = \frac{(T_H - T_C)}{T_H} \cdot \frac{\sqrt{1+ZT_m}-1}{\sqrt{1+ZT_m}+\frac{T_C}{T_H}} = \frac{(400-300)}{400} \cdot \frac{\sqrt{1+0.035}-1}{\sqrt{1+0.035}+\frac{300}{400}} =$$

$$= \frac{1}{4} \cdot \frac{1.01735-1}{1.0173+\frac{3}{4}} = \frac{1}{4} \cdot \frac{0.01735}{1.0173+0{,}75} = \frac{1}{4} \cdot \frac{0.01735}{1.76173} = \frac{1}{4} \cdot \frac{0.01735}{1.76173} = 0.00246$$

The maximum achievable efficiency for PEDOT:PSS :

$$\eta = \frac{(T_H - T_C)}{T_H} \cdot \frac{\sqrt{1+ZT_m}-1}{\sqrt{1+ZT_m}+\frac{T_C}{T_H}} = \frac{(400-300)}{400} \cdot \frac{\sqrt{1+0.084}-1}{\sqrt{1+0.84}+\frac{300}{400}} = ;$$

$$= \frac{1}{4} \cdot \frac{1.041155-1}{1.04115+\frac{3}{4}} = \frac{1}{4} \cdot \frac{0.041155}{1.041155+0{,}75} = \frac{1}{4} \cdot \frac{0.041155}{1.791155} = \frac{1}{4} \cdot \frac{0.041155}{1.791155} = 0.00574$$

The calculation is intentionally detailed so that the influence of individual parameters is obvious.

The theoretical achievable efficiency is less than 1% in accordance with the experiments and data reported in the literature [109,110,111].

Power factor

If the generator is powered from a source with unlimited heat source and cooling and with a guaranteed temperature difference, which is met in our case, it is possible to use the Power Factor parameter.

Power Factor is defined as: $PF = \sigma \cdot \alpha^2 [\mathrm{W}m^{-1}K^{-2}]$

This expression can be obtained by modifying the equation for the electrical power achievable by the thermo-electric generator.

After further modifications we will receive:

$PF = P_{OUT} \cdot (2 \cdot l / A_F) / (\Delta T)^2 = P_{OUT} / A_F \cdot (2 \cdot l) / (\Delta T)^2$ [μWm^{-1}K^{-2}]

If we use the equation modified in this way, we can calculate the power factor from the values of the total power and the active area of the thermoelectric generator from previous calculations. We will use the following parameters:

The length of the PEDOT:PSS functional layer: l = 5 mm.

The cross-section area of PEDOT:PSS functional layer: A_F = 19, 392·10^{-6} m^2.

Total power delivered by TEG: P_{OUT} = 94 μW.

Temperature difference: T = 40 K.

When using the second part of the modified equation:

$PF = (P_{OUT} / A_F) \cdot 2 \cdot l / (\Delta T)^2$ = (94 μW / 19.392·10^{-6} m^2) · (2 · 5·10^{-3} / 1600) =

= 4.847 W m^{-2} · (2. 5 .10^{-3} / 1600) = 4.847 · (10/1.6·10^{-6}) = 30.029·10^{-6} =

= 30 μWm^{-1}K^{-2}

This value is also well comparable with the results given in literature [115,117].

To ensure a defined temperature in the entire area of the hot and cold ends of the coil of the thermoelectric generator, it is advisable to use thermally conductive extensions. Heatsinks for cooling power electronic components are suitable for this purpose.

For the dimensions of thermoelectric-tape-coil as discussed previously the profile 100x100 mm is convenient.

3.3.4 Comparison with TEG based on Ni-NiCr structure

To compare the achieved results and to find further possibilities for the continuation of the work, in this chapter the properties of the designed thermoelectric converter will be compared with the properties of other types of thermoelectric converters and with other materials [112,113].

TEG based on Ni-NiCr

The Ni-NiCr combination is a commonly used thermocouple with the most frequently reported sensitivity of 41 μVK^{-1}. It is referred to as type K and used up to 1100 °C.

NiCr has a Seebeck coefficient of S = 25 μVK^{-1}. This value is very well comparable with the value S = 20 - 35 μVK^{-1} considered for material PEDOT:PSS.

The thermal conductivity and electrical conductivity of NiCr depends on its composition and structure. However, both parameters are always significantly smaller in case of nickel. Electrical conductivity is given in the range of $0{,}6 \cdot 10^6$ Sm^{-1} to approximately $0.9 \cdot 10^6$ Sm^{-1}.

Further, the most frequently reported thermal conductivity is 11.3 $Wm^{-1}K^{-1}$. Even here, however, there is a certain variance and it is possible to find values in the range from 9 $Wm^{-1}K^{-1}$ to 16 $Wm^{-1}K^{-1}$.

Then, it comes out for these values:

$$Z_{NiCr} = \frac{(25\,.10^{-6})^2 \cdot 0.9 \cdot 10^6}{11.3} = \frac{625 \cdot 10^{-12} \cdot 0.9 \cdot 10^6}{11.3} = \frac{625 \cdot 0.9 \cdot 10^{-6}}{11.3} = \mathbf{4.9\ .10^{-5}K^{-1}}$$

As the ZT_m value depends on temperature, at operation by T_H = 400 K and T_C = 300 K is T_m = 350 K and ZT_m for NiCr equals:

$ZT_m = 4.9 \cdot 10^{-5} \cdot 350 = 1715 \cdot 10^{-5} = 1.715 \cdot 10^{-2} = 0{,}017$

The maximum achievable efficiency for NiCr:

$$\eta = \frac{(T_H - T_C)}{T_H} \cdot \frac{\sqrt{1+ZT_m}-1}{\sqrt{1+ZT_m}+\frac{T_C}{T_H}} = \frac{(400-300)}{400} \cdot \frac{\sqrt{1+0.017}-1}{\sqrt{1+0.017}+\frac{300}{400}} = ;$$

$$= \frac{1}{4} \cdot \frac{1.0085-1}{1.0085+\frac{3}{4}} = \frac{1}{4} \cdot \frac{0.0085}{1.0085+0{,}75} = \frac{1}{4} \cdot \frac{00.0085}{1.7585} = \frac{1}{4} \cdot \frac{0.0085}{1.76173} = 0.00120$$

In case of NiCr the achievable efficiency for TEG operation will be even lower than in case of nickel. However, if this system is operated at high temperature, the efficiency of the Carnot cycle will increase and the achievable efficiency will be significantly greater.

Suppose for this case the operation by T_H = 1300 K , T_C = 300 K and T_m = 800 K. Then, neglecting the change of the Seebeck coefficient and the thermal conductivity with temperature, for T_m = 800 K the ZT_m for NiCr will be approximately as follows:

$ZT_m = 4.9 \cdot 10^{-5} \cdot 800 = 3\,920 \cdot 10^{-5} = 3.920 \cdot 10^{-2} = 0.39$

For given temperatures T_H and T_C maximum achievable efficiency for NiCr will be:

$$\eta = \frac{(T_H - T_C)}{T_H} \cdot \frac{\sqrt{1+ZT_m}-1}{\sqrt{1+ZT_m}+\frac{T_C}{T_H}} = \frac{(1300-300)}{1300} \cdot \frac{\sqrt{1+0.039}-1}{\sqrt{1+0.017}+\frac{300}{1300}} =$$

$$= \frac{1}{1.3} \cdot \frac{1.0193-1}{1.0193+\frac{0,3}{1,3}} = 0.77 \cdot \frac{0,0193}{1.0193+0,23} = 0,77 \cdot \frac{0,0193}{1.2493} = \frac{1}{4} \cdot \frac{0,0085}{1.76173} = 0.0118$$

Thanks to the higher efficiency of the Carnot cycle, the efficiency of thermoelectric generation is an order of magnitude higher when the temperature of the hot end increase from 300 K to 1300 K (1027 Celsius). In fact, the increase in efficiency will be even larger, because the Seebeck coefficient will also increase slightly. By higher temperature there will be by the same way an increase in efficiency with Nickel – the second material in the thermoelectric pair. The conversion efficiency of Ni-NiCr thermocouple will be in this case in order of percent. Compared to organic materials, the ability to work at high temperatures is here a great advantage.

Preparation of Ni-NiCr functional layers

The creation of individual parts of thermocouples and their serial connection must be ensured by mass production processes using suitably shaped masks or in case of thin film technology by lithographic processes. The simplest and cheapest is the contact mask. The structures can also be created using a screen-printing template.

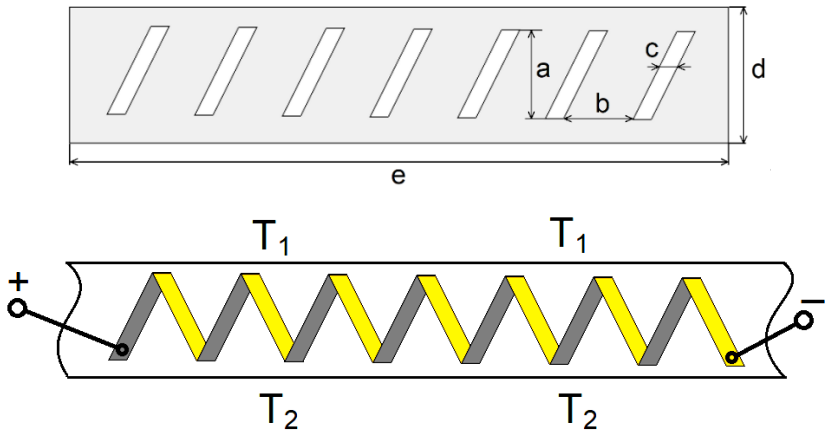

Fig. 53: Simple mask for serial connections of thermo-cells and resulting structure.
DIMENSIONS (mm): **a** = 22; **b** = 17; **c** = 4 ; **d** = 34; **e** = 166

The arrangement of convenient and universal mask is shown in figure Fig. 53. Holes in the mask are at an angle of 60 degrees in respect to the longitudinal axis of the thermocouple tape.

After deposition or printing of the bottom material the mask is flipped 180 degrees and the second material of the thermoelectric pair is deposited. The materials are this way mutually bonded and the straight legs of the structure are also in the angle in of 60°.

A disadvantage of the simple mask given on Fig.53 is the poor utilization of the substrate area. Although the rectangular mask in figure Fig.54 is more complex, the utilization of the substrate area is much better.

In both cases, the TEG operates with a temperature gradient across the tape on which the thermocouple components are applied. The material of the carrier tape must therefore have a low thermal conductivity and the thickness of the tape must be set to ensure sufficient mechanical stability. If a large number of thermocouples is required, the carrier strip can be wound in a spiral - similarly to the case of vertical design described in the previous chapter 3.6.3.

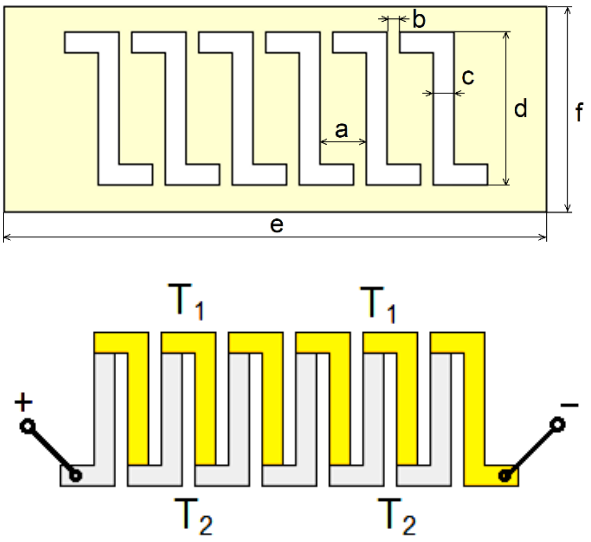

Fig. 54: Rectangular mask for serial connections of thermo-cells and resulting structure. ***DIMENSIONS:*** **a** = 10 mm; **b** = 3 mm ; **c** = 4 mm ; **d** = 33 mm ; **e** = 44 mm ; **f** = 115 mm

The masks thus structured can be used for screen printing as well as for vacuum deposition. In case of vacuum deposition a common disadvantage of both masks is the slow pumping of the gap between the mask and the substrate. This is due to the low vacuum conductivity of the gap. It is necessary to respect this fact when pumping the vacuum system.

Screen printing

NiCr pastes are available in a large selection. However, they are optimized to the production of resistive layers. Their composition and structure can vary according to the

desired resistance value and the Seebeck coefficient then may not correspond to pure NiCr.

Ni pastes are available in a limited selection. The Seebeck coefficient depends on the type of binder and on the binder to active component ratio. Usually, the glass binder tends to have a positive Seebeck coefficient and in case of nickel paste it slightly increases the negative value of Seebeck coeficient.

Vacuum thin film technologies

Vacuum technologies have the common disadvantage of being expensive and time consuming. Because the conductivity of the layers is influenced by their small thickness the dimensions and thickness of the structures must be designed regarding to the expected current load.

Sputtering. Sputtering of NiCr is a standard technology of resistive layers. During sputtering, the ratio of Ni to Cr corresponds to the target material and the resulting layer composition can be set with satisfactory accuracy. Nickel sputtering process is complicated by its magnetic properties. The use of magnetron sputtering is therefore problematic. In a conventional system, the sputtering rate is of the order of magnitude less.

Evaporation. Nickel evaporation process is trouble-free. In case of NiCr, however, due to the very different saturated vapor pressure of Ni and Cr (see Fig. A5.2 in Appendix A5), the evaporation rate of both components Ni and Cr is different and the nickel and chromium content in the deposited layer does not correspond to the original material.

This problem can be solved with the help of "flash off" technology where the material evaporates by individual grains. However, also in this case, even distribution of both elements in the layer is not guaranteed.

In addition, in case of evaporation there is a problem with the low energy of vaporized particles after their condensation on the surface of deposited layers. If the particle has little energy upon impact on the substrate, it cannot migrate across the surface to energy-efficient positions.

The particle is in such a case trapped at random positions. Consequently, the resulting layer has a spongy structure and very poor adhesion [137]. The solution of bad adhesion and structure problems caused by low energy of evaporated particles is the heating of the substrate. However, for efficient results, the heating temperature must be at least 300 ° C. This practically eliminates the possibility of using organic substrates.

3.3.5 Comparison with other types of thermoelectric converters

This chapter compares the achieved results with other types of technologies for the conversion of heat into electricity. The comparison is made in terms of operating temperature and achieved efficiency.

High temperature converters and inorganic converters

As verified on the example of the Ni-NiCr cell, high operating temperatures make a very significant contribution to increasing the efficiency of thermoelectric conversion. This is a great advantage of inorganic materials which can usually operate at temperatures well above 1000 K. With our PEDOT: PSS converter, the maximum temperature is limited to about 400 K and this option cannot be used.

For standard materials for thermoelectric converters a large value of the Seebeck coefficient is essential because in the expression for *ZT* the Seebeck coefficient is squared. For a large *ZT* value, the conditions of low thermal conductivity and high electrical conductivity must also be met. However, as will be shown in the following example, these parameters have a significantly smaller effect.

For comparison, we will use the standard material for thermoelectric converters which is Bismuth-Telluride, Bi_2Te_3. For low-doped material, the Sebeck coefficient significantly exceeds 200 $\mu V\ K^{-1}$. However, the electrical conductivity is very low.

The electrical conductivity can be increased by doping, for example, using Sb for P-type and Se for N-type. However, as shown in Chapter 1, when increasing the electrical conductivity by doping, the Seebeck coefficient decreases.

For the optimal concentration of dopants, the value of the Sebeck coefficient for both types P and N is around 160 $\mu V\ K^{-1}$ and the electrical conductivity of both materials is in the range of $1.1 \cdot 10^5$ S m^{-1} to $1.5 \cdot 10^5$ S m^{-1}. This value is very close to the conductivity of our PEDOT:PSS material.

The value of thermal conductivity for optimally doped material at temperature of 300 K is around 1.2 $Wm^{-1}K^{-1}$. Considering that Bi_2Te_3 is inorganic material, this value can be regarded as very low. It is only 3 times greater than the thermal conductivity of PEDOT:PSS.

The main difference between the two materials is therefore in the value of the Seebeck coefficient. The ratio of electrical and thermal conductivity can be calculated using the parameters from previous considerations.

For given PEDOT:PSS material it is :

$\sigma_{PD} / K_{PD} = (8 \cdot 10^4) / 0.3 = 26.6 \cdot 10^4 = 2.6 \cdot 10^5$ [S K W^{-1}]

and for Bi_2Te_3: $\sigma_{Bi2Te3} / K_{Bi2Te3} = (1.2 \cdot 10^5) / 1.2 = 1 \cdot 10^5$ [S K W^{-1}]

It is obvious that for PEDOT:PSS this ratio is much larger than for Bi_2Te_3.

Having the parameters given above, *Z*-value for hypothetical, optimally doped Bi_2Te_3 is:

$$Z_{\mathrm{Bi2Te3}} = \frac{(160 \cdot 10^{-6})^2 \cdot 1.2 \cdot 10^5}{1.2} = \frac{25600 \cdot 10^{-12} \cdot 1.2 \cdot 10^5}{1.2} = 256 \cdot 10^{-5} = \mathbf{2.56 \cdot 10^{-3} K^{-1}}$$

As the ZT_m value depends on temperature, considering previously defined operation conditions T_H = 400 K , T_C = 300 K and T_m = 350 K , ZT_m equals:

$ZT_m = 2.56 \cdot 10^{-3} \cdot 350 = 896 \cdot 10^{-3} = 0.896$

This value closely corresponds to results of measurements and computations published elsewhere [166]. 164

Because PEDOT has significantly lower thermal conductivity than Bi_2Te_3 to achieve a similar level of *ZTm* the Seebeck coefficient of PEDOT:PSS compound should be less than 160 $\mu S.V^{-1}$ used here for Bismuth Telluride. Considering the electrical to thermal conductivity ratio given above, this value should be approximately 100 $\mu S.V^{-1}$.

Such values appear in the literature for specially doped PEDOT: PSS compounds and can also be found for other organic materials. In all cases, however, there is a very significant decrease in electrical conductivity and efforts to increase the electrical conductivity leads to a reduction in the magnitude of the Seebeck coefficient. Therefore, the development here focuses on finding a compromise.

Compared to standard thermoelectric materials, the disadvantage of PEDOT:PSS is also the difficulty in preparation of bulk PEDOT:PSS material.

Thermoelectric systems with PEDOT:PSS are essentially two dimensional, because PEDOT:PSS does not allow such a thick layer that it can be a leg of the thermocouple itself. The procedures described in the literature for the preparation of thick layers of PEDOT:PSS vary from dripping from a thick solution, deposition of several layers on top of each other to screen printing with the extremely dry thick paste.

The thickness of the layer can be boosted up to several micrometers. However, as we observed in experiments the properties of such layers are usually much worse than those of optimized thin films.

PEDOT:PSS bulk-materials are also prepared as polymer/inorganic composites where various fillers as Carbon Nanotubes, grinded Bi_2Te_3, Te particles, Ag nanowires and other materials have been used as the inorganic component or secondary dopants are used [165]. However, in this work we do not deal with such special materials.

Thermo-galvanic cells

In this work, which is focused on EH converters in the solid phase, the topic of thermo-galvanic generators was not addressed. However, at the time of completion of the work, very rapid progress had been made in the field of thermo-galvanic cells. For this reason, the paragraphs below shortly summarize some of properties of thermo-galvanic cells and prospects for their possible applications in the foreseeable future.

From the above-described structure designs and performed experiments, it follows that in case of thermoelectric converters, their wider use is complicated by number of fundamental limitations. The availability of affordable thermoelectric transducer, especially for low temperature range, in the foreseeable future is therefore debatable. Many thermocouples connected in series are also a potential problem in terms of long-term reliability.

Another principle that can be used for temperature-dependent charge transfer is the diffusion of ions due to the temperature dependence of their concentration. Cells working on this principle are called thermo-galvanic cells.

Operation of thermo-galvanic cells applies to materials that exhibit ionic conductivity. The change in ion concentration as a function of temperature may be due to the temperature dependence of chemical reactions or the temperature dependence of the solubility of ions.

In the absence of electrochemical reaction at the electrodes, ions cannot pass directly into the electrodes to complete the circuit and generate a continuous current. The diffusion of ions stops after some time. In such case the structure work as thermally chargeable super-capacitor [171, 159].

In both cases, the temperature dependence is significant, and the diffusion flux is large and consequently the achieved voltage is an order of magnitude higher than with thermoelectric generators.

The Seebeck coefficient is much higher for thermo-galvanic cells than for thermoelectric cells and can reach up to several $mV.K^{-1}$. Thus, with a larger temperature gradient, only one thermo-galvanic cell is sufficient to generate a voltage in tens of millivolts. The current-flow area of thermo-galvanic cells is naturally larger than the current-flow area of thermoelectric cells and the problems with series resistance are smaller. If a higher voltage is required, it is possible to connect several cells in series without the power consumption being significantly limited by the series resistance.

In case of PEDOT:PSS both electrons and mobile ions can serve as charge carriers [158]. Consequently, PEDOT:PSS can work as a mixed ionic-electronic conductor. The electronic aspects of its conductance have been thoroughly researched but the ionic aspect

of its conductivity is mostly overlooked. In pristine PEDOT:PSS the conduction is dominated by holes, but the ionic conductivity can be enhanced by various methods.

There is an advantage in case of ionic conductive polymers that there is no liquid leakage problem because of solid electrolyte. Nevertheless, in case of PEDOT:PSS the ionic conductive properties only appeared at conditions which ensured the relative humidity (RH) above 40%. Relative humidity is therefore the parameter which must be monitored and maintained. Increasing RH from 10 to 80% increased the total Seebeck coefficient almost by one order of magnitude due to the increase in ionic conductivity. Other possibility to enhance the ionic conductivity is mixing this material with additives or ethylene glycol treatment [160].

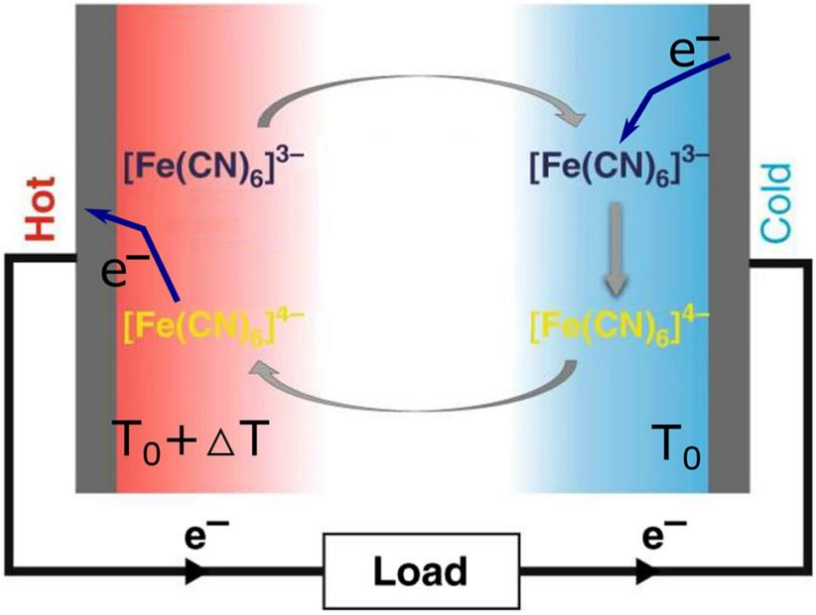

Fig. 55 : Thermogalvanic converter with redox reaction in ferrocyanide solution [161]

To time, aqueous electrolytes are the most researched area of thermo-galvanic converters and currently reach power density as high as 12 W/m^2. With such high performance, they can already be used in many applications, including industrial equipment. The disadvantage is the low working temperature, which must be below 100 Celsius.

The operation of a typical thermo-galvanic converter using a redox reaction in ferrocyanide solution is shown in figure Fig.55.

Compared to thermoelectric generators, the physical function of thermo-galvanic cells is more complicated, but there are no major technological limitations. Therefore, in low temperature applications, their use may be more advantageous than the use of thermoelectric generators.

Thermionic energy converters

Operation principle of thermionic energy converters is based on thermal emission and has been known for a long time. However, interest in this type of conversion has emerged only recently and it is supported by efforts to make the best use of waste heat. The effective use of this mechanism is facilitated by advances in materials science and manufacturing technologies [162].

This technology is mentioned here for completeness, because due to the high working temperatures it is focused more on the processing of large power outputs and thus deviates from the topic of the dissertation.

Thermionic energy converter consists of 2 electrodes - emitter and collector. In the simplest case, there is a vacuum in the gap between the electrodes. The emitter is heated to such a temperature where the thermal emission occur and electrons are released from the emitter. These electrons are captured by the collector, which has a lower temperature and therefore thermal emission does not occur here.

This way a negative charge of electrons captured on the collector surface creates an electromotive voltage between the emitter and the collector. Thermionic energy converters are thus simpler than other heat to electricity converters and their operation resembles photovoltaic cells.

If we connect an appliance between the collector and the emitter, an electron current will pass through the appliance back to the emitter. This closes the current circuit. Consequently, other electrons can be released by emission and move towards the collector. This process is repeated as long as there is a temperature on the emitter that is sufficient for thermal emission.

This principle is very advantageous for operation at extremely high temperatures reaching up to 2000 K where much higher efficiencies can be achieved than in case of generators based on thermocouples. It is also possible to work with a high power density, which can reach up to 100 W/cm^2.

The big advantage is the direct conversion of thermal energy into the electrical energy. However, when compared to large mechanical heat engines with a practical efficiency of about 40% - thermionic converters have a practical efficiency limit of around 20% [162].

To time achieved power densities reported in the literature are still relatively small and range in units of W/cm^2. The development is focused mainly on materials with low work function for use in the active layer of the emitter and the geometric management of electrodes. One of the options that are being explored is to use graphene or high temperature working semiconductive materials [163].

3.3.6 Summary of chapter 3.3 Organic thermoelectric generator

We designed, manufactured and measured the basic parts of a thermoelectric generator and made a comparison with the literature. The achieved results are good and comparable.

In case of a thermoelectric generator large number of thermocouples connected in series is required. Achieving the lowest possible series resistance of functional layers is therefore a major design problem.

This was reflected in the first design of the thermoelectric generator, which was designed to include as few technological steps as possible. This was the combined structure with lateral arrangement of short thermo-coupler legs described at the beginning of chapter 3.6. The individual thermocouples are here applied on both sides of the carrier tape in the form of short strips of thermoelectric materials. The temperature difference is provided by thermally conductive extensions.

However, the attempt. to reduce the series resistance of the individual thermo-cells and series resistance of the assembled thermo-generator to acceptable value, resulted in disproportionately large dimensions. Lateral structure was therefore abandoned in favor of the structure with vertical arrangement of functional layers.

For vertical TEG structure we designed and tested the procedure for making the individual parts of the generator. The PEDOT-PSS layer is applied to the nickel functional layer in the entire required width by screen printing using a very simple rectangular mask. First, the PEDOT-PSS bottom layer is applied. The top PEDOT-PSS layer can be applied only after the bottom PEDOT-PSS layer is completely cured. Then the bottom and top PEDOT-PSS layers are applied in the same way with the tape inverted. Using a parallel layer arrangement thus helps to reduce the series resistance. At the same time, the reliability of the resulting structure is increased.

In terms of the sufficiently low series resistance and efficiency applicable to practical applications, this thermoelectric generator meets the specified requirements. I performed the necessary measurements with the help of my supervisor in the laboratories of the Department of Microelectronics.

The main result is that we have verified that using organic semiconductors it is possible to prepare a thermoelectric harvester, which we have known so far only with inorganic materials.

I prepared the experimental structure with the help of my supervisor. However, the work would not be possible without material support and professional assistance from the BUT Faculty of Chemistry.

4 Conclusion

This thesis focuses on the important question of how to improve the electrical performances low-voltage low-power energy harvesting devices. For this reason, these performances of many different configurations have been studied in detail. The results we can summarize as follows.

1) *DC to DC converters with low input voltage*

In this part of work the scientific and engineering contribution is the extension of existing knowledge towards new suggested and tested concepts of DC / DC converters for voltages less than 100 mV. To achieve high reliability, robust production processes have been preferred. Standard components are used, so the production is not tied to one supplier, or the lack of some type of components.

a) It has been verified that it is possible to work with a BJT with a very low supply voltage and extremely low power consumption, but the use of a BJT in this mode is very unusual. However, it must be considered that for integrated circuits where FET-type transistors are used, it is also necessary to use FET-type transistors under unusual operating conditions to achieve an extremely low operating voltage.

b) The circuit solution of DC to DC converter in integrated circuit technology, which is available at the institute, was designed. However, using available IC technology, to achieve low operating voltage, FET-type transistors must operate in the subthreshold mode or BULK-DRIVEN mode.

c) Two types of inverters have been designed and prototyping.

The Armstrong oscillator allows multiple transducers to be connected in parallel to one load. This is very advantageous when processing energy from multiple sources with unstable power and possible outages. This type of inverter is not sensitive to the stray inductance of the transformer.

A single FET DC to DC converter is more efficient than an Armstrong oscillator. However, it requires a transformer with low stray inductance. Complementary circuits have been tested for the designed and manufactured single FET DC to DC converter, which enable a significant increase in efficiency reaching up to 50 percent.

d) In order to maintain the functionality of the EH transducer at a very low power input, the START-STOP operation of the generator with the start of the generator by means of start pulses was proposed and tested for the single J-FET converter. In this case, the EH transducer is not loaded by the connected DC to DC converter and is able to supply current to charge the capture capacitor at the input of the converter. Under laboratory conditions, this method has proven to be operational. However, it is not recommended for practical use due to the possible uncertainties in starting and stopping the generator and the associated reduction in reliability. Therefore, in the final design stable no-load

operation was preferred over switching off the EH converter and resetting with start pulses.

f) Two types of innovative transformers with extremely high conversion ratios have been designed for low-voltage DC to DC converters:

Flat transformer allows very simple production. With this type of transformer, it is also possible to make miniature transformers, where the nominal power input can be much less than 1W. Scaling of transmitted power can be achieved by using a larger number of toroidal cores or by increasing the dimensions of toroidal cores. It is very easy to achieve a conversion ratio greater than 100. The stray inductance depends on the way the core of flat transformer is composed.

A planar transformer is more complex because it requires high-resolution multilayer PCB technology. The small stray inductance on the secondary winding of the transformer is ensured by a suitable distribution of the primary and secondary windings on the printed circuit boards of the individual layers. The conversion ratio can be much larger than 100 and can be set by the number of individual printed circuit boards in the assembly. The addition of one more plate always increases the conversion ratio by 20. Greater stray inductance on the secondary winding can be achieved by disconnecting one or more individual primary windings, if necessary. The change depends on the location of the currently disconnected winding in the overall assembly. The disadvantage of this type of transformer is the dependence on the range of ferrite cores. It is therefore not possible to achieve arbitrarily small dimensions and extremely small rated power.

I assembled and experimentally verified the converters and transformers described in the section *DC to DC converters with low input voltage* in the laboratories of the Department of Microelectronics with the help of my supervisor. The printed circuit boards of the converters and the windings of the planar transformer were manufactured in a specialized company. However, the work would not be possible without further material support and professional assistance from Department of microelectronics of BUT Faculty of Electrical engineering and Communication.

Objective 3 “Research and design of a low voltage low energy DC/DC converter to process the output from EH transducers on low energy level” set out in Chapter 2 has been met. The correct function of DC to DC converters was subsequently verified in laboratory experiment in the processing of energy from photovoltaic converters under low light conditions. The experience gained in experiments with photovoltaic cells and the study of their properties according to objectives No. 1 and No. 2 defined in Chapter 2 was also used here. In terms of minimum input voltage and efficiency these inverters achieve comparable or slightly better properties than published circuits according to the literature.

2) *Photovoltaic structures*

Photovoltaic cells with different technologies donated or borrowed from various institutions were used in the experiments. In addition to standard measurements, the series resistance and leakage resistance were also measured using a new dynamic method. A great advantage of this method is the possibility of measurement of parasitic resistances of the cell in the dark without the use of special instruments. The measured values do not depend on the lighting conditions and describe the physical properties of photovoltaic cells very well. The following conclusions were drawn from mutual comparison of the cells in the experiments presented in this chapter, which were supplemented by a study of the literature according the objective No 1 defined in Chapter 2.

a) Despite the abundant literature, the application potential of organic photovoltaic cells was overestimated at the time of the assignment. However, the technology of organic photovoltaic cells developed during the solution. The most significant change is the abandonment of fullerene-based absorbers in favor of new materials. When using these materials, the photovoltaic conversion efficiencies achieved in laboratories usually already exceed 10%, but the problems with stability and sensitivity to external influences remain. However, the organic cells available in this work were only around 5% effective. Tests of application possibilities of organic cells were therefore only indicative, although from the point of view of spectral sensitivity these cells very well meet the requirements for use in indoor spaces, where many of their problems associated with short life would not manifest themselves.

b) In addition to technological improvements, the price per Wp of crystalline silicon cells decreased significantly. In experiments, it has been designed and verified that due to current prices and technological possibilities, the single cell variant is very advantageous for low-energy photovoltaic EH converters, where cells with an area from 30 cm^2 to 40 cm^2 are mass-produced on standard-sized silicon wafers and divided into individual functional cells at the end of the production cycle. The cells are highly efficient and very robust. Given their current price of 0.2 Euro per Wp, it is also an economic option.

c) It has also been verified that DC to DC converters designed in this work are able to operate with very low input power delivered from photovoltaic cells in low light operation and that they are able to operate in parallel in one load. This significantly expands the possibilities of capturing energy from various unstable sources with possible outages. Based on the testing of individual types of photovoltaic cells, for these experiments silicon crystal cells were selected.

I prepared the experiments and performed the measurements described in the section *Photovoltaic structures* in the laboratories of the Department of Microelectronics with the help of my supervisor. However, the work would not be possible without material support and professional assistance from Department of microelectronics of BUT Faculty

of Electrical engineering and providing photovoltaic cells for testing and measurement from the BUT Faculty of Chemistry.

Objective 1 “Compile overview concerning preparation of EH photovoltaic structures and suggest solutions for their operation on low energy level.” set out in Chapter 2 has been met. The experience gained in experiments with photovoltaic cells and the study of their properties according was used in experiments to verify the correct operation of the prototypes of DC to DC converters.

3) ***Organic thermoelectric generator***

We designed manufactured and measured the basic parts of a thermoelectric generator and made a comparison with the literature. The achieved results are good and comparable.

Because the voltage of one thermocouple is very small, large number of thermocouples connected in series is required. Achieving the lowest possible series resistance of functional layers is therefore a major design problem.

a) The first design of the organic thermoelectric generator was proposed to include as few technological steps as possible. This was the combined structure with lateral arrangement of short thermo-coupler legs. The individual thermocouples were applied on both sides of the carrier tape in the form of short strips of thermoelectric materials. The temperature difference was provided by thermally conductive extensions. However, to reduce the series resistance of the individual thermo-cells and series resistance of the assembled thermo-generator to acceptable value, the design resulted in disproportionately large dimensions. Lateral structure was therefore abandoned in favor of the structure with vertical arrangement of functional layers.

b) For vertical TEG structure we designed and tested the procedure for making the individual parts of the generator. The PEDOT-PSS layer is applied to the nickel functional layer in the entire required width by screen printing using a very simple rectangular mask. First, the PEDOT-PSS bottom layer is applied. The top PEDOT-PSS layer can be applied only after the bottom PEDOT-PSS layer is completely cured. Then the bottom and top PEDOT-PSS layers are applied in the same way with the tape inverted. Using a parallel layer arrangement thus helps to reduce the series resistance. At the same time, the reliability of the resulting structure is increased.

c) In terms of the sufficiently low series resistance and efficiency applicable to practical applications, the thermoelectric generator with vertical structure meets the requirements for connection of large number of thermoelectric cells in series.

d) The individual thermocouple is designed to connect a large number of thermocouples in series which is ensured by placing individual thermocouples on the carrier tape and winding the carrier tape into the coil. This scaling-up is limited by the total series

resistance of the resulting thermoelectric generator. In practice, the number of thermocouples connected in series is 60 to 100 depending on the current being processed.

e) The proposed solution was also compared with other types of thermoelectric converters. Thermo-galvanic cells, which in principle have very high Seebeck coefficient value, and thermionic converters, which are able to operate at extremely high temperatures and achieve efficiencies in excess of 10%, seem to be very advantageous alternative.

I performed the necessary measurements with the help of my supervisor in the laboratories of the Department of Microelectronics. The main result is that we have verified that using organic semiconductors it is possible to prepare a thermoelectric harvester, which we have known so far only with inorganic materials. However, the work would not be possible without material support and professional assistance from the BUT Faculty of Chemistry.

Objective 4 “Research and design of a thermoelectric converter using simple technologies and available materials” set out in Chapter 4 has been met. The results are comparable to published results for thermocouples using PEDOT: PSS as the active layer. The new contribution is the optimized arrangement of active layers enabling the series connection of large number of thermocouples while achieving a low series resistance of the entire thermoelectric generator. Because the procedures for preparation of a model thermocouple of the thermoelectric generator with vertical arrangement may be copyrighted by people who have helped me with preparation processes, some details are not provided here.

The future of the electronics will depend on its efficiency, cost, and reliability. Thanks to the investigated energy harvesting approach, the total efficiency can increase. It can make some low-power-electronic applications more available for each of us, and in this way, we also can protect a vital environment. This thesis achieved good results in the research of the innovative low-energy and low-voltage energy harvesting devices. Further, this work can be extended to new semiconductor materials and more complex technologies. It could be interesting to investigate in detail newly available organic semiconductors.

5 References

[1] Shockley and H. J. Queisser, "Detailed Balance Limit of Efficiency of p-n Junction Solar Cells," Journal of Applied Physics, vol. 32, no. 3, pp. 510–519, Mar. 1961

[2] K. Ruhle, S. W. Glunz, and M. Kasemann, "Towards new design rules for indoor photovoltaic cells," in Photovoltaic Specialists Conference (PVSC), 2012 38th IEEE, 2012, pp. 002588–002591.

[3] Yasar D.: Energy Conversion, January 2012. Energy book (pp.229-303).

[4] F. Bordry, D. Aguglia,: Definition Of Power Converters, Published by CERN in the Proceedings of the CAS-CERN Accelerator School, Geneva, 2015, pp. 15-43.

[5] Forouzesh M., Siwakoti Y. P., A. Gorji S. A., Blaabjerg F., Lehman B. : Step-Up DC–DC Converters: A Comprehensive Review of Voltage-Boosting Techniques, Topologies, and Applications, IEEE TRANSACTIONS ON POWER ELECTRONICS, VOL. 32, NO. 12, DECEMBER 2017, pp. 9143

[6] Kumar P. M., Babu V. J., Subramanian A., Bandla A., Thakor N., Ramakrishna S. Wei H.: The Design of a Thermoelectric Generator and Its Medical Applications, Designs 2019, 3, 22, This research was funded by a 2016 ASTAR AME IRG grant, 26 April 2019

[7] B. Dimmler, R. Wächter : Manufacturing and application of CIS solar modules, Thin Solid Films**,** Volume 515, Issue 15, 31 May 2007, pp 5973-5978

[8] Snaith H. J.: Present status and future prospects of perovskite photovoltaics**,** Nature Materials**,** Vol. 17**,** pp 372–376 (2018).

[9] S. Savagatrup et all: Mechanical degradation and stability of organic solar cells: molecular and microstructural determinants**,** Sci. Energy Environ., 2015,8, pp 55-80

[10] Shawky A. et all: A Single Cell Integrated Photovoltaic Converter based on Buck-Boost Topology with RCC MPPT Control, In INTELEC 2013, 13-17 October 2013, Hamburg, pp 720-725, ISBN 978-3-8007-3500-6

[11] Znbill L., Bousek J.: Low Voltage Converter for Energy Harvesting, In 2nd IMAPS FLASH CONFERENCE, Brno: NOVPRESS, Brno 2016, pp 78-81. ISBN: ISBN 978-80-214-5419

[12] Yildiz F. Keith L. C.,: Low Power Energy Harvesting with a Thermoelectric Generator through an Air Conditioning Condenser, 121st ASEE Annual Conference & Exposition, June 15-18,2014, American Society for Engineering Education, 2014, pp. 10552.

[13] Gabriel C. Harikrishnan R., Jun Y., Jagadheswaran R., Wong W. R., Pui-In M., Rui P., Martins: Ambient RF energy harvesting system, Article in Analog Integrated Circuits and Signal Processing · December 2018

[14] Hegr O., Bousek J.; Reactive magnetron sputtering silicon nitride layer for passivation of crystalline silicon solar cells. 21st European Photovoltaic Solar Energy Conference, 4-8 September 2006.

[15] Sung-Eun K., Taewook K., Kwang-Il O., Mi J.P., Hyung-Il P., In Gi L., Jae-Jin L.: Energy Management Integrated Circuit for Multi-Source Energy Harvesters in WBAN Applications, Appl. Sci. 2018, 8, 1262, Daejeon 34129, Korea

[16] Cabiling A.P.: Ultra Low Voltage Energy Harvesting, Thesis, NPS Monterey, California, September 2013

[17] A. Herber, A. Hanisch, T. Gnoerrlich, D. Laqua, P. Husar: Design of power management in EH Devices, Biomedizinische Technik/Biomedical Engineering, September 2012, Technical University of Ilmenau, Department of Biomedical Engineering, Ilmenau, Germany, pp.4059

[18] Ferdous A.: MPPT Tracking Energy Harvesting System for Solar and Microbial Fuel Cell, POLITECNICO DI TORINO, Italy, April 2019

[19] Znbill L., Boušek J.: Packaging and installation of the organic photovoltaic cells, ElectroScope 2016, vol. 2016, no. 1, p. 3-5. ISSN:1802-4564.

[20] T. Kim, J.-H. Kim, T. Eui Kang, C. Lee1, H. Kang, M. Shin, C. Wang, B. Ma, U. Jeong, T.-S. Kim, B. J. Kim: Flexible, highly efficient all-polymer solar cells, Nature Communications, October 2015, pp. 1-7

[21] Harald Hoppe et al.: Organic solar cells: An overview, Journal of Materials Research, 2011, Volume 19, Issue 07, pp 1924-1945

[22] Bubnova O., Crispin X.: Towards polymer-based organic thermoelectric generators, Energy & Environmental Science, 2012, ISSN 1754-5692, Vol. 5, no 11, pp 9345-9362

[23] J. Damaschke: Design of a low-input-voltage converter for thermoelectric generator, IEEE Transactions on Industry Applications, vol. 33, no. 5,pp. 1203–1207, Sep./Oct. 1997

[24] Salerno D.: Frequently Asked Questions: Thermoelectric Energy Harvesting With LTC3108 & LTC3109, ANALOG DEVICES

[25] Znbill L., Boušek J. : Printed thermoelectric generators. ElectroScope - 201 7, vol. 2017, no. 2, p. 4-7. ISSN: 1802-4564.

[26] Sherif M. S. , Yasser S. A. , Ahmed A. D. and El-Sayed A. El.: Subthreshold MOSFET Transistor Amplifier Operation, Conference: Design and Test Workshop (IDT), 2009 4th International, November 2009

[27] R. Vaddi, S. Dasgupta and R. P. Agarwal: Device and Circuit Design Challenges in the Digital Subthreshold Region for Ultralow-Power Applications, VLSI Design, March 2009, Volume 2009, Article ID 283702, 14 pages

[28] M. Rakus, V. Stopjakova, D. Arbet: Design techniques for low-voltage analog integrated circuits, Journal of ELECTRICAL ENGINEERING, (2017), No4, 245–255,

[29] Apisak W., Phanumas K.: Analysis and Design of Sub-Threshold R-MOSFET Tunable Resistor, EICE Transactions on Electronics , No.1 JANUARY 2009, pp135-143

[30] D. Grgić, T. Ungan, M. Kostić, and L.M. Reindl, Ultra-low input voltage DC-DC converter for micro energy harvesting, PowerMeMs, 2009, pp. 265-268.

[31] I.G. Hill at al.: Charge-separation energy in films of π-conjugated organic molecules, Chemical Physics Letters 327, 2000, pp181–188

[32] L. Tzounis: Organic Thermoelectrics and Thermoelectric Generators (TEGs), In book: Advanced Thermoelectric Materials for Energy Harvesting Applications, Intech Open, September 2019, pp. 1-25.

[33] C. Wood: Materials for thermoelectric energy conversion, Phys. 51 (1988) 459-539. 580–583

[34] V. Stopjakova, M. Rakus, M. Kovac, D. Arbet, L. Nagy, M. Sovcik, M. Potocny: Ultra-Low Voltage Analog IC Design: Challenges, Methods and Examples, RADIOENGINEERING, VOL. 27, NO, Bratislava, Slovakia, APRIL 2018, pp 171-185.

[35] Thawatchai T., Apirak S. and Varakorn K.: Low-Voltage Bulk-Driven QFG-Regulated Self-Cascode Super MOS Transistor, IEEE, 2016, Thailand.

[36] Anuj D., Laxmi K.: A NEW LOW VOLTAGE P-MOS BULK DRIVEN CURRENT MIRROR CIRCUIT, International Journal of VLSI design & Communication Systems (VLSICS), August 2013, pp 41-53

[37] Trupti B. D., Pratik P. S.: Simulation and analysis of Bulk Driven Circuits for Low Power Applications, International Journal of Engineering and Technical Research (IJETR), February 2014, pp 164-167.

[38] M. Rakus, V. Stopjakova, D. Arbet: Analysis of BD MOS and DT MOS Current Mirrors in 130 nm CMOS Technology, ADVANCES IN ELECTRICAL AND ELECTRONIC ENGINEERING, June 2018, pp. 226-232.

[39] Z. Cao1, E. Koukharenko, R.N. Torah, J. Tudor and S.P. Beeby: Flexible screen printed thick film thermoelectric generator with reduced material resistivity, Journal of Physics: Conference Series 557 (2014) 01201 –55.

[40] Arijit R., Bipul C., Paul C. P., Swarup B., Kaushik R.: Computing With Subthreshold Leakage: Device/Circuit/Architecture Co-Design for Ultralow-Power Subthreshold Operation, IEEE TRANSACTIONS ON VERY LARGE SCALE INTEGRATION (VLSI) SYSTEMS, NOVEMBER 2005, pp. 1213.

[41] Mohammad A. S., Navid S., Martin O.: LLC Converters with Planar Transformers: Issues and Mitigation, Article in IEEE Transactions on Power Electronics, January 2016, pp. 31-21.

[42] D. T. Holmes, K. K. Sum: Flat Transformers for Low Voltage, High Current, High Frequency Power Converters, HFPC Power Conversion, Power Systems World, California, 1996, pp. 1-9.

[43] M. Madsen, A. Knott, M.A. E. Andersen: Low Power Very High Frequency Switch-Mode Power Supply With 50 V Input and 5 V Output, IEEE TRANSACTIONS ON POWER ELECTRONICS, DECEMBER 2014, pp. 6569-6580

[44] M. Pavlovsky, S. W. H. de Haan, J. A. Ferreira: Reaching High Power Density in Multikilowatt DC–DC Converters with Galvanic Isolation, IEEE TRANSACTIONS ON POWER ELECTRONICS, MARCH 2009, pp.603-612.

[45] Naichia Yeh, Pulin Yeh: Organic solar cells: Their developments and potentials Renewable and Sustainable Energy Reviews, Volume 21, May 2013, Pages 421–431

[46] Waldauf, M. Morana, P. Denk, P. Schilinsky, K. Coakley, S.A. Choulis, C.J. Brabec: Highly efficient inverted organic photovoltaics using solution based titanium oxide as electron selective contact, Appl Phys Lett, 89(2006) 233517/1–3

[47] F.C. Krebs: Air stable polymer photovoltaics based on a process free from vacuum steps and fullerenes, Solar Energy Mater Solar Cells, 92 (2008), pp. 715–726

[48] Christopher M. Proctor, Martijn Kuik, Thuc-Quyen Nguyen: Charge carrier recombination in organic solar cells, Progress in Polymer Science, Volume 38, Issue 12, December 2013, Pages 1941–1960

[49] J. Ehlich: Optimization of printing methods for the preparation of organic semiconductor layers. Brno: Brno University of Technology, Faculty of Chemistry, 2017. 60 p, Supervisor doc. Ing. Ota Salyk, CSc.

[50] L. Omasta: Printed biosensor based on organic electrochemical transistor, Brno University of Technology, The Faculty of Chemistry, 2018, 105 p, Supervisor doc. Ing. Ota Salyk, CSc.

[51] R. D. Middelbrook: Transformer less DC-to-DC Converters with Large Conversion Ratios, IEEE TRANSACTIONS ON POWER ELECTRONICS, OCTOBER I988, pp. 484-488

[52] Abdar A., Rizwan U., Zahid U.: DC-to-DC Converters for Low-Voltage High-Power Renewable Energy Systems, International Journal of Electrical, Computer, Energetic, Electronic and Communication Engineering, November 2015, pp.1411-1416.

[53] Jingbi You, Letian Dou, Ziruo Hong, Gang Li, Yang Yang: Recent trends in polymer tandem solar cells research, Progress in Polymer Science, Volume 38, Issue 12, December 2013, Pages 1909–1928

[54] Mojtaba F., Yam P. S., Saman A. G., Frede B., Brad L.: Step-Up DC–DC Converters: A Comprehensive Review of Voltage-Boosting Techniques, Topologies, and Applications, IEEE TRANSACTIONS ON POWER ELECTRONICS, DECEMBER 2017, pp.9143-9178.

[55] Bulucea C.A, Doru A. N., Nikos E. M., Daniel C. C.: Modelling of Electrical Transformers in Dynamic Regimes, Proceedings of the 9th WSEAS/IASME

International Conference on ELECTRIC POWER SYSTEMS, HIGH VOLTAGES, ELECTRIC MACHINES, January 2009

[56] Seyed A. M.: Electromagnetic Modelling of Power Transformers for Study and Mitigation of Effects of GICs, Stockholm, Sweden, 2015

[57] Micha K., Artur S.: Voltage transformer operation in connection with the power quality, Article in Przeglad Elektrotechniczny, November 2008

[58] A. Baggini.: Power Transformers – Introduction to measurement of losses, Horizon 2020 programe of the European Union, August 2016

[59] J. C. Olivares-Galván, P. S. Georgilakis, R. Ocon-Valdez: A Review of Transformer Losses, Article in Electric Power Components and Systems, August 2009, pp. 1046-1062

[60] H. M. Maheri, D. Vinnikov, A.Chub, V. Sidorov, E. Liivik: Impact of Transformer Turns Ratio on the Power Losses and Efficiency of the Wide Range Isolated Buck–Boost Converter for Photovoltaic Applications, Energies 2020, 28 October 2020, pp. 5645(1-21)

[61] E. Benedict, T. Collins, D. Gotham, S. Hoffman, D. Karipides, S. Pekarek, R. Ramabhadran: LOSSES IN ELECTRIC POWER SYSTEMS, Purdue University Purdue e-Pubs, December, 1992

[62] E.A. Anazia, E. S Ugochukwu, J. C. Onuegbu, Onyedikachi S.N: Design and Analysis of Losses in Power Transformer, American Journal of Electrical and Electronic Engineering, 2017, pp. 94-101

[63] M. Krasl, J. Jiřičková, R. Vlk: STRAY LOSSES IN TRANSFORMER TANK, KTE FACULTY OF ELECTRICAL ENGINEERING, Czech Republic, Cheb, September 7-9-2009

[64] Lenart K., Damijan M.: Stray losses in power transformer tank walls and construction parts, Conference: Electrical Machines (ICEM), October 2010.

[65] Arikan O., Kumru C.F., Kocatepe C.: Measurement of the Dielectric Performance of an Instrument Transformer at Different Voltage and Frequencies, Conference: High Voltage Engineering and Application (ICHVE), September 2001.

[66] Anders B., Göran E.: A model for magnetomechanical hysteresis and losses in magnetostrictive materials, Article in Journal of Applied Physics · May 1996, pp. 6476 – 6478.

[67] M. Prauzek, J. Konecny, M. Borova, K. Janosova, J. Hlavica, P. Musilek: Energy Harvesting Sources, Storage Devices and System Topologies for Environmental Wireless Sensor Networks: A Review, Sensors 2018,18 2446 27 July 2018,pp.1-22

[68] R. D. Fazio, D. Cafagna, G. Marcuccio, P. Visconti: Limitations and Characterization of Energy Storage Devices for Harvesting Applications, Energies 2020, 13, 783, February 2020, pp. 1-18.

[69] Saif A.: Storage System for Harvested Energy in IoT Sensors, Dawit Mengistu, 2018

[70] Sehwan K., Pai H. C.: Energy Harvesting with Supercapacitor-Based Energy Storage, In book: Smart Sensors and Systems Chapter: 4, Publisher: Springer, Cham, January 2015, pp.215-241

[71] P. Mars.: Coupling a supercapacitor with a small energy-harvesting source, Edn - Boston then Denver then Highlands Ranch Co, June 7, 2012, pp. 39-42

[72] Kwadwo M. D., Camila Z., Pawan K. K., Ram K. G.: Supercapacitor Energy Storage Device Using Biowastes: A Sustainable Approach to Green Energy, Sustainability 2019, 11, 414, 2019, pp. 1-22

[73] Lehtimäki S.: Printed Supercapacitors for Energy Harvesting Applications, Tampere University of Technology, Finland, 2017

[74] S. Abdul-Ganiyu, D. A Quansah, E. W. Ramde, R. Seidu, M. S. Adaramola: Investigation of Solar Photovoltaic-Thermal (PVT) and Solar Photovoltaic (PV) Performance: A Case Study in Ghana, Energies 2020,13, 2701, May2020, pp. 1-17

[75] K. Jäger, O. Isabella, A. H. M. Smets, R.A.C.M.M. van Swaaij, M. Zeman: Solar Energy Fundamentals, Technology, and Systems, Delft University of Technology, 2014

[76] G. M. Wilson, M. Al-Jassim, W. K. Metzger, S. W. Glunz, P. Verlinden, G. Xiong, L. M. Mansfield, B. J. Stanbery, K. Zhu, Y. Yan, J. J. Berry, A. J. Ptak, F. Dimroth, B. M. Kayes, A.C. Tamboli, R. Peibst, K. Catchpole, M. O. Reese, C. S. Klinga, P. Denholm, M. Morjaria, M. G. Deceglie, J. M. Freeman, M. A. Mikofski, D. C. Jordan, G. TamizhMani, D. B. Sulas-Kern: The 2020 photovoltaic technologies roadmap, Journal of Physics D: Applied Physics 53(49), 2020, pp. 1-47

[77] R. W. Miles, G. Zoppi, I. Forbes: Inorganic photovoltaic cells, Article in Materials Today, NOVEMBER 2007, pp. 20-27

[78] Meng T.: Inorganic Photovoltaic Solar Cells: Silicon and Beyond, The Electrochemical Society Interface, 2008, pp.30-35

[79] D. Li, P. Liao, X. Shai, W. Huang, S. Liu, H. Li, Y. Shen, M. Wang : Recent progress on stability issues of organic–inorganic hybrid lead perovskite-based solar cells, Issue 92, 2016, RSC Advances, 2016

[80] S. C. Agarwal: Role of Heterogeneities in Staebler-Wronski Effect, Philosophical Magazine , September 2012, pp.1-15.

[81] D. Han: Microscopic Mechanism of the Staebler-Wronski Effect in a-Si Films and High-Efficiency Solar Cells, National Renewable Energy Laboratory, University of North Carolina Chapel Hill, North Carolina, May 2005.

[82] M. Stuckelberger, M. Despeisse, G. Bugnon, J.W. Schüttauf, F.J. Haug, C. Ballif,: Comparison of amorphous silicon absorber materials: Light-induced

degradation and solar cell efficiency, Journal of Applied Physics, September 2013.

[83] N.H. Reic, W.G.J.H.M. van Sark, E.A. Alsema, R.W. Lof , R.E.I. Schropp, W.C. Sinke, W.C. Turkenburg: Crystalline silicon cell performance at low light intensities, Article in Solar Energy Materials and Solar Cells, September 2009

[84] R. E.I. Schropp, R. Carius, G. Beaucarne: Amorphous Silicon, Microcrystalline Silicon, and Thin-Film Polycrystalline Silicon Solar Cells, Article in MRS Bulletin, March 2007, pp. 219-224

[85] Sandra S.: Amorphous and microcrystalline silicon applied in very thin tandem solar cells, Forschungszentrum Jülich GmbH, 2011

[86] R. M. Geisthardt, M. Topic, R. S. James: Status and Potential of CdTe Solar-Cell Efficiency, Article in IEEE Journal of Photovoltaics, July 2015, pp. 1217-1221

[87] N. M. Ravindra, L. Lin: CIGS and Perovskite Solar Cells - An Overview, Emerging Materials Research, July 2020, pp. 1-19

[88] A. M. Bagawan, K. S. Ghiwari: Perovskite Solar Cells, International Journal of advance Research in Science and Engineering, October 2017, pp. 1345-1353.

[89] J. Stenberg: Perovskite solar cells, UMEA UNIVERSITY, Sweden, 2017

[90] N-G. Park: Perovskite solar cells: an emerging photovoltaic technology, Materials Today, August 2014, p. 8

[91] I. Arbouch, Y. Karzazi1, B. Hammouti, ORGANIC PHOTOVOLTAIC CELLS: OPERATING PRINCIPLES, RECENT DEVELOPMENTS AND CURRENT CHALLENGES – REVIEW, Physical and Chemical News, November 2014, pp. 73- 84

[92] J. C. Bernede: ORGANIC PHOTOVOLTAIC CELLS: HISTORY, PRINCIPLE AND TECHNIQUES, Chilean Chemical Society, September 2008, pp. 1549-1564

[93] M.-Su. Kim: Understanding Organic Photovoltaic Cells: Electrode, Nanostructure, Reliability, and Performance, University of Michigan, 2009

[94] S. Kim, M. Jahandar, J. Jeong, D. C. Lim: Recent Progress in Solar Cell Technology for Low-Light Indoor Applications, Current Alternative Energy, 2018, pp.1-16

[95] G. Apostolou, A. Reinders, M. Verwaal,: Comparison of the indoor performance of 12 commercial PV products by a simple model, Society of Chemical Industry and John Wiley & Sons Ltd, 2016, pp. 69-85

[96] A. Marti, J. L. Balenzategui, R. F. Reyna: Photon recycling and Shockley's diode equation, Journal of Applied Physics, October 1997, pp. 4067-4075

[97] D. Leitao, J. P. N. Torres, J. F. P. Fernandes : Spectral Irradiance Influence on Solar Cells Efficiency, Energies 2020, 13, 5017, 24 September 2020, pp.1-18

[98] J. Day, S. Senthilarasu, T. K. Mallick: Improving spectral modification for applications in 2 solar cells: Renewable Energy, March 2019, pp. 186-205

[99] A. L. Bris, J-F. Guillemoles: HOT CARRIER SOLAR CELL EFFICIENCY SIMULATION WITH CARRIER EXTRACTION THROUGH NON IDEAL SELECTIVE CONTACTS, Institut de Recherche et Développement sur l'Energie Photovoltaique, France, 2010, pp. 61-64

[100] A. Tharabsheh, M. Akmal, M. Ghazal: Series Connected Photovoltaic Cells-Modelling and Analysis, Sustainability, March 2017, pp. 1-9

[101] V.V. Tyagi, Nurul A. A. R., N.A. Rahim, Jeyraj A./L. S. : Progress in solar PV technology: Research and achievement, Renewable and Sustainable Energy Reviews, April 2013, pp. 443-461

[102] M. Imaamzai, M. Aghaei, Y. H. Md. Thayoob, M. Forouzanfar: A Review on Comparison between Traditional Silicon Solar Cells and Thin- Film CdTe Solar Cells, Proceedings National Graduate Conference 2012 (NatGrad2012), Universiti Tenaga Nasional, Putrajaya Campus, Nov 2012

[103] S. Shittu, G. Li, X. Zhao, X. Ma: Thermoelectric Generator Performance Enhancement by the Application of Pulsed Heat Power, International Conference of Fluid Flow, Heat and Mass Transfer (FFHMT'19), June 2019, Paper No. FFHMT 146

[104] M. A. Zoui, S. Bentouba, J. G. Stocholm, M. Bourouis: A Review on Thermoelectric Generators: Progress and Applications, Article in Energies 2020, 13, 3606, July 2020, pp. 1-32

[105] V. Agarwal, S.Jacinto, Y.Zhang: Thermoelectric Generator Powered Wireless Sensor Node Prototype for Nuclear Applications, Idaho National Laboratory, January 2018

[106] C. Xia, D. Zhang, W. Pedrycz, K. Fan, Y. Guo: Human Body Heat Based Thermoelectric Harvester with Ultra-Low Input Power Management System for Wireless Sensors Powering, Energies 2019, 12, 3942, October 2019, pp. 1-16

[107] D. Kandris, C. Nakas, D. Vomvas, G. Koulouras: Applications of Wireless Sensor Networks: An Up-to-Date Survey, Applied System Innovations, February 2020, pp. 1-24

[108] Uri L.: Thermoelectric Effect Peltier Seebeck and Thomson, 10.13140/RG.2.2.25436.13444, Guma science, March 2020, pp. 1-12

[109] D. Nemir, J. Beck: On the Significance of the Thermoelectric Figure of Merit Z, Journal of Electronic Materials, September 2010, pp. 1-6

[110] A. Hilaal, R. Seeram: A Review on the enhancement of Figure of Merit from Bulk to Nano Thermoelectric Materials, Nano Energy, March 2013, pp. 1-37

[111] H. S. Kima, W. Liua, G. Chenb, C.-W. Chua, Z. Rena: Relationship between thermoelectric figure of merit and energy conversion efficiency, PNAS, July 2015, pp. 8205-8210

[112] H.Wang, C. Yu: Organic Thermoelectrics: Materials Preparation, Performance Optimization and Device Integration, Joule 3, 53–80, January 16, 2019, pp. 53-80

[113] Y. Zhang, Y. J. Heo, M. Park, S. J. Park: Recent Advances in Organic Thermoelectric Materials: Principle Mechanisms and Emerging Carbon-Based Green Energy Materials, Polymers 2019, 11 (167), January 2019, pp 1-22

[114] A.I. Casian, I. I. Sanduleac: ORGANIC THERMOELECTRIC MATERIALS: NEW OPPORTUNITIES, Journal of Thermoelectricity, June 2013, pp.11-20

[115] E. Kanimba, Z. Tian: Modeling of a Thermoelectric Generator Device, Thermoelectrics for Power Generation - A Look at Trends in the Technology, December 2016, pp. 461-479

[116] L. Zhang, S. Lin, T. Hua, B. Huang, S. Liu, X. Tao: Fiber-Based Thermoelectric Generators: Materials, Device Structures, Fabrication, Characterization, and Applications, Article in Advanced Energy Materials, · September 2017, pp. 1700524(1-18)

[117] J. Chen, K. Li, C. Liu, M. Li, L. Jia, S. Jiang: Enhanced Efficiency of Thermoelectric Generator by Optimizing Mechanical and Electrical Structures, Energies 10 (1329), September 2017, pp. 1-15

[118] D. Zhou, S. Chu-ping: Study on thermoelectric material and thermoelectric generator, Journal of Chemical and Pharmaceutical Research, 2015, pp. 395-401

[119] Nader B., Glenn I. S.: Design of High Voltage Low Power Supply Device, Universal Journal of Electrical and Electronic Engineering, January 2015, pp. 6-12

[120] N. Jaziri, A. Boughamoura, J. Müller, B. Mezghani, F. Touns, M. Ismail: A comprehensive review of Thermoelectric Generators: Technologies and common applications, Article in Energy Reports, December 2020, pp. 264-287

[121] R. Freer, A. V. Powell: Realising the potential of thermoelectric technology: a Roadmap, Journal of Materials Chemistry C, 2020

[122] R. Søndergaard, M. Hösel, D. Angmo, T. T. Larsen-Olsen, F. C. Krebs: Roll-to-roll fabrication of polymer solar cells, Materials Today, February 2012, pp. 36-49

[123] B. Dou, J. B. Whitaker, K. Bruening, D. T. Moore, L. M. Wheeler, J. Ryter, N. J. Breslin, J. J. Berry, S. M. Garner, F. S. Barnes, S. E. Shaheen, C. J. Tassone, K. Zhu, M. F. A. M. van Hest: Roll-to-Roll Printing of Perovskite Solar Cells, ACS Energy Letters, September 2018, pp. 2558-2565

[124] A. Willfahrt : Screen Printing Technology for Energy Devices, Linköping Studies in Science and Technology, Sweden, February 2019

[125] P. H. Chien, H. G. Rong, C. H. Chi, L. S. Cheng, T. C. Wei, I. C. Tien: Effect of polymer binders in screen printing technique of silver pastes, Journal of Polymer Research, · October 2013, pp. 277(1-8)

[126] E. Gusarova, B. Viala , A. Plihon , B. Gusarov, L. Gimeno, O. Cugat,: FLEXIBLE SCREEN-PRINTED PIEZOELECTRIC P(VDF-TRFE) COPOLYMER

MICROGENERATORS FOR ENERGY HARVESTING, TRANSDUCERS 2015 - 2015 18th International Solid-State Sensors, Actuators and Microsystems Conference, June 2015, pp. 1901-1904

[127] R. Dhakal, Y. Jung, H. Park, G. Cho, N. Y. Kim: Screen-Printed Flexible Bandstop Filter on Polyethylene Terephthalate Substrate Based on Ag Nanoparticles, Article in Journal of Nanomaterials, October 2015, pp. 1-9

[128] C. Amruth, B. Luszczynska, B. G. R. Dupont, Z. Sieradzki,: Inkjet Printing Technique and Its Application in Organic Light Emitting Diodes, Display and Imaging, July 2017, pp. 339-358

[129] A. Teichler, J. Perelaer, U. S. Schubert: Inkjet printing of organic electronics – comparison of deposition techniques and state-of-the-art developments, Journal of Materials Chemistry C, 2013

[130] C. T. Chen: Inkjet Printing of Microcomponents: Theory, Design, Characteristics and Applications, In book: Features of Liquid Crystal Display Materials and Processes, November 2011, pp.43-60

[131] Gerard C., Marc P.Y. D.: Inkjet printing of conductive materials: a review, Article in Circuit World, November 2012, pp. 193-213

[132] ZNBILL, L.; BOUŠEK, J. Photovoltaic single cell energy harvesting. ElectroScope - 2018, vol. 2018, no. 1, p. 36-39. ISSN: 1802-4564

[133] J. Dearden: ELECTROLESS PLATING ITS APPLICATIONS IN RESISTOR TECHNOLOGY, Electrocomponent Science and Technology, 1976, pp. 103-111

[134] H. Zhang, J. Zou, N. Lin, B. Tang : REVIEW ON ELECTROLESS PLATING Ni-P COATINGS FOR IMPROVING SURFACE PERFORMANCE OF STEEL, Surface Review and Letters, August 2014, pp. 1430002(1-13)

[135] Sudagar J., Lian J., Sha W.: ELECTROLESS NICKEL, ALLOY, COMPOSITE AND NANO COATINGS - A CRITICAL REVIEW, Journal of Alloys and Compounds, 2013, pp. 1-92

[136] O. S. I. Fayomi1, I. G. Akande, A. A. Sode,: Corrosion Prevention of Metals via Electroless Nickel Coating: A review, International Conference on Engineering for Sustainable World, 2019, pp. 1-8

[137] Stefan C. L.: THIN FILM DEPOSITION & VACUUM TECHNOLOGY, Brigham Young University Idaho, April 2013

[138] E. Alfonso, J. Olaya, G. Cubillos: Thin Film Growth Through Sputtering Technique and Its Applications, In book: Crystallization - Science and Technology, Colombia, September 2012, pp. 398-432

[139] A. Jilani, M. Shaaban A.-w., A. H. Hammad,: Advance Deposition Techniques for Thin Film and Coating, in book: Modern Technologies for Creating the Thin-film Systems and Coatings, March 2017, pp. 137-149

[140] Angelo L. G., P. A. P. Nascente : D.C. Sputtering, In book: Encyclopedia of Tribology Publisher: Springer International Publishing AG, January 2013, pp.699-706

[141] D. Depla, S. Mahie, J. E. Greene: Sputter deposition processes, December 2010

[142] A. Baptista, F. Silva, J. Porteiro, J. Míguez, G. Pinto: Sputtering Physical Vapour Deposition (PVD) Coatings: A Critical Review on Process Improvement and Market Trend Demands, Coatings 2018, 402, November 2018, pp. 1-22

[143] L. LILJEHOLM: Reactive Sputter Deposition of Functional Thin Films, UPPSALA UNIVERSITET, 2012, pp. 9-52

[144] M. Taborelli,: Cleaning and surface properties, CERN, Geneva, Switzerland, pp. 321-340

[145] E. Brachmann, M. Seifert, S. Oswald, S. B. Menzel, G. Thomas: Evaluation of Surface Cleaning Procedures for CTGS Substrates for SAW Technology with XPS, Article in Materials, November 2017, pp. 1373(1-10)

[146] O. Chmela: DIFFERENT IMAGING TECHNIQUES FOR INVESTIGATION OF TREATMENT EFFECTS ON VARIOUS SUBSTRATE SURFACES, Conference STUDENT EEICT 2015, FEEC BUT, 2015. Pp. 351-355

[147] A. Uddin, M. O. Alam, Y. C. Chan, H. P. Chan: Plasma Cleaning of the Flex Substrate for Flip-Chip Bonding with Anisotropic Conductive Adhesive Film, Article in Journal of Electronic Materials, January 2003, pp. 1117-1124

[148] The ChemQuest Group): Surface Treatment, The Adhesive and Sealant Council, Inc, March 2009, pp. 1-9

[149] H. REYNES, C. BUTTAY, H. MOREL: Protruding Ceramic Substrates for High Voltage Packaging of Wide Bandgap Semiconductors, Conference: 2017 IEEE 5th Workshop on Wide Bandgap Power Devices and Applications (WiPDA), France, October 2017

[150] Ulrich K.: Dielectric-barrier Discharges: Their History, Discharge Physics, and Industrial Applications, Plasma Chemistry and Plasma Processing, · March 2003, pp. 1-46

[151] J. Li, C. Ma, S. Zhu, F. Yu, B. Dai, D. Yang: A Review of Recent Advances of Dielectric Barrier Discharge Plasma in Catalysis, Nanomaterials 2019, 9, 1428, October 2019, pp. 1-34

[152] J. Muck, R. Dobosz, R. Strzelecki: Dielectric Barrier Discharge Systems with HV Generators and Discharge Chambers for Surface Treatment and Decontamination of Organic Products, Energies, October 2020, pp. 5181(1-17)

[153] F. D. Nascimento, M. Machida, M. A. Canesqui, S. A. Moshkalev: Comparison Between Conventional and Transferred DBD Plasma Jets for Processing of PDMS Surfaces, IEEE TRANSACTIONS ON PLASMA SCIENCE, MARCH 2017, pp. 346-355

[154] F. D. Nascimento, M. Machida, K. G. Kostov, S. Moshkalev: Four-electrodes DBD plasma jet device with additional floating electrode, The European Physical Journal D, January 2020, pp. 1-7

[155] R. Brandenburg: Dielectric barrier discharges: progress on plasma sources and on the understanding of regimes and single filaments Plasma Sources Science and Technology, Greifswald, Germany, July 2018, pp. 1-29.

[156] M. Šimor, J. Ráhel, P. Vojtek, M. Černák: Atmospheric-pressure diffuse coplanar surface discharge for surface treatments, Article in Applied Physics Letters, Czech Republic, Brno, October 2002, pp. 2716-2718.

[157] P. Šrámková, A. Zahoranová, J, Kelar, Z. K.Tučeková, M. Stupavská, R. Krumpolec, J. Jurmanová, D. Kováčik, M. Černák,: Cold atmospheric pressure plasma: simple and efficient strategy for preparation of poly(2-oxazoline)- based coatings designed for biomedical applications, Scientific Reports, June 2020

[158] W.B. Chang, H. Fang, J. Liu, C.M. Evans, B. Russ, B.C. Popere, S.N. Patel, M.L. Chabinyc, R.A. Segalman, ACS Macro Lett. 5 (2016) 455–459: Electrochemical Effects in Thermoelectric Polymers, ACS Macro Lett. 2016, 5, 4, 455–459

[159] Robert F. Stout, Aditya S. Khair : Diffuse charge dynamics in ionic thermo-electrochemical systems. Physical Review E 2017***, 96*** (2)

[160] Y. J. Lin, W. S. Ni, J. Y. Lee : Effect of incorporation of ethylene glycol into PEDOT:PSS on electron phonon coupling and conductivity, Journal of Applied Physics 117, 215501 (2015)

[161] Yang, B., Portale, G. Ionic thermoelectric materials for waste heat harvesting. *Colloid Polym Sci* **299,** 465–479 (2021).

[162] D. B. Go, J. R. Haase, J. George, J. Mannhart, R. Wank[4], A. Nojeh, R. Nemanich : Thermionic Energy Conversion in the Twenty-first Century: Advances and Opportunities for Space and Terrestrial Applications, Front. Mech. Eng., 08 November 2017

[163] F. A. M. Koeck, R. J. Nemanich Advances in Thermionic Energy Conversion through Single-Crystal n-Type Diamond Front. Mech. Eng., 06 December 2017

[164] Z. Fan, J. Ouyang: Thermoelectric properties of PEDOT:PSS, Adv. Electron. Mater. 2019, 5, 1800769

[165] D. A. Mengistie, C.H. Chen, K. M. Boopathi, F. W. Pranoto, L. J. Li, C. W. Chu: Enhanced Thermoelectric Performance of PEDOT:PSS Flexible Bulky Papers by Treatment with Secondary Dopants, ACS Applied Materials & Interfaces 2015 ***7*** (1), 94-100

[166] I. T. Witting, T. C. Chasapis, F. Ricci, M. Peters, N. A. Heinz, G. Hautier, G. J. Snyder: The Thermoelectric Properties of Bismuth Telluride, Adv. Electron. Mater. 2019, 1800904

[167] L. Abadlia, F. Gasser, K. Khalouk, M. Mayoufi, J. G. Gasser : New experimental methodology, setup and LabView program for accurate absolute thermoelectric

power and electrical resistivity measurements between 25 and 1600 K: Application to pure copper, platinum, tungsten, and nickel at very high temperatures REVIEW OF SCIENTIFIC INSTRUMENTS 85, 095121 (2014)

[168] B. Mojrová: High Efficiency n-type Monocrystalline Silicon Solar Cells; doctoral thesis. Brno: Brno University of Technology, Faculty of Electrical Engineering and Communication, Department of Microelectronics, 2019. 108 p

[169] https://pdf1.alldatasheet.com/datasheet-pdf/view/444832/TI/BQ25504.html

[170] R. Deng, N. L. Chang, Z. Ouyang, C. M. Chong: A techno-economic review of silicon photovoltaic module, Renewable and Sustainable Energy Reviews Volume 109, July 2019, Pages 532-55

[171] D. Zhao, H. Wang, Z. U. Khan, J. C. Chen, R. Gabrielsson, M. P. Jonsson, M. Berggren and X. Crispin : Ionic thermoelectric supercapacitors, Energy Environ. Sci., 2016, 9, 1450-1457

[172] M. Pollak, L. Mateu, P. Spies : Step-up DC-DC-Converter with Coupled Inductors for low Input Voltages Proc. Power MEMS 2008 (Sendai, Japan, 9-12 Nov. 2008) pp 145-148

6 A P P E N D I X ES

A1 Efficiency of low power DC to DC converters

A2 Organic Photovoltaic Materials

A3 Photovoltaic Tandem Cells

A4 Organic Thermoelectric Materials

A5 Vacuum Thin Film deposition

A6 Dielectric Barrier Discharge

A7 Design of Transformer Windings

A8 Leakage Resistance of Photovoltaic cells

A9 Efficiency of Low Light Photovoltaic Converters

A10 Design of planar transformer

A11 PCB for DC to DC converters

A12 Thermoelectric generator

A13 Symbols and abbreviations

A1 Efficiency of low power DC to DC converters

A1.1 Power loss on rectifiers.

The voltage drop across the rectifier diodes is given by the built-in voltage and the series resistance of the diode. At low currents, the series resistance will not apply and the voltage required to open the diode will be relatively small. Due to the logarithmic dependence of the voltage on the current, each decrease of the forward current by an order corresponds to a voltage drop in the forward direction of approximately 0.1 V. The voltage on the silicon diode can then be less than 0.5 V in the forward direction. When using a Schottky diode, for the same reasons, a voltage in the forward direction in the range of 0.1 V to 0.2 V can be expected when processing such small currents.

A1.2 Resistance losses.

They are manifested mainly in the energy transmission circuit. These losses are proportional to the square of the current flowing through this circuit. To suppress these losses, it is necessary to ensure the smallest possible resistances of all elements in the power transmission circuit.

The series resistance of transformer winding

For a transformer, it is necessary to consider the series resistance of the primary and secondary windings. The series resistance of the respective winding is determined by the number of its turns and the cross-section of the conductor.

Because a core with a very small cross-section is sufficient to transmit a small power, the number of turns per 1 volt of processed voltage is large and it is necessary to consider a relatively large series resistance even at low operating voltage.

It does not make sense to use a significantly oversized transformer, because then capacitance and magnetization losses would increase. Due to the very small power processed, the transformer will be slightly oversized even when using a very small core.

The resistance of the transistor-switch ion the ON state R_{DSON}

Depending on the type of transistor used, R_{DSON} takes values from several tens of milliohms to tens of ohms. However, transistors with very small R_{DSON} must have a large channel area and thus also have large parasitic capacitances. The reduction of resistance losses is then redeemed by losses for charging and discharging parasitic capacitances. These losses increase linearly with frequency. For DC / DC converters with extremely low power currents, therefore, the transistors with a small channel area and with small parasitic capacitances are optimal.

Table AS1.1: Overview of available J-FET switches

TYPE	V_{DS}/V_{DG}	$V_{(BR)GSS}$	$V_{GS(off)}$		$r_{DS(on)}$	I_{DSS}	
			Min	Max		Min	Max
	[V]	[V]	[V]		[Ω]	[mA]	
BF245A	± 30	-30	-0.4	-2.2	–	2.0	6.5
BF245B	± 30	-30	-1.6	-3.8	–	6.0	15.0
BF245C	± 30	-30	-3.2	-7.8	–	12.0	25.0
BF545A	± 30	-30	-0.4	-2.2	–	2.0	6.5
BF545B	± 30	-30	-1.6	-3.8	–	6.0	15.0
BF545C	± 30	-30	-3.2	-7.8	–	12.0	25.0
BSR58	40	-40	-0.8	-4.0	60	8.0	80.0
MMBF4091	40	-40	-5.0	-10.0	30	30.0	–
MMBF4092	40	-40	-2.0	-7.0	50	15.0	–
MMBF4093	40	-40	-1.0	-5.0	80	8.0	–
MMBF4391	30	-30	-4.0	-10.0	30	50.0	150.0
MMBF4392	30	-30	-2.0	-5.0	60	25.0	75.0
MMBF4393	30	-30	-0.5	-3.0	100	5.0	30.0
J109/MMBFJ108	25	-25	-2.0/-3.0	-6.0/-10.0	12/8	40.0/80.0	–/–
J111/MMBFJ111	35	-35	-3.0	-10.0	30	20.0	–/–
J112/MMBFJ112	35	-35	-1.0	-5.0	50	5.0	–/–
J113/MMBFJ113	35	-35	-0.5	-3.0	100	2.0	–/–
2SK2394	15	-15	-0.3	-1.5	–	6.0	32.0
2SK35557	15	-15	-0.3	-1.5	–	10.0	32.0
2SK3666	30	-30	-0.18	-2.2	200	0.6	3.0
2SK545	40	-40	-1.20	4.0	–	0.055	0.095
2SK932	15	-15	-0.2	-1.4	–	7.3	24.0
CPH3910	25	-25	-0.6	-1.8	–	20.0	40.0
CPH6904	25	-25	-0.6	-1.8	–	20.0	40.0

An overview of the basic parameters of low-power J-FET switches is in table Tab A1.1. Of the available J-FET switches for use in a low-energy DC to DC converter, the J1xx series of transistors is best suited. Obviously, for a small R_{DSON} value, there must be a large I_{DSS} current and large threshold voltage associated with it.

A1.3 Power loss in inductors

Inductor losses are a combination of the power dissipated by the magnetization of the core and the ohmic losses in winding (copper loss). Core losses are ***no-load losses*** and they are function of applied voltage. In case of the transformer they occur even when there is no load current. Copper losses are ***load losses*** and they are a function of the winding currents. At full load coper losses can be as high as 90% of total loses.

Hysteresis loss

When the magnetic field alternates, a small amount of energy is lost due to hysteresis in the magnetic core. The level of hysteresis loss is affected by the core material. Hysteresis loss can be determinate using a semi-empirical equation:

$$P_H = K_H \cdot (B_m)^{1,6} \cdot f \cdot V \quad [W]$$

Where K_H is a proportionality constant which depends upon the quality of core material, f is operating frequency, B_{max} is peak value of the flux density, V is volume of the core.

Eddy Current Loss

When the magnetic flux is linked with a closed circuit the current flows through this circuit because the magnetic field creates here an induced voltage which acts as the electromotive force. The value of the current depends upon the induced voltage and the resistance of the circuit.

Since the inductor core is made of conducting material the change of magnetic flux causes electric currents which circulate in the core. These circulating currents are called Eddy Currents and they produce an ohmic power loss in the magnetic material of the core.

The eddy current loss is minimized by creating a barrier for circulating currents. This can be done by making the core with thin laminations or in case of ferrite core it is made by means of low conductivity of the core material. The equation of the eddy current loss is given as:

$$P_E = K_E \cdot (B_m)^2 \cdot f^2 \cdot V \quad [W]$$

Where, K_E is coefficient of eddy current for given material and core shape, B_m is maximum value of flux density, f is frequency and V is the volume of magnetic material.

Ohmic loss in winding

(copper loss) occurs due to ohmic resistance of the winding. In case of the transformer, the total ohmic losses are given with simple formula:

$$P_E = (I_1)^2 \cdot R_1 + (I_2)^2 \cdot R_2 \quad [\mathrm{W}]$$

Where I_1 and I_2 are the primary and the secondary current and R_1 and R_2 are the resistance of primary and secondary winding respectively. These losses vary according to the load as the square of the load current.

Stray losses

Stray losses are due to the presence of leakage field. The percentage of these losses are very small as compared to the core and copper losses so they mostly can be neglected. However, in case that a part of the leakage flux cause eddy currents within nearby conductive objects and this way is converted to heat, the stray losses can be considerable [63].

Dielectric loss

Dielectric loss occurs in the insulating material of the transformer winding. It is important in case of high voltage transformers and high frequency transformers [65].

Mechanical loss, magnetostriction

The flux in the core causes it to physically expand and contract slightly with the alternating magnetic field. It is significantly applied in case of ferrite cores working at low frequencies [66].

A1.4 Power losses in the control circuit of switching elements

Here, the same loss mechanisms apply as in the power transmission circuit. In standard devices, the operating currents of the control circuits are orders of magnitude smaller than the currents in the power transmission circuits. In this case, the power losses in the control circuits do not have much effect on the overall efficiency of the device. However, at extremely small power transmitted, the currents in the power transmission circuit and in the control circuits are comparable, and the losses in the control circuits contribute very significantly to the total losses.

A1.5 Internal resistance of the energy converter

To the above losses it is necessary to add the losses caused by the internal resistance of the power converter. The internal resistance of the power supply significantly affects the achievable efficiency of the entire converter. It is added to the series resistance of the entire device and determines the optimal conditions for achieving the highest efficiency.

Unlike a DC to DC converter, which can be optimized to a certain extent, the series resistance of a transducer is determined mainly by its technology.

In case of photovoltaic cells, in addition to the conductivity of the materials used, the series resistance of the entire structure is also affected by the quality of the contacts and the design of the collecting electrodes. Technological processes for their preparation influence each other and a compromise must be sought in optimization [168].

For thermoelectric cells, the series resistance is determined by the electrical conductivity of the materials from which the thermocouple is assembled. Because many thermocouples are connected in series in a thermoelectric generator, the total series resistance of the thermo-generator is a critical parameter.

When optimizing, it is necessary to find a suitable compromise between the electrical and thermal conductivity of the materials used, which must also have a large Seebeck coefficient. This issue is addressed in detail in Chapter 3.3.

A2 Organic Photovoltaic Materials

Each photovoltaic cell is in principle semiconductor diode that converts light into direct current. Depending on the Band Gap of the light-absorbing material photovoltaic cells can convert incident light energy into DC electricity. However, in case of organic photovoltaic cells this process is rather complicated because of electronic properties of organic semiconductors.

A2.1 Materials for photovoltaic cells.

Organic semiconductor are based on conjugated system where carbon atoms covalently bond with alternating single and double bonds. These hydrocarbons' electrons p_Z orbitals delocalize and form a delocalized bonding π orbital with a π* antibonding orbital.

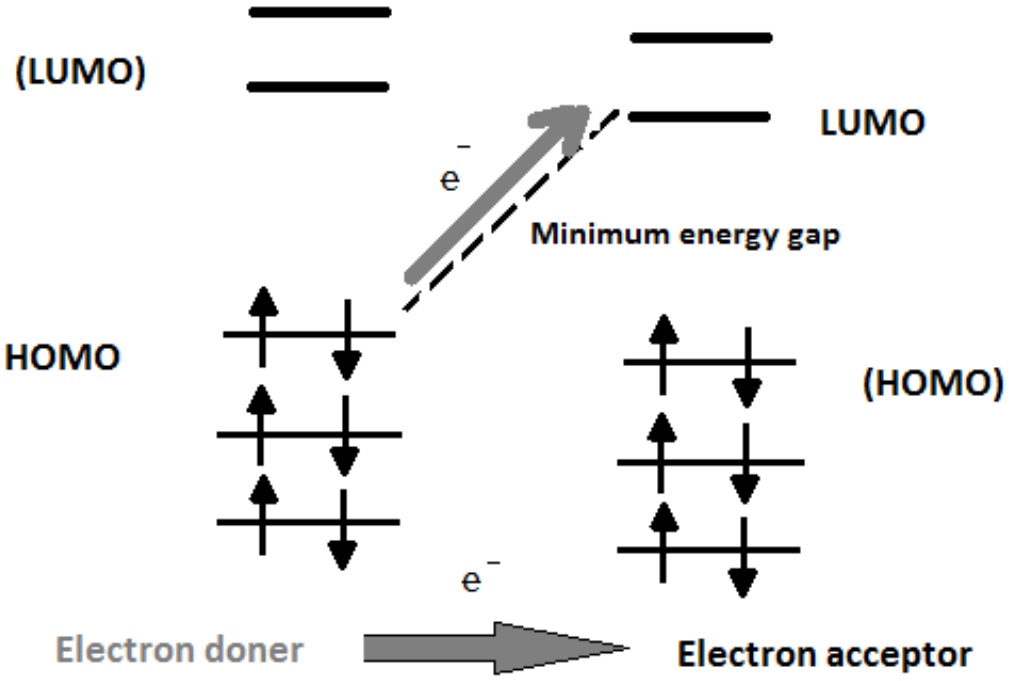

Fig. A2.1: Schematic HOMO and LUMO levels [4].

The electronic structure of organic semiconductor is depicted in figure Fig. A2.1. The delocalized π orbital is the highest occupied molecular orbital (HOMO), and the π* orbital is the lowest unoccupied molecular orbital (LUMO). Consequently, the HOMO orbital takes the role of the valance band while the LUMO orbitals serves as the conduction band.

The energy separation between the HOMO and LUMO energy levels is considered the band gap of organic electronic materials and is typically in the range of 1-4 eV. Examples of molecular structures of some organic semiconductors is given on figure Fig. A2.2

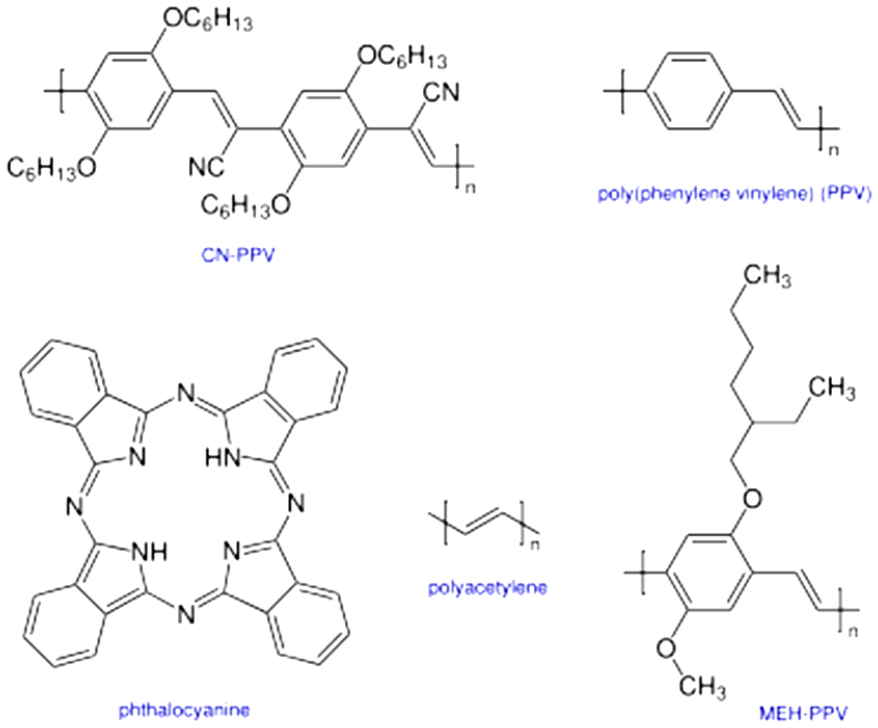

Fig. A2.2: Organic photovoltaic materials, examples of molecular structure [2,11].

The conversion process starts by absorbing the light and consequent creation of the electron-hole pair called exciton. In next step excitons diffuse to donor/acceptor interface [99]. Different work function of materials on donor/acceptor interface creates the electric field which helps to split the excitons into isolated electrons and holes. In the last step the carriers move to the electrodes [48, 9].

For a good function of a photovoltaic cell, it is necessary to ensure that the radiation is absorbed in a layer of organic semiconductor whose width of the band gap corresponds to the energy of the processed radiation. This layer is called the absorber.

A variety of organic materials can be used as the absorber. Due to its significantly enhanced light-harvesting and improved hole-transporting properties, PTB7-Th has boosted the PCE of PSCs to the levels that exceed 10% in single-junction cells with PC71BM as acceptor [27].

Moreover, PTB7-Th have been widely used as the standard donor material in non-fullerene solar cells and the best efficiency over 12% has been achieved [28]. These

results demonstrate high potential of PTB7-Th donor material for the large-area PSC application.

However, previous results showed that the PCE of the PTB7-Th:PC71BM based devices with thicker BHJ film was decreased due to the dramatic decrease of FF although the JSC was increased [29]. Therefore, it is necessary to introduce the PTB7-Th into parallel tandem cells to further improve its performance as well as realize high-efficiency.

The thickness of the absorber is thus another parameter of the organic photovoltaic cell that needs to be optimized. The large thickness is suitable for capturing all radiation that falls on the photovoltaic cell. However, the cell will be less efficient because it will have a large series resistance.

One of the ways to meet these conflicting requirements is the structure of a tandem photovoltaic cell where the cells with an optimally set absorber thickness are connected in parallel. This arrangement is described in detail in the following appendix A3.

A3 Photovoltaic Tandem Cells

Photovoltaic tandem cells give very high efficiencies because they incorporate more materials which are active from different light wavelengths. The efficiency can exceed the 40% value in some cases. However, the implementation of series connected tandem cells is not without problems.

In series connection of the cells there is always a boundary between P-type and N-type layers of different cells. Consequently, a voltage of opposite direction to the main voltage cell can arise on this boundary. To avoid that an additional layer must be inserted resulting in the tunnel diode which split the respective cells. This diode allows the current in reverse direction to their PN junction with maintaining very low voltage losses.

However, to allow the penetration of light without reflection the dielectric constant of inserted layers must be close to those of the surroundings materials. Also, their lattice constant must be in concordance with their neighbors. Further, their band gap must be large enough to not produce light absorptions.

This problem can be solved by parallel connection of respective photovoltaic cells through a transparent conducting interlayer that acts as a common electrode to the two sub-cells.

A3.1 Different materials of light absorber

Figure Fig.A3.1 a) shows the equivalent circuit and the structure of a three materials series connected solar cell.

Parallel connected tandem cells, as indicated in figure Fig.A.3.1 b) have a different number of PN junctions for each material. Instead of matching the current in this structure each part of parallel connection thus provides the same voltage.

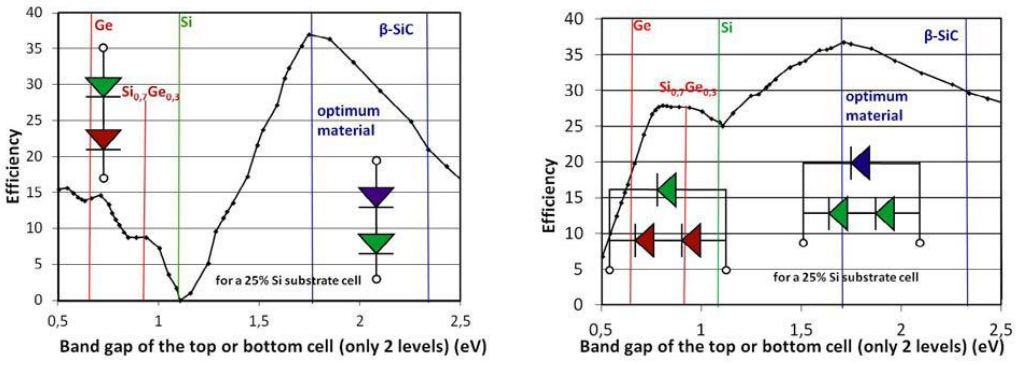

Fig. A3.1: Photovoltaic tandem cells with different absorber material. **a)** Combination of three materials in series connection. **b)** Different number of PN junctions to match the voltage in parallel connection.

This structure could work with two or three junction levels. If different cells are interconnected in parallel a greater number of the lower band gap cells would be needed in order to equalize the operating voltage of all the structure.

Considering that the voltage of a PN junction depends as the logarithmic of the current these structures are less sensitive to irradiation level, solar spectrum and device degradation than traditional series connected devices. Also, even in case of using materials with band-gap values far from the optimum values for a given light spectrum the limitation from the different operating voltages is less restrictive than the current limitation of traditional devices, giving to gains in efficiency for a wide range of band-gap values.

A3.2 The same materials of light absorber

In case of low dielectric constants of used materials, the resulting photovoltaic cells have poor absorption characteristic. Improvement of the device efficiency is possible by enhancement of light absorption increasing the active layer thickness. However, in case of thick absorbers layer the low charge carrier mobility will significantly increase the internal resistance and decrease the charge collection efficiency. Moreover, large distance that the generated carriers travel from the generation site to the collecting electrodes significantly increases the probability of recombination.

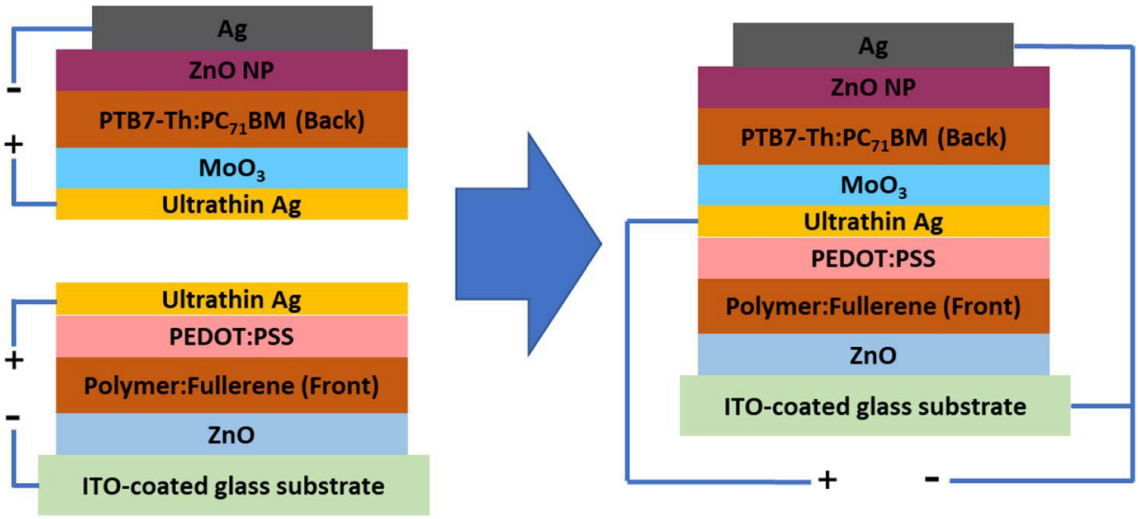

Fig. A3.2: Example of the structure of photovoltaic tandem cells with similar open circuit voltage.

Therefore, optimal thickness of the photoactive layer for best performance of thin layer photovoltaic devices is usually not much more than about 100 nm to avoid charge recombination. To extend the optical path of incident light and increase the light

absorption one of possible light-trapping strategies is the multi-junction stack architecture. The basic arrangement is shown in Fig.A3.2.

If two sub-cells with similar open-circuit voltage, V_{OC} are used the circuit current J_{SC} of the tandem cell is the summation of individual currents of each sub-cell. Obviously, using a parallel-connected tandem (PCT) structure needs matching the V_{OC} of each sub-cell instead of matching the currents in case of series connection. For materials with similar band-gap this is automatically satisfied.

Since the two sub-cells work individually in parallel-connected device, it is more convenient to optimize and characterize the two sub-cells independently. Moreover, because of the three-terminal structure instead of two-terminal structure for series connection, parallel tandem cells can still function even if one of the cells fails.

It has been demonstrated that the optimum bandgap of donor material used in the sub-cells for homo-tandem solar cell would be between 1.2 and 1.6 eV to achieve high efficiency.

It was found the long-wavelength absorption in the top-illuminated ITO-free back cell was significantly enhanced due to the resonant microcavity effect, leading to an efficient utilization of the incident light and increased photocurrent.

A3 References

[A3.1] S. Sista, Z. Hong, M.-H. Park, Z. Xu, Y. Yang, High-efficiency polymer tandem solar cells with three-terminal structure. Adv Mater **22**, 77 (2010)

[A3.2]. F. Guo, P. Kubis, N. Li, T. Przybilla, G. Matt, T. Stubhan, T. Ameri, B. Butz, E. Spiecker, K. Forberich, C.J. Brabec, Solutionprocessed parallel tandem polymer solar cells using silver nanowires as intermediate electrode. ACS Nano **8**, 12632–12640 (2014)

[A3.3] L. Zuo, C.-C. Chueh, Y.-X. Xu, K.-S. Chen, Y. Zang, C.-Z. Li, H. Chen, A.K.Y. Jen, Microcavity-enhanced light-trapping for highly efficient organic parallel tandem solar cells. Adv Mater **26**, 6778–6784 (2014)

[A3.4]. L. Zuo, J. Yu, X. Shi, F. Lin, W. Tang, A.K.Y. Jen, High-efficiency nonfullerene organic solar cells with a parallel tandem configuration. Adv Mater **29**, 1702547 (2017)

A4 Organic Thermoelectric Materials

The majority of organic thermoelectric materials are based on conductivity polymers, including conjugated polymers and certain coordination polymers. These materials may be listed as follows:

1) Highly conducting polymers. In this case, thermoelectric properties of the polymers are strongly affected by the synthesis and/or processing conditions. This efficient approach is the most adopted.

2) Materials prepared by solution-process developed in the past two decades for organic electronics, whose thermoelectric properties are optimized through doping and blending.

3) New molecular structures are prepared through derivation and novel design of building blocks appropriate for thermoelectric purposes. This is an elegant demonstration of chemical versatility of organic electric materials

A4.1 Conductive polymers

Conductive polymers are of great importance. Their conductivity could be changed in wide range when changing the structure of polymer chains.

Conjugated conducting polymers constitute a special class of organic materials whose ability to conduct electrical charge originates uniquely from π–conjugation. In regular saturated polymers, that are practically insulators, all the available electrons are bound in strong covalent bonds and are characterized by sp^3 hybridization.

In contrast to this situation, in conjugated polymers planer $\boldsymbol{\sigma}$-bond arises from hybridization of one ***s*** and two $\boldsymbol{\sigma}$ orbitals.

There is a region where **p**-orbitals overlap, bridging the adjacent single bonds and creating a π collective orbital in which **p**-electrons do not belong to one single bond, but rather delocalized over a group of atoms.
Depending on the ground state of conjugated polymer, different excited states can occur:

A polymer whose ground state energy remains unaffected when interchanging single and double bonds is referred to as degenerate ground system

A phase link in a single-double bond sequence in trans-polyacetylene made of odd number of carbon atoms resulting in a formation of an in-band defect in a form of an unpaired electron called a neutral soliton. In doped trans-polyacetylene positive or negative spineless solitons can be created.

Most of the conjugated polymers have non-degenerate ground state, which impedes the soliton formation. It is suggested that in these polymers polarons and bipolarons are created upon doping.

The oxidation (an electron removal) of the polymer leads to a formation of radical cation. Its presence causes an attenuation of neighboring bond alteration amplitudes and a half-filled electronic level above the valence band along with a new anti-bonding level below the bottom of the conduction band results.

Polaron is a single charge excitation that can be either positive as discussed above or negative in case if an electron is added to a polymer chain. A polarinic distortion can spread over three to four monomers depending on polymer chemical structure. A removal /addition of the electron from a polaron produces a bipolaron, a radical ion pair associated with a strong local lattice distortion.

A4.2 Doping of conductive polymers

Chemical doping is method that involves an exposure of polymer to solution or vapor of the dopant. A suitable dopant (donor or acceptor) used in this process should have a proper redox potential and the polymer's ionization potential (electron affinity) shall be such as to facilitate the doping process.
Throughout the exposure chemical dopants can physically penetrate into or move out of the polymer putting a strain on the polymer film, which can cause its swelling, shrinking or other morphology change. Increase in charge- carriers concentration manifests in a tremendous change in electrical conductivity that can be nearly metallic in some highly ordered polymers.

In electrochemical doping an electrolyte is used between a conducting polymer and the electrode that supplies the charge to the polymer while ions from the electrolyte diffuse in and out to the maintain polymers' charge neutrality.
In case of n-doping the polymer is reduced and the electrolyte cations are introduced into the polymer as counter ions.
Upon p-doping the polymer is oxidized and the anions penetrate into the polymer film as charge balancing ions.
This method provides precise control of the doping level, which is set by the applied potential between the electrode and the polymer film.
Almost any conjugated polymer can be electrochemically doped but the stability of the obtained samples strongly depends on the applied voltage.

Compared to the chemical doping the electrochemical doping procedure is technologically more complicated to perform as it necessitates an electrolyte and counter electrode.

A4.3 PEDOT:PSS

Promising candidates for electrodes are conducting polymers, among which great attention is given to PEDOT or poly (3, 4-ethylenedioxythiophene), which was developed in 1980s at Bayer AG research laboratories in Germany. Its backbone is shown on the figure Fig.A4.1.

PEDOT has high conductivity (~300 S/cm), good stability on oxidized state and transparency. But it has a large disadvantage which is poor solubility.

PEDOT low solubility problem was solved with further research by mixing it with water-soluble poly (styrene sulfonate) (PPS). The resulting combination of PEDOT:PSS is water-soluble compound system with good film forming properties, high conductivity (~10s/cm), high visible light transmissivity, and excellent stability.

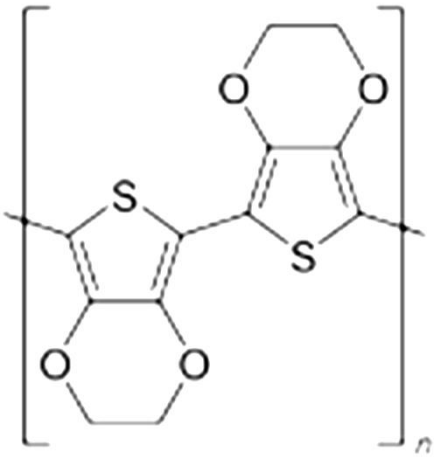

Fig. A4.1: PEDOT - basic molecular structure [164].

The disadvantage of this process is the high acidity of the resulting compound system. This is caused by hydrogen ions that are easily released from the PSS. For clarity, the structure of the PSS is shown in Fig. A4.2.

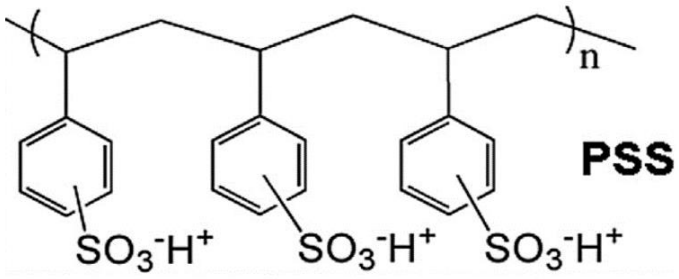

Fig. A4.2: PSS causes the acidity of the PEDOT:PSS compound [164].

Thanks to combination of good conductive properties and transparency, PEDOT:PSS is widely used in different type of organic electronic devices.

Due to its high electrical conductivity and low thermal conductivity, PEDOT:PSS has suitable properties for use in organic thermocouples. Moreover, films of PEDOT:PSS can be heated in air at 100^0C for over 1000 hours with only a minimal change in conductivity.

Therefore, the PEDOT:PSS compound is very suitable for applications in TEGS its use for this purpose has already been described in the literature.

A5 Vacuum Thin Film deposition

A5.1 Thin film deposition

Thin layers are layers with a thickness ranging from a few nanometers to several micrometers. Thin-film deposition technologies are either purely physical, such as evaporative technology methods, or purely chemical, such as gas-and liquid-phase chemical processes.

A considerable number of processes that are based on glow discharges and reactive sputtering combine both physical and chemical reactions; these overlapping processes can be categorized as physical-chemical methods.

There will be briefly described only two most common technologies applicable for thin film deposition in this work – evaporative technology and sputtering technology.

A5.2 Thermal evaporation

Thermal evaporation or vacuum evaporation is still used in the laboratory and some industry processes despite that it is one of the oldest techniques used for depositing thin films. The biggest advantage is a very simple deposition apparatus very simple deposition process.

A vapor is generated by boiling or subliming a source material. The vapor is transported from the vapor source. Subsequently it impinges on all surfaces that are in direct line of sight from the vapor source. At this point, the vaporized particles lose energy and condense.

There are many ways to ensure the evaporation of materials, so there are also many evaporation sources including resistance-heated filaments, electron beams, crucibles heated by conduction, radiation, or RF induction, arcs, exploding wires, and lasers.

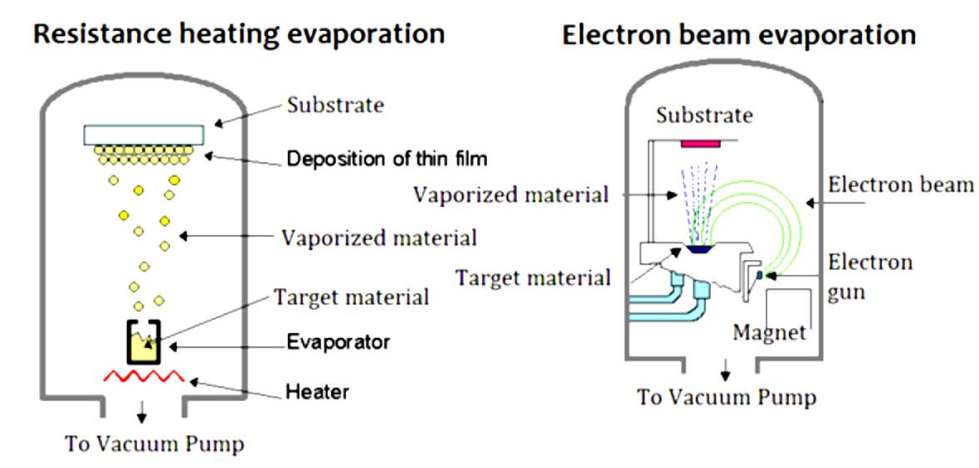

Fig. A5.1: Evaporative equipment: Resistance heating / Electron gun [139].

The arrangement of mostly used Resistance heating and Electron gun heating are in figure Fig.A5.1. In case of electron heating, the electron beam is deflected by magnetic field to prevent the collisions of beam electrons with the evaporated particles.

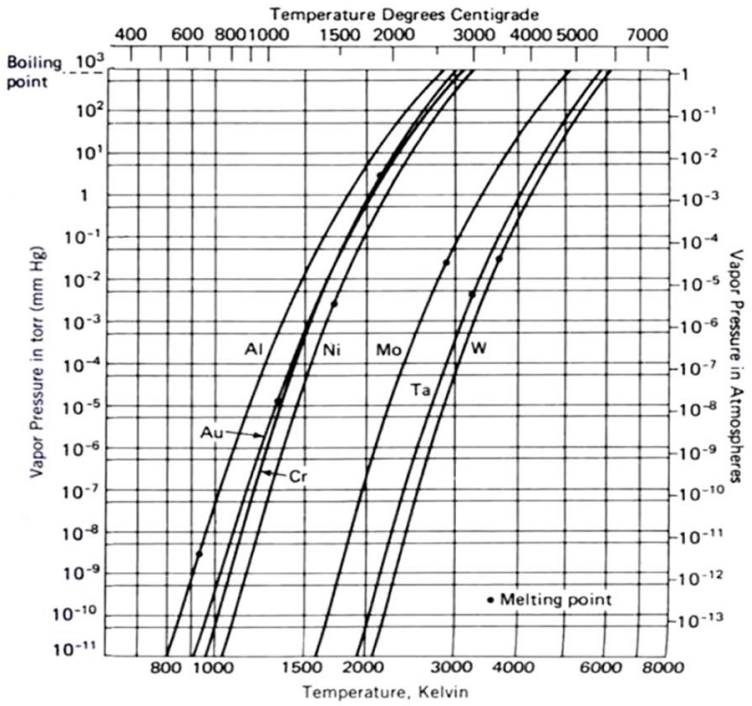

Fig. A5.2: Dependence of saturated vapor pressure on temperature for metals [137].

The dependence of the saturated vapor pressure on temperature can be described by August equation, which gives a linear relation between the logarithm of the pressure and the reciprocal temperature:

$\log p = A - (B/\mathrm{T})$,

where A and B are component-specific constants.

However, this equation does not respect the temperature dependency of heat of vaporization and the results may differ from the measured value. Example of measured saturated pressure dependence on temperature for different metals is in figure Fig.A5.2.

In principle the coating process is very simple but in few cases it could be very complicated and give different results using the same material and basic process parameters. Therefore, there is a need for very good knowledge in vacuum physics including kinetic theory of gases and in a special knowledge in material science concerning surface mobility, and condensation phenomena to ensure the desired layer quality and reproducible results.

A5.3 Sputtering

The sputtering process is based on particle to particle collisions involving an elastic transfer of momentum, which causes the releasing of the surface atoms of the target and consequently can be utilized to deposit a thin film of target material on the substrate.

In this technique, ions are accelerated toward a target by utilizing electric field. These ions are usually originated by exciting a neutral gas by electrical discharge. In special cases the ions are produced in ion gun and are accelerated to the target at precisely given energy.

As the ions bombard the target surface, they dislodge the target atoms. The forceful collision of ions onto target thus ejects target atoms into the space. Ejected atoms then travel some distance until they reach the substrate and start condense into a film. The individual parts of the sputtering process are depicted in figure Fig.A5.3.

To prevent the collision of the sputtered particles with the gas the sputtering process is possible only in low pressure gas. A negative voltage is applied to the target (cathode) and the substrate is attached to the ground or to the insulated electrode which may be biased with DC or Radio-Frequency (RF) voltage.

By sufficiently high voltage between the electrodes there is an electrical discharge which produces the plasma containing the ions of sputtering gas and electrons. This type of plasma is called as a glow discharge due to the light emitted.

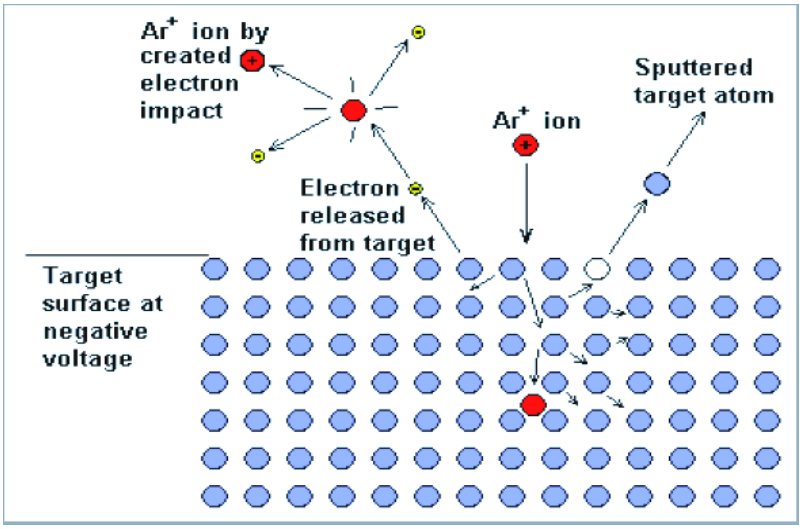

Fig. A5.3: Individual parts of the sputtering process [140].

The arrangement of the whole system is shown in fig A5.4. In discharge plasma Argon ions are accelerated to the target. Their collision with the target ejects target atoms, which

travel to the substrate and after a short period of migration they settle there and shape the film on the substrate surface.

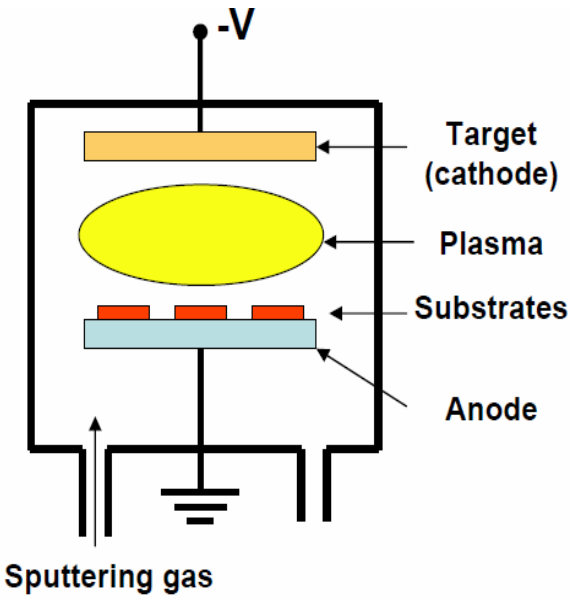

Fig. A5.4: Arrangement of sputtering equipment [141].

Electrons originated in process of Argon ionization are accelerated to the anode. Again, they may collide with additional Argon atoms, creating more ions and free electrons and this process can continue in so-called avalanche ionization.

The working pressure is between 1 Pa and 10^{-2} Pa. By pressure higher than about 1 Pa the mean free path of particles in the gas is less than 1 cm. Consequently, the particles collide frequently in the space between the target and the substrate thus preventing the effective transfer of target particles to the substrate. By pressure lower than about 10^{-2}Pa the breakdown voltage of the gas is too high and there is not possible to maintain discharge between electrodes.

The sharp grow of the breakdown voltage by low pressure is described by Paschen´s law. Paschen studied the breakdown voltage of various gases between parallel metal plates where both gas pressure and gap distance were varied. The voltage necessary to arc across the gap decreased as the pressure was reduced and then increased gradually, exceeding its original value.

He also found that at normal pressure, the voltage needed to cause an arc reduces as the gap size was reduced but only to a certain point. As the gap was reduced further, the breakdown voltage began to rise and exceeded its original value.

It was concluded that for given gas, the breakdown voltage is function of product of the pressure and gap length and can be described by the equation [140]:

$$V_{br} = \frac{a.p.d}{ln(p.d) + b}$$

Where V_{br} is the breakdown voltage, p is the pressure, and d is the gap distance.

The constants (a) and (b) depend upon the composition of the gas.

The graph of this equation called the Paschen curve is given in the figure Fig.A5.5.

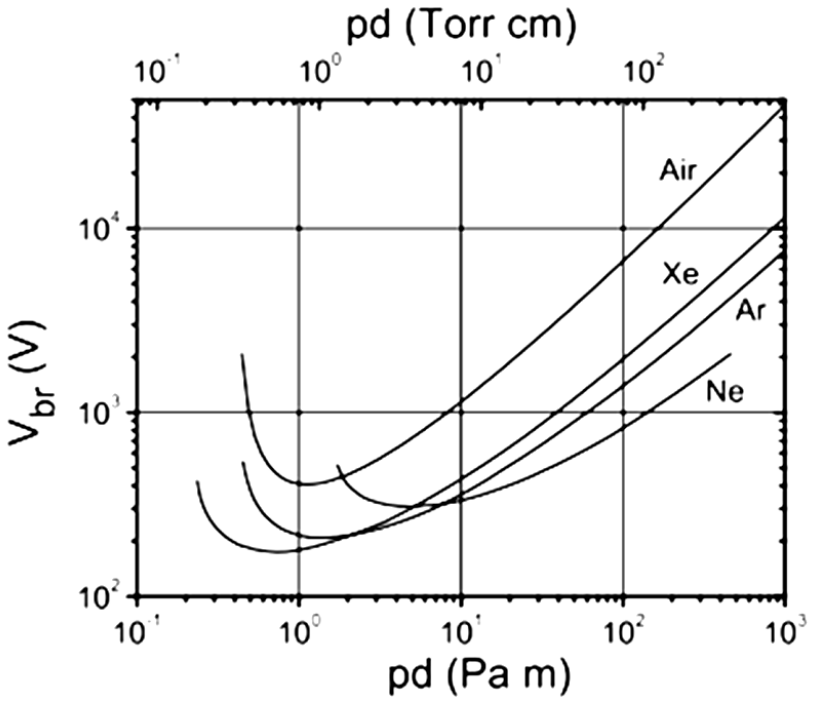

Fig. A5.5: Paschen curves: Breakdown voltage V_{br} is a function of $p.d$ [140].

By distance of electrodes between 1 cm and 10 cm (which is in most cases) the best conditions for ignition of the discharge are by pressure approximately 1 Pa. Grow of the breakdown voltage is very sharp by low pressure.

To maintain the gas discharge in the pressure beneath the 10^{-1} Pa range there is a need to enlarge the distance which the electron must travel in the electrical field. In magnetron sputtering system this is done by magnetic field. There is the Lorenz force acting to an electron moving in a magnetic field.

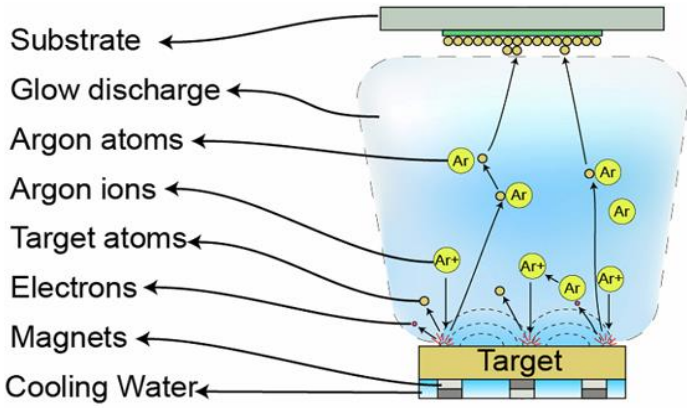

Fig. A5.6 : Basic components of a magnetron sputtering system. Ionized Argon bombards a target, releasing atoms which form layers on a substrate. Electrons and Argon ions form a plasma, which is located near the target due to magnetic field, resulting on greater efficiency and quality of deposited layers [142].

The electron path curves under Lorenz's force and under optimum conditions the electrons move along a spiral path and their path is thus substantially extended. Magnetron sputtering then gives a higher deposition rate at lower pressure. The magnetron sputtering system is very efficient and the energy density could be up to 50 W/cm^2. Target is therefore always water cooled. The basic scheme of magnetron sputtering system is on the Fig.A5.6.

Advantages and limitations of Sputtering

The greatest advantage of sputtering technology is the high energy of the particles that strike the substrate and consequently very good adhesion and quality of the sputtered layers.

The disadvantage is relatively low sputtering rate, which for most materials is in the order of tens of nanometers per minute. To get reasonable deposition rate, a sputtering chamber must operate at relatively high pressure. These high pressure means that there is a high concentration of gas particles. Also, at high pressure there is a lot of interaction between gas molecules and chamber walls. This all can degrade film quality. Using bias sputtering, that means small negative bias to substrate reduces, could suppress the contamination to substrate to an acceptable level.

A6 Dielectric Barrier Discharge

A6.1 Plasma Surface Cleaning and Activation

To increase adhesion the surface of the samples needs to be cleaned and plasma activated prior to printing. Plasma activation disrupts the bonds in the molecules that are on the surface of the film. These molecules are then chemically active and tend to bind to the printed material. This process results in a very substantial increase in adhesion. The advantage of using plasma is that the whole process takes place at ambient temperature. The energy required to break the surface bonds is supplied primarily by electrons and excited particles from the plasma.

The surface activation device uses the Dielectric Barrier Discharge (DBD). It is a discharge that occurs at atmospheric pressure. The dielectric barrier discharge plasma is non-isothermal. The electrons here have the energy in the order of electron-volts, but the gas atoms and ions that are produced during the gas ionization have a temperature corresponding to the ambient temperature. Electron energy is sufficient to initiate chemical reactions, but the activated surface is not thermally loaded. Depending on the gas composition, there may also be excited particles in the plasma that can transfer the energy upon return to the ground state. This process also takes place at a temperature close to ambient temperature.

A6.2 Dielectric barrier discharge.

Dielectric-barrier discharge (DBD) is the electrical discharge between two electrodes separated by an insulating dielectric barrier. Originally called silent discharge and is also known as ozone production discharge or partial discharge.

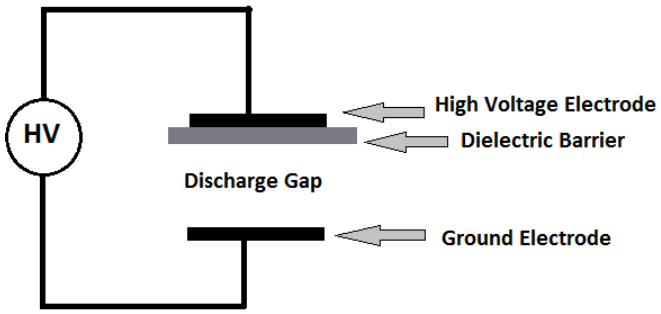

Fig. A6.1:: Arrangement of a DBD electrode system [150].

The schematic diagram in the figure Fig. A6.1 shows a typical arrangement of a DBD electrode system. One of the two electrodes is here covered with a dielectric barrier material. In another variation, both electrodes may be covered by the dielectric, or the dielectric may only be inserted between the electrodes.

The discharge may ignite at any point between the electrodes. The electrons produced by ionization move towards the electrode with positive polarity and gain energy in the electric field between the electrodes. During collisions with gas particles ionization occurs and other electrons are formed which, when moving in the electric field between the electrodes, cause further ionization. This creates a micro discharge that is visible to the naked eye.

While the electrons move towards the positive electrode, the ions formed in the micro-discharge move to the negative electrode. At that point in surface of dielectric, the dielectric gradually charges. After electron impact, the surface of the dielectric is negatively charged. After the ion impact, the surface of the dielectric is positively charged. This creates an electric field that counteracts the external electric field and stops the discharge.

If the voltage is further increased, a micro-discharge occurs at that other point. This gradually charges the entire surface of the dielectric and the discharge stops. Therefore, to continue the discharge, it is necessary to change the voltage polarity between the electrodes. The dielectric barrier discharge must therefore be supplied with AC voltage. The frequency can range from several Hz up to several hundreds of MHz. The voltage is usually sinusoidal but in principle may have any shape.

A6.3 Types of DBD

Depending on the geometry, DBD can be generated in a volume (Volume Dielectric Barrier Discharge, VDBD) or on a surface (Surface Dielectric Barrier Discharge, SDBD).

VDBD plasma is generated between two electrodes, for example between two parallel plates with a dielectric in between.

In case of SDBD, the microdischarges are generated on the surface of a dielectric, which results in a more homogeneous plasma than can be achieved using the VDBD configuration.

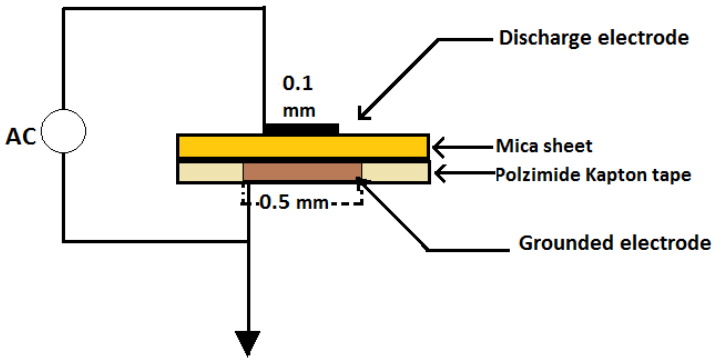

Fig. A6.2: Arrangement of a Surface Dielectric Barrier Discharge, (SDBD) electrode system [151].

As SDBD microdischarges are limited to the surface, their density is higher compared to the VDBD. The plasma is generated on top of the surface of an SDBD plate. Arrangement of a Surface Dielectric Barrier Discharge is shown in the figure Fig. A6.2.

A variant of the SDBD technology is a surface discharge with coplanar electrode arrangement. The electric field above the dielectric surface is in this case created by means of symmetrically placed electrodes.

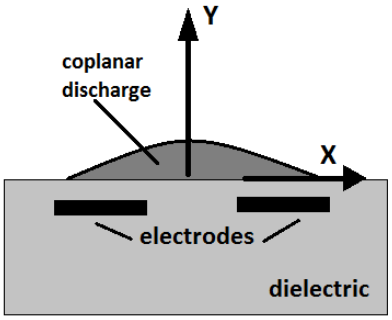

Fig. A6.3: Arrangement of a DBD in coplanar electrode arrangement [156].

Figure Fig. A6.3 shows the basic arrangement of coplanar DBD system. In a practical embodiment, the electrodes are in comb-interdigital arrangement with alternating polarity of the electrodes. Thus, a discharge occurs between all electrodes, and with a suitable arrangement it is possible to produce a homogeneous discharge over the entire dielectric surface.

The DBD plasma equipment that was used to activate the surface uses this variant of the DBD process. This process is called as the Diffuse Coplanar Surface Barrier (DCSBD) discharge.

A7 Design of Transformer Windings

A DC/DC converter with an extremely low input voltage requires a transformer with a large conversion ratio. The number of turns of the primary and secondary windings will therefore be very different and parasitic properties can be applied if the transformer is not designed properly. Therefore, the basic properties of the transformer and their influence on its behavior are discussed in more details in this chapter [52, 54].

Magnetic field generated by a coil.

From a physical point of view, a transformer is a system of two magnetically coupled coils. To describe the transformer, it is therefore necessary to first describe the behavior of the coil as a general inductor.

The magnetizing phenomena in the coil are governed by Faraday's law of electromagnetic induction:

$$\oint_l \vec{E} \cdot d\,\vec{l} = -\frac{d\Psi}{dt} \qquad \text{(A7.1)}$$

The voltage on the wire loop with length *l* will then be:

$$V(t) = \frac{d\Psi(t)}{dt} \qquad \text{(A7.2)}$$

It follows from equation (A7.2) that after applying a time-varying voltage *V(t)*, a variable magnetic field is created.

$$\Psi(t) = \Psi_0 + \int V(t) \cdot dt \qquad \text{(A7.3)}$$

This equation expresses the coupled magnetic flux through a coil. The Ψ_0 constant captures the initial conditions here. Clearly, the magnitude of the coupled magnetic flux is proportional to the voltage integral and may not be directly proportional to the coil current.

The following also applies to coupled magnetic flux:

$$\Psi(t) = \oint_S \vec{B}(t) \cdot \mathrm{d}\vec{S} \qquad \text{(A7.4)}$$

Where S is the oriented bounded area, the boundary of which is formed by the current position of the conductor. Assuming all induction lines passing through the ferromagnetic core, the coupled magnetic flux can be expressed very simply:

$$\Psi(t) \approx N \cdot B\,(t) \cdot S = N \cdot \Phi(t)$$

Where

$$\Phi(t) \approx B\,(t) \cdot S \qquad \text{(A7.5)}$$

If the magnetic flux through the loop can close outside the ferromagnetic core, the situation is more complicated. (This simplified consideration cannot be used at all for air coils.)

Linear model of voltage transformer

A simplified model of the transformer [55, 57] is shown in Fig. 5. The direction of the currents in both windings is chosen to correspond to the passive load. There is then a negative sign in the equations (expressing the voltage on the primary and secondary windings).

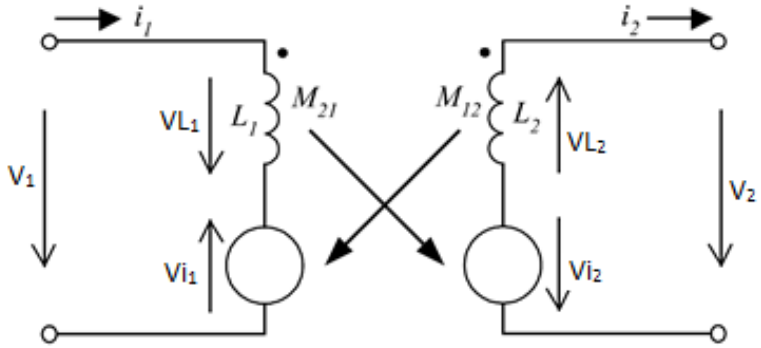

Fig. A7.1: The basic model of the transformer.

There is a mutual connection between the windings, which allows the formation of a secondary voltage. This coupling is expressed by the mutual inductance factors M_{12}, M_{21}. When a load is connected to the secondary winding, current i_2 begins to flow.

$$V_1(t) = V_{L1}(t) - V_{i1}(t) \qquad \text{(A7.6)}$$

$$V_2(t) = V_{i2}(t) - V_{L2}(t) \qquad \text{(A7.7)}$$

These equations can be rewritten to:

$$V_1(t) = L_1 \cdot \frac{di_1(t)}{dt} - M_{12} \cdot \frac{di_2(t)}{dt} \qquad \text{(A7.8)}$$

$$V_2(t) = M_{21} \cdot \frac{di_1(t)}{dt} - L_2 \cdot \frac{di_2(t)}{dt} \qquad \text{(A7.9)}$$

M is the mutual inductance between the primary and secondary windings.

$M = M_{12} = M_{21}$.

A relationship can be derived for mutual inductance:

$$M = k \cdot \sqrt{L_1 \cdot L_2} \qquad \text{(A7.10)}$$

The coupling factor k expresses the existence of a leakage magnetic flux. According to the size of the factor k, we can divide the transformers as follows [57, 55]:

Leakage transformer (*k* <1): Technically easy to implement (eg conventional mains transformers). The voltage and current transmission do not correspond to the ratio of the number of turns. The transformer has a large output reactance.

Tight transformer (*k* = 0.9990 to 0.9995): Technically feasible difficult to implement (eg measuring transformers, pulse transformers and transformers for switched power supplies). Voltage and current transmission are close to the ratio of the number of turns. The output reactance is significantly lower than with a leakage transformer.

Ideal transformer *(k* = 1): Technically not feasible. Voltage and current transmission are given by the ratio of the number of turns. The output reactance is zero.

The equations (A7.8) and (A7.9) represent the basic physical model of the transformer. They are clear but not suitable for practical use. In transformer circuit applications we need to know the input current and the output voltage of the transformer. Therefore, a modified model in the form of a hybrid H_U matrix is used:

$$i_1 = f_1(V_1, i_2) \qquad \text{(A7.11)}$$

$$V_2 = f_2(V_1, i_2) \qquad \text{(A7.12)}$$

We obtain the necessary equations after algebraic modifications of previously used relations.

The resulting formulas are:

$$i_1(t) = I_{\mu 0} + \frac{1}{L_1} \cdot \int V_1(t) \cdot dt + k \cdot \sqrt{\frac{L_2}{L_1}} \cdot i_2(t) \qquad \text{(A7.13)}$$

$$V_2(t) = k \cdot \sqrt{\frac{L_2}{L_1}} \cdot V_1(t) - L_2 \cdot (1 - k^2) \cdot \frac{di_2(t)}{dt} \qquad \text{(A7.14)}$$

The control variable here is the input voltage. Other variables can be calculated.

Note that $(L_2 / L_1)^{1/2}$ is transformer ratio N_2/N_1, as $L \sim N^2$.

The model according equations (3.13) and (3.14) can be used to derive all transformer parameters:

Magnetizing current: $i_\mu(t) = I_{\mu 0} + \frac{1}{L_1} \cdot \int V_1(t) \cdot dt$

Output current converted to primary: $i_2^{/}(t) = k \cdot \sqrt{\frac{L_2}{L_1}} \cdot i_2(t)$

No-load output voltage: $V_{2,0}(t) = k \cdot \sqrt{\frac{L_2}{L_1}} \cdot V_1(t)$

Secondary voltage drop: $\Delta u_2(t) = L_2 \cdot (1 - k^2) \cdot \frac{di_2(t)}{dt} = L_{\text{out}} \cdot \frac{di_2(t)}{dt}$

Output inductance (short-circuit input): $L_{\text{out}} = L_2 \cdot (1 - k^2)$

Voltage transmission (no load): $p_0 = k \cdot \sqrt{\frac{L_2}{L_1}}$

It follows from the above relations that the parameters of the transformer are very dependent on the coupling factor k.

1) The transformer ratio is equal to the ratio of the number of turns of the primary and secondary windings, N1 / N2, only in case of an ideal transformer when k = 1.

2) The output inductance of the transformer is zero only for an ideal transformer. As the coupling factor k decreases, the output inductance increases significantly.

Consequently, it is possible to build a simplified circuit model of a voltage transformer. A scheme of simplified circuit model of voltage transformer is in the figure Fig.A7.2.

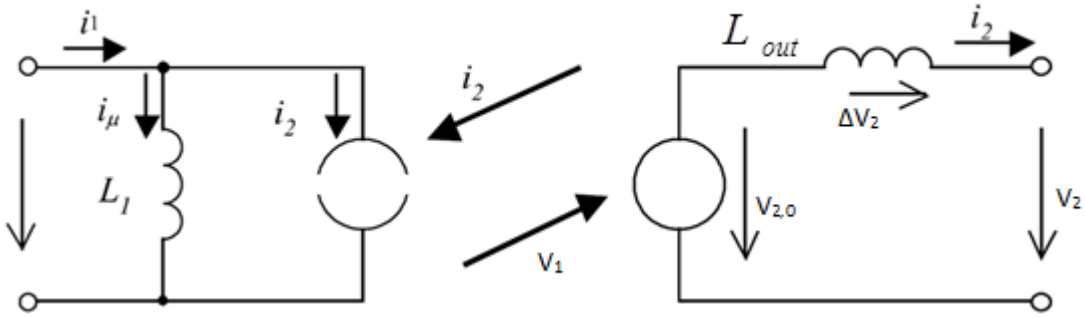

Fig. A7.2: Simplified model of the transformer.

Do design the magnetic circuit of a transformer first it is necessary to determine the number of turns of the primary winding. For a given size, shape and frequency of the primary voltage, the maximum permissible induction B_{max} must not be exceeded for the core material used. The number of turns of the secondary winding is calculated according to the required output voltage.

Note that in simplified calculations, the coupling factor $k = 1$ is assumed.

A8 Leakage Resistance of Photovoltaic cells

Dynamic resistance of PN junction

When forward biased voltage is applied to the p-n junction diode, the width of depletion region decreases. However, the depletion region cannot be completely vanished. There exists a thin depletion region or depletion layer in the forward biased diode. Therefore, a thin depletion region and atoms in the diode offer some resistance to electric current. This resistance is called forward resistance.

Static and dynamic resistance of PN junction have the same meaning as in case of other devices. To drive static and dynamic resistance we compute at first the junction voltage:

$$V = V_T \ln\left(1 + \frac{I}{I_0}\right) \approx V_T \ln\left(\frac{I}{I_0}\right) \qquad \text{(A8.1)}$$

Second relation in equation (A8.1) is valid for $I >> I_0$.

From equation (3.25) it is seen that the static resistance is nonlinear function of junction voltage or current. For practical use the static resistance is not much important.

On the other hand the dynamic resistance of the junction (which is the junction resistance for AC current and voltage of small amplitude) is very useful in consideration about semiconductor circuits. To obtain the dynamic resistance we must compute First derivative of the junction voltage:

$$R_d = \frac{dV}{dI} = \frac{V_T}{(I + I_0)I_0} \cdot \frac{I_0}{1} = \frac{V_T}{I + I_0} \approx \frac{V_T}{I} \qquad \text{(A8.2)}$$

The last relation equation (A8.2) is again valid for $I >> I_0$.

For $I = V = 0$ both static and dynamic resistances have the same value:

$$R_0 = R_{d0} = \frac{V_T}{I_0} \qquad \text{(A8.3)}$$

Shunt resistance

Significant power losses caused by the presence of shunt resistance, R_{SH}, are typically due to manufacturing defects, rather than poor solar cell design. Low shunt resistance causes power losses in solar cells by providing an alternate current path for the light-generated current. Such a diversion reduces the amount of current flowing through the solar cell junction and reduces the voltage from the solar cell. The effect of shunt resistance is particularly severe at low light levels, since there will be less light-generated current. The loss of this current to the shunt therefore has a large impact. In addition, at lower voltage

where the effective resistance of the solar cell is high, the impact of a resistance in parallel is large.

Shunt path also exists due to the effect of shadowing in the typical solar PV cell. When connecting a number of cells in series under shadow effect all the cells may not produce the same amount of current. Due to the shadow problem, a partial amount of current will flow to the shunt resistance and the current flow through the load resistance is reduced. Thus, the shunt current is the current that finds a way around the solar cell junction without producing power leading to the output.

Best quality cells have large value of shunt resistance and hence low shunt current. Shunt current may lead to heating of the cell and hotspots will appear in the modules, affecting the encapsulating material.

Shunt current is typically associated with highly localized defects either within the solar cell or at cell inter connections. In ideal conditions, shunt resistance is assumed to be an infinite value, and then chances of current flow through the shunt resistance are nearly zero.

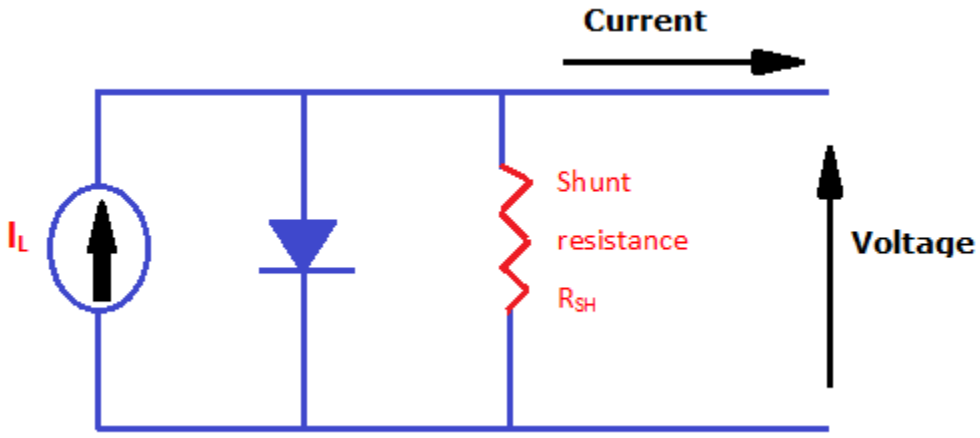

Fig. A8.1: Simplified model Shunt resistance [75]

The figure Fig. A8.1 shows the equivalent circuit of solar cell, in operating process. I_L is generated current for which I_D current increases exponentially. The two types of resistances, namely series or parallel resistances often determine the performance of a solar cell.

A considerable amount of power losses in the solar cell caused by the presence of parallel resistance is typically due to manufacturing defects. Shunt resistance would cause power losses in solar photovoltaic module, providing an alternate path of light generated current.

The current flow through the output circuit, due to this shunt-load current, decreases simultaneously.

Decreases of load current gives a large impact on the solar photovoltaic module which in turn, reduces the characteristic parameters like fill factor, output power and efficiency. The effect of parallel resistance performance is very high at changing the light-illumination. At lower level of irradiation correspondingly changes the parallel resistance value. Hence, the variation in solar irradiation plays a major role of parasitic shunt resistance value by which, output could be changed.

The equation for a solar cell in the presence of a shunt resistance is:

$$I = I_L - I_0 \exp\left(e^{q(V_L)+I_S R_S} - 1\right) - \frac{V_L + I_L R_S}{R_{SH}}$$

Decrease in shunt resistance

The shunt resistance represents any parallel high conductivity paths (shunt) across the solar cell p-n junction or on the cell-edges. These are due to the crystal scratch and impurities in and near the junction and give rise to the shunt current. Shunt paths lead the current away from the intentional, and their effects are detrimental to the module performance mainly at low light intensity levels.

A9 Efficiency of Low Light Photovoltaic Converters

Efficiency of photovoltaic cells is highly dependent on their own losses, which are mostly determined by losses on the series resistance, R_S, and on the leakage (shunt) resistance, R_{SH}, of the cell. However, both parameters, R_S and R_{SH}, are also very important when considering the behavior of photovoltaic cells in low light intensity.

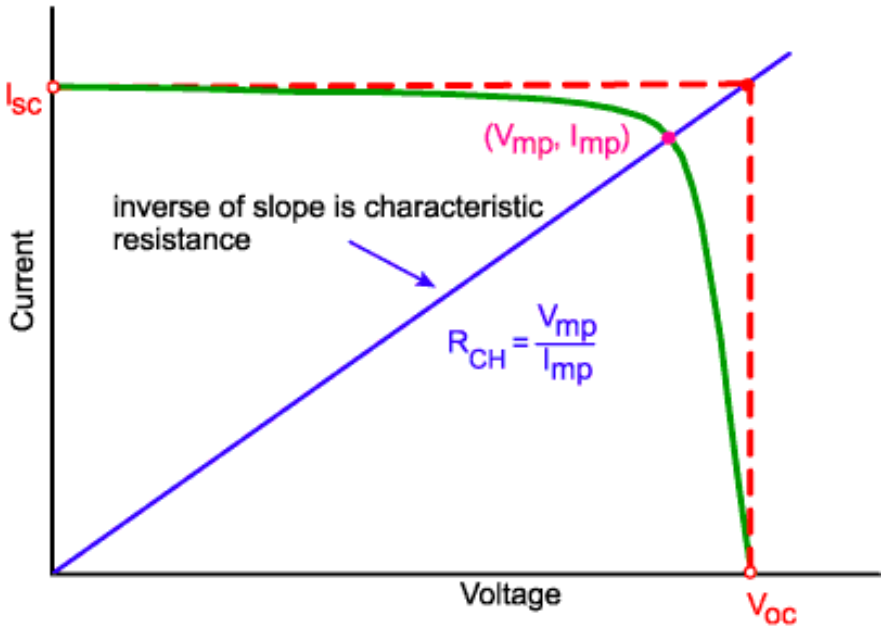

Fig. A9.1: Characteristic resistance of the photovoltaic cell [75]

Characteristic resistance of the photovoltaic cell

Characteristic resistance, R_{CH}, is very useful when considering the efficiency of photovoltaic cells.

The characteristic resistance is determined as the inverse of slope of the line connecting the origin of the coordinates to the working point for maximal output power.

For the cells with low power loss this parameter can be approximated by V_{OC} and I_{SC}:

R_{CH} is given in Ω when using I_{MP} or I_{SC}. Alternatively, using the current density (J_{MP} or J_{SC}) then the units of R_{CH} are given in Ωcm².

The characteristic resistance is useful because it puts in mutual relation series resistance and shunt resistance and fractional power on the cell.

As an example we will use the crystalline silicon cell measured in Chapter 3.2. For the illumination given the voltage was 0.61 V and current density was 28 mA/cm².

This gives the Characteristic resistance:

R_{CH} = 610 mV/ 28 mA = 21.8 Ωcm².

For the case that the power loss caused by series and shunt resistances in not much more than about 20% the characteristic resistance also allows an estimation of the power loss by a mutual dependence between the fractional power and both resistances.

Power loss caused by series resistance:

$f = R_S / R_{CH}$ or $f . R_{CH} = R_S$

Where f is the fraction power loss which has the value from 0 to 1. R_S must have the same units (dimensions) as R_{CH}, that is Ω or Ω cm².

For crystalline silicon cell measured in Chapter 3.2 the series resistance is

R_S = 1.9 Ω cm², Then for R_{CH} = 21.8 Ωcm². The resulting fractional power loss is

$f = R_S / R_{CH}$ = 1,9/21,8 = 0,087 = 8,7 %.

Power loss casused by shunt resistance:

Similarly, the estimation of power loss related to the shunt resistance can be done by using the relation :

$R_{SH} = R_{CH} / f$

or $f . R_{SH} = R_{CH}$

Again, f is here the fraction power loss which has the value from 0 to 1. R_{SH} must have same units as R_{CH}, either or Ω or Ω cm².

Measured values of silicon crystalline silicon cell were:

R_{shunt} = 5062 Ω cm², and R_{CH} = 21,8 Ω cm²

Then the fractional power loss is

$f = R_{CH} / R_{SH}$ = 21,8 / 5062 = 0,0043 = 0,43 %

Power loss in low light conditions

Obviously, the characteristic resistance increases with decreasing light intensity. Because the voltage decreases logarithmically with the intensity of illumination, the change in the characteristic resistance is given mainly by the change in the current I_{SC0} or the current density J_{SC0}.

When the light intensity decreases by one order of magnitude, the voltage drops by approximately 100 mV and the current drops 10 times. The characteristic resistance of the measured Si cell will then be:

R_{CH} = 0,51 V/ 2.8 mA/cm² = 510 mV / 2.8 mA/cm² = 182 Ωcm².

Consequently, the fractional power loss on series resistance is

f = R_S / R_{CH} = 1,9/182 = 0,0104= 1,04 %.

However the fractional power loss on the shunt resistance will be in this case larger:

f = R_{CH} / R_{SH} = 182/5062 = 0.036 = 3,6 %

Further decrease about one order gives approximately 410 mv and 0.28 mA. Characteristic resistance then will be:

R_{CH} = 410 mV/ 0.28 mA/cm². = 1464 Ωcm².

When estimating the power loss, the fractional loss on the series resistance will be negligible and the fractional power loss on the shunt resistance will be

f = R_{CH} / R_{SH} = 1464/5062 = 0.29 = 29 %

It is clearly visible that the shunt resistance is a key parameter for low light applications of photovoltaic cells. It is necessary that its value should be in the range of several kΩ per cm^2, to have the power losses in low light condition on the acceptable level. Among the measured cells, only crystalline silicon cells meet this requirement.

This estimation is already very approximate because no longer meets the above condition that power losses should not significantly exceed 20 %. A more accurate evaluation of the power dissipation can be made by considering the actual current flowing through the leakage resistor as is shown in next paragraph.

Shunt resistance in low light conditions

Shunt resistance is a current source that takes the generated current from the cell.

For illustration we will use data from experiments with crystalline silicone cells described in Chapter 3.2. Here, a voltage of 610 mV was measured under the given illumination of the cell. The value of the measured leakage resistance was R_S = 5062 Ω cm^2

The leakage current density at no-load voltage will then be:

J_{SH} = 610 mV / 5062 Ω cm^2 = 120 μA / cm^2

Compared to the current I_{SC0} = 28 mA/cm^2, this current is very small and can be neglected in most considerations.

When the light intensity is reduced, the voltage on the cell drops. The voltage drop is less than 100 mV for each order of illumination intensity.

For clarity, we again consider the same conditions which were used by testing crystalline silicon cells in an experiment with DC / DC converters. The voltage on the cells here was around 300 mV for all cells. For a given leakage resistance, the leakage current corresponds to:

I_{LSH} = 300 mV / 5062 Ω cm^2 = 59.3 μA /cm^2

Tables Tab A9.1 and Tab A9.2 show the current density at which the individual cells worked. For all photovoltaic cells, this value is around 80 μA /cm^2.

The estimated current density of the current drawn through the leakage resistor is in this case comparable to the current density of the current supplied to the input of the DC to DC converter. The sum of both currents is approximately the same for all cells and takes on value around J_{SUM} = 140 μA /cm^2.

Note:.
In experiments with DC/DC converters, a 50 W halogen lamp placed at a distance of d_{DC} =150 cm was used as the lighting source. According to the balance sheet explained in detail in chapter 3.2.2, a lighting of E_{DC} = 444 lx corresponds to this situation.
In an experiment comparing individual photovoltaic cells, a current density of 28 mA / cm^2 was measured for a crystalline silicon cell. Here, the light intensity was determined by a pair of 50 W halogen bulbs placed at a distance of d_{CMP} = 155 mm from the irradiated photovoltaic cell. Using the same balance as in the previous case, the irradiation intensity was estimated at E_{CMP} = 83240 lx. The actual value may have some variance due to the estimation of the radiation intensity according to the power of the lamp and the sensitivity to set the exact distance in such small dimensions.
The ratio of the light intensity applied in the first experiment to the light intensity which was set for testing cells with a DC / DC converter is in this case:

E_{CMP}/ E_{DC} = 83240 / 444 = 187,5

And the corresponding current ratio:

J_{SC0} / J_{SUM} = (28 mA/cm^2) / (140 μA /cm^2) = 200

It is obvious that the ratios of the light intensity in the respective experiments and the ratios of the measured currents correspond to each other well. However, equality of currents does not mean lossless conversion. It should be considered that the voltage on the cell in this case is approximately half compared to full ilumination and a large part of the generated current is dissipated by a leakage resistance.

The conversion efficiency compared to the direct power consumption of a fully illuminated cell it is therefore possible to estimate as follows:

η_{LL} = 0.5 x (80/140) = 8/28 = 0.286 ~ 28.6 %

Efficiency of designed DC / DC converters

Additional losses must be considered in the DC / DC converter. Tables Tab A9.1 and Tab A9.1 show the input power at the input of both converters - Armstrong oscillator and single J-FET DC / DC converter. The input power is determined from the voltage and current of the photovoltaic cell. The power at the inverter output is determined by the output voltage and the load resistor R_L = 100 kΩ.

Samples: (Parameters are given in Chapter 3.2) Crystalline silicon cells. Screen printed BUS-bars. Area and dimension as follow:
PH_1, PH_3: A = 15 cm^2 (50 mm x 30 mm) ;
PH_2: A = 25 cm^2 (50 mm x 50 mm) ;
PH_4a, PH_4b: A = 25 cm^2 (50 mm x 50 mm) ;
PH_5a, PH_5b: A = 15 cm^2 (50 mm x 50 mm)

Tab A9.1: Photovoltaic EH transducers. Measured values of input and output parameters using single J-FET DC/DC converter. T= 300 K

Sample	PH_1	PH 2	PH_3	PH _4_a	PH _4_b	PH _5_a	PH _5_b
V_{EP} *[V]*	0.31	0.33	0.30	0.31	0.32		0.33
I_{EP} *[mA]*	1.24	2.01	1,15	2.00	1.90		1.17
V_{OUT} *[V]*	3.5	4.6	3.3	4.4	4.5		3.4
P_{IN} *[μW]*	384	660	345	620	627		386
P_{OUT} *[μW]*	123	212	109	194	203		116
η [%]	32.0	32.1	31.6	31.3	32.4		30.1
I_{PA}*[*μA/cm^2*]*	83.0	80.4	76.7	80.0	76.0		78.0

The efficiency of the single J-FET converter with the power efficiency $\eta_A \sim 35\%$ is about ten percent higher than the efficiency of the converter with an Armstrong oscillator with the power efficiency $\eta_{SF} \sim 32\%$.

In both cases, however, it is necessary to consider the relatively large power loss that DC/DC converters will introduce into the energy conversion process.

Compared to direct energy consumption from a photovoltaic cell at full illumination, the overall efficiency is in case of the Armstrong oscillator approximately:

$\eta_{OA} = \eta_{LL} . \eta_A = 0.28 \cdot 0.32 = 0.0896 \sim 8.96\ \% \cdot$

Tab A9.2: Photovoltaic EH transducers. Measured values of input and output parameters using single J-FET DC/DC converter. T= 300 K

Sample	PH_1	PH_2	PH_3	PH _4a	PH_4b	PH _5a	PH _5b
V_{EP} *[V]*		0.32	0.29		0.31	0.29	
I_{EP} *[mA]*		2.1	1.24		2,1	1.3	
V_{OUT} *[V]*		4.9	3.6		4.8	3.6	
P_{IN} *[μW]*		672	356		651	377	
P_{OUT} *[μW]*		240	130		230	130	
η *[%]*		35.7	36.5		35.3	34.5	
J_P*[*μA/cm^2*]*		84	82.6		84	86.7	

In the case of the single J-FET converter, the overall conversion efficiency is

$\eta_{OSF} = \eta_{LL} \cdot \eta_{SF} = 0.28 \cdot 0.35 = 0.0896 \sim 9.8\ \%$

This value is close to 10% compared to the direct power consumption of a fully illuminated cell. This is, of course, very small value. In many cases, however, this solution may be suitable if no other source is available.

A10 Design of planar transformer

In this section, there are photographs illustrating the process of manufacturing the primary and secondary windings of a planar transformer on a printed circuit board.

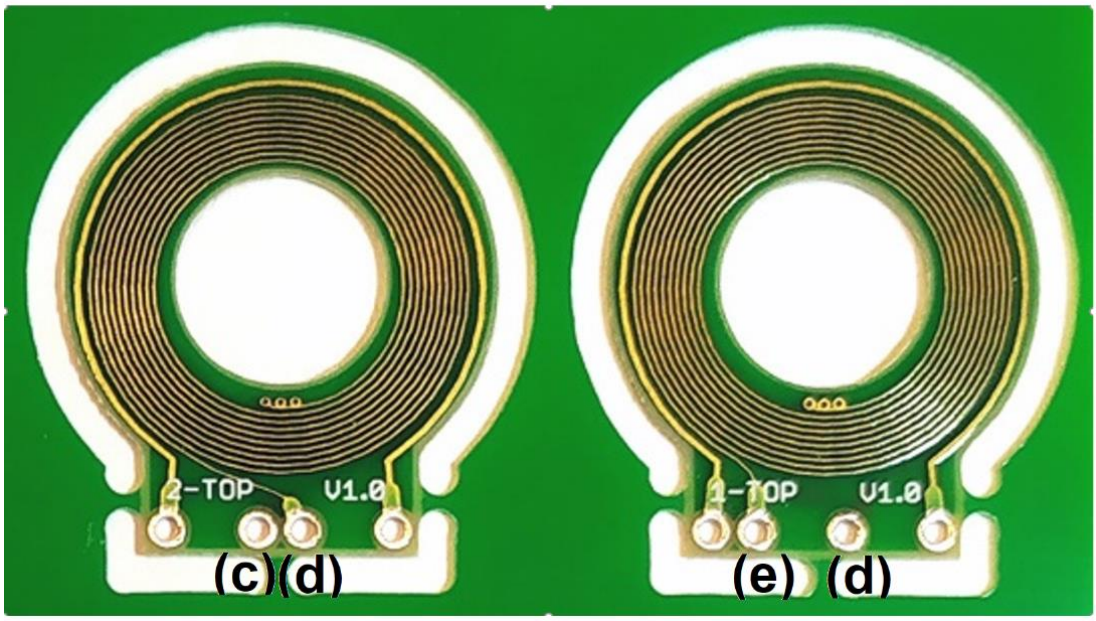

Fig. A10.1: Placement of primary and secondary windings on PCBs no_1 and no_2.

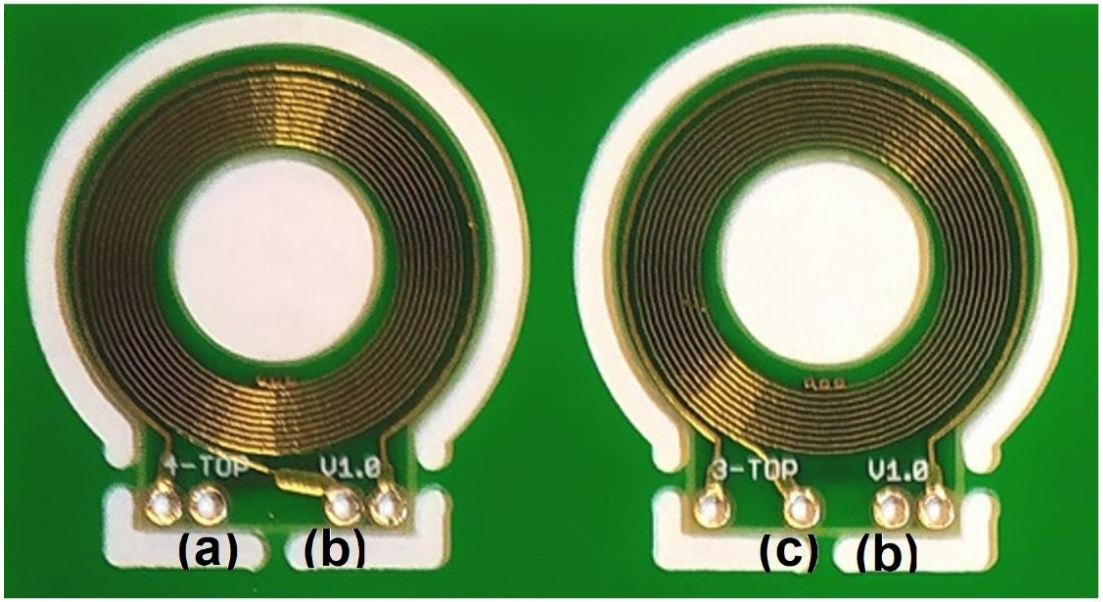

Fig. A10.2: Placement of primary and secondary windings on PCBs no_3 and no_4.

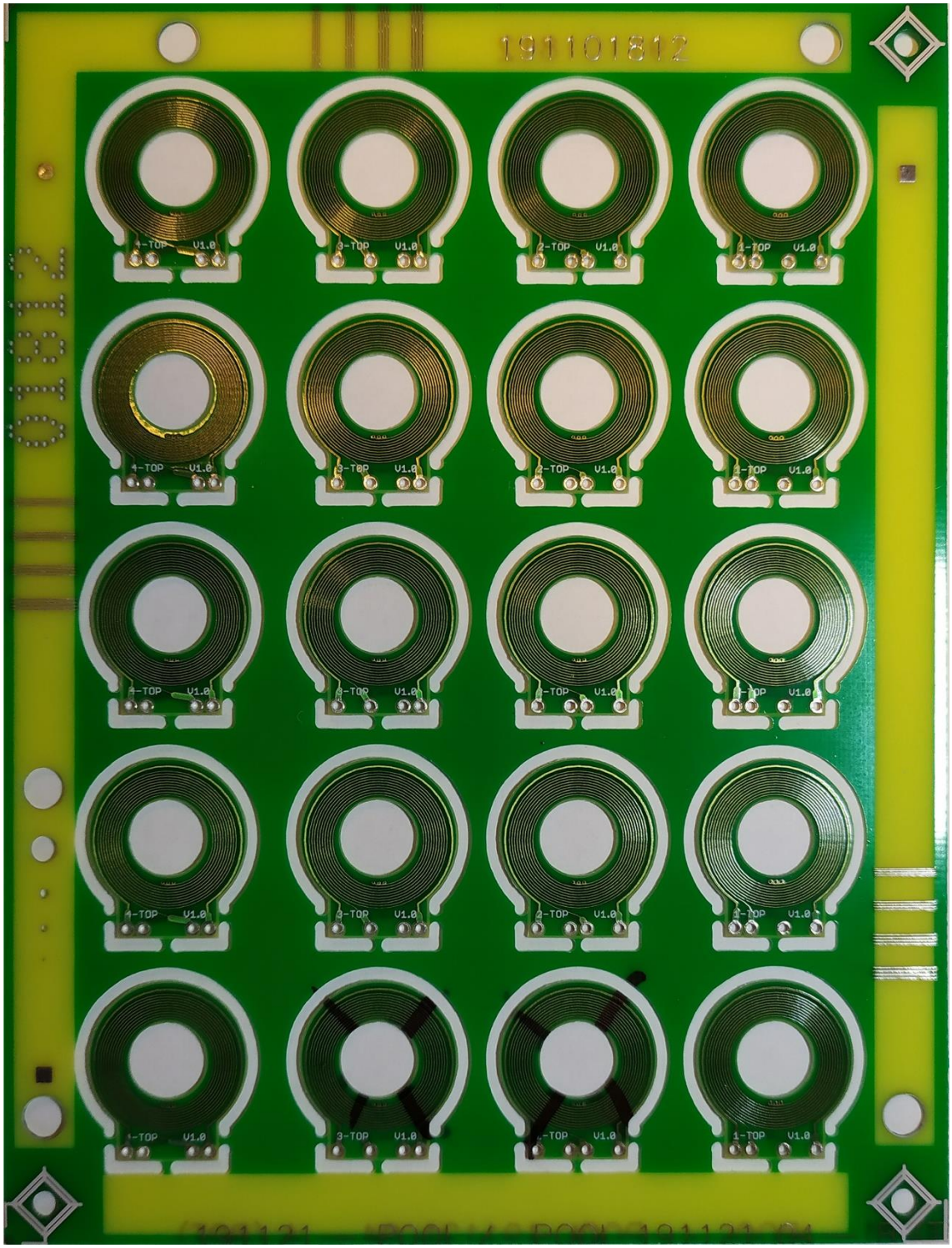

Fig. A10.3: Arrangement of individual boards no_1 to no_4 on a printed circuit board blank.

A11 PCB for DC to DC converters

In this section, there are photographs illustrating the process of manufacturing of individual PCBs for Single J-FET DC to DC converter, for DC converter based on Armstrong oscillator and for the generator of starting pulses.

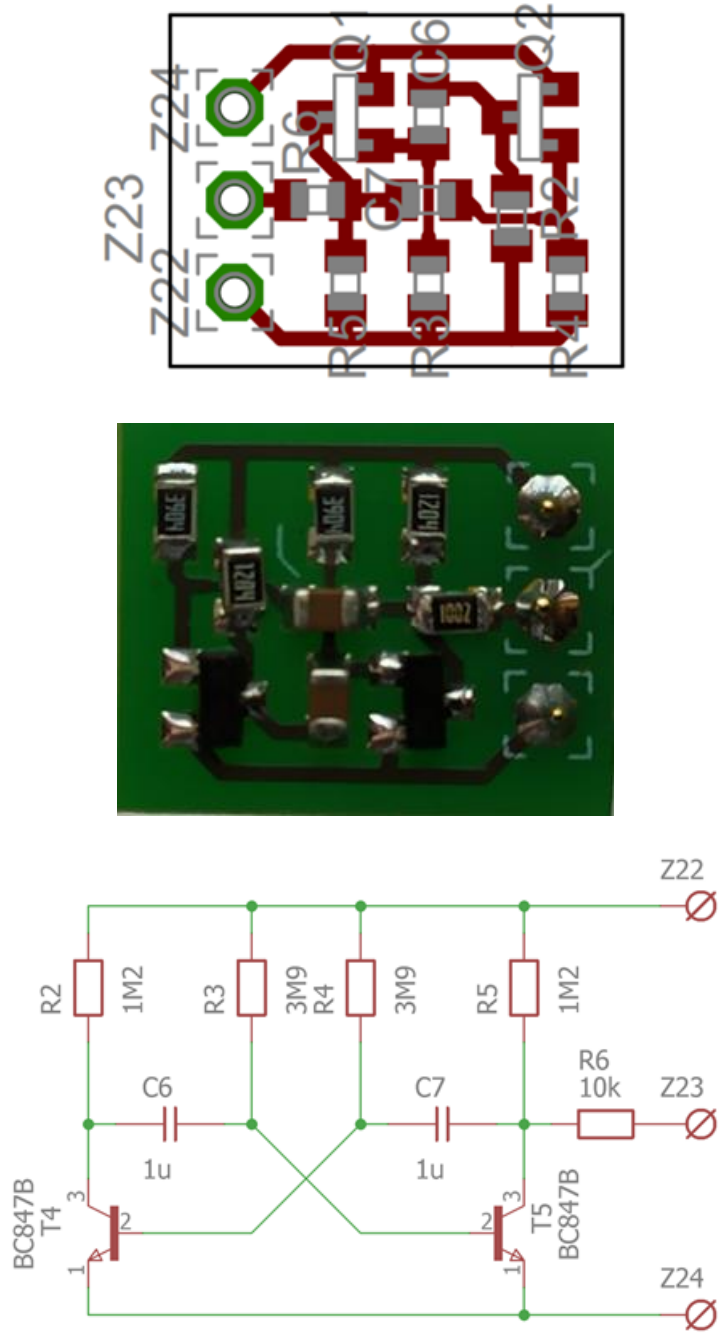

Fig. A11.6: **S**tarting pulse generator. Dimensions: 16 mm x 12 mm

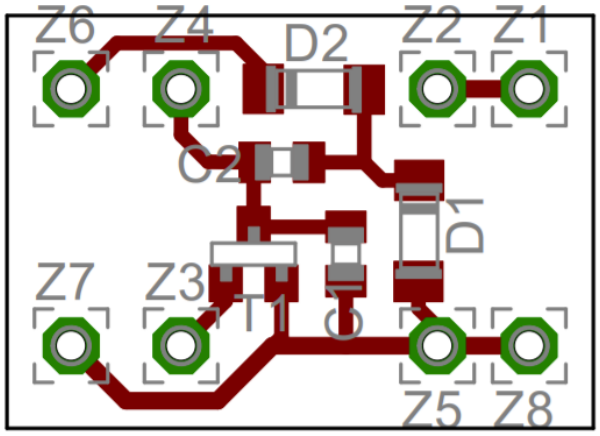

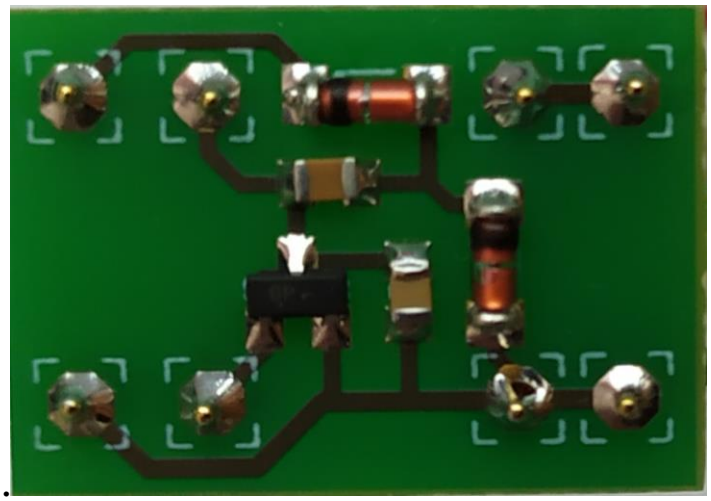

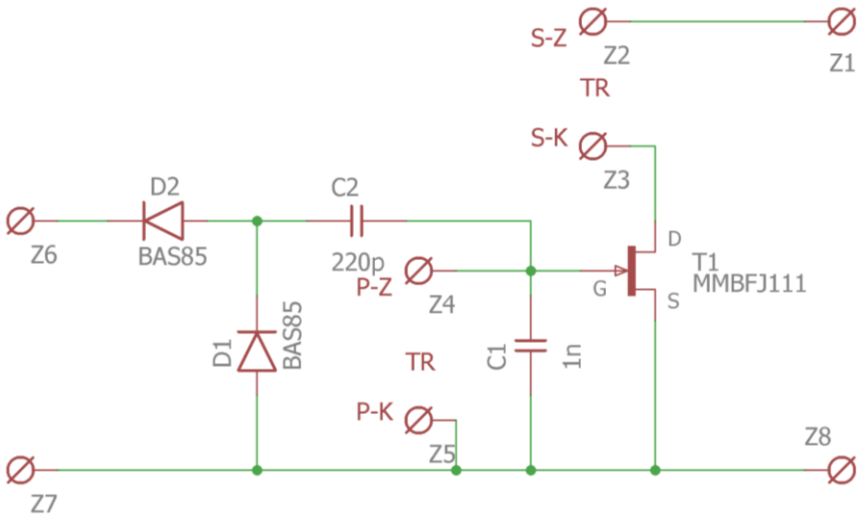

Fig. A11.4: Armstrong's oscillator. Dimensions: 21 mm x 15 mm

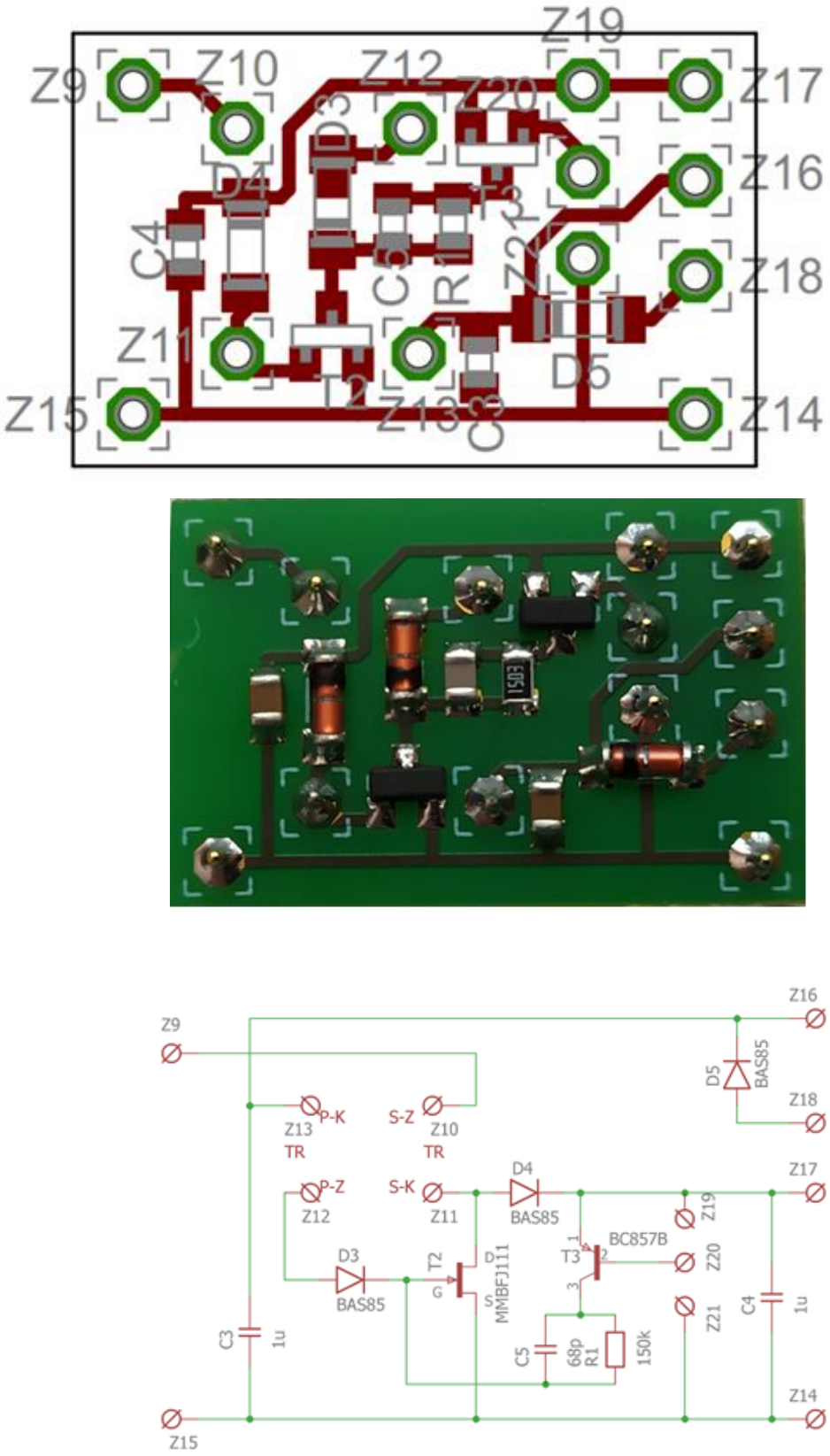

Fig. A11.5: Single J-FET DC / DC converter. 16 mm x 12 mm

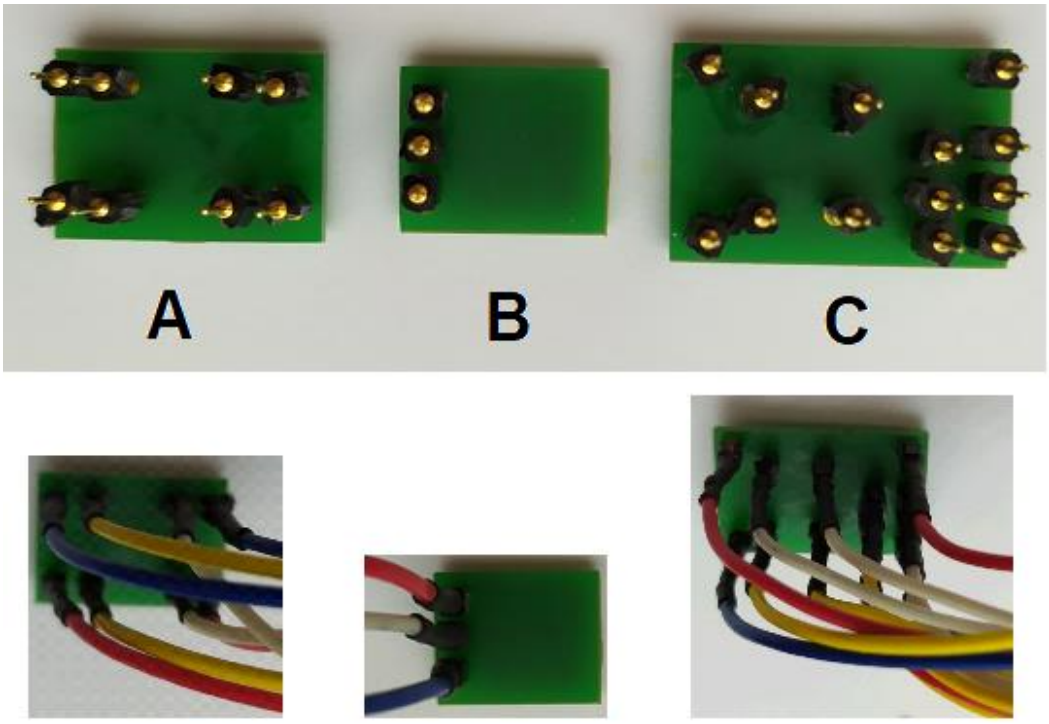

Fig. A11.6: DC to DC converters: Connection via connectors on the back side.

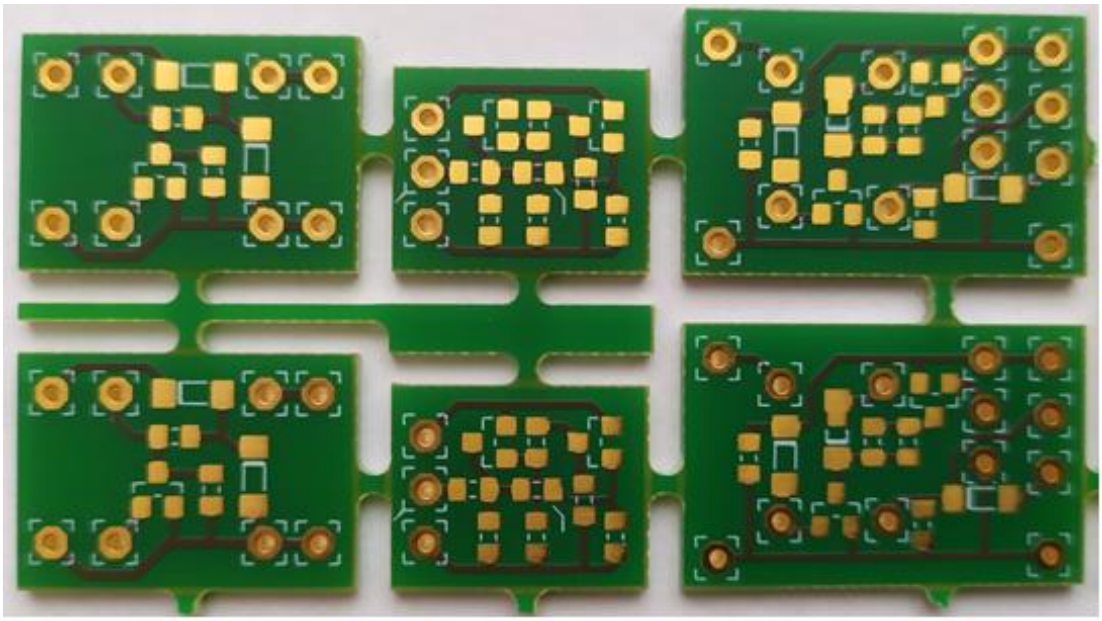

Fig. A11.6: DC to DC converters: Layout of individual PCBs on the blank.

A12 Thermoelectric generator

In this part, the processes for the preparation of a model thermocouple for verifying the correctness of the design of a thermoelectric transducer with a vertical arrangement are briefly described.

The mechanical assembly of the thermoelectric generator is reminded in figure Fig. 12.1A (see also Fig.50 in Chapter 3.3.3). To verify the functionality, layers for one thermocouple were prepared in the arrangement which is obviously shown in figure Fig. 12.1B.

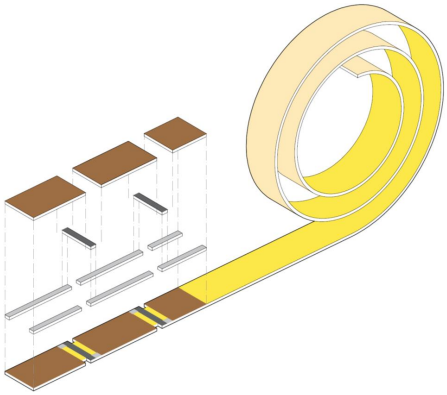

A

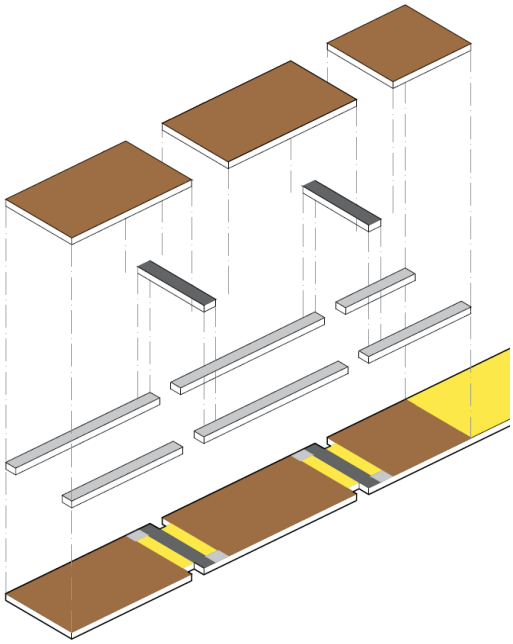

B

Fig. A12.1: The mechanical assembly of the thermoelectric generator.

The supplied Ni:P layer deposited by electrodeless deposition was used for the model cell. For experimental verification of the functionality of the cell, it was therefore necessary to optimize the setting of parameters for printing the PEDOT: PSS layer and, consequently, after printing the optimized layer to measure the temperature sensitivity of the resulting structure. The work would not be possible without material support and professional assistance from the BUT Faculty of Chemistry, where there is relevant technological and material equipment and extensive experience with the application of printed PEDOT: PSS layers [49,50].

The process of preparing the PEDOT layer: PSS can be divided into several sub-steps:

Selection of a suitable substrate.
Substrate surface treatment to increase adhesion.
Selection of PEDOT: PSS paste and setting of its exact composition.
Preparation of PEDOT: PSS paste for printing. Optimizing print parameter settings.
Printing and thermal annealing of PEDOT: PSS layer.
Functionality verification by measuring temperature sensitivity.

Substrates

Polyethylene terephthalate

Polyethylene terephthalate (PET) is a thermoplastic polymer of the polyester family. Its has working range from – 40 °C up to115 °C. However, the upper temperature is already the maximum usable temperature, because at temperatures above 90 °C, deformations and irreversible changes can already occur. Obviously, for the intended use, this material has a small temperature range.

Polyethylene naphthalate

Polyethylene naphthalate (PEN) is similar to a PET compound and is often intended as a PET replacement. Its resistance to heat is greater and it can be used up to 180 °C. Similarly, as in case of PET, the optimal operation temperature is lower and should not exceed about 140 °C. So, for the intended use, this material has a small temperature range. However, its operating temperature is comparable to the maximum operating temperature of PEDOT: PSS.

Poly(4,4'-oxydiphenylene pyromellitimide)

Poly(4,4'-oxydiphenilene pyromellitimide) is known under the name Kapton. It has wide temperature working range in comparison with previous candidates. Kapton can be used in from - 270°C up to + 300 °C. Due to the high heat resistance, this material (purchased from Goodfellow) with thickness of 50 μm was chosen. Structure of Poly(4,4'-oxydiphenilene pyromellitimide) is shown in figure Fig. A12.2.

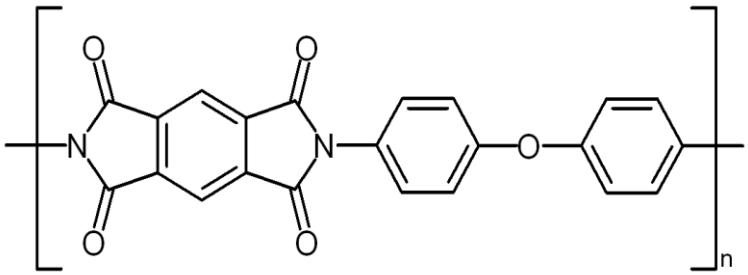

Fig. A12.2: Poly(4,4'-oxydiphenylene pyromellitimide) [118].

Surface treatment

For successful deposition, it is necessary to treat the surface of the substrate. BDB plasma surface treatment proved to be the best for this process. Plasma treating significantly modifies surface energy and causes a decrease in surface tension.

The difference in the structure of the layer deposited on the treated and untreated surface is very significant. An example is shown in figure Fig. A12.3.

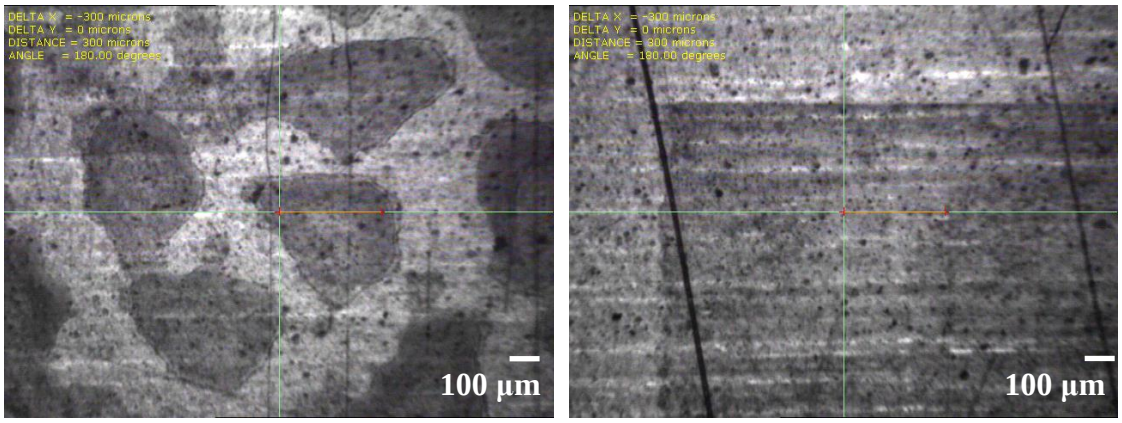

Fig. A12.3: The difference in PEDOT:PSS layer formation in case of plasma treated substrate (Right) and the substrate without plasma treatment (Left)

Surface activation prior to printing by plasma DBD treatment is therefore widely used and proved to be very well suited for the experiment.

Selection of PEDOT: PSS; Selection of the paste and setting of its exact composition

For the intended use is suitable PEDOT:PSS paste Heraeus with trade name Clevios™ S. Paste Clevios™ S V3 was selected from this type-series which has viscosity from 15 dPa·s to 60 dPa·s, sheet resistance 350 Ω/square to 500 Ω/square and solids content 3%.

Preparation of PEDOT: PSS; Optimizing print parameter settings

The supplied paste is in the form of a gel, which must be mixed very well to reduce its viscosity. The paste must be mixed for a very long time to sufficiently reduce the viscosity and thus ensure good printing properties. Stirring takes place in a magnetic stirrer. The required mixing time depends on the temperature. At elevated temperatures, the required mixing time is reduced.

Once mixing is complete, the viscosity of the paste returns relatively quickly to its original value. Therefore, the printing operation must be performed shortly after mixing. The delay should not exceed a few minutes.

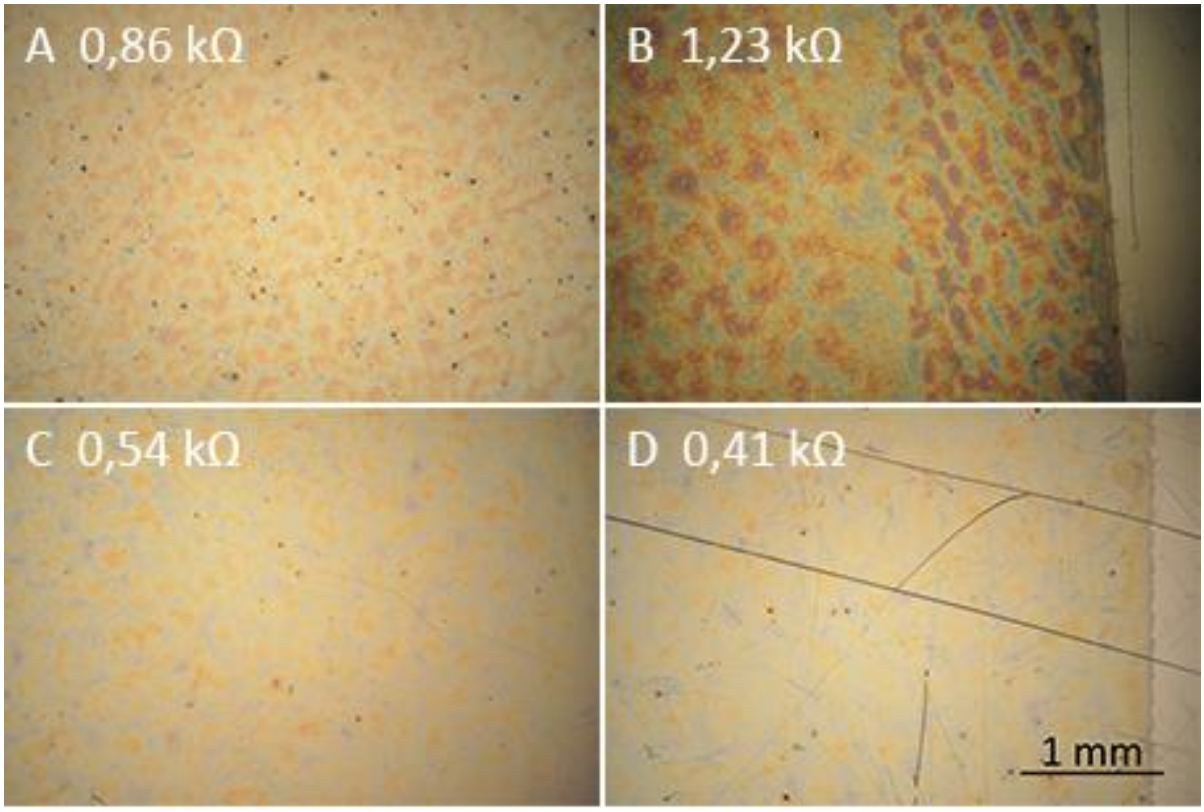

Fig. A12.4: PEDOT: PSS layers; paste Clevios S V3 : Influence of stirring.
A) no stirring, (B) stirring 30 min in an ultrasonic bath, (C) stirring 2 h (D) stirring 70 h at 25 °C.

The resulting parameters of the printed layers considerably depend on the mixing time and the mixing intensity. Of the monitored properties especially the surface structure, the thickness of the layer and the sheet resistance of the layer are affected. The extent of the dependence it is possible to judge according to the figure Fig. A12.4. Both a change in the structure and a significant decrease in the resistivity of the layer, which is more than twofold, are evident here.

The printing mechanism also significantly depends on the roughness of the screen printing sieve and on the tear-off that is set during printing. The process of penetrating the paste through the sieve further depends on the speed of movement of the printing squeegee.

The effect of sieve roughness and sieve tear is evident from figure Fig.A12.5. Obviously, a coarser sieve gives better results. With the coarser screen (140F), it is very clear that greater tear provides a finer layer structure and lower resistivity.

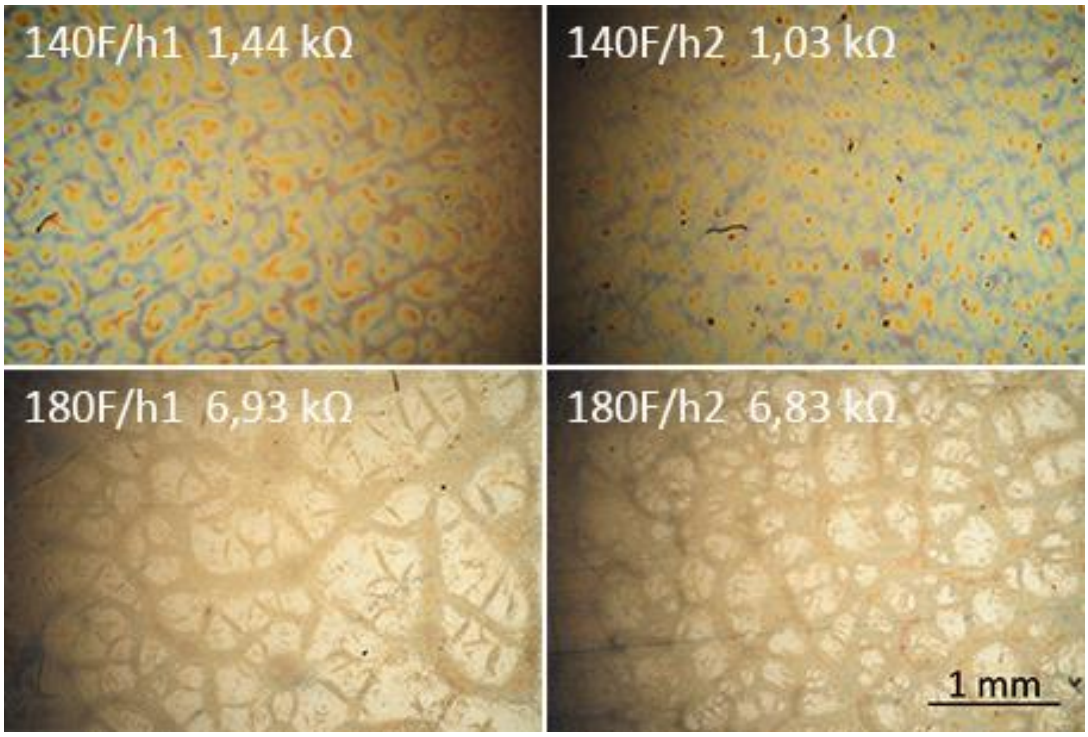

Fig. A12.5: Figure: Micrographs of prepared experimental layers showing the effect of sieves 180F and 140F. The resulting experimental layers using a 1 mm (h1) tear are in the left column and the results for a 2 mm (h2) tear are in the right column.

As the printing speed increases, the properties of the layers improve with all combinations of screen roughness and tear. For high speeds, a larger tear-off is advantageous. However, for fine motifs, a larger tear may result in reduced print accuracy.

In our case of thermoelectric generator, the PEDOT: PSS active layer for the printed thermocouple has relatively large dimensions. Consequently, this disadvantage is not significant in our case. Thus, a maximum print speed (2 $m \cdot s^{-1}$) and 3 mm tear-off was selected.

Printing and thermal annealing of PEDOT: PSS layer

PEDOT: PSS layers were applied to the supplied substrates with a galvanically applied Ni: P layer. The model thermocouple was made according to the procedure described in chapter 3.3 by superimposing two printed PEDOT:PSS layers.

The printed layers were annealed after drying. Drying was carried out for 30 minutes at 120 °C. The time of annealing was 15 minutes and annealing temperature was 125 °C.

Functionality verification by measuring temperature sensitivity

The temperature sensitivity was measured on the finished samples. The temperature was measured with a non-contact thermometer and the voltage with laboratory multimeter KEYSIGHT 34465A.

At an ambient temperature of 22 °C and a heated surface temperature of 70 °C, a voltage difference V_T = 1.380 mV was measured.

This corresponds to the temperature sensitivity:

$S_T = V_T / (T_1 - T_2) = 1.380 / 48 = 28{,}75 \cdot 10^{-3} = 28{,}75\ \mu V/K$.

Here, T_1 and T_2 are the temperatures in Kelvin.

A13 Symbols and abbreviations

C	Capacitance
D	Diode
D	Duty cycle
E	Energy
E_G	Band Gap energy
f	Frequency
I	Current
I_S	Saturation current
I_{SCA}	Short-circuit current
K	Thermal conductivity
L	inductance
M	Mutual inductance
P	Power
PF	Power factor
P_H	Hysteresis loss
P_E	Eddy current loss
Q	Charge
R	Resistance
R_{CH}	Characteristic resistance
R_S	series resistance
R_{SH}	Leakage (shunt) resistance
R_{DSON}	Channel resistance
S_{12}	Temperature sensitivity
T	Temperature
V	Voltage
V_{OC}	Open Circuit Voltage
V_T	Thermal voltage
V_{TH}	Threshold voltage
V_{BE}	Voltage base-emitter
V_{CE}	Voltage collector-emitter
W	*P*ower
ZT	Figure of merit
α	Seebeck coefficient
λ_0	Threshold wavelength
σ	Electrical conductivity
η	Efficiency

BD	Bulk-driven transistor
BJT	Bipolar junction transistor
CdTe	Cadmium telluride
CGS	Copper indium gallium selenide
CIGS	Copper indium gallium selenide
CIS	Copper indium selenide
CS	Current source
DBD	Dielectric barrier discharge
EH	Energy harvesting
GBW	Gain bandwith
IPA	Iso-Propyl-Alcohol
ITO	Indium thin oxid
LP	Low power
LV	Low voltage
PCB	Printed circuit board
PV	Photovoltaic
PCT	Parallel-connected tandem
RH	Relative humidity
TEG	Thermoelectric generators

DCSBD	Diffuse coplanar surface barrier discharge
HOMO	Highest occupied molecular orbital
LUMO	Lowest unoccupied molecular orbital
JFET	Junction field effect transistor
MOSFET	Metal oxide field effect transistor
PEDOT	Poly 3, 4 - ethylene - dioxy - thiophene
PSS	Poly - styrene - sulfonate